2nd Conference
for Green Engineering, Sustainable Materials and Technologies for Circular Economy
GREEN CIRC 2025

P R O C E E D I N G S

Faculty of Technology and Metallurgy,
University Ss. Cyril and Methodius in Skopje,
April 22–25, 2025

2nd Conference for Green Engineering, Sustainable Materials and Technologies for Circular Economy

CIRC 2025

P R O C E E D I N G S

Faculty of Technology and Metallurgy,
University Ss. Cyril and Methodius in Skopje

22–25 April, 2025

Title:
2nd Conference for Green Engineering, Sustainable Materials and Technologies for Circular Economy, GREEN CIRC 2025, PROCEEDINGS

Publisher:
Ss. Cyril and Methodius University in Skopje,
Faculty of Technology and Metallurgy,
"Rudjer Bošković" 16, 1000 Skopje
www.tmf.ukim.edu.mk

Editor for publishing of Faculty of Technology and Metallurgy:
Prof. Dr. Stefan Kuvendžiev,
Ss. Cyril and Methodius University in Skopje,
Faculty of Technology and Metallurgy

Editor-in-chief:
Prof. Dr. Anita Grozdanov,
Ss. Cyril and Methodius University in Skopje,
Faculty of Technology and Metallurgy

Technical Editor:
Prof. Dr. Perica Paunović,
Ss. Cyril and Methodius University in Skopje,
Faculty of Technology and Metallurgy

CIP - Каталогизација во публикација
Национална и универзитетска библиотека "Св. Климент Охридски", Скопје

502.1(062)

CONFERENCE for green engineering, sustainable materials and technologies for circular economy CIRC (2 ; 2025 ; Skopje)
Proceedings [Електронски извор] : Faculty of technology and metallurgy, University Ss. Cyril and Methodius in Skopje 22-25 April 2025 / 2st Conference for green engineering, sustainable materials and technologies for circular economy CIRC 2025 ; [editor-in-chief Anita Grozdanov]. - Skopje : University Ss. Cyril and Methodius in Skopje, Faculty of technology and metallurgy, 2025

Начин на пристапување (URL):
https://congress.sctm.mk/event/6/book-of-abstracts.pdf. - Текст во ПДФ формат, содржи 184 стр., илустр. - Наслов преземен од екран. - Опис на изворот на ден 12.06.2025 година. - Библиографија кон трудовите

ISBN 978-9989-650-42-0

а) Екологија -- Инженерство -- Материјали -- Технологија -- Економија -- Собири

COBISS.MK-ID 66104837

Scientific Committee

President:

Prof. Dr. **Anita Grozdanov,** Faculty of Technology and Metallurgy, Ss. Cyril and Methodius University in Skopje, R. N. Macedonia

Members:

Prof. Dr. **Perica Paunovic**, Faculty of Technology and Metallurgy, Ss. Cyril and Methodius University in Skopje, R. N. Macedonia

Prof. Dr. **Stefan Kuvendziev**, Faculty of Technology and Metallurgy, Ss. Cyril and Methodius University in Skopje, R. N. Macedonia

Prof. Dr. **Jadranka Blazhevska Gilev**, Faculty of Technology and Metallurgy, Ss. Cyril and Methodius University in Skopje, R. N. Macedonia

Prof. Dr. **Mishela Temkov**, Faculty of Technology and Metallurgy, Ss. Cyril and Methodius University in Skopje, R. N. Macedonia

Prof. Dr. **Maja Jankoska**, Faculty of Technology and Metallurgy, Ss. Cyril and Methodius University in Skopje, R. N. Macedonia

Prof. Dr. **Aleksandar Dimitrov**, Faculty of Technology and Metallurgy, Ss. Cyril and Methodius University in Skopje, R. N. Macedonia

Prof. Dr. **Emilija Fidanchevski**, Faculty of Technology and Metallurgy, Ss. Cyril and Methodius University in Skopje, R. N. Macedonia

Prof. Dr. **Igor Jordanov**, Faculty of Technology and Metallurgy, Ss. Cyril and Methodius University in Skopje, R. N. Macedonia

Prof. Dr. **Elena Velichkova Nikova**, Faculty of Technology and Metallurgy, Ss. Cyril and Methodius University in Skopje, R. N. Macedonia

Prof. Dr. **Vojo Jovanov**, Faculty of Technology and Metallurgy, Ss. Cyril and Methodius University in Skopje, R. N. Macedonia

Prof. Dr. **Goran Nachevski**, Faculty of Technology and Metallurgy, Ss. Cyril and Methodius University in Skopje, R. N. Macedonia

Prof. Dr. **Mirko Marinkovski**, Faculty of Technology and Metallurgy, Ss. Cyril and Methodius University in Skopje, R. N. Macedonia

Prof. Dr. **Darko Dimitrovski**, Faculty of Technology and Metallurgy, Ss. Cyril and Methodius University in Skopje, R. N. Macedonia

Prof. Dr. **Slavcho Aleksovski**, Faculty of Technology and Metallurgy, Ss. Cyril and Methodius University in Skopje, R. N. Macedonia

Prof. Dr. **Vesna Rafajlovska**, Faculty of Technology and Metallurgy, Ss. Cyril and Methodius University in Skopje, R. N. Macedonia

Prof. Dr. **Kiril Hristovski,** Polytechnic School, Arizona State University, USA

Prof. Dr. **Ana Vukelic,** Faculty of Food Technology and Biotechnology, University of Zagreb, Croatia

Prof. Dr. **Ilirjan Malollari,** Faculty of Natural Science, University of Tirana, Tirana, Albania

Prof. Dr. **Gregory Makrides,** University of National Education Commission, Krakow, Poland

Prof. Dr. **Riste Shkrekovski,** Faculty of Mathematics and Physics, University of Ljubljana, Slovenia

Prof. Dr. **Mirjana Pejic,** Faculty of Economics and Business, University of Zagreb, Croatia

Prof. Dr. **Pavle Spasojevic,** Faculty of Technical Science, University of Kragujevac, Serbia

Prof. Dr. **Amra Bratovcic,** Faculty of Technology, University in Tuzla, Bosnia and Hercegovina

Prof. Dr. **Gjore Nakov,** College of Sliven, Technical University of Sofia, Bulgaria

Prof. Dr. **Nastia Ivanova,** College of Sliven, Technical University of Sofia, Bulgaria

Prof. Dr. **Violeta Raykova,** College of Sliven, Technical University of Sofia, Bulgaria

Prof. Dr. **Angela Angeleska,** University of Tampa, Florida, USA

Prof. Dr. **Vladimir Grupcev,** University of South Florida, USA

Prof. Dr. **Kemal Delijic,** Faculty of Metallurgy and Technology, University of Montenegro, Podgorica, Montenegro

Prof. Dr. **Ljiljana Stanojević,** Faculty of Technology in Leskovac, University of Niš, Serbia

Prof. Dr. **Dragan Cvetković,** Faculty of Technology in Leskovac, University of Niš, Serbia

Prof. Dr. **Yordan Georgiev,** University in Burgas, Bulgaria

Prof. Dr. **Assen Zlatarov,** University in Burgas, Bulgaria

Prof. Dr. **Magdalena Jasińska,** Faculty of Chemical and Process Engineering, Warsaw University of Technology, Warsaw, Poland

Dr. **Otton Roubinek,** Łukasiewicz–Industria Chemiatria Instytutem, Departament of Pharmacy, Cosmetic Chemistry and Biotechnology, Warsaw, Poland

Dr. **Katarzyna Kozak**, Łukasiewicz–Industria Chemiatria Instytutem, Departament of Pharmacy, Cosmetic Chemistry and Biotechnology, Warsaw, Poland

Dr. **Maurizio Avella**, Institute for Polymers, Composites and Biomaterials – CNR, Napoli, Italy

Dr. **Gennaro Gentile**, Institute for Polymers, Composites and Biomaterials – CNR, Napoli, Italy

Dr. **Rachele Castaldo**, Institute for Polymers, Composites and Biomaterials – CNR, Napoli, Italy

Dr. **Mariacristina Cocca**, Institute for Polymers, Composites and Biomaterials – CNR, Napoli, Italy

Dr. **Maria Emanuela Errico**, Institute for Polymers, Composites and Biomaterials – CNR, Napoli, Italy

Dr. **Aleksandra Ivanovska**, Innovation Center of the Faculty of Technology and Metallurgy, University in Belgrade, Serbia

Dr. **Tamara Dapčević Hadnađev**, FINS Institute in Novi Sad, Serbia

Prof. Emeritus Dr. **Ana Marija Grancaric**, Faculty of Textile Technology, University of Zagreb, Croatia

Prof. Dr. **Filip Snezana**, Technical Faculty "Mihajlo Pupin" - Zrenjanin, University of Novi Sad, Serbia

Prof. Dr. **Mitar Perušić,** Faculty of Technology Zvornik, University of East Sarajevo, Bosnia and Herzegovina

Prof. Dr. **Elvis Ahmetović**, Department of Chemical Engineering, Faculty of Technology, University of Tuzla, Bosnia and Herzegovina

Dr. **Irena Andreevska**, Chief Actuary and Vice President of Underwriting Health Alliance Plan, USA

Prof. Dr. **Željko Kamberović**, Faculty of Technology and Metallurgy, University of Belgrade, Serbia

Dr. **Miroslav Sokić**, Institute for Technology of Nuclear and other Mineral Raw Materials, Belgrade, Serbia

Dr. **Bas Paris**, Agricultural University of Athens, Greece

Dr. **Suzana Gotovac-Atlagić**, Faculty of Natural Science and Mathematics, University of Banja Luka, Bosnia and Herzegovina

Dr. **Smilja Marković,** Institute of Technical Sciences of SASA, Belgrade, Serbia

Prof. Dr. **Ivana Stojković-Simatović**, Faculty of Physical Chemistry, University of Belgrade, Serbia

Dr. **Miroslav Pavlović**, Institute of Chemistry, Technology and Metallurgy, National Institute of the Republic of Serbia, University of Belgrade, Serbia

Prof. Dr. **Marijana Pantović Pavlović**, Institute of Chemistry, Technology and Metallurgy, National Institute of the Republic of Serbia, University of Belgrade, Serbia

Prof. Dr. **Snezana Vucevic**, Faculty of Technology Novi Sad, University of Novi Sad, Serbia

Prof. Dr. **Srecko Stopic**, Faculty of Georesources and Materials Engineering, RWTH Aachen University, Germany

Organizing Committee

Presidents:

Prof. Dr. **Beti Andonovikj**, Faculty of Technology and Metallurgy, Ss. Cyril and Methodius University in Skopje, R. N. Macedonia

Prof. Dr. **Biljana Angjusheva**, Faculty of Technology and Metallurgy, Ss. Cyril and Methodius University in Skopje, R. N. Macedonia *(Vice President)*

Members:

Prof. Dr. **Ana Tomova**, Faculty of Technology and Metallurgy, Ss. Cyril and Methodius University in Skopje, R. N. Macedonia

Prof. Dr. **Katerina Atkovska**, Faculty of Technology and Metallurgy, Ss. Cyril and Methodius University in Skopje, R. N. Macedonia

Prof. Dr. **Boshko Boshkovski**, Faculty of Technology and Metallurgy, Ss. Cyril and Methodius University in Skopje, R. N. Macedonia

Iva Dimitrievska, M.Sc., Faculty of Technology and Metallurgy, Ss. Cyril and Methodius University in Skopje, R. N. Macedonia

Marija Prosheva, M.Sc., Faculty of Technology and Metallurgy, Ss. Cyril and Methodius University in Skopje, R. N. Macedonia

Martin Stojchevski M.Sc., Faculty of Technology and Metallurgy, Ss. Cyril and Methodius University in Skopje, R. N. Macedonia

Bojan Atkovski, Faculty of Technology and Metallurgy, Ss. Cyril and Methodius University in Skopje, R. N. Macedonia

Dejan Nikolovski, Faculty of Technology and Metallurgy, Ss. Cyril and Methodius University in Skopje, R. N. Macedonia

Content

2nd Conference for Green Engineering, Sustainable Materials and Technologies for Circular Economy, GREEN CIRC 2025
PROCEEDINGS

ECO-FRIENDLY REGENERABLE ADSORBENTS FROM CELLULOSE AND PHOTOCATALYTIC NANOPARTICLES

Antonio Maglione[1], Antonia Cerbone[1,2], Pierluigi Lasala[3], Khalid Tahla[3], Marica Tancredi[3], Federico Olivieri[1], Rachele Castaldo[1], Maria Lucia Curri[3,4,5], Elisabetta Fanizza[3,4,5], Gennaro Gentile[1]*

[1] - *Institute of Polymers, Composites and Biomaterials - IPCB, National Research Council of Italy - CNR, Via Campi Flegrei 34, 80078 Pozzuoli, Italy*

[2] - University *of Naples, Department of Chemical Science, Strada Comunale Cinthia, 26, 80126, Naples, Italy*

[3] - *University of Bari A. Moro, Department of Chemistry, Via Orabona 4, 70126 Bari, Italy*

[4] - *Institute for chemical and physical processes – IPCF, National Research Council of Italy - CNR, Via Orabona 4, 70126 Bari, Italy*

[5]*National Interuniversity Consortium of Materials Science and Technology, INSTM, Bari Research Unit, 70126, Bari, Italy*

gennaro.gentile@cnr.it

Abstract: *Water pollution is a pressing global issue, with a wide range of organic pollutants such as dyes, antibiotics, phenols, commonly found in water sources. Among existing purification methods, adsorption stands out for its efficiency, lack of toxic by-products, and reversibility. Within the PHOTOPAD project (Photocatalytically-Regenerable Hierarchically Porous Adsorbents for Efficient Water Treatment) cellulose-based microporous materials with high surface area and adsorption capacity are developed. These materials are capable of removing various organic contaminants including cationic and anionic dyes and non-ionic aromatic pollutants.*

To promote sustainability, PHOTOPAD introduces a new concept of smart adsorbents that enable both effective pollutant capture and in-situ regeneration. This is achieved through heterogeneous photocatalysis, providing an energy-efficient method to degrade adsorbed contaminants. Metal oxide nanoparticles, synthesized via colloidal approaches, are employed as photocatalysts and integrated into the microporous adsorbents.

Finally, microporous adsorbents and photocatalytic nanoparticles are assembled into hierarchically porous systems that are easy to handle, offer excellent adsorption performance and allow repeated regeneration, making them highly promising for advanced, sustainable water treatment solutions.

Keywords: adsorption, photocatalysis, sustainable regenerable adsorbents, water remediation

INTRODUCTION

Water pollution arising from intensive agricultural practices and industrial activities poses significant environmental challenges. Among the various contaminants, chlorophenols, widely used in pesticides and pharmaceutical products, and dyes, are particularly concerning. These aromatic organic compounds are classified as priority pollutants by the U.S. Environmental Protection Agency (EPA) due to their toxicity and persistence in the environment [1].

Among remediation strategies, adsorption stands out as an effective and versatile method, favored for its spontaneity, reversibility, and the absence of harmful by-products. In the realm of microporous materials, hyper-crosslinked resins (HCLR) are particularly attractive due to their high specific surface area (SSA), cost-effective synthesis, mild reaction conditions, and customizable porosity and chemical functionality [2]. However, most monomers used in HCLR synthesis are fossil-based, which raises sustainability concerns. In this work, novel microporous adsorbents characterized by extensive microporosity, are developed starting from cellulose-based precursors.

Moreover, since the validation of an adsorbent should not be limited to prove the efficiency of the adsorption process, but it must also address adsorbent lifetimes, reusability, and economic and environmental cost of regeneration treatments, the concept of smart adsorbents where enhance adsorption is combined to in situ regeneration by heterogeneous photocatalysis, is proposed.

RESULTS AND DISCUSSIONS

A novel, biobased microporous adsorbent material obtained starting from fibrous cellulose was developed. Cellulose was selected for its rich surface chemistry enabling functionalization and its ability to form highly macroporous self-assembled structures. Cellulose was treated with sulfolane and ferric chloride to obtain a highly crosslinked structure. The hyper-crosslinked cellulose displayed specific surface area up to 1500 m^2/g and a micro/mesoporous structure.

The same protocol was also applied to natural biomasses such as hemp, obtaining comparable results in terms of surface area and porosity, demonstrating that the proposed approach is an effective strategy to valorize waste lignocellulosic biomasses.

Then, photocatalytic nanoparticles (PC NPs) able to exploit solar light were synthesized through colloidal methods.. Solution-phase approaches under mild

reaction conditions have been exploited towards the design and fabrication of metal oxide nanoparticles (TiO_2, CeO_2).

Then, two methodologies have been developed to obtain micro/mesoporous resins embedding PC NPs: (i) the in-situ synthesis of the colloidal nanoparticles in the presence of microporous adsorbent and (ii) the ex-situ approach, where pre-synthesized nanoparticles have been let to adsorb on the adsorbent.

The nanoparticle-modified adsorbent has been evaluated paying particular attention to the adsorbent structural stability, adsorption properties, nanoparticle loading and photocatalytic performance, since they will affect the adsorption and regeneration technology. Different aspects involved in the combination of large specific surface area adsorbents with nanometer-sized photocatalyst have been studied. In-depth investigation by structural, morphological, chemical and optical characterization have been exploited to assess the best photocatalyst candidate, understand the photocatalytic mechanisms involved in the contaminant degradation and, hence adsorbent regeneration, and the suitable functionalization procedure selected.

CONCLUSIONS

Novel biobased microporous adsorbents were obtained from cellulose and waste biomasses through a low-impact synthetic process. These adsorbents displayed specific surface area up to 1500 m^2/g, a micro/mesoporous structure, and demonstrated high adsorption capacity towards aromatic pollutants. The proposed approach demonstrated to be an effective strategy to valorize waste lignocellulosic biomasses for environmental application. Then, to ensure a sustainable regeneration of the adsorbent, photocatalytic nanoparticles were embedded into the micro/mesoporous resin to exploit heterogeneous photocatalysis as an energy-efficient approach for the degradation of adsorbed contaminants.

Ultimately, the microporous adsorbents embedding the photocatalytic nanoparticles will be integrated into hierarchically porous composite systems that are easy to handle, exhibit excellent adsorption capacity, and support multiple regeneration cycles. These features make them highly attractive candidates for next-generation, sustainable water purification technologies.

Acknowledgements: The authors acknowledge financial support under the National Recovery and Resilience Plan (NRRP), Mission 4, Component 2, Investment 1.1, Call for tender No. 1409 published on 14.09.2022 by the Italian Ministry of University and Research (MUR), funded by the European Union – NextGenerationEU– Project Title

"Photocatalytically-regenerable hierarchically porous adsorbents for efficient water treatment" (PHOTOPAD, code P2022FP2W4, 2023-2025), CUP B53D23027540001, Grant Assignment Decree No. 1389 adopted on 01.09.2023 by the Italian MUR.

REFERENCES

1. Y. Liu, B. Men, A. Hu, Q. You, G. Liao, D. Wang, Facile synthesis of graphene-based hyper-cross-linked porous carbon composite with superior adsorption capability for chlorophenols, *Journal of Environmental Sciences* **90** (2020) 395-407. https://doi.org/10.1016/j.jes.2019.11.018
2. R. Castaldo, R. Avolio, M. Cocca, M. E. Errico, M. Avella, G. Gentile, Amino-functionalized hyper-crosslinked resins for enhanced adsorption of carbon dioxide and polar dyes, *Chemical Engineering Journal* **418** (2021) 129463. https://doi.org/10.1016/j.cej.2021.129463

REDUCING THE BAND-GAP ENERGY OF TiO_2 AS A CRUCIAL OBJECTIVE IN GREEN PHOTOCATALYSIS

Perica Paunović, Anita Grozdanov, Petre Makreski, Martin Stojčevski, Kiril Stoimčev, Gorazd Čepiševski

Faculty of Technology and Metallurgy, Ss. Cyril and Methodius University in Skopje, North Macedonia

pericap@tmf.ukim.edu.mk

Abstract: *Green photocatalysis focuses on developing processes to address various environmental challenges, such as the treatment of contaminated water and air, the generation of renewable energy, biomass management, carbon monoxide oxidation, and organic synthesis. TiO_2 nanoparticles are relatively inexpensive, non-toxic, and chemically stable. They are available in diverse structural forms and exhibit unique semiconductive properties, making them the most widely utilized photocatalysts in this domain. TiO_2 has a wide array of applications in green photocatalysis, including i) photocatalytic remediation and ii) the development of alternative, sustainable energy sources. A significant challenge in modern green photocatalysis is the reduction of the band gap energy (E_g), which is essential for determining the suitability of materials for photocatalytic activity. Decreasing E_g enables TiO_2 to effectively harness visible light rather than being limited to ultraviolet light. This study investigates the structural changes and subsequent reduction in E_g resulting from two types of TiO_2 modification: i) ionizing irradiation and ii) the incorporation of carbon nanotubes. We synthesized TiO2 nanoparticles using our proprietary sol-gel method, followed by thermal treatment at 400 °C. Structural changes were analyzed using X-ray powder diffraction (XRPD) and Raman spectroscopy, while the band gap energy of the samples was assessed through UV-Vis spectroscopy*.

Keywords: Green photocatalysis, TiO_2 nanoparticles, band-gap energy, ionizing irradiation, TiO_2/CNTs nanocomposites.

INTRODUCTION

Chemical processes driven by light and enhanced by suitable semiconductive materials, known as photocatalysts, are referred to as photocatalytic processes. These processes include three sequential steps as is shown in Fig.1 [1,2]. In the first step, when the photocatalytic material is exposed to light with energy that exceeds its band gap energy, electron-hole pairs are created. In the subsequent step, these electrons and holes move across the photocatalyst's surface and interact with surface water and oxygen, leading to the formation of radical species such as $^{\bullet}OH$ and $^{\bullet}O_2^-$. Finally, these generated radical species react with pollutant molecules, decomposing them into harmless substances like CO_2, H_2O, NO, NO_2, etc.

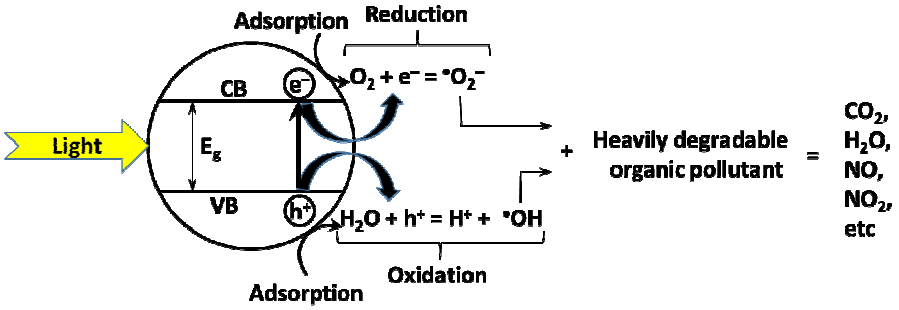

Figure 1 *Schematic view of the mechanism of the photocatalytic degradation of heavily degraded pollutant*

TiO_2 is renowned for its excellent semiconductive properties, making it an ideal photocatalyst and the most widely used material in photocatalysis. It is characterized by being low-cost, non-toxic, and chemically stable, and it is available in various polymorphic forms. In its nanoparticle form, TiO_2 demonstrates significantly enhanced photocatalytic activity compared to its bulk counterpart. The reduced particle size facilitates the easier movement of photoelectrons and holes to the surface, thereby lowering the recombination rate [3]. Additionally, nanostructured materials possess a greater surface-to-bulk atom ratio, which results in an increased real surface area and, subsequently, a significantly higher number of active photocatalytic centers.

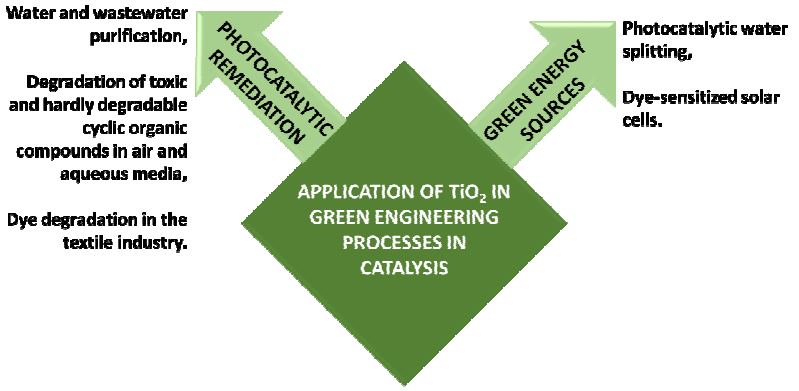

Figure 2 *The main application of TiO_2 in green photocatalysis*

In 1972, Fujishima and Honda [4] conducted groundbreaking research on photocatalytic water splitting utilizing a TiO_2 cathode, marking the dawn of a new era in photocatalysis. This landmark study spurred a notable increase in research focused on photocatalytic processes aimed at energy production and

environmental protection. As a photocatalyst, TiO_2 offers a wide variety of applications in green photocatalysis, including i) photocatalytic remediation and ii) alternative green energy sources, as illustrated in Fig. 2.

The band gap energy (E_g) is a key property that dictates the suitability of materials for photocatalytic applications. Additionally, the band gap is crucial for facilitating charge separation, which reduces recombination rates and enhances photocatalytic activity under specific wavelengths [3]. Titanium dioxide (TiO_2), classified as an n-type semiconductor, possesses a relatively wide energy band gap of 3.2 eV in its anatase form and 3.0 eV in its rutile form. Despite its larger energy band gap, anatase is regarded as a more effective photocatalyst [5], owing to its indirect band gap, as opposed to rutile's direct band gap. In the case of an indirect band gap, an excited electron can be stabilized at a lower level in the conduction band, leading to a prolonged lifespan and increased mobility. Moreover, due to its higher Fermi level compared to rutile, anatase demonstrates a stronger affinity for hydroxyl group ($^{\bullet}OH$) adsorption while exhibiting a lower affinity for oxygen adsorption.

A major limitation is that TiO_2 is most effective under ultraviolet (UV) light due to its wide band gap. It's worth noting that only approximately 4% of the solar spectrum is composed of UV light, resulting in a substantial amount of unused solar energy. As a result, a primary goal and challenge in photocatalysis is to develop photocatalysts that are active in visible light.

There are several techniques to reduce the band gap energy of TiO_2: 1) doping with various ions [6,7], 2) employing non-stoichiometric titanium oxides (Magneli phases) [8], 3) hydrogen plasma treatment [9], 4) exposure to ionizing radiation [10-12], and 5) compositing with CNTs [13,14].

This paper examines the structural changes in sol-gel prepared TiO_2 resulting from electron-beam and x-ray irradiation, as well as the effects of CNT compositing, and how these alterations influence the band gap energy.

EXPERIMENTAL

The TiO_2 nanoparticles the subject of study in this paper were prepared using the sol-gel method under normal atmospheric pressure. Titanium tetraisopropoxide (TTIP) at 97% purity from Aldrich was used as the precursor. The synthesis procedure is described elsewhere [15].

The as-prepared TiO_2 was subjected to two types of irradiation: electron-beam

irradiation (low energy and a corpuscular nature) and x-ray irradiation (high energy and a wave nature). Due to their significant differences in energy levels, the e-beam irradiation dose was set at 50 kGy, while the x-ray irradiation dose was only 7 mGy.

The TiO_2/CNTs nanocomposites were synthesized using a sol-gel method similar to that used for pure TiO_2. Before adding the TiO_2 precursor (TTIP), carbon nanotubes (CNTs) were adequately dispersed in absolute ethanol. Both single-walled carbon nanotubes (SWCNTs) and multi-walled carbon nanotubes (MWCNTs) were employed. The compositions of the nanocomposites examined were 80% TiO_2 + 20% MWCNTs and 80% TiO2 + 20% SWCNTs.

The structural analysis, which involved the identification of current structural phases and parameters, was conducted using X-ray powder diffraction (XRD) and Raman spectroscopy. A Rigaku Ultima IV diffractometer operating with CuKα radiation (λ = 1.54178 Å) was employed for XRD measurements. The X-ray tube voltage was set to 40 kV, with a current of 40 mA, and a Kβ filter was utilized. Diffraction patterns were recorded in the 20° to 80° range (2θ) at a rate of 5°/min using a D/teX Ultra high-speed (1D) detector. For micro-Raman spectrum collection, the Horiba Jobin Yvon LabRam 300 Infinity was utilized, using ANd:YAG frequency-doubled laser operating at 532 nm without an attenuation filter. The Raman peak of the silica wafer at 520.7 cm^{-1} facilitated the calibration of the Raman shift. A grating with 1800 grooves/mm was selected to disperse the signal onto the CCD detector, ensuring high dispersion and excellent spectral resolution.

The optical properties were studied using UV-Vis spectroscopy. The UV-Vis absorption spectra of the TiO_2-water suspension were collected with a Varian Cary Scan 50 spectrophotometer (Switzerland) in 1 cm quartz cells at a temperature of 25 °C, covering the range from 200 to 900 nm with a scan speed of 200 nm. These spectra were used to determine the energy of the band gap of the studied materials.

RESULTS AND DISCUSSIONS

According to the literature [16,17], exposure to ionizing radiation can cause structural changes in TiO_2, such as an increase in the Ti^{3+}/Ti^{4+} ratio and the creation of oxygen vacancies. These modifications may result in a decrease in band gap energy, thereby enhancing the photocatalytic activity under visible light. The interaction between CNTs and TiO_2 significantly extends the lifespan of electron-hole pairs. This improvement is due to the differing work functions of TiO_2 (4.2–4.3 eV [18]) and CNTs (4.7–5.1 eV [19]). Electrons migrate from the conduction

band of TiO2, which has a lower work function, to the CNTs, which have a higher work function. This transfer continues until the Fermi levels of both materials align, resulting in the formation of a Schottky barrier at their interface [20].

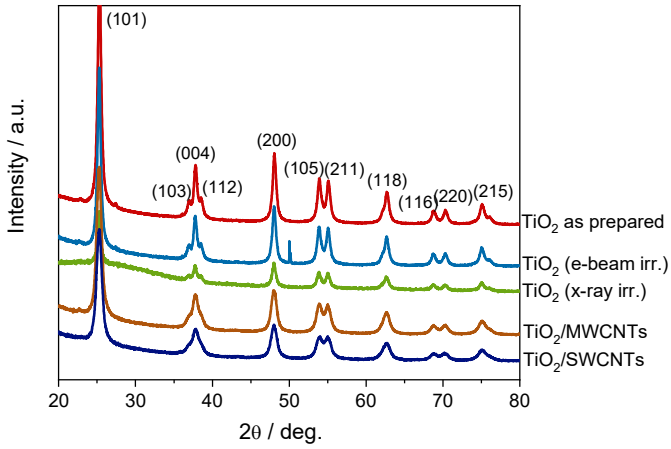

Figure 3 *XRD spectra of the studied TiO_2 samples*

Table 1 *Calculated values of interplanar distance, cell parameters, and particle size from XRD spectra and wave number values of the E_g Raman peaks*

Sample	$d_{\{101\}}$, Å	a, Å	c, Å	D, nm	E_g, cm^{-1}
as-prepared	3.5175	3.7832	9.5546	16.9	140.42
e-beam irradiated	3.5229	3.7860	9.6182	16.0	141.89
x-ray irradiated	3.5245	3.7874	9.6278	14.5	144.45
TiO_2/MWCNTs	3.5216	3.7872	9.5724	12.8	137.10
TiO_2/SWCNTs	3.5233	3.7888	9.5807	10.0	133.13

To identify the crystalline form of TiO_2 and assess the changes at the crystalline level, including crystal parameters and nanoparticle size, the samples were analyzed using X-ray diffraction (XRD). The XRD spectra presented in Figure 3 clearly display the characteristic features of the anatase crystalline form across all analyzed samples. A comparison of the shapes and intensities of the characteristic anatase peaks in the various XRD spectra reveals that the irradiation treatments of TiO_2 and its compositing with CNTs resulted in alterations to the structure and size of the nanoparticles. Notably, the as-prepared sample exhibited the most intense and distinct peaks, whereas the irradiated and composite samples displayed broader and less defined peaks. These findings imply that the as-prepared sample likely contained the largest nanoparticles and that the irradiation treatments and compositing led to a

reduction in nanoparticle size. Table 1 summarizes the crystal parameters determined through XRD and Raman measurements. Following exposure to ionizing radiation or the incorporation of CNTs, both the distance between atomic planes and the cell parameters increase, while the size of the particles diminishes due to electronic excitation or collective electron excitation. This effect is particularly pronounced when using SWCNTs, with TiO_2 nanoparticles decreasing in size from 16 nm to as low as 10 nm. The increase of the interplanar distance and cell parameters indicate an expansion of the crystal lattice which is the result of interaction of the TiO_2 crystalline lattice with both ionizing irradiation and CNTs.

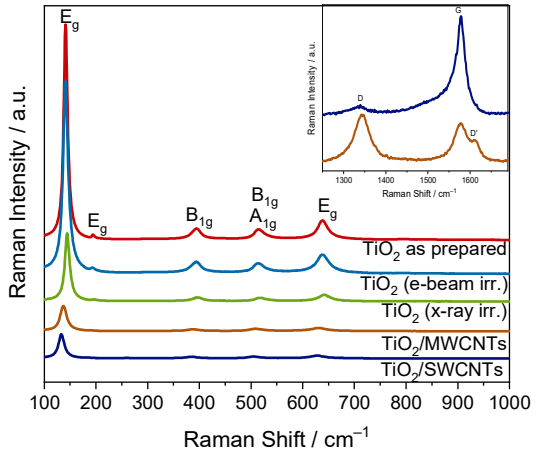

Figure 4 *Raman spectra of the studied samples*

The structural analysis conducted using Raman spectroscopy is illustrated in Fig. 4. The Raman modes observed in the spectra correspond to those of the anatase single crystal identified by Osaka [21]. The Raman spectra of the analyzed samples exhibit similar trends to those recorded by X-ray diffraction (XRD) analysis. For the irradiated samples or those composited with CNTs, the spectral features are less intense and broader compared to those of the as-prepared TiO_2.

The most intense Raman mode, E_g, displays a blue shift, meaning it shifts to higher wave number values as a result of irradiation (see Table 1). The shift and broadening of the Raman bands can be attributed to phonon confinement [22]. When irradiated, phonons become confined within the particles, leading to a decrease in particle size and an increase in the distribution of phonon momentum. Consequently, this results in the broadening of the Raman bands. Additionally, the presence of defects, such as oxygen vacancies, within the material can also influence the shift and broadening of the Raman bands [23]. Therefore, ionizing irradiation has a similar effect on oxygen vacancies as introducing certain

elements through doping [24]. Considering the phonon confinement model and the observed reduction in nanoparticle size due to the integration of CNTs, as indicated by the XRD analysis, it was initially anticipated that the prominent E_g vibrational modes would shift to higher wavenumbers (a blue shift) [25]. However, this expectation mainly applies to the pure TiO_2 system. In the case of the TiO_2/CNTs nanocomposites, a red shift was observed instead (shifts to higher wave number values). This red shift can be attributed to the strong interaction between TiO_2 and CNTs, which results in the formation of Ti-O-C bonds. Such bonding distorts the TiO_2 structure [26,27]. Furthermore, if the frequency of the phonons interacting with the incident photons decreases, the material experiences tensile strain, leading to an expansion of the crystalline lattice. Consequently, this results in a red shift of the Raman vibrational modes, which aligns well with the observations from the XRD analysis.

For the TiO_2 nanocomposites containing CNTs, several significant bands were detected in the Raman spectra region corresponding to CNTs, as shown in the intersect of Fig. 4. These include the D band, indicating the presence of disordered carbon; the G band, representing highly ordered carbon; and the D' bands associated with multi-walled carbon nanotubes (MWCNTs). Notably, these bands were shifted to higher wavenumbers than pure MWCNTs and single-walled carbon nanotubes (SWCNTs). This upshift indicates a strong interaction between TiO_2 and CNTs, which enhances charge transfer from TiO_2 to the CNTs.

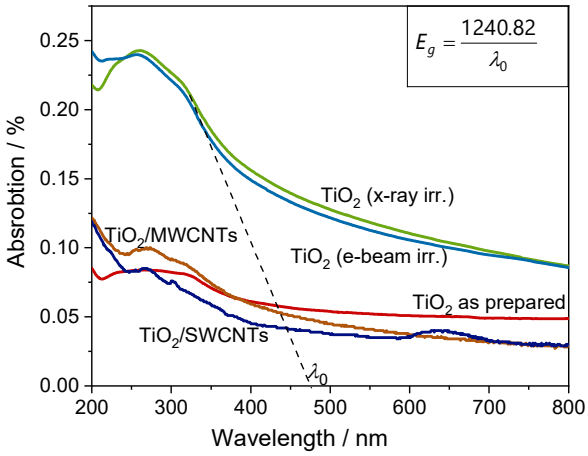

Figure 5 *UV-Vis spectra of the studied samples*

In Fig. 5, UV-Vis spectra of the sol-gel prepared TiO_2 before and after ionizing irradiations and compositing are shown. The cut-off wavelength (λ_0) is determined at the point where the tangent extended from the right side of the absorption peak intersects with the x-axis. The energy of the band gap (E_g) can be

calculated using the equation shown in the intersection of Fig. 5. The determined values of λ_0 and E_g are summarized in Table 2.

Table 2 *Calculated values of cut-off wavelength and energy of the band gap of the studied samples*

Sample	λ_0, nm	E_g, eV
as-prepared	427.58	2.90
e-beam irradiated	512.22	2.42
x-ray irradiated	523.07	2.37
TiO_2/MWCNTs	495.05	2.51
TiO_2/SWCNTs	521.02	2.38

In Figure 5, the UV-Vis spectra of sol-gel synthesized TiO_2, both prior to and after ionizing irradiation and compositing, are presented. The cut-off wavelength (λ) is identified at the intersection point where the tangent, drawn from the right side of the absorption peak, meets the x-axis. The energy of the band gap (E_g) is calculated using the equation indicated in the intersection of Figure 5. A summary of the values for λ_0 and E_g is provided in Table 2.

It is notable that the as-prepared TiO_2 nanoparticles display a significantly reduced band gap energy of 2.9 eV, in contrast to the 3.2 eV band gap energy of bulk anatase. This reduction suggests that structural modifications in TiO_2 resulting from ionizing irradiation contribute to a decrease in band gap energy. Specifically, the band gap energy diminishes from 2.9 eV to 2.42 eV with e-beam irradiation and to 2.37 eV with x-ray irradiation. Among the TiO_2/CNTs nanocomposites, the most pronounced reduction in band gap energy was observed in the composite containing single-walled carbon nanotubes (SWCNTs), where E_g decreased from 2.9 eV to 2.38 eV.

The results of this study, particularly concerning the effects of ionizing irradiation and the development of TiO_2 nanocomposite materials using carbon nanotubes (CNTs), represent a noteworthy advancement in the field. They highlight a significant achievement in reducing the band gap energy of TiO_2 in comparison to existing literature [6-14].

CONCLUSIONS

The research findings indicate that both ionizing radiations, such as X-rays and electron beams, as well as the incorporation of carbon nanotubes (CNTs), result in similar structural changes in titanium dioxide (TiO2). These changes encompass a decrease in nanoparticle size, an increase in interplanar distance, and alterations to lattice parameters. Consequently, these structural modifications lead

to a reduction in band gap energy, which shifts light absorption into the visible spectrum and enhances photocatalytic activity.

Acknowledgments: This paper has been supported by the Science and Research Fund of Ss. Cyril and Methodius University in Skopje, 2024.

REFERENCES

1. P. Thangadurai, R. Beura, J. S. Kumar, *Nanomaterials with Different Morphologies for Photocatalysis*, in *Green Photocatalysts*, M. Naushad, S. Rajendran, E Lichtfouse, Eds., Springer Nature, Switzerland, 2000, p. 47-87. https://doi.org/10.1007/978-3-030-15608-4_3

2. S. Peiris, Haritha, B. de Silva, K. N. Ranasinghe, I. R. Perera, Recent development and future prospects of TiO_2 photocatalysis, *Journal of the Chinese Chemical Society* **68** (2021) 739–769. https://doi.org/10.1002/jccs.202000465

3. M. B. Tahir, M. Sohaib, M. Sagir, M. Rafique, Role of nanotechnology in photocatalysis, *Encyclopedia of Smart Materials* **2** (2022) 578-589. https://doi.org/10.1016/B978-0-12-815732-9.00006-1

4. A. Fujishima, K. Honda, Electrochemical photolysis of water at a semiconductor electrode, *Nature* **238** (1972) 37-38. https://doi.org/10.1038/238037a0

5. T. Luttrell, S. Halpegamage, J. Tao, A. Kramer, E. Sutter, M. Batzill, Why is anatase a better photocatalyst than rutile? - Model studies on epitaxial TiO_2 films, *Scientific Reports* **4** (2014) 4043. https://doi.org/10.1038/srep04043

6. A. Zaleska, Doped-TiO_2: A Review, *Recent Patents on Engineering* **2** (2008) 157-164. https://doi.org/10.2174/187221208786306289

7. M. B. Kanoun, F. Ahmed, C. Awada, C. Jonin, P-F. Brevet, Band gap engineering of Au doping and Au – N codoping into anatase TiO_2 for enhancing the visible light photocatalytic performance, *International Journal of Hydrogen Energy* **51** (2024) 907-913. https://doi.org/10.1016/j.ijhydene.2023.10.244

8. M. Toyoda, T. Yano, B. Tryba, S. Mozia, T. Tsumura, M. Inagaki, Preparation of carbon-coated Magneli phases Ti_nO_{2n-1} and their photocatalytic activity under visible light, *Applied Catalysis B: Environment* **88** (2008) 160-164. https://doi.org/10.1016/j.apcatb.2008.09.009

9. H. An, S. Y. Park, H. Kim, C. Y. Lee, S. Choi, S. C. Lee, S. Seo, E. C. Park, Y. Oh, C. Song, J. Won, Y. J. Kim, J. Lee, H. U. Lee, Y. Lee, Advanced nanoporous TiO_2 photocatalysts by hydrogen plasma for efficient solar-light photocatalytic application, *Scientific Reports* 6 (2016) 29683. https://doi.org/10.1038/srep29683

10. K.P. Priyanka, S. Joseph, A.T. Sunny, T. Varghese, Effect of high energy electron beam irradiation on the optical properties of nanocrystalline TiO_2, *Nanosystems: Physics, Chemistry, Mathematics* **4** (2013) 218-224.

11. M.C. Molina Higgins, J.V. Rojas, X-ray radiation enhancement of gold-TiO_2 nanocomposites, *Applied Surface Science* **480** (2019) 1147-1155. https://doi.org/10.1016/j.apsusc.2019.02.234

12. K.R. Diab, M.M. Doheim, S.A. Mahmoud, S.A. Shama, H.A. El-Boohy, Gamma-Irradiation Improves the Photocatalytic Activity of Fe/TiO_2 for Photocatalytic Degradation of 2-Chlorophenol, *Chemistry and Materials Research* **9** (2017) 49-60.
13. W.D. Wang, P. Serp, P. Kalck, J.L. Faria, Visible light photodegradation of phenol on MWNT-TiO_2 composite catalysts prepared by a modified sol–gel method, *Journal of Molecular Catalysis A: Chemical* **235** (2005) 194. https://doi.org/10.1016/j.molcata.2005.02.027
14. P. Paunović, A. Grozdanov, P. Makreski, I. Dimitrievska, A. Petrovski, Structural changes of TiO_2 as a result of CNTs incorporation, *Material Science & Engineering International Journal* **6** (2022) 31-39. https://doi.org/10.15406/mseij.2022.06.00177
15. P. Paunović, A. Grozdanov, P. Makreski, G. Gentile, A.T. Dimitrov, *Application of Ionizing Irradiation for Structure Modification of Nanomaterials*, in *Nanoscience and Nanotechnology in Security and Protection against CBRN Threats*, P. Petkov, M.E. Achour, C. Popov, Eds., Springer Nature B.V., Dordrecht, The Netherlands, 2020, p. 23-43. https://doi.org/10.1007/978-94-024-2018-0_2
16. S.S. Latthe, S. An, S. Jin, S.S. Yoon, High energy electron beam irradiated TiO_2 photoanodes for improved water splitting, *Journal of Materials Chemistry A* **1** (2013) 13567-13575. https://doi.org/10.1039/C3TA13481D
17. P. Wronski, J. Surmacki, H. Abramczyk, A. Adamus, M. Nowosielska, W. Maniukiewicz, M. Kozanecki, M. Szadkowska-Nicze, Surface, optical and photocatalytic properties of silica-supported TiO_2 treated with electron beam, *Radiation Physics and Chemistry* **109** (2015) 40-47. https://doi.org/10.1016/j.radphyschem.2014.12.009
18. S.S. Surah, M. Vishwakarma, R. Kumar, R. Nain, S. Sirohi, G. Kumar, Tuning the electronic band alignment properties of TiO_2 nanotubes by boron doping, *Results in Physics* **12** (2019) 1725-1731. https://doi.org/10.1016/j.rinp.2019.01.081
19. Z. Dong, W. Li, H. Wang, X. Jiang, H. Liu, L. Zhu, H. Chen, Carbon nanotubes in perovskite-based optoelectronic devices, *Matter* **5** (2022) 448-481. https://doi.org/10.1016/j.matt.2021.12.011
20. M. Shaban, A.M. Ashraf, M.R. Abukhadra, TiO_2 nanoribbons/carbon nanotubes composite with enhanced photocatalytic activity; fabrication, characterization, and application, *Scientific Reports* **8** (2017) 781. https://doi.org/10.1038/s41598-018-19172-w
21. T. Oshaka, F. Izumi, Y. Fujiki, Raman spectrum of anatase TiO_2, *Journal of Raman Spectroscopy* **7** (1978) 321-324. https://doi.org/10.1002/jrs.1250070606
22. H.C. Choi, Y.M. Jung, S.B. Kim, Size effects in the Raman spectra of TiO_2 nanoparticles *Vibrational Spectroscopy* **37** (2005) 33-38. https://doi.org/10.1016/j.vibspec.2004.05.006
[23. J.C. Parker, R.W. Siegel, Raman microprobe study of nanophase TiO_2 and oxidation-induced spectral changes, *Journal of Materials Research* **5** (1990) 1246-1252. https://doi.org/10.1557/JMR.1990.1246
24. M.M. Khan, S.A. Ansari, D. Pradhan, M.O. Ansari, D.H. Han, J. Lee, M.H. Cho, Band gap engineered TiO_2 nanoparticles for visible light induced photoelectrochemical and photocatalytic studies, *Journal of Materials Chemistry A* **2** (2014) 637-644. https://doi.org/10.1039/C3TA14052K
25. C.Y. Xu, P.X. Zhang, L. Yan, Blue shift of Raman peak from coated TiO_2 nanoparticles, *Journal of Raman Spectroscopy* **32** (2001) 862-865. https://doi.org/10.1002/jrs.773

26. M.M. Gui, S-P. Chai, B-Q. Xu, A.R. Mohamed, Visible-light-driven MWCNT@TiO_2 core–shell nanocomposites and the roles of MWCNTs on the surface chemistry, optical properties and reactivity in CO_2 photoreduction, *RSC Advances* **4** (2014) 24007-24013. https://doi.org/10.1039/C4RA02561J
27. A. Saha, A. Moya, A. Kahnt, D. Iglesias, S. Marchesan, R. Wannemacher, M. Prato, J.J. Vilatela, D.M. Guldi, Interfacial charge transfer in functionalized multi-walled carbon nanotube@TiO_2 nanofibres, *Nanoscale* **9** (2017) 7911-7921. https://doi.org/10.1039/C7NR00759K

CHARACTERIZATION OF POLYMERS REINFORCED WITH CARBON NANOSTRUCTURES

Aleksandar T. Dimitrov, Mimoza Kovaci Azemi, Anita Grozdanov, Perica Paunović, Beti Andonović

Ss. Cyril nad Methodius University in Skopje, Faculty of Technology and Metallurgy

mimoza.covaci@umib.net

Abstract: *The main goal in this paper is the production and characterization of conductive nanocomposites with PMMA – Poly (methyl methacrylate) and PVDF – Poly (vinylidene fluoride) matrix reinforced with graphene, MWCNTs (multi-walled carbon nanotubes) and a hybrid mixture of graphene, MWCNTs, and fullerenes. The nanocomposites were produced as thin films. The thin films are obtained by solvent casting method. Using the ultrasonication process, carbon nanostructures are mixed with PMMA solution. The PMMA polymer is dissolved in chloroform. The solvent evaporates in approximately 72 hours.*

The carbon based nanostructures (CNs) that are dispersed in different weight fractions (5% and 15%) are functionalized in two ways: by acid functionalization with HNO_3 and using X-ray irradiation. For comparison, non-functionalized reinforcements were used as well. The effects of these functionalization methods on the graphene, MWCNTs and the hybrid mixture are evaluated through measurement of their conductive properties.

Physical characterization of the nanocomposites was performed by means of Raman spectroscopy, transmission electron microscopy (TEM), scanning electron microscopy (SEM) and thermogravimetric analysis (TGA). The conductivity of the nanocomposite is measured with a four-point probe method. Chemical analysis of graphene and carbon nanotubes was performed with ICP-OES.

Key words: nanocomposites, PMMA, graphene, MWCNTs, PVDF, SEM, TEM.

INTRODUCTION

For many years, metals like copper, aluminum, silver, and gold have been known for their excellent electrical conductivity. However, with advancements in science and technology, there has been a shift towards developing new materials that have improved mechanical, electrical, and thermal properties. Nanomaterials have become a primary focus, especially those with electrical properties that outperform traditional metallic conductors. Materials like graphene, carbon nanotubes (CNTs), and other nanostructures demonstrate exceptional electrical conductivity, sparking extensive research into conductive nanocomposites.

Graphene and CNTs are known for their extraordinary electrical conductivity, which is largely due to the unique arrangement of carbon atoms, particularly in

graphene. Discovered in 2004, graphene boasts impressive physical and chemical properties such as high thermal and electrical conductivity, a large surface area, and a high Young's modulus of elasticity. Similarly, CNTs are valuable for enhancing the electrical, chemical, mechanical, and thermal properties of polymers, depending on their structure, functioning as conductors or semiconductors [1]. As a functionalization method, the irradiation treatment was also used. In fact, when the carbon nanostructures are irradiated and due to the passing the ionizing electrons through the solid material, they interact with atoms on both atomic and crystal levels, inducing structural changes. This interaction resulted in various defects or disorders. In the case of carbon nanostructures (CNs), mainly two defects can occur, such as i) defect formation and ii) graphitization. During the irradiation treatment, the energy from ionizing radiation can eliminate specific functional groups, providing conditions for additional carbon atoms to bond in their place, forming new C–C or C=C bonds. This is additional graphitization process that results in enhanced crystallinity, improved thermal stability, and increased electrical conductivity.

Because it is not feasible to use graphene or CNTs as pure conductors, these nanoparticles incorporated into polymer matrices, create nanocomposites. These nanocomposites are an emerging class of materials with superior thermal, mechanical, and dielectric properties compared to regular polymer composites. These improvements arise from the interaction between the polymer matrix and the nanoparticles [2].

Poly (methyl methacrylate) (PMMA) is a polymer of interest due to its amorphous structure, optical transparency, and biocompatibility. However, PMMA can be brittle in its unmodified form. When small amounts of graphene and CNTs are added, its electrical conductivity significantly improves [3]. PMMA-based composites with carbon nanostructures are used for applications such as electromagnetic interference shielding, transparent conductive films, and gas sensors [4,5,6].

Research on PMMA/CNT systems has focused on techniques like solution mixing/casting and in situ polymerization. More advanced methods, such as coagulation, electrospinning, latex technology, and combinations of casting and melt mixing, have also been explored [5-12]. Studies have examined factors such as grain size, the aspect ratio of CNTs, and their functionality, observing improvements in thermal degradation onset and tensile strength in PMMA/CNT composites [13,14].

The main objective of this research is to create conductive nanocomposites with a PMMA matrix, reinforced with graphene, multi-walled carbon nanotubes

(MWCNTs), and a mix of graphene, MWCNTs, and fullerenes. The study involves several steps: characterizing the nanomaterials, functionalizing them, preparing polymer nanocomposites, evaluating the impact of functionalization on electrical conductivity using the four-point probe method, and analyzing both the carbon nanostructures and nanocomposites using advanced techniques.

EXPERIMENTAL

In Table 1 is presented the preparation scheme of nanocomposite thin films with PMMA matrix. The reinforcement added to the polymer solution is in 15% (0.15 g) weight. A small amount of reinforcement is sufficient for optimal parameters, due to the particle size and properties of the nanomaterials.

Thin films numbered 1 contain unmodified carbon nanostructures, films 10, 11 and 12 contain nitric acid-activated reinforcements, and films 14, 16, and 18 contain X-ray irradiated carbon nanostructures. To prepare the nanocomposite films, 250 ml of chloroform dissolves 10 g of PMMA, sonicated for 1 hour and 45 minutes. The polymer is divided into smaller beakers with added reinforcements, then sonicated for 30 minutes and stirred for 5 minutes to prevent nanoparticle agglomeration. After stirring, the contents are poured into Petri dishes and left for 72 hours to allow the solvent to evaporate. The dried films are then ready for further examination. Raman analyses are performed with a "Horiba Jobin Yvon LabRam 300 Infinity" instrument, using a green laser with 532 and 633 nm wavelengths.

Table 1 *Preparation scheme of thin films containing PMMA and reinforcements*

Sample	Graphene	MWCNTs	Mixture (G+MWCNT)
2	0.15 g non-functionalized		
4		0.15 g non-functionalized	
6			0.15 g non-functionalized
10	0.15 g (activated – HNO_3)		
11		0.15 g (activated-HNO_3)	
12			0.15 g (activated-HNO_3)
14	0.15 g-X-ray irradiated		
16		0.15 g-X-ray irradiated	
18			0.15 g-X-ray irradiated

RESULTS AND DISCUSSIONS

Transmission electron microscopy of graphene and MWCNTs (TEM)

Characterization of the graphene produced at FTM Skopje was performed by means of transmission electron microscopy (TEM). The TEM image in Fig. 1a shown that the graphene used in this research has several layers with different

layer thicknesses. The image shown below represents the produced graphene through exfoliation of graphite electrodes using the melt electrolysis. The images show that the produced graphene has different two dimensional forms and shapes with different thickness, width and length [17,18].

The TEM images in Fig. 1b show the characteristic structure of multi-walled carbon nanotubes. Their specific tubular structure allows their application as electric conductors in nanocomposites with polymer matrices. The image shows the presence of some inclusions and impurities, such as lithium or lithium carbides. There are also some metal particles and amorphous carbon structures. The MWCNTs are formed from multiple layers with a diameter in the range of 10-50 nm. Their length may reach 100+ μm. Over 98% of the graphite has successfully transformed into carbon nanotubes.

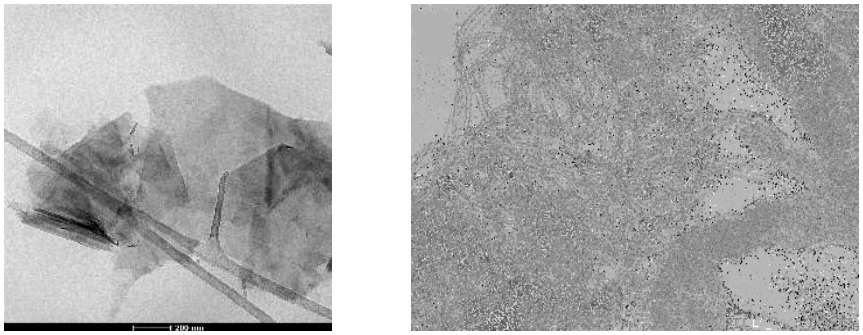

a b

Figure 1 *TEM images of a) graphene and b) MWCNTs*

Scanning electron microscopy of activated graphene (SEM)

SEM images of the used activated graphene are shown in Fig. 2a and Fig. 2b. It is clearly visible that the obtained graphene flakes consist of very thin layers with different dimensions. These thin layers are of extremely high quality.

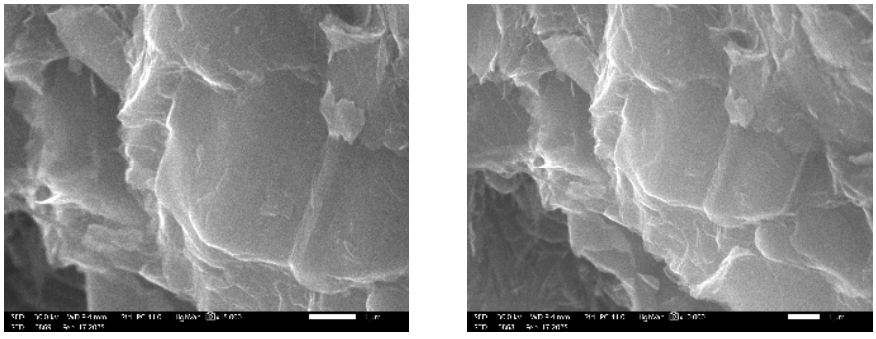

Figure 2 *SEM images of activated graphene*

SEM of activated MWCNTs

SEM images of the activated MWCNTs are shown in Fig. 3a and Fig. 3b. It is evident that the MWCNTs are curved and with different diameters (from 2 to 30 nm). Also, some minor impurities are registered.

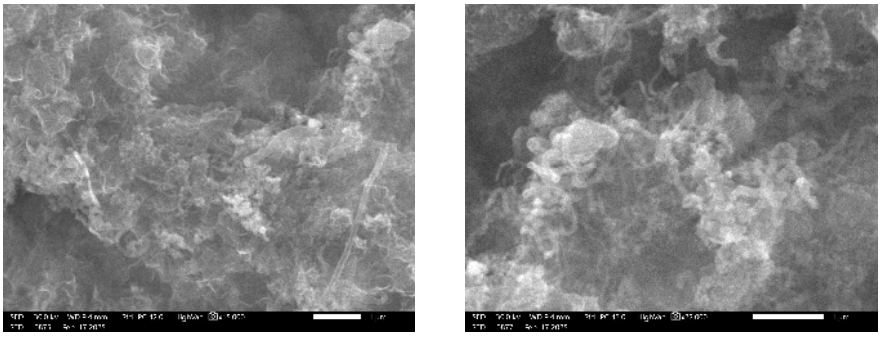

Figure 3 *SEM images of activated MWCNTs*

SEM of the mixture of activated graphene and MWCNT,s

SEM images of a mixture of graphene and MWCNTs (Fig. 4), show that graphene flakes consist of very thin layers and carbon tubes with different diameters. The mixture of graphene and CNTs is of extremely high quality. The MWCNTs have diameters ranging from 5 to 50 nm.

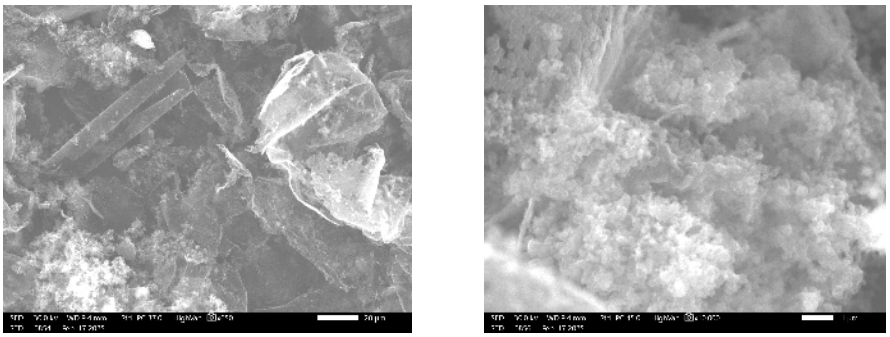

Figure 4 *SEM images of activated mixture of graphene and MWCNTs*

Raman spectroscopy

In order to determine the layer thickness and structural defects in the carbon nanostructure (Fig. 5), the obtained graphene samples are analyzed using Raman spectroscopy. Each spectrum is acquired in 5 s, with 10 accumulations. Spectra

are analyzed in the 500-3500 cm^{-1} range, with a spectral resolution of 4 cm^{-1}. Presented Raman at Fig. 5 shows that the graphene used as reinforcement has a highly ordered crystal structure and the ID/IG ratio is minimal [20-21].

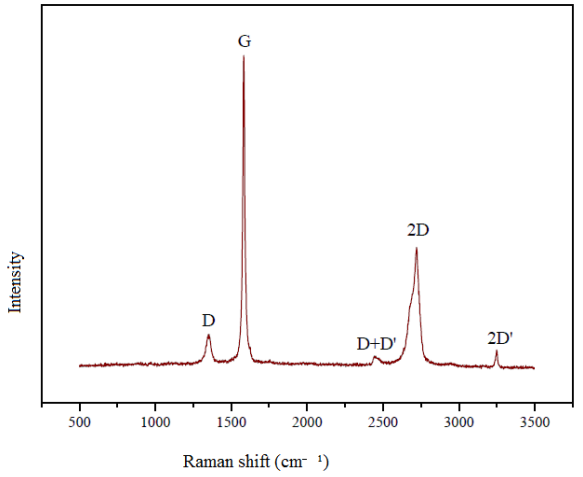

Figure 5 *Raman spectum of graphene used as reinforcement*

The Raman spectra provide valuable information about the structure of multi-walled carbon nanotubes (MWCNTs). Fig. 6 displays the spectrogram of MWCNTs produced at the Faculty of Technology and Metallurgy in Skopje, Macedonia.

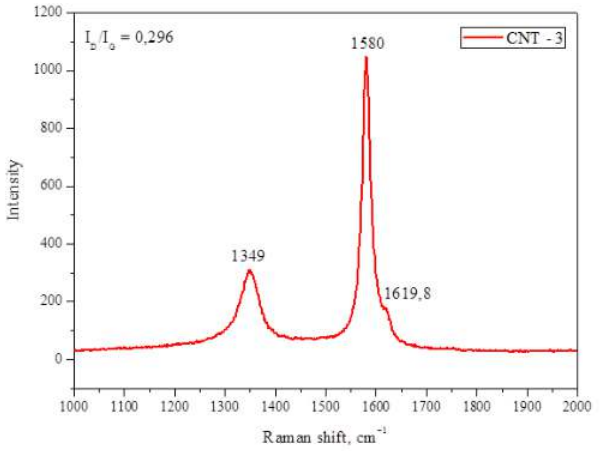

Figure 6 *Raman spectrum of MWCNTs*

The D peak around 1350 cm^{-1}indicates defects in the carbon nanotube structure, caused by pentagons and heptagons in the hexagonal arrangement or the edges of the cylindrical shape. Some graphite crystals and amorphous carbon are also present. The G peak at 1580 cm^{-1} represents the graphitic region, while the D' peak appears as a left shoulder at around 1620 cm^{-1}. The intensity ratio of the G and D peaks (IG/ID) reflects the crystalline size; a smaller ID/IG ratio suggests larger crystals and higher crystallinity.

In this case, the D peak intensity is three times that of the G peak, indicating a highly organized crystal structure of the MWCNTs [17-19, 22-24].

ICP-OES chemical analyses of graphene and multi-walled carbon nanotubes

To ascertain the chemical purity and presence of other metal elements in graphene, we have conducted a chemical analysis using optical emission spectrometry. The obtained results are shown in table 2. The produced graphene is incredibly pure (99.418% purity).

Table 2 *ICP-OES data of graphene*

Tests	Method of analysis	Results
Purity, %	Optical emission spectrometry, ICP-OES	99.418
Total impurities, %		0.582

The same analysis was performed with carbon nanotubes samples. Table 3 shows the list of impurities and purity percentage of MWCNTs. The produced MWCNTs are also incredibly pure (97.927% purity).

Table 3 *ICP-OES data of MWCNTs*

Tests	Method of analysis	Results
Purity, %	Optical emission spectrometry, ICP-OES	97.927
Total impurities, %		2.073

Four-point probe method of measuring electrical conductivity

The electrical conductivity of nanocomposites was measured using the "Jandel four-point probe Model RM3000" instrument. Literature indicates that the electrical percolation threshold (pc) for the PMMA/MWCNT system is between 0.5 vol.% and 0.75% MWCNT, with a sharp conductivity increase of about seven orders of magnitude. Conductivity saturates for concentrations above 1.0 wt.% MWCNT. Resistance and voltage measurements were used to calculate electric current, as shown in equation (1).

$$\rho_0 = \frac{V}{I} \cdot 2\pi S \quad (1)$$

The following diagrams compare the conductivity of polymer nanocomposites with PMMA. The applied voltage, current, and resistance values are shown in Table 4.

Table 4 *Current, resistance and voltage values for each PMMA nanocomposite*

Ordinal number of sample	Electrical current (I)	Resistance (R)	Voltage (U)
2	$4.15*10^{-13}$ A	78.61 MΩ	520 mV
4	$8.3*10^{-9}$ A	7.042 KΩ	930.8 mV
6	$1.38*10^{-9}$ A	770.5 Ω	16.99 mV
10	$4.008*10^{-13}$ A	143.91 MΩ	918.6 mV
11	$1.35*10^{-9}$ A	2.605 KΩ	56.09 mV
12	$1.42*10^{-9}$ A	455.23 Ω	10.3 mV
14	$1.46*10^{-13}$ A	440.3 MΩ	1027.2 mV
16	$1.38*10^{-9}$ A	1.68 KΩ	37.02 mV
18	$3.29*10^{-9}$ A	1299 Ω	68.13 mV

The diagrams (Fig. 7 and Fig. 8) compare the conductivity of different thin film nanocomposites with a PMMA matrix. The obtained results clearly confirmed that the irradiation treatment of carbon nanostructures (G and MWCNTs) induced the additional graphitization process that results in highly-ordered crystallinity and consequently, increased electrical conductivity of their nanocomposites.

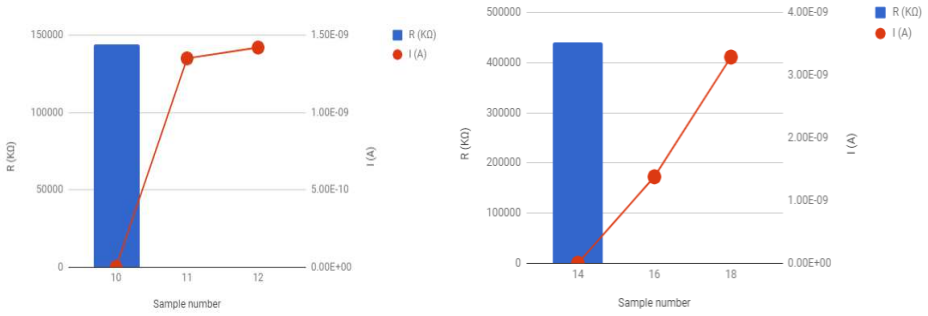

Figure 7 *A PMMA/G with 15% HNO_3 activated graphene (10), PMMA/MWCNT with 15% HNO_3 activated MWCNTs (11) and PMMA/mix with 15% HNO_3 activated mixture (12), and B. PMMA/G with 15% X-ray irradiated graphene (14), PMMA/MWCNT with 15% X-ray irradiated MWCNTs (16) and PMMA/mix with 15% X-ray irradiated mixture (18).*

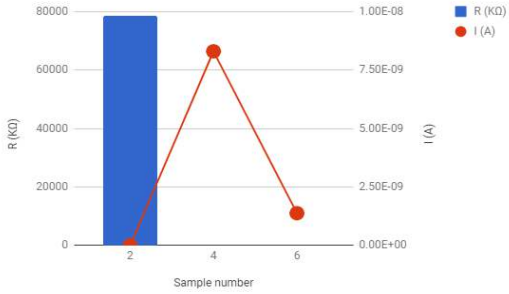

Figure 8 PMMA/G with 15% non-functionalized graphene (2), PMMA/MWCNT with 15% non-functionalized MWCNTs (4) and PMMA/mix with 15% non-functionalized mixture (6)

Key observations include:

- Graphene-reinforced nanocomposites are poorer conductors compared to MWCNT-reinforced and G+MWCNT mixture-reinforced nanocomposites.
- PMMA nanocomposites with X-ray irradiated G+MWCNT mixtures show higher conductivity than those with HNO_3 activated or non-functionalized G+MWCNT mixtures (diagrams no. 7 and 8).
- PMMA nanocomposites with HNO_3 activated or X-ray irradiated MWCNTs or G+MWCNT mixtures are much better conductors than those with activated or irradiated graphene (diagram 8).

Thermogravimetric analysis of PMMA nanocomposite

Carbon nanostructures demonstrate good barrier action, which can improve the thermal stability of polymer/CNs composites.

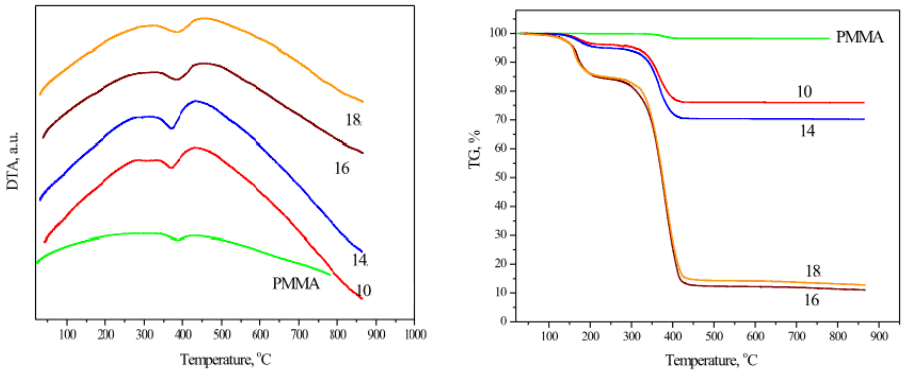

Figure 9 DTA and TGA thermogram of pure PMMA and PMMA/mixture with 15% X-ray functionalized mixture (18), PMMA/MWCNT with 15% X-ray functionalized MWCNT (16), PMMA/G with 15% X-ray functionalized graphene (14), PMMA/G with 15% functionalized with HNO_3 (10)

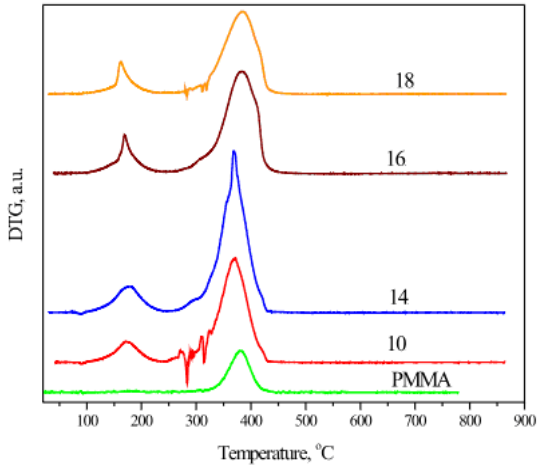

Figure 10 DTG thermogram of pure PMMA and PMMA/mixture with 15% X-ray functionalized mixture (18), PMMA/MWCNT with 15% X-ray functionalized MWCNT (16), PMMA/G with 15% X-ray functionalized graphene (14), PMMA/G with 15% HNO_3 functionalized graphene (10).

The thermograms in Figures 9 and 10 show two main regions of thermal decomposition: the first between 145 and 153°C, and the second between 315 and 330°C. The initial decomposition temperature (onset) is around 80-90°C, due to the evaporation of water and other volatiles in the thin films, with all volatile components decomposing below 100°C.

The DTG thermogram reveals the oxidation and decomposition of carbon nanostructures at 360-385°C, confirmed by a negative peak in the DTA thermogram within the same range. Among the three carbon nanostructures studied, PMMA/MWCNT nanocomposites exhibit the highest Td1, though there are no significant differences in thermal stability among the systems.

Table 5 *Thermal parameters of pure PMMA, PMMA/MWCNT (16), PMMA/mixture (18), PMMA/G (14 and 10)*

PMMA nanocomposites	Td_1 [°C]	Td_2 [°C]	DTG_1 [°C]	DTG_2 [°C]	DTA_1 [°C]
Pure PMMA	150,2	329,4	/	380,4	385,2
18 / PMMA/mixture	148,2	322,1	162,1	384,8	383,0
16 / PMMA/MWCNT	152,3	319,9	169,4	384,8	381,9
14 / PMMA/Gxr	143,1	317,9	181,8	367,7	366,5
10 / PMMA/Gact	147,7	323,2	172,4	372,1	366,8

CONCLUSIONS

The main goal of this paper was to measure and compare the electrical conductivity of thin film nanocomposites using a PMMA matrix, reinforced with 15% graphene, carbon nanotubes, and a mixture of both. Graphene and carbon nanotubes were functionalized with nitric acid and X-ray irradiation treatment to enhance interactions with the polymer matrix, prevent agglomeration, and achieve differences in conductivity.

The electrical conductivity was measured using a four-point probe method. PMMA nanocomposites exhibited better conductivity with functionalized MWCNT and the mixture compared to functionalized graphene. In the PMMA/CNs mixture system, the highest conductivity was observed with samples containing 15% (0.15 g) of the mixture (graphene, carbon nanotubes, and fullerenes), showing resistance in the range of 450-1000 Ω. In contrast, PMMA/graphene nanocomposites recorded much higher resistance levels (70-400 MΩ).

Acknowledgment: This paper has been supported by the Science and Research Fund of Ss. Cyril and Methodius University in Skopje

REFERENCES

1. A. K. Geim, K. S. Novoselov, The rise of graphene, *Nature Materials* **6** (2007) 183-191. https://doi.org/10.1038/nmat1849
2. L. Banks-Sills, D. G. Shiber, V. Fourman, R. Eliasi, A. Shlayer, Experimental determination of mechanical properties of PMMA reinforced with functionalized CNTs, *Composites Part B: Engineering* **95** (2016) 335-345. https://doi.org/10.1016/j.compositesb.2016.04.015
3. Z. Jia, Z. Wang, C. Xu, J. Liang, B. Wei, D. Wu, S. Zhu, Study on poly(methyl methacrylate)/carbon nanotube composites, *Materials Science and Engineering: A* **271** (1999) 395-400. https://doi.org/10.1016/S0921-5093(99)00263-4
4. S.M. Yuen, C.C.M. Ma, C.Y. Chuang, K.C. Yu, S.Y. Wu, C.C. Yang CC, et al., Effect of processing method on the shielding effectiveness of electromagnetic interference of MWCNT/PMMA composites, *Composites Science and Technology* **68** (2008) 963-968. https://doi.org/10.1016/j.compscitech.2007.08.004
5. D.O. Kim, M.H. Lee, J.H. Lee, T.W. Lee, K.J. Kim, Y.K. Lee, et al., Transparent flexible conductor of poly(methyl methacrylate) containing highly-dispersed multi walled carbon nanotube, *Organic Electronics* **9** (2008) 1-13. https://doi.org/10.1016/j.orgel.2007.07.004
6. Y. Li, X.C. Wang, M.J. Yang, n-Type gas sensing characteristics of chemically modified multi-walled carbon nanotubes and PMMA composite, *Sensors and Actuators B: Chemical* **121** (2007) 496-500. https://doi.org/10.1016/j.snb.2006.04.074
7. S.M. Yuen, C.C.M. Ma, C.Y. Chuang, K.C. Yu, S.Y. Wu, C.C. Yang, et al., Effect of processing method on the shielding effectiveness of electromagnetic interference of MWCNT/PMMA composites, *Composites Science and Technology* **68** (2008) 963-938. https://doi.org/10.1016/j.compscitech.2007.08.004

8. F. Du, J.E. Fischer, K.I. Winey, Coagulation method for preparing single-walled carbon nanotube/poly(methyl methacrylate) composites and their modulus, electrical conductivity, and thermal stability, *Journal of Polymer Science B: Polymer Physics* **41** (2003) 3333-3338. https://doi.org/10.1002/polb.10701
9. B. Sundaray, V. Subramanian, T.S. Natarajan, K. Krishnamurthy, Electrical conductivity of a single electrospun fiber of poly(methyl methacrylate) and multiwalled carbon nanotube nanocomposite, *Applied Physics Letters* **88** (2006) 143114. https://doi.org/10.1063/1.2193462
10. O. Regev, P.N.B. ElKati, J. Loos, C.E. Koning, Preparation of conductive nanotube–polymer composites using latex technology, *Advanced Materials* **16** (2004) 248-251. https://doi.org/10.1002/adma.200305728
11. Z. Jin, K.P. Pramoda, G. Xu, S.H. Goh, Dynamic mechanical behavior of melt processed multi-walled carbon nanotubes/poly(methyl methacrylate) composites, *Chemical Physics Letters* **337** (2001) 33-47. https://doi.org/10.1016/S0009-2614(01)00186-5
12. C. McClory, T. McNally, M. Baxendale, P. Pötschke, W. Blau, M. Ruether, Electrical and rheological percolation of PMMA/MWCNT nanocomposites as a function of CNT geometry and functionality, *European Polymer Journal* **46** (2010) 854-868. https://doi.org/10.1016/j.eurpolymj.2010.02.009
13. R.E. Gorga, R.E. Cohen, Toughness enhancements in poly(methyl methacrylate) by addition of oriented multiwall carbon nanotubes, *Journal of Polymer Science B: Polymer Physics* 42 (2004) 2690-2702. https://doi.org/10.1002/polb.20126
14. E. Logakis, Ch. Pandis, P. Pissis, J. Pionteck, P. Pötschke, Highly conducting poly(methyl methacrylate)/carbon nanotubes composites: Investigation on their thermal, dynamic-mechanical, electrical and dielectric properties, *Composites Science and Technology* **71** (2011) 854-862. https://doi.org/10.1016/j.compscitech.2011.01.029
15. C. N. R. Rao, K. Biswas, K. S. Subrahmanyam, A. Govindaraj, Graphene, the new nanocarbon, *Journal of Materials Chemistry* **19** (2009) 2457-2469. https://doi.org/10.1039/B815239J
16. G. Wang, J. Yang, J. Park, X. Gou, B. Wang, H. Liu and J. Yao, Facile Synthesis and Characterization of Graphene Nanosheets, The Journal of Physical Chemistry C **112** (2008) 8192-8195. https://doi.org/10.1021/jp710931h
17. A. T. Dimitrov, A. Ademi, A. Grozdanov, P. Paunović, Production and Characterization of MWCNTs Produced by Non-Stationary Current Regimes in Molten LiCl, *Applied Mechanics and Materials* **328** (2013) 772-777. https://doi.org/10.4028/www.scientific.net/AMM.328.772
18. C. Schwandt, A.T. Dimitrov, D.J. Fray, High-yield synthesis of multi-walled carbon nanotubes from graphite by molten salt electrolysis, *Carbon* **50** (2012) 1311-1315. https://doi.org/10.1016/j.carbon.2011.10.054
19. A. Tomova, G. Gentile, A. Grozdanov, M.E. Errico, P. Paunović, M. Avella, A.T. Dimitrov, Functionalization and Characterization of MWCNT Produced by Different Methods, Acta Physica Polonica A **129** (2016) 405-408. https://doi.org/10.12693/APhysPolA.129.405
20. B. Andonovic, A. Grozdanov, P. Paunović, A.T. Dimitrov, X-ray diffraction analysis on layers in graphene samples obtained by electrolysis in molten salts: a new perspective, *Micro & Nano Letters* **10** (2015) 683-685. https://doi.org/10.1049/mnl.2015.0325
21 B. Andonović, A. Grozdanov, A. Petrovski, P. Paunović, A. Dimitrov, Determining

graphene layers number andN-layer region coverage by XRD data distribution model, *Material and Environment Protection* **4** (2015) 19-25.
22. C. Schwandt, A.T. Dimitrov, A.R. Kamali, D.J. Fray, The preparation of nanoscale carbon from graphite via molten salt electrolysis, FRAY INTERNATIONAL SYMPOSIUM, Cancun, Mexico, 27 Nov-01 Dec 2011.
23. C. Schwandt, A.T. Dimitrov, D.J. Fray, The preparation of nano-structured carbon materials by electrolysis of molten lithium chloride at graphite electrodes, *Journal of Electroanalytical Chemistry* **647** (2010)150-158.
https://doi.org/10.1016/j.jelechem.2010.06.008
24. A.T. Dimitrov, G.Z. Chen, I.A. Kinloch, D.J. Fray, A Feasibility study of Scaling-up the Electrolytic Production of Carbon Nanotubes in Molten Salt, *Electrochimica Acta* **48** (2002) 91-102. https://doi.org/10.1016/S0013-4686(02)00595-9

EVALUATION OF BIODEGRADABLE PLASTICS AS A SUSTAINABLE SOLUTION TO MARINE POLLUTION BY MICROPLASTICS AND NANOPLASTICS

Immacolata Liotta[1,2], Roberto Avolio[1], Rachele Castaldo[1], Maria Emanuela Errico[1], Gennaro Gentile[1], Federico Olivieri[1], Mariacristina Cocca[1]

[1] - *Institute of Polymers, Composites and Biomaterials National Research Council of Italy Via Campi Flegrei 34 -80078 Pozzuoli (NA) Italy*

[2] - *Department of Chemical, Material and Industrial Production Engineering of the University of Naples Federico II Piazzale Tecchio 80 - 80125 Napoli Italy*

mariacristina.cocca@cnr.it

Abstract: *Global plastic production has rapidly increased in the past two decades, reaching 400 million tons in 2023, with 8.4% from recycled plastics and 0.7% from bio-based plastics. Due to mismanagement, between 10 and 20 million tons of plastic enter the oceans annually, and by 2050, plastic could exceed fish stocks. Plastic waste is a source of secondary microplastics and nanoplastics, as larger pieces are broken down and fragmented through a combination of photochemical, biological, mechanical and chemical degradation, depending on the environmental conditions to which they are exposed. Biodegradable plastics, made from renewable or fossil resources such as polylactic acid (PLA), polyhydroxyalkanoates (PHA), poly(ε-caprolactone) (PCL), polybutylene succinate (PBS), and polybutylene succinate-co-butylene adipate (PBSA), are seen as alternatives to non-degradable plastics. However, some of these polymers have been found as microplastics in marine environments. For instance, PCL fragments have been found in the Mediterranean, indicating that biodegradable plastics may not degrade easily in natural conditions, failing to offer a complete solution to marine pollution. Long-term use of biodegradable plastics could create issues similar to traditional plastics due to ineffective end-of-life management and environmental accumulation. In such scenario, research is increasingly needed to evaluate the degradation of biodegradable plastics under conditions simulating the marine environment, to determine whether they can represent a sustainable solution to marine pollution or whether, in turn, they could accumulate in marine ecosystems under current and future environmental conditions.*

Keywords: microplastics, nanoplastics, biodegradable plastics, degradation, marine pollution

INTRODUCTION

The global plastic production has grown rapidly in the last twenty years reaching 400 Mt (million tons) in 2023 [1]. The unique properties of the plastics, like low-cost, lightness, stability and good mechanical performances, make them suitable for several applications [2]. The increase of plastic demand induce an increase in

the generation of post-consumer plastic waste. In 2020, 29.5 million tonnes of post-consumer plastics waste were collected in Europe [1]. Due to mismanagement of plastics at the end of life, a large amount of these materials end up in marine environment with impacts on the ecosystem [3]. Plastics were found to be largely accumulated on beaches, in sediments, in deep marine environment, etc [4]. It was esteemed that between 10 and 20 million tons of plastic enter the oceans annually, and by 2050, plastic could exceed fish stocks [5,6]. Plastic objects dispersed in the environment can degrade due to environmental factors such as UV radiation, wind, waves, seawater, and bacteria, leading to the formation of fragments classified as mesoplastics (~5–20 mm), large microplastics (~1–5 mm), small microplastics (~20–999 µm), and nanoplastics (<1 µm), depending on the chemical-physical properties of the plastic debris [7]. In this frame, several public policies have been introduced aimed at reducing use and disposal of plastic items, while encouraging recycling or even progressive phase-out of lightweight plastics [8]. Biodegradable plastics such as poly(lactic acid) (PLA) and poly(hydroxyalkanoate)s (PHA), poly(ε-caprolactone) (PCL), poly(butylenesuccinate) (PBS) and poly(butylenesuccinate-co-butyleneadipate) (PBSA) are considered promising substitutes for traditional non-degradable plastics and can be obtained from both renewable, or fossil resources. Despite their biodegradability, some of these polymers have been found as fragments in submillimetric size, i.e microplastics, in the marine environment. For example, PCL fragments were found in the Mediterranean Sea, suggesting that in some cases biodegradable polymers do not readily degrade under natural conditions and therefore do not represent an a priori solution for reducing marine litter [9]. Therefore, biodegradable plastics are not always degradable in environmental conditions and their long-term use could cause problems similar to those currently attributed to traditional plastics due to uncontrolled end-of-life management and subsequent accumulation in the environment. Starting from these considerations, studies are being conducted on biodegradable plastics to evaluate the release of microplastics, which similarly to traditional ones, could adsorb many pollutants with different mechanisms and could release additives [10]. In this context, there is a growing need for research focused on assessing the degradation of biodegradable plastics under conditions that closely mimic the marine environment. This research is essential to determine whether biodegradable plastics can offer a truly sustainable solution to the growing problem of marine pollution. It is crucial to assess whether these materials will effectively decompose in marine ecosystems over time or whether, despite their biodegradable nature, they could still accumulate in these environments. Furthermore, understanding how biodegradable plastics degrade under different environmental factors, including temperature and pH

changes, will provide valuable insights into their long-term behavior. As the impacts of climate change and ocean acidification intensify, it becomes even more important to study how these plastics interact with marine ecosystems, particularly in terms of the formation of microplastics and nanoplastics.

In this study, blends of polybutylene adipate terephthalate (PBAT), PBS, and cellulose were prepared to evaluate their degradation behavior under conditions simulating the marine environment. Degradation was assessed in abiotic solutions with different temperature and pH levels, designed to mimic the effects of climate change and ocean acidification. Three different environmental conditions were tested to observe how these factors influence the degradation of these bioplastics. The objective was to understand the impact of these changes on plastic degradation rates, particularly in relation to the increasing severity of climate change and ocean acidification.

EXPERIMENTAL

Blends of different compositions of PBAT, PBS and callulose were made. The blends were prepared using a Thermo HAAKE MiniLab twin-screw extruder and the compositions made are summarized in Table 1. About 5 g of material were mixed for 5 minutes in the extruder by setting a temperature of 160°C, higher than the melting temperature of the two polymers, and 60 rpm.

Table 1 *Blends made*

Sample ID	% PBAT	% PBS	% Cellulose Fibers
PBAT	100	0	0
PBAT20-PBS80	20	80	0
B2080-CF5	20	80	5
PBS	0	100	0

A 100-day degradation study was initiated under abiotic conditions simulating seawater. Abiotic seawater simulant solutions were made using milliQ water in which Instant Ocean sea salt (Aquarium Systems) was dissolved to obtain a salinity of 35%, typical of the marine environment. HCl was used to obtain solutions with different pH. The mixtures were cut into 5x5 mm pieces, with a thickness of 0.5 mm and were immersed in 90 ml of simulant solution in closed transparent soda-lime glass bottles of 100 ml to obtain a polymer concentration of 3.3 g/l of solution. Three different experiments were conducted by varying the temperature and pH of the simulant solutions, parameters chosen to evaluate the relationship between climate change and plastic pollution:

A. Experiment A was conducted at room temperature (which in the three months of exposure was on average 15°C), pH 8.3, under an OSRAM

ULTRA VITALUX 300 Watt lamp to simulate sunlight, turned on 24 hours a day.

B. Experiment B was conducted in the same conditions as experiment A but at a pH of 7.3.

C. Experiment C was conducted in an Angelantoni Challenge 250E climate chamber at a fixed temperature of 35°C, under a UV lamp and pH of the solutions of 8.3.

Every month the samples were collected, weighed and characterized by differential scanning calorimetry (DSC), thermogravimetric analysis (TGA) and attenuated total reflectance Fourier transform infrared spectroscopy (FTIR-ATR). Furthermore, scanning electron microscope (SEM) images of the surface were acquired before and at the end of the aging period. The pH of the solutions was also measured at the beginning and at the end.

RESULTS AND DISCUSSIONS

Preliminary results showed that during the 100 days of exposure, the samples showed a maximum weight loss of 2%. Degradation was mainly influenced by temperature, with experiment C causing the greatest weight loss, especially for the B2080-CF5 blend. pH changes in experiments A and B had a similar effect on degradation, with PBAT showing the greatest weight loss. In figure 1 it is possible to observe some sample SEM micrographs, before and after aging, of the B2080-CF5 sample in experiment A.

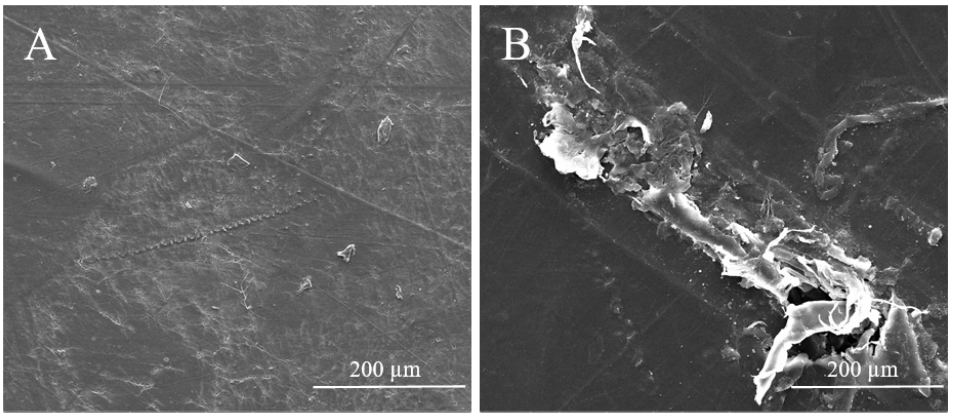

Figure 1 *SEM micrographs, before and after aging, of the B2080-CF5 sample in experiment A. A) Unaged sample; B) Aged sample*

Polymer degradation affected the pH of the solutions, lowering it in particular in experiments A and C, with a greater acidification in the mixture with cellulose fibers. The higher temperature in experiment C did not show a significant impact. In experiment B, with a lower initial pH, the lowering was less. The pH changes are similar to those predicted for the oceans by the end of the century due to anthropogenic emissions [11]. No pH changes were observed in the control solutions without polymers placed at the same conditions. The acidification seems to result from the release of organic acids and CO_2 from the plastic [12].

CONCLUSIONS

In conclusion, preliminary results indicate that samples experienced a maximum weight loss of 2% over 100 days, with temperature being the main factor influencing degradation, particularly in Experiment C. The pH of the solutions decreased during degradation, with more significant acidification observed in the mixtures containing cellulose fibers. pH changes were less pronounced in Experiment B, with a lower initial pH. The observed acidification is consistent with predictions for ocean pH changes due to anthropogenic emissions. There was no pH change in the control solutions without polymers, suggesting that acidification is related to the release of organic acids and CO_2 from plastics.

Acknowledgements: This work was realized in the framework of the Project – Biomonitoraggio di micro e nanoplastiche biodegradabili: dall'ambiente all'uomo in una prospettiva one health (BioPlast4Safe) – with the technical and economic support of the Italian Ministry of Health - PNC.

REFERENCES

1. Plastics Europe, «Plastics – The Fast Facts 2024».
2. A. Andrady, M. Neal, Applications and societal benefits of plastics, *Philos. Trans. R. Soc. B* **364** (2009) 1977–1984. https://doi.org/10.1098/rstb.2008.0304
3. J. Prata, A. Patrício Silva e J. da Costa, Solutions and integrated strategies for the control and mitigation of plastic and microplastic pollution., *Int J Environ Res Public Health* **16** (2019) 1-19. https://doi.org/10.3390/ijerph16132411
4. R. Thompson, Y. Olsen, R. Mitchell, A. Davis, S. Rowland e A. John, Lost at sea: where is all the plastic?, *Science* **304** (2004) 838. https://doi.org/10.1126/science.1094559
5. A. Barron, T.D. Sparks, Commercial Marine-Degradable Polymers for Flexible Packaging. IScience, 23 (2020) 101353. https://doi.org/10.1016/j.isci.2020.101353
6. Paul, M. B., Stock, V., Cara-Carmona, J., Lisicki, E., Shopova, S., Fessard, V., Braeuning, A., Sieg, H., & Böhmert, L. (2020). Micro- and nanoplastics – current state of knowledge with the focus on oral uptake and toxicity. Nanoscale Advances, 2(10), 4350–4367. https://doi.org/10.1039/D0NA00539H

7. A. Ter Halle, L. Ladirat, X. Gendre, D. Goudouneche, C. Pusineri, C. Routaboul, C. Tenailleau, B. Duployer, E. Perez, Understanding the fragmentation pattern of marine plastic debris., *Environ. Sci. Technol.* **50**, (2016) 5668–5675. https://doi.org/10.1021/acs.est.6b00594 .
8. European Commission, Directive (EU) 2019/ of the European Parliament and of the Council of 5 June 2019 on the Reduction of the Impact of Certain Plastic Products on the Environment., 2019.
9. G. Suaria, C. Avio, A. Mineo, G. Lattin, M. Magaldi, G. Belmonte e C. Moore, The Mediterranean Plastic Soup: synthetic polymers in Mediterranean surface waters., *Sci. Rep.* **6** (2016) 37551. https://doi.org/10.1038/srep37551
10. D. Falco, R. Avolio, M. E. Errico, E. D. Pace, M. Avella, M. Cocca e G. Gentile, Comparison of biodegradable polyesters degradation behavior in sand, *Journal of Hazardous Materials* **416** (2021) 126231. https://doi.org/10.1016/j.jhazmat.2021.126231
11. N.L. Bindoff, W.W.L. Cheung, J.G. Kairo, J. Arístegui, V.A. Guinder, R. Hallberg, N. Hilmi, N. Jiao, M.S. Karim, L. Levin, S. O'Donoghue, S.R. Purca Cuicapusa, B. Rinkevich, T. Suga, A. Tagliabue, P. Williamson, Changing Ocean, Marine Ecosystems, and Dependent Communities. In: IPCC Special Report on the Ocean and Cryosphere in a Changing Climate, H.-O. Pörtner, D.C. Roberts, V. Masson-Delmotte, P. Zhai, M. Tignor, E. Poloczanska, K. Mintenbeck, A. Alegría, M. Nicolai, A. Okem, J. Petzold, B. Rama, N.M. Weyer (eds.). Cambridge University Press, 2019. https://doi.org/10.1017/9781009157964.007
12. C. Romera-Castillo, A. Lucas, R. Mallenco-Fornies, M. Briones-Rizo, E. Calvo, C. Pelejero, Abiotic plastic leaching contributes to ocean acidification, *Science of The Total Environment* **854** (2023) 158683. https://doi.org/10.1016/j.scitotenv.2022.158683

TRANSFORMING BIOMASS WASTE INTO HIGH-PERFORMANCE INSULATING AND FIRE-RETARDANT MATERIALS

Rachele Castaldo[1*], Noemi Faggio[1], Federico Olivieri[1], Roberto Avolio[1], Gennaro Gentile[1], Paolo Bettotti[2], Marina Scarpa[2], Lorenza Maddalena[3], Federico Carosio[3]

[1] - *Institute of Polymers, Composites and Biomaterials - IPCB, National Research Council of Italy - CNR, Via Campi Flegrei 34, 80078 Pozzuoli, Italy*

[2] - *Department of Physics – University of Trento, via Somarive, 14, I-38050 Povo, Italy*

[3] - *Department of Applied Science and Technology - Politecnco di Torino, via Teresa Michel 5, 15121, Alessandria, Italy*

rachele.castaldo@cnr.it

Abstract: *The GAIA (Green cellulose bAsed fire safe and lightweight Insulating mAterials) project aims to develop sustainable insulating porous materials using natural fibers from lignocellulosic waste. Raw materials are selected based on availability, economic impact, lignocellulosic content, and fiber structure, which affect mechanical and thermal performance. Fibers are extracted using eco-friendly methods to ensure compatibility with further treatments. Both raw fibers and extracts undergo Layer-by-Layer (LbL) functionalization through scalable, water-based processes. These coatings, made from natural substances like polysaccharides, phytates, and inorganic nanoparticles, enhance mechanical strength and flame resistance. Two product types are targeted: freeze-dried foams, where coatings improve fiber bonding to form strong aerogels, and thermobonded panels, where coatings enhance interactions between natural and thermoplastic fibers for low-density insulation. Mechanical, thermal, and flame-retardant properties are analyzed to link coating design to performance. Grape pomace, draff, rice husk and hemp were chosen as raw biomasses. Planetary ball milling was employed as pre-treatment to cellulose extraction from the biomasses. Insulating and fire-retardant thermobonded panels were obtained using LbL functionalized hemp and poly(lactic acid) fibers.*

Keywords: lightweight materials, biomasses, thermal insulation, flame retardancy

INTRODUCTION

Growing societal demand for more sustainable products and the transition to a circular economy, combined with the scarcity of raw materials due to current geopolitical challenges, have spurred increasing interest in the reuse, recycling, and upcycling of biomass for a wide range of applications [1]. The annual production of biomass waste continues to rise, yet effective strategies for its true upcycling remain limited.

One promising area for biomass valorization is the development of insulating and flame-retardant materials. Polymer foams and non-woven low-density panels are commonly used as insulating materials due to their ease of processing, low density, and excellent acoustic and thermal insulation performance. However, these materials face significant challenges in terms of sustainability and safety: they are largely petroleum-derived, difficult to recycle, and highly flammable. When exposed to heat sources, they ignite easily, producing intense flames and releasing toxic smoke.

In this context, natural fibers sourced from renewable feedstocks, such as plants and lignocellulosic waste, offer a valuable opportunity to develop eco-friendly, high-performance materials that meet the growing demands for sustainability and safety. While natural fibers have shown promising results in bulk biocomposites, their application in insulation materials remains limited by both functional and processing constraints.

On one hand, the production of porous structures from natural fibers is hindered by poor fiber–fiber interactions, which prevent the formation of stable, self-supporting 3D structures. On the other hand, the inherent flammability of natural fibers poses serious safety concerns. Conventional approaches to improve structural integrity, such as the use of polymeric binders or thermoplastic synthetic fibers, reduce the overall fiber content and compromise the sustainability of the resulting materials, while failing to address flammability issues.

RESULTS AND DISCUSSIONS

The GAIA project aims to establish a sustainable strategy for producing high-performance insulating porous materials based on natural fibers extracted from lignocellulosic biomass waste.

To achieve this, raw materials will be evaluated based on several criteria:

(i) availability and abundance of the feedstock; (ii) the potential economic impact of biomass waste recovery; (iii) lignocellulosic content and the presence of minor components that may enhance compatibility with the components used for porous material production; (iv) the structural properties of coarse plant fibers that influence mechanical and thermal performance.

Lignocellulosic fibers will be extracted using low-impact, environmentally friendly methods, with a focus on maximizing compatibility with subsequent functionalization steps.

Both raw fibers and lignocellulosic extracts will be functionalized via Layer-by-

Layer (LbL) assembly techniques using water-based, scalable processes. The objective is to incorporate environmentally benign compounds, such as polysaccharides, phytates, and inorganic nanoparticles, to tailor mechanical properties and flame retardancy [2,3]. The composition and structure of the coatings will be optimized for two main target applications:

i) Freeze-dried foams with a wide range of densities: coatings will be designed to promote fiber–fiber interactions during drying, enabling the formation of stable and mechanically robust aerogels.

ii) Thermobonded panels: the coatings will be tuned to enhance interactions with thermoplastic fibers in non-woven structures, enabling the production of low-density insulating panels through simple and scalable processes.

The resulting foams and panels will be thoroughly characterized in terms of mechanical strength, thermal insulation, and flame-retardant performance. The goal is to correlate the LbL coating design and resulting microstructure with the observed functional properties.

During the initial stages of the project, grape pomace, brewers' spent grain, and rice husks were selected as the most promising biomass sources. These materials were subjected to planetary ball milling as a pre-treatment step for cellulose extraction and to facilitate the fabrication of lightweight porous structures.

Preliminary oxidation tests on grape pomace revealed a high content of unsaturated compounds and a significant cellulose fraction. The morphology, thermal stability, and flame-retardant behavior of both raw materials and extracted fibers have been studied.

Initial surface functionalization strategies have also been developed. Two LbL systems, based on gelatin/alginate and gelatin/polyacrylic acid, have emerged as promising candidates for coating raw biomass, ball-milled material, and extracted fibers.

CONCLUSIONS

The GAIA project brings together the complementary expertise of three research institutions, Politecnico di Torino, University of Trento, and the National Research Council of Italy, to develop innovative, sustainable, cellulose-based insulating materials that are lightweight and fire-safe.

The project is structured around three main objectives:

(i) to establish green, reliable methods for extracting functional natural fibers from lignocellulosic waste;

(ii) to develop aqueous-based surface functionalization and thermobonding strategies for the fabrication of low-density panels;

(iii) to produce sustainable lightweight materials from functionalized fibers that demonstrate outstanding mechanical strength, flame resistance, and thermal insulation performance.

Acknowledgements: The author acknowledge financial support under the National Recovery and Resilience Plan (NRRP), Mission 4, Component 2, Investment 1.1, Call for tender No. 1409 published on 14.9.2022 by the Italian Ministry of University and Research (MUR), funded by the European Union – NextGenerationEU– Project Title Green cellulose bAsed fire safe and lightweight Insulating mAterials (GAIA) – CUP project (CUP: E53D23017860001- Grant Assignment Decree No. 1389 adopted on 01/09/2023 by the Italian Ministry of Ministry of University and Research (MUR).

REFERENCES

1. F. Olivieri, R. Capuano, A. Pirozzi, R. Castaldo, R. Avolio, M. E. Errico, C. Licini, S. Garzoli, G. Spigno, F. Donsì, G. Gentile, Poly(butylene succinate-co-adipate)/Croatina Grape Skin Biocomposites with Antioxidant Properties and Enhanced Biodegradation Rate, *ACS Sustainable Chemistry & Engineering* **13** (2025) 5121–5130. https://doi.org/10.1021/acssuschemeng.5c00459
2. M. Marcioni, M. Zhao, L. Maddalena, T. Pettersson, R. Avolio, R. Castaldo, L. Wågberg, F. Carosio, Layer-by-Layer-Coated Cellulose Fibers Enable the Production of Porous, Flame-Retardant, and Lightweight Materials, *ACS Applied Materials & Interfaces* **15** (2023) 36811. https://pubs.acs.org/doi/10.1021/acsami.3c06652
3. L. Maddalena, J. M. Indias, P. Bettotti, M. Scarpa, F. Carosio, Cellulose nanocrystals polyelectrolyte complexes as flame retardant treatment for cotton fabrics, *Polymer Degradation and Stability* **220** (2024) 110646. https://doi.org/10.1016/j.polymdegradstab.2023.110646

VALORIZATION OF MEAT INDUSTRY WASTE USING PYROLYSIS

Karmina Miteva[1], Slavcho Aleksovski[1], Jelena Stanojević[2], Aleksandra Milenković[2] Ljilljana Stanojević[2]

[1] - *Faculty of Technology and Metallurgy, Ss. Cyril and Methodius University in Skopje, North Macedonia*

[2] - *University of Niš, Faculty of Technology, Bulevar Oslobodenja 124, 16000 Leskovac, Serbia*

karmina@tmf.ukim.edu.mk

Abstract: *One of the main sources of organic waste in the food processing industry is the meat sector. Various materials such as bones, fats, teeth, hair, skins, bacon fringes, and tallow are examples of the waste that remains. This type of waste has the potential to contaminate the environment and endanger human health. The ability to convert waste into energy could lead to new alternative fuels and specific adsorbent materials, suggesting enhanced resource management and sustainability. Several thermal treatments for destroying these wastes through combustion, incineration, gasification, or pyrolysis could serve as interesting alternatives*

This study used a revolutionary waste recovery strategy to investigate the possibility of using various meat waste components (fat and bone) for green energy applications. The study has specifically focused on pyrolysis as a possible thermal treatment of meat waste to transform it into products with higher energetic values. Processes of pyrolysis is the thermal decomposition of waste, typically at 400–800 °C, in the absence of oxygen, that produces a carbon-rich solid residue (biochar), liquid (bio-oil), gaseous products (syngas which were not condensable gases) with high energy value. Furthermore, the quality and distribution of the pyrolysis products mostly depend on a few experimental parameters: reaction temperature, heating rate, residence time, reactor type, and used raw material. The fundamental objectives of this study were to establish the optimal pretreatment approach and pyrolysis conditions, and then investigate their effect on yields and qualities of pyrolysis products.

Keywords: Meat bones, Fats, Thermal treatment, Pyrolysis

INTRODUCTION

It is undeniable that the world is currently facing major issues like climate change, the energy crisis, resource scarcity, and pollution. Since humanity's influence on the environment has significantly increased over the past century due to quickly growing populations, sustainable development has emerged as a top priority for policymakers worldwide [1]. Fresh meat consumption increasing worldwide, so today discarded waste animal bones and fats pose significant environmental challenges. Over the past few decades, the world's meat consumption has grown dramatically, reaching 350.64 million metric tonnes in

2024 [2]. The most consumed meat is poultry (mostly chicken), accounting for 40 %, pork 35 %, beef and veal 21 %, and sheep (lamb and mutton) 5 %. Worldwide, a large waste from waste animal bones (WABs) are estimated to exceeding 130 million metric tons [3]. Inappropriate disposal increases the environmental impact and can result in health problems. Therefore, the only environmentally and hygienically appropriate way for meat waste disposal is typically in landfills [4]. The potential for generating energy from waste as a raw material could result in the creation of novel alternative fuels and specific adsorbent materials and improved resource management, sustainability, and longevity. Since animal fatty wastes (AFW) are primarily composed of triglycerides and have a high energy value, they are valuable resources for the development of second-generation biofuels [5]. On the other side about 10–18% of an animal's total weight is thought to be bone waste [6]. Generally, a composition of animal bone is 65–70 % inorganic matter primarily (calcium, phosphor, and combinations-sodium, silicon, metals, etc.), and 30–35 % organic (95 % collagen and proteins) [7,8]. Various valorization techniques such as biochemical, thermochemical, and physical and/or chemical processes are currently available for recovering bio-fuels from triglyceride-based materials [7]. The good solution for eliminating of meat waste is thermochemical processes include gasification, pyrolysis and combustion [9]. Waste-to- energy processes are best in energy recovery and reduction of the volume of the waste for landfill.

This paper used a novel concept of disposal by recovery to explore the possibility of employing various raw meat waste materials for green energy applications. The investigation of pyrolysis as a potential thermal treatment of meat waste components (fat and bone) to convert it into products with higher energetic values is the main focus of this work. The majority of research on bone waste was done in batch reactors, with an emphasis on the generation and use of biochar [7,10]. Bio-oil and pyrolysis gas were not given much attention. Otherwise, the pyrolysis of fatty wastes is not very established in the literature. The biofuels are mainly produced from fatty materials through transesterification [10, 11], but pyrolysis was used in this investigation to treat the fatty waste. For both raw materials (fat and bones), the effects of temperature and heating rate, two key parameters, and the distribution of pyrolysis products were investigated, as well as the characterization of biochar and biofuels produced by pyrolysis under optimal conditions. The usable applications of different pyrolytic products that were obtained were also performed.

EXPERIMENTAL

Materials and Methods

The raw material used for the pyrolysis experiments was waste from the meat industry, such as animal (lamb, cattle, swine, or poultry) bones or fatty wastes obtained from various meat factories. The used bone materials are usually in powder form with a particle size smaller than 3 mm or crushed into pieces of 3–6 mm size. Micro-analytical methods determined the elemental composition of bones or fatty waste.

Pyrolysis Process

Pyrolysis experiments are carried out in a different reactor, usually on a laboratory-scale fixed reactor heated by an electric furnace or a tubular batch reactor [2,4]. Pyrolysis of fatty materials can also be carried out in a rotary stirrer-type autoclave with electromagnetic induction [12]. For this type of experiment, a stainless-steel reactor of various dimensions is used, and the temperature is controlled by a thermocouple immersed in the reactor. Pyrolysis experiments can also be carried out under a vacuum but are often conducted in an inert atmosphere at atmospheric pressure. The reactor is continuously purged with nitrogen during the experiments to remove all gases generated during pyrolysis and air from the reactor. A programmable PID temperature controller measure and controls the reactor temperatures using different heating rates (5, 10, or 20 $^{o}C\ min^{-1}$) and maintains them at the desired temperature. For condensation of liquid product, the reactor shown in Figure 1 was connected via an air-cooled tube and a water-cooled glass condenser with a collection vessel. Non-condensable gases were removed from the system via a glass tube.

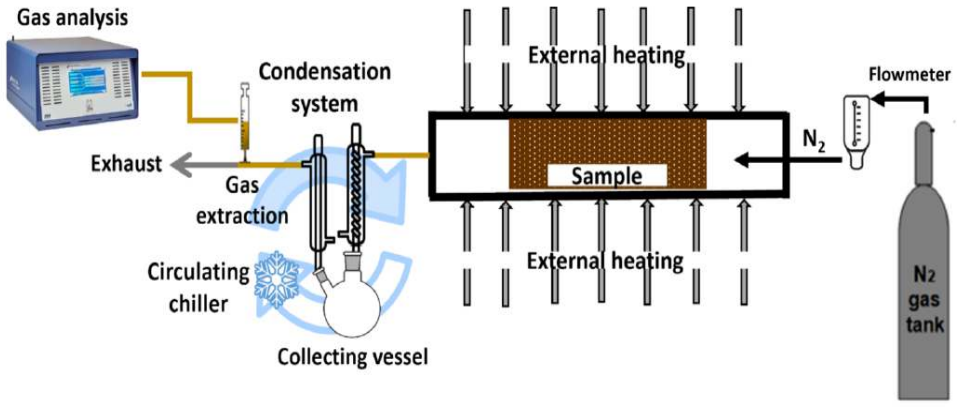

Figure 1 *Experimental set-up for the FBW pyrolysis [4]*

The thermal pyrolytic breakdown process of meat waste typically occurs at 400–800°C in the absence of oxygen, producing a solid residue (bio-char), a liquid (bio-oil), and gas products [13]. The liquid product derived from animal fat has two phases: an aqueous phase (bottom) and organic-rich compounds (upper phase), which require decantation for separation [14]. The yields of bio-char and liquid bio-oil were determined by weight, while the gas product was calculated by difference.

Gas [wt%] = Raw material [wt%] – Bio-oil[wt%] – Biochar [wt%] [15]

Obtained biochar is a form of coal that can be used as a soil conditioner or as a solid amendment fuel. The energy content of bio-oil is higher than that of pyrolysis gas and biochar. Obtained products were stored until further analysis.

Analysis and Methods for Characterization

The following methods are commonly used in the analysis of raw materials and pyrolysis products: Moisture content is determined according to ISO 18122:2022 standard [4]; ash content is also assessed using the same ISO 18122:2022 standard [4]. Elemental analysis for carbon (C), hydrogen (H), nitrogen (N), and sulfur (S) is included [4,8]. To identify functional groups, Fourier Transform Infrared Spectroscopy (FTIR) is employed within the 400–4000 cm^{-1} range [7,9]. Biochars are analyzed using thermal analysis, Scanning Electron Microscopy — Energy Dispersive X-ray Analysis (SEM-EDAX), and Brunauer – Emmett - Teller (BET) methods [2,6]. For the analysis of chemical composition and quantities, a Gas Chromatography Flame Ionization Detector (GC-FID) is utilized, and gas product analysis is carried out using a micro-gas chromatograph.

RESULTS AND DISCUSSIONS

Table 1 lists the most important characteristics of the raw animal waste, fat, and bones that were examined.

Table 1 *Proximate analysis of the animal bone and fatty wastes.*

Elemental Composition (%)	MBM [15]	Cattle Bone [16]	Lamb fat [10]	Poultry fat [10]	Swine fat [10]
C	45.92	32.9	74.63	63.25	65.38
O	38.40	36,3	12.50	23.64	21.99
H	6.35	8	12.11	11.26	11.32
S	0.44	0.35	0.27	0.23	0.09
Ash	17.48	64.7	0.34	0.59	0.64
Volatile matter	71.45	76.2	99.2	99.0	98.5

The first sample is meat and bone meal (MBM) generated in substantial quantities from bovine, ovine, and caprine. The second sample is dry cattle bone and the rest are fatty samples. All presented samples of fats and waste bones have high carbon contents, but fats have almost double the content of carbon compared to bone. Oxygen content in all samples is moderate but opposite of carbon the oxygen content is double in bone. The other elements hydrogen and sulfur have lower values. The ash content of bones is expected, and its value is extremely low for fat samples.

The yields of pyrolytic products depend on raw materials and the process parameters. Different experiments using pyrolytic setups with fats and those with bones were carried out at a temperature of 600 °C and a constant heating rate of 5 °C/min. The results are presented in Table 2.

Table 2 *Product yield of animal fats and bone pyrolysis at 600°C*

	Organic phase	Aqueous phase /pyrolysis water of bone	Char	Gas
Lamb fat [10]	61.6	16.3	1.8	20.3
Poultry fat [10]	46.1	21.5	1.1	31.3
Swine fat [10]	45.8	12.2	1.5	40.5
Lamb bone [15]	4.04	17.80	65.92	12.04
Poultry bone [17]	6.45	9.55	61.31	23.56

Products distribution from pyrolysis with temperature are shown on Figure 1. The main products are gas, liquid fraction and char for both pyrolysis.

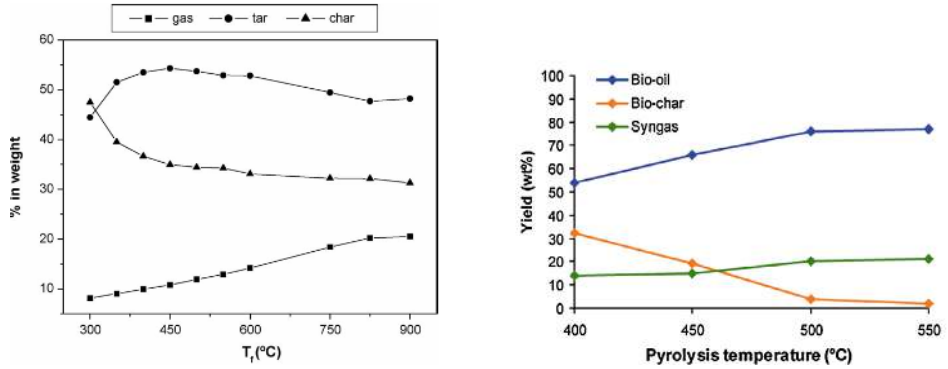

Figure 2 *The effect of final temperature on pyrolysis products distribution of a) - animal bone (left graphic) [18], and b) - animal fat (right graphic) [10]*

As can be observed in Figure 2-a, the main products in the bone pyrolysis process at any temperature studied are tar or bio-oil and biochar. An

approximate 20% increase in gas yield occurs as the temperature increases. The pyrolysis of animal fats, illustrated in Fig. 2-b, indicates that increases in the pyrolysis temperature gradually raised the fraction of bio-oil while decreasing the fraction of bio-char. The gas fraction also exhibited a slight increase.

FTIR spectra of the solid product biochar from animal bone samples show characteristic peaks of Hydroxyapatite (HA), the major mineralogical component of bones. The spectra exhibit compounds with characteristic groups at 553 and 562 cm^{-1}, 603 and 692 cm^{-1}, and 1010 and 1020 cm^{-1} related to the PO_4 compound, as well as symmetric stretching in the range of 962–985 cm^{-1} and bending vibrations in the range of 439–498 cm^{-1} [16,17]. Weak absorption bands of aromatic -CH groups are observed at 1000-1300 cm^{-1} and 700-800 cm^{-1}, along with strong bands of aliphatic -CH_3, -CH_2, and -CH groups at 2853-2924 cm^{-1}, as well as for H of -OH and -NH, -NH_2 groups at 3358 cm^{-1}. Bone tar (bone bio-oil) is a multicomponent mixture that primarily consists of organic substances with aliphatic chains and aromatic structures featuring oxygen and nitrogen functionalities. Additionally, strong bands at 1400-1642 cm^{-1} indicate skeletal vibrations of >C=O groups in ketones, aldehydes, esters, and quinones. The FTIR spectra of bio-oil, a primary byproduct of animal fats, display a broad range of chemical groups (oxygenated groups; aliphatic saturated and unsaturated molecules). This suggests that the chemical composition of the bio-oil is complex.

The application of obtained animal pyrolytic products (gas, bio-oil, and biochar) is extensive. The main product biochar from animal bone pyrolysis has various applications depending on its characteristics and porosity. Utilizing biochar is an economical and environmentally responsible way to remove fluoride, heavy metals, color, as well as cleanup, ecological remediation, and soil amendment applications with less impact on human health. Adsorbents, catalysts and catalyst supports, hierarchical carbon sources for energy storage applications, HA for biological purposes, and phosphate sources for soil remediation or fertilizer are some of the uses for these materials. For the required surface properties of produced bone char, the production conditions, such as temperature and residence time, are important factors in designing an efficient pollutant removal adsorbent or catalyst. Based on these conclusions pyrolytic bone char or HA has low-cost, excellent ion-exchange properties, high adsorption capacity, and mesoporous structure, with a large surface area of 80–120 $m^2\ g^{-1}$. The process parameters, temperature, and heating rate hardly influence the specific surface area. However, the specific surface area decreases with increases in heating rate as can also be observed in the SEM images of char microphotography in Figure 3 for the three different heating rates. The different morphology of the biochar at

different pyrolysis temperatures is evident and was also analyzed by scanning electron microscopy (SEM).

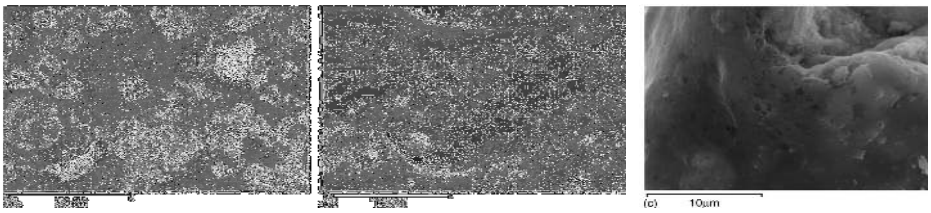

a) b) c)

Figure 3 *SEM images of chars obtained at 450◦ C and different heating rates: (a) 2 ◦C/min; (b) 8 ◦C/min; (c) 14 ◦C/min [15].*

Figure 4 shows many structural changes due to the decomposition of organic components and the crystalline transformations of minerals when organic components are transforming into various gaseous and liquid products leaving behind a porous scaffold composed of Ca, P, and O-containing minerals such as calcium phosphates and hydroxyapatite crystals. The first effect of the densification of the bone structure is an increase in mineral content, which produces the appearance of biochar when the organic components are eliminated. The process of compaction is observed at higher pyrolysis temperatures, 800 °C and 900 °C, which is even more apparent compared to lower temperatures of 500 °C, 600 °C, and 700 °C.

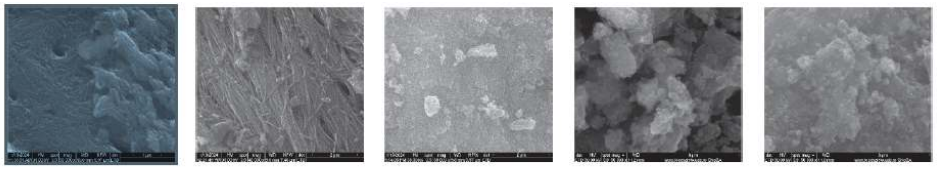

Figure 4 *SEM images of bone chars obtained different temperatures [4]*

The caloric value of the char is 6.4 times lower than that of the initial bone, which confirms the lower content (8.4%) of C in the char. Obtained liquid products from bone pyrolysis (tar and water) can be used for the production of low-molecular epoxy resin [18]. High quantities of alkanes, fatty acids, fatty acid esters, furan derivates, phenolic compounds, and other aromatic compounds in pyrolytic bio-oils are of interest to the industrial sector. For instance, propionic acid can be used in various sectors: pharmaceuticals, artificial fruit flavors, coating, herbicides, or chemical intermediates [19], but hexanoic acid can be utilized in cleaning, plant protection, waxes and polishes, food additives,

perfumes, medicine, and tobacco essences [20,21]. Other, compounds like acetic acid, butanoic acid, or other phenolic compounds can be used as scaffolds in medicinal chemistry and related sectors [22]. Bio-oil also can be used as a fuel because of, the n-alkane chemical compounds. The obtained gases from animal bone pyrolysis primarily consist of CO_2, and CO, and temperature rise leading to the rise of CO and H_2, and more regularly for CH_4 and ≥ C_2 [23].

According to the GC-MS [24] chemical composition of liquid product, obtained with pyrolysis of animal fats, a main component of the neutral fraction of bio-oil was identified. These compound families are present in this fraction: carboxylic acids (Heptanoic acid, Octanoic acid, Nonanoic acid, Decanoic acid, etc.); alkanes (Dodecane, Tridecane, Tetradecane, Pentadecane, Hexadecane, etc.); alkenes (1-Dodecene, 1-Tridecene, 2-Tetradecene, 6-Tridecene, etc.) and cyclic hydrocarbons (1-Cyclodecene, Bicyclopentyl, etc.). Many other compounds are identified but in small amounts (ketones, aldehydes, alcohols, etc.). Bio-oil has a low aromatic nature but has a high aliphatic character with the content of high oxygenated groups, and these indicate that bio-oil can be used as engine fuel. These liquid complex mixtures with a large variety of organic components can be used in the chemical industry or as a fuel. The fuel qualities of the upper organic phase of the bio-oils under study are quite comparable to those of petroleum diesel, confirming the products' suitability as fuel and their potential for use as a renewable energy source. The goal of pyrolyzing animal fats is to maximize the amount of liquid fraction that is produced.

CONCLUSIONS

The worldwide production of meat generates waste fat and bones which increased due to urbanization and growing global populations. An overview of the pyrolytic conversion of waste animal bones and fat into new materials and their uses — as opposed to being disposed of in landfills—has been given by this study. This study confirms that animal fatty and bone wastes are precious raw materials for bio-oil and biochar production by pyrolysis. The reaction temperature and the heating rate are the most convenient conditions to get useable products with high yields. The proper reaction conditions lead to the desired product quality. The application of obtained animal pyrolytic products (gas, bio-oil, and biochar) is extensive. There a various environmentally friendly utilizations of biochar such as removal of fluoride, and heavy metals, color cleanup, ecological remediation, adsorbents, catalysts, and catalyst supports hierarchical carbon sources for energy storage applications, and phosphate sources for soil remediation or fertilizer are some of the uses for these materials. Liquid products obtained with pyrolysis of animal fats are a complex mixture

with a large variety of organic components that can be used in the chemical industry or as a fuel.

REFERENCES

1. V. Cheela, M.John, W. Biswas,B. Dubey, Environmental Impact Evaluation of Current Municipal Solid Waste Treatments in India Using Life Cycle Assessment. *Energies* **14** (2021) 3133-3144. https://doi.org/10.3390/en14113133
2. A. Hart, K. Ebiundu, E. Peretomode, H. Onyeaka, O. F. Nwabore, K. Obileke, Value-added materials recovered from waste bone biomass: technologies and applications, *RSC Advances* **12** (2022) 22302–22330. https://doi.org/10.1039/d2ra03557j
3. Statista, 2024, https://www.statista.com/statistics/237632/production-of-meatworldwide-since-1990/.
4. G. Ionescu, M. Macavei, M. Patrascu, A. Volceanov, R. P˘atrascu, S. Werle, A. Mlonka-Mędrala, A. E. Coman, A. Magdziarz, C. Marculescu, New integrated processing of chicken bone waste using an enzymatic pretreatment and slow pyrolysis to produce green chemicals, *Energy Conversion and Management* 323 (2025) 119281. https://doi.org/10.1016/j.enconman.2024.119281
5. K.D. Maher, D.C. Bressler,Pyrolysis of triglyceride materials for the production of renewable fuels and chemicals. *Bioresour. Technol.* **98** (2007) 2351–2368. https://doi.org/10.1016/j.biortech.2006.10.025
6. F. Hussain, S. Alshahrani, M.M. Abbas, H.M. Khan, A. Jamil, H. Yaqoob et al., Waste animal bones as catalysts for biodiesel production; a mini-review. *Catalysts* **11** (2021) 630. https://doi.org/10.3390/catal11050630.10.1016/j.rser.2022.112577.
7. A.B. Hassen-Trabelsi, T. Kraiem, S. Naoui, H. Belayouni, Pyrolysis of waste animal fats in a fixed-bed reactor: production and characterization of bio-oil and bio-char. *Journal of Waste Management* **34** (2014) 210–218. https://doi.org/10.1016/j.wasman.2013.09.019.
8. Feng X. Chemical and biochemical basis of cell-bone matrix interaction in health and disease. *Curr. Chem. Biol.* **3** (2009)189–96. https://doi.org/10.2174/87231309788166398.
9. A. Hart, Circular economy: closing the catalyst loop with metal reclamation from spent catalysts, industrial waste, waste shells and animal bones, *Biomass Conversation Bioren* **13** (2023) 11483-11498. https://doi.org/10.1007/s13399-021-01942-8
10. A. Demirbas, The influence of temperature on the yields of compounds existing in bio-oils obtained from biomass samples via pyrolysis, *Fuel Processing Technology* **88** (2007) 591–597. https://doi.org/10.1016/j.fuproc.2007.01.010
11.. H. Fukuda, A. Kondo, H. Noda, Biodiesel fuel production by transesterification of oils. *Journal of Bioscience Bioengineering*. **92** (2001) 406–416. https://doi.org/10.1263/jbb.92.405
12. T. Sakurai, Y. Kakuta, M. Sugano, K. Hirano, Biodiesel production from waste animal fats using pyrolysis method, *Fuel Processing Technology* **94** (2012) 47–52. https://dx.doi/10.1016/j.fuproc.2011.10.004
13. E. Cascarosa, A. Boldrin, T. Astrup, Pyrolysis and gasification of meat-and-bone-meal: energy balance and GHG accounting. *Waste Management* **33** (2013), 2501–2508. https://doi.org/10.1016/j.wasman.2013.07.014

14. M. Ayllon, M. Aznar, J.L. Sanchez, G. Geab, J. Arauzo, Influence of temperature and heating rate on the fixed bed pyrolysis of meat and bone meal, *Chemical Engineering Journal* **121** (2006) 85–96. https://dx.doi/10.1016/j.cej.2006.04.013
15. B. Purevsuren, B. Avid, J. Narangerel, T. Gerelmaa, Ya. Davaajav, Investigation on the pyrolysis products from animal bone, *Journal of Materials Science* **39** (2004) 737–740. https://dx.doi/10.1023/B:JMSC.0000011545.51724
16. M.Macavei, V. Gheorghe, G.Ionescu, A. Volceanov, R. Patrascu, C. Marculescu Thermochemical conversion of animal-derived waste: a mini-review with a focus on chicken bone waste, *Processes* **12** (2024) 358-368. https://doi.org/10.3390/pr12020358.
17. S. Alkurdi, R.A. Al-Juboori, J. Bundschu, L. Bowtell, S. McKnight, Effect of pyrolysis conditions on bone char characterization and its ability for arsenic and fluoride removal, Environmental Pollution 262 (2020) 114221-https://doi.org/10.1016/j.envpol.2020.114221
18. B. Purevsuren, Ya. Davaajav, J. Namkhainorov, Z. I. Glavcheva-Laleva, V. Genadiev, I. K. Glavchev, Pyrolysis of animal bone, characterization of the obtained char and tar and application of bone tar for crosslinking of epoxy resin Pyrolysis of animal bone, characterization of the obtained char and tar and application of bone tar for crosslinking of epoxy resin, *Bulgarian Chemical Communications* **49** (2017) 34–39.
https://www.researchgate.net/publication/375447887
19. P. San-Valero, HN Abubackar, M.C.Veiga, C. Kennes C. Effect of pH, yeast extract and inorganic carbon on chain elongation for hexanoic acid production. *Bioresources Technology* **300** (2020) 122659-122674. https://doi.org/10.1016/j.biortech.2019.122659
20. J. Son, JC. Joo, KA Baritugo, S. Jeong, JY. Lee, HJ. Lim HJ, Consolidated microbial production of four-, five-, and six-carbon organic acids from crop residues: current status and perspectives. *Bioresources Technology* **351** (2021) 127001-127010.
https://doi.org/10.1016/j.biortech.2022.127001
21. R. Aitken, R. Alan. Five-membered rings with two heteroatoms, and their fused carbocyclic derivatives. *Comprehensive Heterocyclic Chemistry IV* **4** (2022) 113-307. https://doi.org/10.1016/B978-0-12-818655-8.00140-2.
22. C.K. Westbrook, W.J. Pitz, O. Herbinet, H.J. Curran, E.J. Silke, A comprehensive detailed chemical kinetic reaction mechanism for combustion of n-alkane hydrocarbons from n-octane to n-hexadecane, *Combust Flame* **156** (2009) 181–199.
https://doi.org/10.1016/j.combustflame.2008.07.014
23. C. Dıez, O. Martınez, L.F. Calvo, J. Cara, A. Moran, Pyrolysis of tyres. Influence of the final temperature of the process on emissions and the calorific value of the products recovered. *Waste Management* 24 (2004) 463–4729.
https://doi.org/10.1016/j.wasman.2003.11.006
24. I. Goldberg, J.S Rokem, Book Chapter Organic and Fatty Acid Production, Microbial, Encyclopedia of microbiology. Academic Press, 2009, pp. 358-392.
https://doi.org/10.1016/B978-0-12-809633-8.13083-3

PHYSICOCHEMICAL CHARACTERISTICS OF BIO-OIL OBTAINED BY CATALYTIC PYROLYSIS OF OAK CHIPS

Slavcho Aleksovski[1], Igor Aleksovski[2], Karmina Miteva[1], Jelena Stanojevıć[3], Ljıljana Stanojevıć[3], Aleksandra Milenković[3]

[1] - *Faculty of Technology and Metallurgy, Ss. Cyril and Methodius University in Skopje, North Macedonia*

[2] - *Alkaloid, A.D. Skopje, Blvd. Aleksandar Makedonski 12*, Skopje, Republic of North Macedonia

[3] - *University of Niš, Faculty of Technology, Bulevar Oslobodenja 124, 16000 Leskovac, Serbia*

slavcho@tmf.ukim.edu.mk

Abstract: *Biomass stands out as a plentiful renewable energy resource. The development of biomass refineries can play a crucial role in advancing cost-effective and sustainable energy solutions. Pyrolysis, a thermochemical method, converts organic materials derived from biomass into valuable products. Typically, pyrolysis takes place with a catalyst present and in an oxygen-free environment. This process yields solid residues as well as liquid and gaseous fuels.*

During the course of this work, several experiments were conducted using different mass ratios of biomass to catalysts (Al_2O_3 and opalized tuff) to examine their influence on the density, viscosity, pH value, and refractive index of the produced bio-oil. The changes in the physicochemical characteristics of the obtained bio-oils indicate a variation in composition due to the adjustment in the quantity and ratio of the catalysts used. This approach allows for the preparation of bio-oils with specific compositions, tailored for predetermined applications. A larger quantity of catalyst reduces the density and viscosity of the bio-oil resulting from the increased number of active sites in the catalyst used for biomass cracking. With a higher amount of catalyst, the cracking process of long-chain hydrocarbons is more pronounced, and the resulting bio-oil contains lighter hydrocarbons compared to bio-oil produced with a lower amount of catalyst. The pH value of the obtained bio-oil, based on the conducted analyses, ranges between 2.1 and 3, which is characteristic for bio-oil produced through pyrolysis of solid biomass. A larger amount of catalyst reduces the refractive index.

Keywords: pyrolysis, biomass, catalysts, bio-oil, physicochemical characteristics.

INTRODUCTION

Harnessing renewable energy sources plays a crucial role in reducing the emission of greenhouse gases and particulate matter into the air. This method is environmentally sustainable because the carbon dioxide released during their

combustion is absorbed by plants through photosynthesis. Despite biomass having a lower energy content compared to fossil fuels, it remains one of the most widely used energy sources. The use of biomass waste as a raw material for fuel production through methods like pyrolysis and gasification is increasingly becoming a significant challenge for many researchers. Recently, this trend of converting both solid and liquid waste into valuable resources has started to impact our country as well. The conversion of biomass waste, particularly lignocellulosic materials from second-generation renewable energy sources, into liquid, gaseous, and solid fuels, along with the plentiful natural biomass resources available in our nation, makes this raw material a promising option for producing biofuels and chemicals.

The pyrolysis of biomass represents a thermochemical process that transpires in an oxygen-deprived environment, generally in the presence of nitrogen. Conducted at temperatures ranging from 250 to 550 °C, either under vacuum or atmospheric conditions, and with or without the use of catalysts, biomass is transformed into gaseous pyrogas (35-55%), liquid bio-oil (35-40%), and solid bio-char (5-20%). This process entails the disintegration of large hydrocarbon molecules into smaller fragments. Fast pyrolysis predominantly yields a liquid fuel known as bio-oil, characterized by its high content of aromatic compounds, whereas slow pyrolysis is more inclined to produce a larger volume of biogas. Recently, to improve the properties of the liquid output, the co-pyrolysis of biomass with specific synthetic polymers, including rubber and plastic, has been investigated. This method employs a combination of two materials in various ratios. Notably, a combined effect has been observed, resulting in a significant increase in the amount and better quality of the liquid produced compared to when the materials are processed separately [1-2].

Bio-oil is a viscous liquid that can vary in color from orange to dark brown, nearing black. Its viscosity may increase over time, suggesting a limited shelf life. This liquid is referred to by several names, including pyrolytic oil, wood oil, liquid smoke, and liquid wood. The density of bio-oil ranges from 1.10 to 1.25 g/cm^3, making it denser than water and fuel and significantly denser than the original biomass. The viscosity can range from 25 cP to 1000 cP, depending on the water content of the raw materials. Due to the high concentration of oxygen-containing compounds, bio-oil has a polarity akin to water, which limits its miscibility with hydrocarbons. The breakdown of biomass generates organic acids, such as formic and acetic acid, which contribute to the low pH of bio-oil. Water is a vital component of bio-oil, typically accounting for 15% to 35% of its makeup. When the water content is between 30% and 45%, it becomes possible to separate the water from the organic fraction. The higher heating value (HHV)

of bio-oil is below 26 MJ/kg, compared to 42–44 MJ/kg for traditional fuel oils. Recent research has shown that bio-oil derived from grass, corn cobs, dry corn residues, and early bloom alfalfa stems has higher calorific values of 10.5, 11.6, 10.6, and 14.8 MJ/kg, respectively [3-4].

Characterization of bio-oil obtained from biomass pyrolysis

The physical properties of bio-oils have been determined by several authors [5–10]. These properties result from the chemical composition of the oils, which differs significantly from that of petroleum-derived oils. Bio-oils are multicomponent mixtures consisting of molecules of varying sizes, primarily obtained through depolymerization and fragmentation reactions of the three key structural components of biomass: cellulose, hemicellulose, and lignin. Consequently, the elemental composition of bio-oils is more similar to that of biomass than petroleum oils.

One of the fundamental physical characteristics of bio-oils is their density, which changes over time due to their unstable nature and compositional changes. These properties stem from the oils' chemical composition, which markedly differs from that of oils derived from petroleum. Bio-oils produced via biomass pyrolysis typically exhibit a density between 1.1 and 1.3 g/cm^3, with measurements conducted using a standard Anton Paar densitometer.

Viscosity, defined as a fluid's resistance to gradual deformation under shear or tensile forces, can vary significantly in bio-oils (ranging from 35 to 1000 cP at 40°C) based on factors such as feedstock type, processing conditions, and the effectiveness of separating components that evaporate at lower temperatures. Notably, bio-oils experience a more rapid decrease in viscosity at elevated temperatures compared to petroleum oils, allowing even highly viscous bio-oils to be easily pumped after moderate heating. The addition of polar solvents like methanol and acetone can lead to a substantial reduction in viscosity.

However, an undesirable consequence often observed during the storage or treatment of bio-oils at elevated temperatures is an increase in viscosity over time. This phenomenon is likely attributed to chemical reactions among the components of bio-oil, resulting in the formation of larger molecules. There is also evidence suggesting reactions with atmospheric oxygen [11]. Viscosity is assessed using various viscometers and rheometers, with the glass capillary Cannon-Fenske viscometer being one of the most widely used instruments for measuring kinematic viscosity.

The acidity of bio-oils is assessed with a pH meter. Typically, bio-oils contain organic acids, resulting in pH values that range from 2.0 to 3.8. These bio-oils are corrosive to carbon steel and aluminum, but they do not affect stainless steel.

The refractive index is a dimensionless quantity that characterizes how light interacts with an optically transparent substance. It is calculated as the ratio of the speed of light in a vacuum to that in the material. A refractometer serves as the instrument for measuring the refractive index.

EXPERIMENTAL

Methodology and equipment utilized for wood chip pyrolysis

The pyrolysis of biomass was conducted in a semi-batch reactor with a diameter of 5 cm and a volume of 400 cm^3. The reactor was filled with alternating layers of 30–40 g of biomass and catalyst, creating a packed bed configuration. Subsequently, the reactor was sealed with a lid that featured a tube for the collection of volatile substances, which was connected through silicone-reinforced tubing to three sequentially arranged thermostatically controlled separators. These separators facilitated the condensation and fractionation of the vaporized biomass. Non-condensable gases were expelled into the atmosphere via the tubing. The first separator was maintained at a temperature of 70 °C using heated water, while the second and third separators were cooled with ice, maintaining a temperature of 0 °C. Aluminum oxide (92.70% Al_2O_3) and opalized silicate –tuff (94.51% SiO_2) were used as catalysts.

Experimental conditions

The heating rate for the reactor during the experimental procedures was determined based on previous thermogravimetric analysis (TGA) results (10 min/°C) and relevant literature [12, 13–17]. The temperature for maximum cracking reactions ranged from 550 to 600 °C. The operational mode and temperature of the reactor were regulated using a PID controller. A temperature program for reactor operation was established based on previously optimized process conditions. This PID controller program was developed following an analysis of experimental data derived from kinetic studies of biomass pyrolysis conducted via TGA, which defined the heating rate, reaction temperature, and duration. The cracking reaction was performed in an inert nitrogen (N_2) atmosphere. The volume of liquid fuel generated during pyrolysis was estimated by measuring the condensed phase in the graduated separators over time. In the course of this study, a series of experiments were carried out utilizing different weight ratios of biomass in conjunction with catalysts (Al_2O_3 and opalized

silicate) to assess their effects on the density, viscosity, pH, and refractive index of the resulting bio-oil (Table 1).

Table 1 *Weight ratio of biomass with catalysts and quantities of obtained liquid, gas, and solid phases and heating rate of β = 10 °C min^{-1}*

No.	Biomass	Al_2O_3	Tuff	Bio-oil (mas.%)	Gas (mas.%)	Bio-char (mas.%)
1	1	1	1	58.06	22.12	19.82
2	1	0.25	0.25	51.59	10.54	37.87
3	1	0.25	0.75	50.48	21.33	28.19
4	1	0.75	0.25	52.59	20.79	26.62
5	1	1.5	0.5	58.83	23.43	17.74
6	1	0.5	0.5	49.16	10.06	40.78

Physicochemical characteristics of the obtained bio-oil

For the purpose of comparison and analysis, only a limited selection of experimental outcomes was considered. The observed alterations in the physicochemical properties of the produced bio-oils suggest a variation in composition that correlates with the amount and ratio of catalysts employed. Consequently, bio-oils with tailored compositions can be synthesized for specific applications.

Table 2 *The physicochemical properties of the obtained bio-oil*

No.	ρ_{20^oC} (kg m^{-3})	ν_{40^oC} (mm^2 s^{-1})	pH	n_D
1	1.0418	0.74527	2.47	1.3618
2	1.0599	0.82097	2.10	1.3724
3	1.0610	0.84482	2.49	1.3750
4	1.0483	0.77076	2.64	1.3642
5	1.0219	0.59500	2.41	1.3500
6	1.0530	0.78425	2.51	1.3681

RESULTS AND DISCUSSIONS

The Influence of the catalysts on the density of bio-oil

A comparative analysis was conducted on three experimental samples, maintaining a consistent mass ratio of the two catalysts while varying the mass ratio of biomass to catalysts to assess their influence on the bio-oil density. The findings presented in Table 1 and Table 2 indicate that the highest catalyst quantity used in Experiment 1 corresponds to the lowest density measurement. In contrast, Experiment 6, which utilized half the catalyst amount, resulted in a higher density. Furthermore, when an even smaller catalyst quantity was applied in Experiment 2 compared to Experiment 6, the highest density was recorded. A similar pattern is evident in Experiments 4 and 5, where Experiment 5 employed double the catalyst amount of Experiment 4, leading to a reduction in bio-oil density. This phenomenon is attributed to the increased availability of active sites on the catalyst, which facilitates the cracking of biomass. To investigate the effect of catalyst type on density values, a comparison was conducted between two experimental samples. In these samples, the weight ratio of biomass to catalyst remained constant, while the catalyst composition was altered, specifically in Experiments 3 and 4. The findings indicate that the use of tuff as a catalyst in greater amounts contributes to an increase in density values and promotes the formation of longer-chain paraffins. In contrast, Al_2O_3 is more influential in the production of olefins and aromatics, which are hydrocarbons characterized by lower molecular weights.

The Influence of the catalysts on the pH value of bio-oil

The pH value of the obtained bio-oil, based on the conducted analyses, ranges between 2.10 and 2.64, which is characteristic of bio-oil produced through pyrolysis of hard biomass, unlike others where the pH value of bio-oil derived from soft biomass is around 4.

Regarding the influence of the amount of catalysts on the pH value of the obtained bio-oil, a comparison was made between Experiments 1, 2, and 6, which experimented with different amounts but the same catalyst composition. From the obtained results, it can be concluded that a higher amount of catalyst makes the bio-oil more stable and with a higher pH value. The low pH value is a result of the greater presence of acids and O_2. Al_2O_3 and tuff as catalysts aid in the transfer of hydrogen from naphthenes to olefins when they react, leading to the formation of paraffins and aromatics. The hydrogen transfer makes the bio-oil more stable by reducing the reactivity of the olefins within it. On the other hand, prolonged storage of the bio-oil makes it unstable, as can be observed from Experiment 6. The same conclusion can be drawn by analyzing the pH value

of the bio-oils obtained from Experiments 4 and 5. To investigate the effect of catalyst type on the pH level of bio-oil, a comparison was conducted between two experimental samples, 3 and 4, which utilized the same biomass-to-catalyst weight ratio while varying the catalyst composition. The results indicate that a higher concentration of tuff as a catalyst leads to a decrease in pH value, resulting in a less stable bio-oil compared to that produced with a greater proportion of aluminum oxide as the catalyst.

The influence of the catalysts on the viscosity value

The viscosity of bio-oil serves as an indicator of the predominant compound groups within its chemical makeup. An increase in the viscosity of a sample suggests a rise in paraffin concentration, an increase in hydrogen content, and a reduction in the aromatic fraction. To assess the impact of catalyst quantity on the viscosity of the produced bio-oil, a comparative analysis was conducted among three experimental samples, each differing in the biomass-to-catalyst weight ratio (Experiments 1, 2, and 6). The results presented in Table 1 and Table 2 demonstrate that a reduced quantity of catalysts negatively influences the viscosity of the bio-oil, leading to an increase in viscosity. A lower viscosity is generally preferred for bio-oil to prevent issues such as thickening and sedimentation, thus indicating that a higher catalyst quantity is advantageous. This conclusion is further supported by the viscosity analysis of bio-oils from Experiments 4 and 5, where the sample produced with double the catalyst amount exhibited lower viscosity, signifying a greater concentration of aromatics and a diminished concentration of paraffins compared to the sample with a lesser catalyst amount. Viscosity measurements were conducted using a Cannon-Fenske viscometer. To investigate the effect of catalyst type on viscosity, two experimental samples were compared, maintaining a consistent weight ratio of biomass to catalyst while varying the catalyst composition. The results indicate that the application of Al_2O_3 as a catalyst during the pyrolysis of wood chip biomass leads to a decrease in viscosity. This suggests that Al_2O_3 promotes the reactions responsible for the formation of aromatic compounds.

The influence of the catalysts on the refractive index

The effect of catalyst quantity on the refractive index was assessed by examining three samples that utilized the same weight ratio of catalysts yet varied in biomass composition, specifically Experiments 1, 2, and 6. The findings indicate that an increased catalyst amount leads to a decrease in the refractive index. This observation is further supported by the analysis of the bio-oil produced in Experiments 4 and 5. To investigate how the type of catalyst affects the refractive index, a comparison was conducted between two experimental samples,

specifically Experiments 3 and 4, which utilized equal quantities of biomass along with the catalyst and its composition. The findings, illustrated in Table 1 and Table 2, indicate that an increased concentration of Al_2O_3 as a catalyst leads to a decrease in the refractive index of the bio-oil. The refractive index was determined using a Carl Zeiss Jena refractometer, with measurements taken at a temperature of 20 °C.

CONCLUSIONS

An increased amount of catalyst leads to a decrease in the density of bio-oil, primarily due to the generation of lighter hydrocarbons during the cracking process. The pH level of the produced bio-oil falls within the range of 2.10 to 2.64, a typical characteristic of bio-oil derived from the pyrolysis of hard biomass. Utilizing a larger quantity of catalyst, along with a higher ratio of Al_2O_3 in comparison to tuff, contributes to the bio-oil's stability and elevates its pH level. Experiments reveal that a higher catalyst quantity and an increased presence of Al_2O_3 result in lower viscosity values, promoting the formation of aromatic compounds rather than paraffins, which tend to have higher viscosity. Measurements of the refractive index demonstrate that both a greater quantity of catalyst and a higher aluminum oxide content lead to a reduction in the refractive index of the bio-oil.

REFERENCES

1. O. Oyedun, T. Gebreegziabher, C.W. Hui, Co-pyrolysis of Biomass and Plastics waste: A Modelling Approach, *Chemical engineering transactions*, **35** (2013) 883-888 https://doi.org/10.3303/CET1335147
2. S. Sinha, A. Jhalani, M. R. Ravi, and A. Ray, Modeling of pyrolysis in wood: a review, *SESI-Journal, (New Delhi, India)*, **10** (2000) 41–62.
3. P.C. Badger and P. Fransham, Use of Mobile Fast Pyrolysis Plants to Densify Biomass and Reduce Biomass Handling Costs-A Preliminary Assesment, *Biomass and Bioenergy*, **30** (2006) 321-325 http://dx.doi.org/10.1016/j.biombioe.2005.07.011
4. M. Asadullah, N.S. Ab Rasid, S.A.S.A. Kadir, A. Azdarpour, Production and detailed characterization of bio-oil from fast pyrolysis of palm kernel shell, *Biomass and Bioenergy*, **59** (2013) 316-324 http://dx.doi.org/10.1016/j.biombioe.2013.08.037
5. J.Lédé, F. Broust, F-T. Ndiaye, M. Ferrer, Properties of bio-oils produced by biomass fast pyrolysis in a cyclone ractor, *Fuel*, **86** (2007) 1800-1810 http://dx.doi.org/10.1016/j.fuel.2006.12.024
6. Didem Özçimen, An Approach to the Characterization of Biochar and Bio-Oil, *Yildiz Technical University*, Turkey, Thesis 2013
7. I. Aleksovski, S. Aleksovski, Z. Koneska, Chemical composition of bio-oil produced by fast pyrolysis of wood chips, *Mechanical Engineering-Scientific Journal*, **34** (1) (2016) 169–172

8. I. Aleksovski, S. Aleksovski, Z. Koneska, Characterization of bio-oil obtained with pyrolysis of wheat straw, *Mechanical Engineering-Scientific Journal,* **34** (2) (2016) 397-399
9. J.A.C. Durange, M.R.L. Santos, M.M. Pereira, L.A.P. Fernandes Jr., M.N. Souza, A.N.Mendes, L.M. Mesa, C.G. Sánchez, E.M.S. Sanchez, J.M.M. Pérez, N.M.F. Carvalho, Physicochemical Properties of Pyrolysis Bio-Oil from Sugarcane Straw and Sugarcane in Natura, *Journal of Biomaterials and Nanobiotechnology*, **4** (2013) 10-19 http://dx.doi.org/10.4236/jbnb.2013.42A002
10. S. Nanda, P. Mohanty, J. A. Kozinski & A. K. Dalai, Physico-Chemical Properties of Bio-Oils from Pyrolysis of Lignocellulosic Biomass with High and Slow Heating Rate, *Energy and Environment Research*, **4** (3) (2014) 21-32 http://dx.doi.org/10.5539/eer.v4n3p21
11. J. Piskorz, D. S. Scot, D. Radlien, Composition of oils obtained by fast pyrolysis of different woods. In Pyrolysis Oils from Biomass: Producing Analyzing and Upgrading, *American Chemical Society: Washington, DC* (1988) 167-178
12. W.N. R. Wan Isahak, M. W. M. Hisham, M. A. Yarmo, T. Y. Hin, A review on bio-oil production from biomass by using pyrolysis method, *Renewable and Sustainable Energy Reviews*, **16** (2012) 5910–5923 http://dx.doi.org/10.1016/j.rser.2012.05.039
13. T. Kan, V. Strezov,T.J. Evans, Lignocellulosic biomass pyrolysis: A review of product properties and effects of pyrolysis parameters, *Renewable and Sustainable Energy Reviews*, **57** (2016) 1126–1140 https://doi.org/10.1016/j.rser.2015.12.185
14. D. Mohan, C.U. Pittman, Jr, and P.H. Steele, Pyrolysis of Wood/Biomass for Bio-oil: A Critical Review, *Energy & Fuels*, **20** (2006) 848-889
15. I.Wilkomirsky, E. Moreno, A. Berg, Bio-Oil Production from Biomass by Flash Pyrolysis in a Three-Stage Fluidized Bed Reactors System, *Journal of Materials Science and Chemical Engineering*, **2** (2014) 6-10 http://dx.doi.org/10.4236/msce.2014.22002
16. A.Imran, E.A. Bramer, K. Seshan and G. Brem, Catalytic Flash Pyrolysis of Biomass Using Different Types of Zeolite and Online Vapor Fractionation, *Energies*, 2016, **9**, 187; https://doi.org/10.3390/en9030187
17. G. Lyu, S. Wu and H. Zhang, Estimation and comparison of bio-oil components from different pyrolysis conditions, *Frontiers in Energy Research*, **3** (2015) Article 28, 1-11 http://dx.doi.org/10.3389/fenrg.2015.00028

ELECTROCHEMICAL SENSORS BASED ON POLYMER-MODIFIED SCREEN-PRINTED GRAPHENE ELECTRODES FOR DETECTION OF PHARMACEUTICALS IN AQUATIC ENVIRONMENTS

Iva Dimitrievska*, Perica Paunović, Anita Grozdanov

Faculty of Technology and Metallurgy, Ss. Cyril and Methodius University in Skopje, North Macedonia

*iva@tmf.ukim.edu.mk

Abstract: *Detecting pharmaceutical contaminants in aquatic environments, including wastewater and natural water bodies such as rivers, lakes, and seas, is essential for safeguarding environmental health and ensuring water quality. Pharmaceuticals, often incompletely metabolized by humans and animals, persist in the environment and pose risks to ecosystems due to their bioactivity and potential for accumulation. This study investigates the application of polymer-modified screen-printed graphene electrodes, specifically those modified with polyvinylidene fluoride and chitosan, for the sensitive detection of doxorubicin as a widely used chemotherapeutical compound. Electrochemical analysis was performed using cyclic voltammetry to evaluate the performance of the modified electrodes and compare it to the commercial one at three different pH values (4.0, 6.7, and 11.0). The polymer-modified electrodes are characterized by enhanced sensitivity through improved adsorption and hydrophobic interactions, especially when tested at pH 6.7. The chitosan-modified electrode possesses the lowest limit of detection and limit of quantification among the tested electrodes, with values of 9.822 and 32.741 µmol L^{-1}, respectively, within a linear concentration range from 1.5 to 7.4 µmol L^{-1}. Moreover, the electrodes demonstrate excellent stability, reproducibility, and repeatability. These results highlight the potential of polymer-modified graphene electrodes as cost-effective and rapid tools for monitoring pharmaceutical residues in diverse aquatic environments, contributing to pollution management and environmental protection efforts.*

Keywords: doxorubicin, polyvinylidene fluoride, chitosan, environment, aquatic ecosystems.

INTRODUCTION

Electrochemical sensors based on screen-printed electrodes (SPEs) have emerged as powerful analytical tools for real-time monitoring of pharmaceutical compounds. These sensors offer significant advantages for practical applications including rapid response time, minimal sample preparation, cost-effective instrumentation, and the ability to perform measurements in complex matrices using small sample volumes (20-100 µL). The single-use nature of SPEs eliminates cross-contamination concerns, making them ideal for clinical environments [1].

Surface modification of SPEs with nanomaterials has revolutionized their sensing capabilities. Carbon nanomaterials such as graphene and carbon nanotubes significantly enhance electrode sensitivity by increasing the electroactive surface area and accelerating electron transfer rates. Additionally, polymer modifications with chitosan (Ch) and polyvinylidene fluoride (PVDF) further improve sensor performance through interaction mechanisms that promote analyte adsorption and specificity.

These advanced electrochemical platforms have proven particularly valuable for monitoring doxorubicin hydrochloride (DOX), a widely used anticancer medication effective against numerous malignancies. Despite its efficacy, the treatment with DOX is associated with high risks [2], such as dose-dependent cardiotoxicity that can cause irreversible heart damage [3]. Moreover, DOX has a short half-life in the blood, and about half is excreted. The biodegradability of DOX as a pollutant from wastewater can be difficult and might have long-lasting negative effects. Therefore, developing a method for sensitive detection and remediation is crucial. Polymer-modified electrochemical sensors can successfully detect DOX in wastewater samples with low detection limits.

Conventional analytical methods for DOX determination include high-performance liquid chromatography and mass spectroscopy techniques that require complex sample preparation and expensive equipment, making electrochemical sensors an attractive alternative for wastewater monitoring. The continued development of these sensing platforms promises to deliver accessible field-deployable devices for environmental monitoring, ultimately improving water quality assessment through rapid detection of pharmaceutical contaminants in wastewater treatment facilities and natural water bodies. In our work, we propose a simple development of an electrochemical sensor based on screen-printed electrodes (SPEs) for detection of doxorubicin (DOX) in aquatic media.

EXPERIMENTAL

Graphene-based SPEs (model DS1100, Dropsens Ltd, Spain) were modified with drop-casting chitosan (Ch) and polyvinylidene fluoride (PVDF) polymers (Sigma Aldrich) prepared as 2 wt.% solutions in N,N-dimethylacetamide and allowed to dry on the electrode surfaces at room temperature (Fig. 1).

All measurements were performed in 25 mL 0.1 mol/L phosphate buffer saline (PBS), at pH 4.0, 6.7, and 11.0, by adding DOX (Ebewe a.d., 2 mg/mL) to a concentration of 0.002 mol L^{-1}. The influence of pH on the electrochemical detection of DOX was investigated for optimal electrolyte conditions determination.

Electrochemical characterization employed cyclic voltammetry (CV) using a SPELEC potentiostat with Dropview software. Measurements ran from -0.05 to +0.6 V for 5 scans collected at a scan rate of 25 mV/s, chosen as an optimal rate for balancing the sensitivity and stability of the DOX's redox signals. A calibration curve (1.5-7.4 µmol L^{-1}) established detection and quantification limits based on signal-to-noise ratios of 3 and 10, respectively. All measurements were performed in triplicate at 25°C.

The repeatability of the electrodes was investigated using 10 consecutive CV measurements, performed in triplicates. The stability was evaluated in a timeframe of 7 consecutive days. The precision i.e. reproducibility of the SPEs was calculated using three different SPEs from each modification.

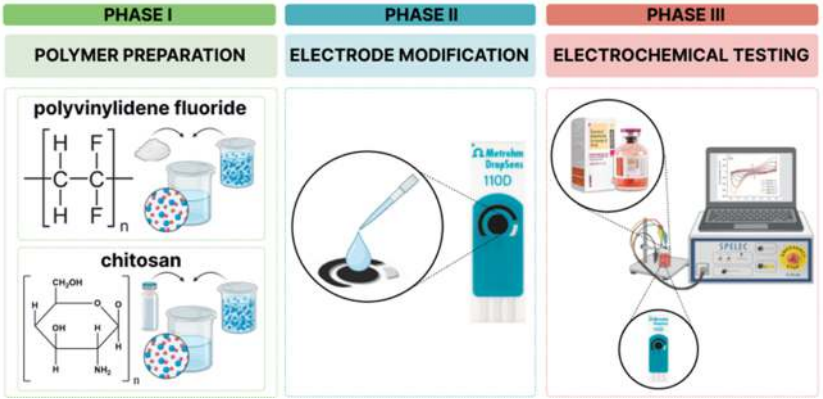

Figure 1 *Schematic of the electrodes' preparation, modification, and electrochemical testing*

RESULTS AND DISCUSSIONS

Three electrode systems based on commercial graphene (G), chitosan-modified graphene (G/Ch), and PVDF-modified graphene (G/PVDF), were evaluated by cyclic voltammetry in 0.1 mol/L PBS with and without doxorubicin, at three different pH values (4.0, 6.7 and 11.0). The voltammograms were recorded in a potential range of -0.05 to 0.6 V at a scan rate of 25 mV s^{-1}.

In PBS alone (Fig. 2a, 3a, and 4a), all electrodes showed minimal background current with no redox peaks, confirming a stable baseline for measurements. This absence of peaks indicates that the electrolyte solution does not contain electroactive species under the experimental conditions, ensuring a clear distinction between background response and signals from added analytes.

Upon addition of DOX (0.002 mol L^{-1}) at pH 6.7, all electrodes displayed characteristic oxidation (P_{ox}) and reduction (P_{red}) peaks, indicating a reversible

reaction occurring on the electrode surface. The commercial graphene electrode, shown in Fig. 2b exhibited the strongest current response due to its superior conductivity and large surface area but required higher oxidation potential (P_{ox}) (427 mV) with a high peak-to-peak separation (ΔE_p), indicating less reversible electron transfer kinetics. The polymer-modified electrodes demonstrated enhanced electrochemical performance. G/PVDF, showed slightly higher current density (26 μA cm^{-2}) than G/Ch (20.5 μA cm^{-2}), while G/Ch demonstrated lower oxidation potential and lower peak separation, indicating more favorable electron transfer kinetics and better reversibility. These improvements result from specific interactions between DOX and the polymers, including π-π stacking, hydrogen bonding, and hydrophobic interactions [4-6]. The electrochemical parameters for all SPEs at pH 4.0 and 6.7 are shown in Table 1.

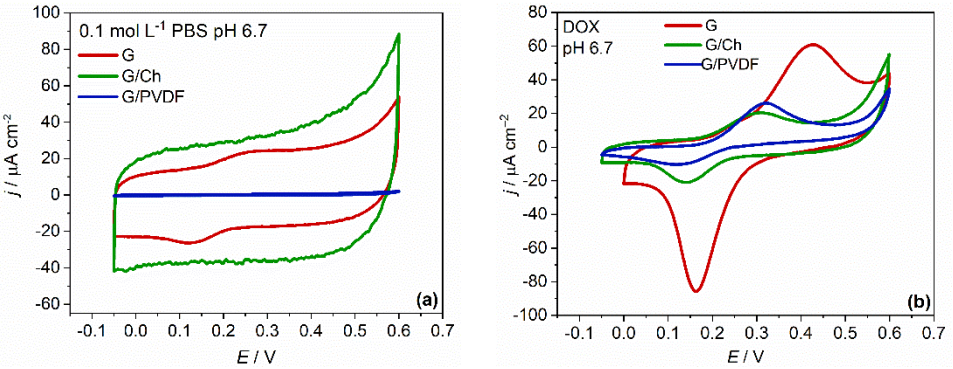

Figure 2 *SPEs' response in (a) 0.1 mol L^{-1} PBS and (b) 0.002 mol L^{-1} DOX solution at pH 6.7.*

Table 1 *Electrochemical parameters calculated for all graphene electrodes*

Electrode	P_{ox} [mV]	P_{red} [mV]	ΔE_p [mV]
	pH 4.0		
G	427	164	263
G/Chitosan	310	142	167
G/PVDF	322	195	195
	pH 6.7		
G	523	357	166
G/Chitosan	451	322	129
G/PVDF	473	312	161

The reversibility of the redox reaction depends on the electrode material. When oxidation and reduction peaks appear at the same potential with equal intensities, the reaction is fully reversible. Compared to the commercial graphene electrode, the smaller peak-to-peak separation potentials observed for G/Ch and G/PVDF indicate faster and more reversible electron exchange in the redox reaction. The

chitosan modification demonstrated the best performance.

In an acidic environment (pH 4.0), all electrodes exhibited a notable shift in the position and intensity of redox peaks compared to neutral conditions. The commercial graphene electrode showed a decrease in P_{ox} with reduced peak current intensity. While literature [7,8] suggests that mildly acidic media (pH 4.5-5.5) is favorable for DOX detection due to protonation facilitating electron transfer, the more strongly acidic pH environment (4.0) proved detrimental to electrode performance. The wider peak-to-peak separation indicates decreased reversibility in acidic conditions. Both polymer-modified electrodes demonstrated similar performance at this pH, with G/Ch exhibiting enhanced characteristics related to the smaller peak separation. This can be attributed to the protonation of amino groups in chitosan, creating additional interaction sites with DOX molecules [9,10].

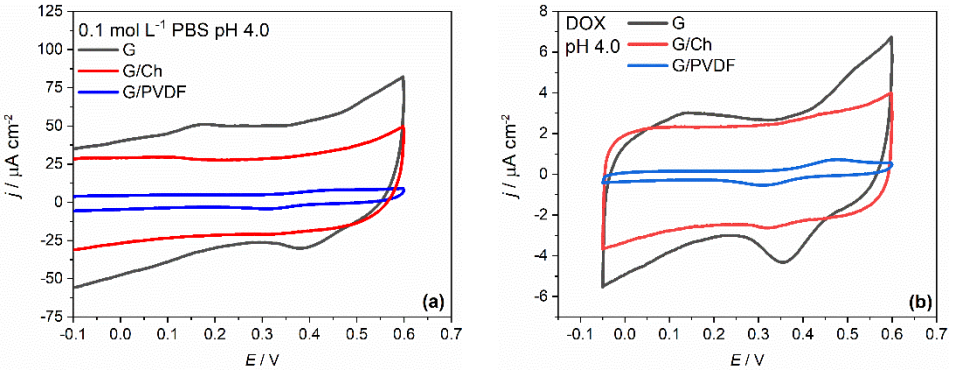

Figure 3 *SPEs' response in (a) 0.1 mol L^{-1} PBS and (b) 0.002 mol L^{-1} DOX solution at pH 4.0.*

No redox activity was observed at pH 11.0, indicating unfavorable electron transfer under alkaline conditions. The voltammograms are displayed in Fig 4.

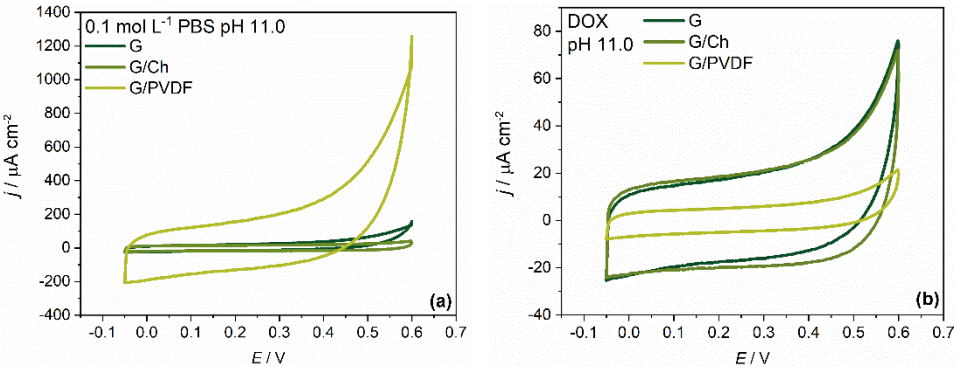

Figure 4 *SPEs' response in (a) 0.1 mol L^{-1} PBS and (b) 0.002 mol L^{-1} DOX solution at pH 11.0.*

These pH-dependent responses demonstrate the versatility of polymer-modified electrodes across different chemical environments, with G/Ch and G/PVDF performing optimally in neutral to acidic conditions. The consistent improvement in electrochemical parameters compared to unmodified graphene electrodes confirms that strategic polymer modification creates more favorable environments for DOX detection through combined effects of increased surface area, enhanced conductivity, and specific chemical interactions.

Calibration curves constructed within a linear concentration range of 1.5 to 7.4 μmol L^{-1} DOX at neutral pH showed excellent linearity across all electrodes, as displayed in Fig. 5.

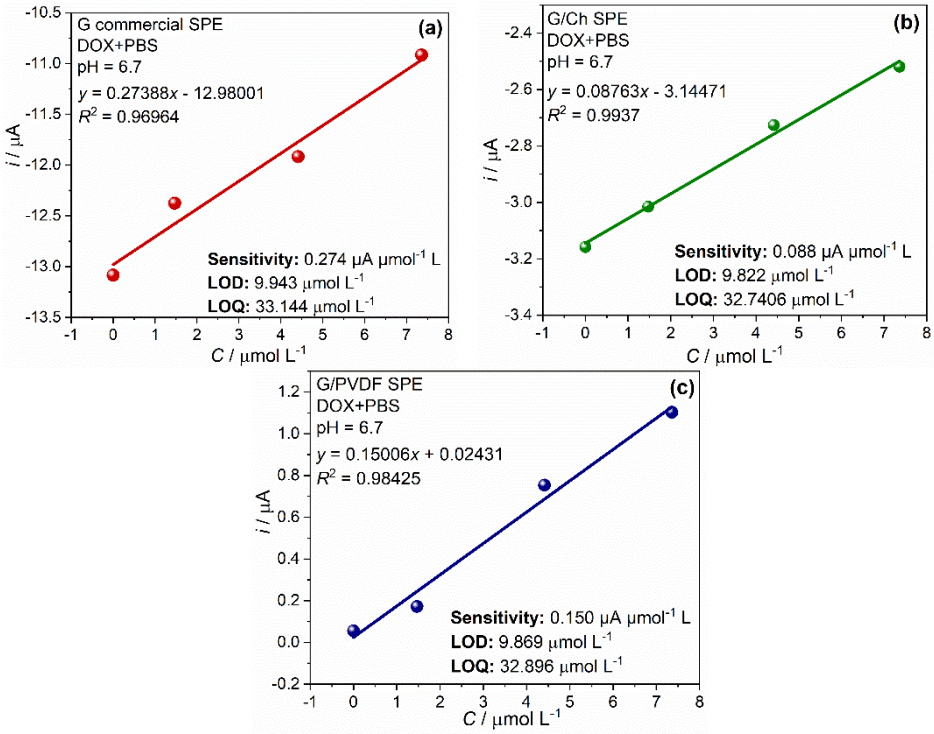

Figure 5 *Current (i) – concentration correspondence (C) at pH 6.7 for the (a) commercial graphene electrode; (b) chitosan-modified electrode and (c) PVDF-modified electrode*

The G/Ch electrode (Fig. 5b) demonstrated the highest correlation coefficient (R^2 = 0.9937). The G/PVDF system (Fig. 5c) followed with R^2 = 0.9843, while the unmodified graphene electrode (Fig. 5a) showed a correlation of R^2 = 0.9696. Sensitivity values were determined to be 0.088, 0.150, and 0.274 μA μmol^{-1} L for G/Ch, G/PVDF, and G systems, respectively. Both modified electrodes achieved lower detection limits (LOD), and quantification limits (LOQ) compared to the

unmodified electrode. The G/Ch system performed best with LOD and LOQ values of 9.822 and 32.741 μmol L^{-1}, respectively, followed closely by G/PVDF with values of 9.869 and 32.896 μmol L^{-1}. The commercial graphene electrode showed the highest limits at 9.943 and 33.144 μmol L^{-1} for LOD and LOQ, respectively.

In contrast, calibration curves constructed at pH 4.0 revealed noticeably lower linearity and reduced analytical performance across all electrodes (Fig. 6).

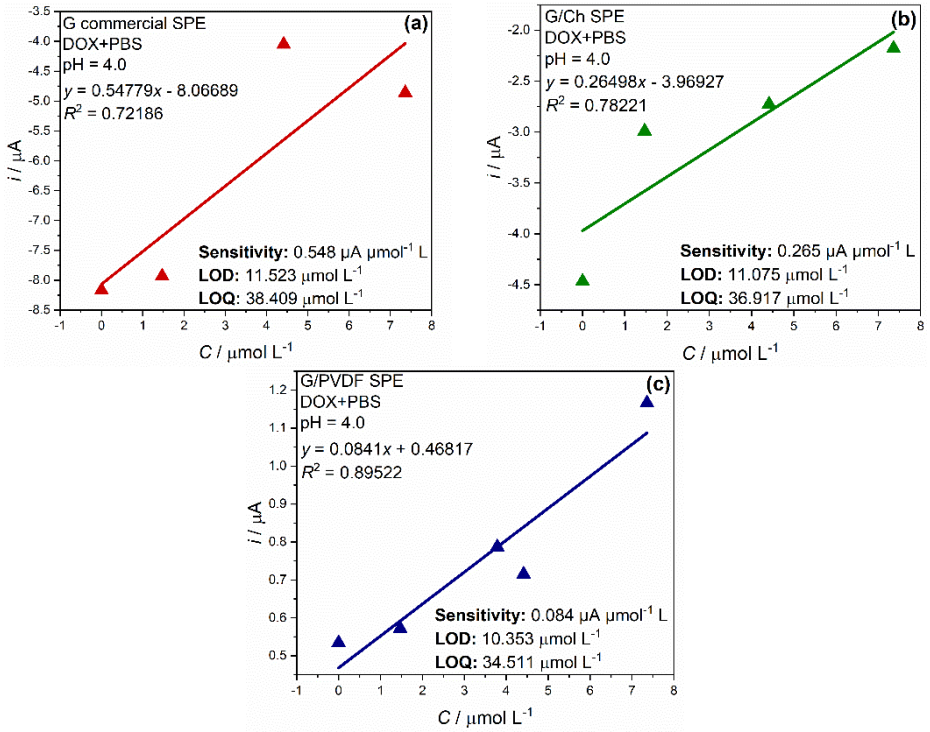

Figure 5 *Current (i) – concentration correspondence (C) at pH 4.0 for the (a) commercial graphene electrode; (b) chitosan-modified electrode and (c) PVDF-modified electrode*

Although the linear concentration range remained the same, the correlation coefficients decreased, indicating less consistent electrochemical response under acidic conditions. Sensitivity values were notably different compared to those at neutral pH, with the commercial graphene electrode exhibiting the highest sensitivity (0.548 μA μmol^{-1} L), followed by the G/Ch electrode (0.265 μA μmol^{-1} L) and the G/PVDF system (0.084 μA μmol^{-1} L). Despite the commercial electrode showing the highest sensitivity in this medium, all systems experienced an increase in both LOD and LOQ values, confirming the less favorable electron transfer dynamics in acidic environments. The PVDF-modified SPE possesses the lowest LOD and LOQ values in an acidic environment, suggesting the overall stability of

the polymer. These results suggest that although DOX remains electrochemically active at low pH, the signal reproducibility and sensitivity are significantly diminished, likely due to altered protonation states of DOX or electrode surface interactions.

These results highlight the improved electrochemical performance of the polymer-modified electrodes, particularly the chitosan modification, which demonstrated superior sensitivity and analytical performance for DOX determination in neutral media.

Repeatability, stability, and precision

The repeatability, stability, and reproducibility of the commercial and modified SPEs were evaluated using cyclic voltammetry (CV) in a 0.002 mol L^{-1} DOX solution prepared in 0.1 mol L^{-1} PBS at pH 6.7. The relative standard deviation (RSD) values for repeatability were 4.47% for the commercial graphene (G), 1.76% for the G/Ch, and 3.43% for the G/PVDF electrode. The stability study revealed a decrease in the oxidation peak current of 4.95% and 12.45% from the initial values for the G/Ch and G/PVDF electrodes, respectively, indicating excellent and acceptable stability. The commercial G electrode exhibited a slightly higher current loss of 12.88%. The precision analysis yielded low RSD values of 3.05%, 3.48%, and 3.04% for the commercial G, G/Ch, and G/PVDF electrodes, respectively, demonstrating the excellent reproducibility of all developed sensors.

CONCLUSIONS

This research successfully developed polymer-modified screen-printed graphene electrodes for sensitive electrochemical detection of doxorubicin in aquatic media. The modified electrodes, particularly the chitosan-modified graphene electrode (G/Ch), exhibited superior performance compared to commercial, unmodified electrode in terms of sensitivity, stability, and reproducibility. The electrochemical response was significantly influenced by pH, with optimal performance observed at neutral pH (6.7), while strongly acidic (pH 4.0) and alkaline (pH 11.0) conditions proved less favorable for DOX detection. At optimal pH, the G/Ch electrode demonstrated excellent analytical parameters with the lowest limits of detection and quantification, alongside the highest correlation coefficient within the linear concentration range of 1.5 to 7.4 µmol L^{-1}. Both polymer modifications enhanced the electrochemical performance through improved electron transfer kinetics and increased reversibility, evidenced by reduced peak-to-peak separation potentials compared to the commercial electrode. The exceptional repeatability, stability, and reproducibility of the G/Ch electrode further highlight its potential for practical applications. These findings demonstrate that polymer-modified screen-

printed electrodes represent a promising platform for the development of cost-effective, portable, and reliable sensors for monitoring pharmaceutical contaminants in environmental water samples. Their implementation could significantly contribute to monitoring efforts in wastewater treatment facilities and natural water bodies, providing a valuable tool for environmental protection and water quality assessment.

REFERENCES

1. I. Dimitrievska, P. Paunović, A. Grozdanov. Polymer-modified screen-printed electrode-based electrochemical sensors for doxorubicin detection, *Journal of Electrochemical Science and Engineering,* **15(1)** (2024) 2501. https://doi.org/10.5599/jese.2501.

2. L. I. Jinga, M. Tudose, P. Ionita. Laccase–TEMPO as an Efficient System for Doxorubicin Removal from Wastewaters. *International Journal of Environmental Research and Public Health* ***19*****(11)** (2022) 6645. https://doi.org/10.3390/ijerph19116645.

3. M. A. Mitry, J. G. Edwards, Doxorubicin induced heart failure: Phenotype and molecular mechanisms, *International Journal of Cardiology Heart & Vasculature* **10(17-24)** (2016) 17-24. http://doi.org/10.1016/j.ijcha.2015.11.004.

4. F. Chekin, V. Myshin, R. Ye, S. Melinte, S. K. Singh, S. Kurungot, R. Boukherroub, S. Szunerits, Graphene-modified electrodes for sensing doxorubicin hydrochloride in human plasma, *Analytical and Bioanalytical Chemistry* **411** (2019) 1509-1516. https://doi.org/10.1007/s00216-019-01611-w.

5. H. Imran, Y. Tang, S. Wang, X. Yan, C. Liu, L. Guo, E. Wang, C. Xu, Optimized DOX Drug Deliveries via Chitosan-Mediated Nanoparticles and Stimuli Responses in Cancer Chemotherapy: A Review, *Molecules* **29(1)** (2024) 31. https://doi.org/10.3390/molecules29010031.

6. I. M. Apetrei, C. Apetrei, Voltametric determination of melatonin using a graphene-based sensor in pharmaceutical products, *International Journal of Nanomedicine* **11** (2016) 1859-1866. http://doi.org/10.2147/IJN.S104941.

7. E. M. Materon, A. Wong, O. F. Filho, R. C. Faria, Development of a simple electrochemical sensor for the simultaneous detection of anticancer drugs, *Journal of Electroanalytical Chemistry* **827** (2018) 64-72. https://doi.org/10.1016/j.jelechem.2018.09.010.

8. M. Mahdavi, F. Rahmani, S. Nouranian, Molecular Simulation of pH-dependent Diffusion, Loading, and Release of Doxorubicin in Graphene and Graphene Oxide Drug Delivery Systems, *Journal of Materials Chemistry B* **4** (2016) 7441-7451. https://doi.org/10.1039/C6TB00746E.

9. C. Rungnim, T. Rungrotmongkol, R. P. Pooarporn, pH-controlled doxorubicin anticancer loading and release from carbon nanotube noncovalently modified by chitosan: MD simulations, *Journal of Molecular Graphics and Modelling* **70** (2016) 70-76. http://dx.doi.org/10.1016/j.jmgm.2016.09.011.

10. J. Li et al. Molecular dynamics study on the encapsulation and release of anti-cancer drug doxorubicin by chitosan, *International Journal of Pharmaceutics* **580** (2020) 119241. https://doi.org/10.1016/j.ijpharm.2020.119241.

ECO-FRIENDLY MATERIALS FOR ELECTROCHEMICAL CAPACITORS

Dragica Chamovska[1], Aleksandra Porjazoska Kujundziski[2]

[1] - *Faculty of Technology and Metallurgy, Ss. Cyril and Methodius University in Skopje, North Macedonia*

[2] - *Faculty of Engineering, International Balkan Univercity, Skopje, R. North Macedonia*

dragica@tmf.ukim.edu.mk

Abstract: *High energy consumption and, at the same time, the depletion of fossil fuels have directed the focus of scientific interest toward alternative energy sources of renewable origins. Technologies introduced to reduce emissions of toxic and greenhouse gases, considered "clean" energy resources, include processes based on wind power, water flow, solar radiation, and geothermal solutions. On the other hand, the unexpected meteorological conditions affect efficiency. A solution to this problem related to these sustainable energy sources has been seen in the combination of various energy storage devices. Due to the comparable electrochemical performances to conventional capacitors and batteries, electrochemical capacitors, also known as supercapacitors or ultracapacitors, attract significant interest in the possibility of their application as renewable energy storage devices. High energy per unit volume and rapid charging/discharging cycles make electrochemical capacitors suitable for applications in electric and hybrid vehicles. Supercapacitors encounter applications such as energy storage and power backup, electric buses and trains, portable devices, defibrillators, power tools, and much more, emphasizing their advantages, mainly when carbon-based materials are used as electrode components in electrochemical capacitors. Their low cost, availability, and sustainability are among the main benefits of activated carbons. Biomass precursors, invoving mostly by-products from food industry, as coffee grounds, various seeds, and shells, for the synthesis of activated carbon has lately attracted additional attention. This study focuses on the characteristics of bio-based activated carbons and their potential uses in electrochemical capacitors.*

Keywords: carbon electrodes, activated carbon, biomass precursor, electrochemical capacitors

INTRODUCTION

High-performance energy storage devices, i.e., supercapacitors or ultracapacitors, more widely referred to as electrochemical capacitors (ECs), have been the focus of intense interest among the scientific community as well as the industry [1]. Conventional storage devices, e.g., capacitors, deliver high power output with lower energy density than batteries. ECs that deliver moderate power and energy density are midpoints between them. Because they can customise the power and energy output for specific uses, ECs act as trustworthy

power sources, providing quick charge release. Recently, efforts have been focused on boosting their energy density [2].

The responsibility of the charge storage in supercapacitors belongs to the development of the electric double layer (EDL) and the electrostatic interaction at the solid electrode/electrolyte interface, unlike conventional batteries, where this function relies on faradaic redox reactions, Table 1 [1-6]. The EDL formation explains the energy storage mechanism in electrochemical capacitors. The EDL consists of two primary regions: the Helmholtz inner and outer planes and the diffuse layer. Inner Helmholtz's plane is a monolayer of specifically adsorbed ions that are tightly attached to the electrode surface by the electrostatic interaction. The Helmholtz outer plane comprises closely packed solvated ions near the electrode, while the outer diffuse layer involves counter-ions distributed in the electrolyte. These two layers form a capacitive interface that can store significant amounts of charge. After the voltage application, polarised electrodes attract oppositely charged species from the electrolyte. Possible desolvation permits ions to get closer to the electrode surface, which affects the increase of capacitance [1-4]. The typical carbon-based electrode materials for electrochemical capacitors provide a large surface area for the formation of the EDL [5]. The electrode material type, electrolyte composition, ion size and solvation are key factors impacting charge storage [6]. A larger surface area increases the number of available charge storage sites [5]. The conductivity of the electrode influences charge distribution efficiency [6]. Electrolyte composition influences ionic mobility and capacitance [1, 6]. Aqueous electrolytes (H_2SO_4, KOH) enable fast ion movement but support lower voltage windows (~1 V) [7].

Table 1 *The energy storage comparison between electric double-layer capacitors and traditional batteries [1-6]*

Feature	Electric double layer capacitor (EDLC) (Supercapacitor)	Battery
Charge storage	Electrostatic (double layer)	Electrochemical (redox)
Reaction type	Non-faradaic	Faradaic
Energy density	Lower	Higher
Power density	Higher	Lower
Charge time	Seconds to minutes	Minutes to hours
Cycle life	Millions of cycles	Thousands of cycles

On the other hand, organic electrolytes (acetonitrile, ionic liquids) support higher voltages (~2.5–3 V) and increase energy storage. Smaller ions penetrate deeper into pores, improving charge density [8]. Functional groups containing oxygen, nitrogen, boron, sulfur, and phosphorus that might be present on the carbon

surface may induce another interesting effect—pseudocapacitance, redox reactions taking place at the electrode/electrolyte interface. This coupling of typical EDL charging and redox reaction produces higher current output and capacitance [1,4,7,8].

Their acceptable power/energy density, extended cycle life, and fast charge-discharge capabilities make ECs ideal candidates for different applications. Increased global energy demand and the uncontrolled utilisation of fossil fuels resulted in the discovery of alternative sustainable and renewable energy sources concerning conventional ones. Modification and hybridization with other energy storage alternatives increase the applicability of ECs in hybrid and electric vehicles [1]. Choosing the right materials for electrochemical energy-storage devices as emerged as an important issue, facing increasing environmental consciousness and green chemistry concepts with sustainable development objectives. The utilisation of sustainable, biocompatible, and natural materials from renewable resources reduces the ecological footprint linked with conventional material extraction, processing, and disposal [1]. One should consider the environmental contribution of all parts involved in electrochemical capacitors, such as separators, packaging, and current collectors. The continuous technological advancement and increased demands for efficient and reliable energy storage devices have also triggered studies concerning sustainable supercapacitor materials [9]. Particular interest as sustainable substitutes for conventional electrode materials have shown biomass-derived materials, mainly activated carbon from agricultural waste, cellulose nanocrystals, or lignin-based polymers, due to their developed porosity, biodegradability, and high surface area [1,11]. Similarly, regarding biocompatibility, biodegradability, and film-forming features, polymers like chitosan, alginate, and starch have been recognized as materials for binders and separators in electrochemical capacitors [9-11].

Carbon-based materials are, so far, the most widely used electrodes for supercapacitors. This popularity is attributed to the need for low maintenance and great cycle life. However, there are still huge limitations when biomass and biowaste are used as a carbon precursor because the starting material's carbonisation at high temperatures results in a lack of nitrogen and oxygen species, which results in poor self-doping. It indicates the need to conduct more research and innovation to realise their full potential [12-15].

Implementing bio-nanotechnology for functional nanomaterial fabrication gives a unique approach to developing precisely controlled morphologies and microstructures of these materials. Thus, developing tailored nanostructured carbon materials of green origin has led to significant progress, enhancing

supercapacitors' energy and power densities [12].

Further discussion will focus on carbon-based electrodes for supercapacitors, concentrating on activated carbon. A systematic literature review adapted to the web was applied using Scopus, Science Direct, and Science Citation Index (SCI) databases, where papers were selected by keywords related to carbon electrodes, activated carbon, biomass precursor, and electrochemical capacitors.

CARBON-BASED ELECTRODES

The performance of a supercapacitor, among others, depends on the types and/or properties of the electrode materials. The fast electron, i.e., charge transport within the electrode, guarantees supercapacitors' high electrical conductivity and increased power density. Some of the electrode material's characteristics include resistance to multiple charging-discharging cycles, i.e., more considerable stability and good cycle life [10,16]. Long-term stability is characteristic of carbon-based electrodes such as activated carbon and graphene) and metal oxides, including RuO_2 and MnO_2 [16,17].

The high specific capacitance of conducting polymers and transition metal oxides enhances electrochemical capacitors' storage capacity. A larger specific surface area indicates increased capacitance of ECs because more active sites are available for ion adsorption. However, excessive pore size reduction leads to decreased charge storage efficiency. Namely, the small and narrow pores like those in activated carbon, do not match the size of the ions restricting their access. Additionally, porous materials can also lead to inhomogeneous current distribution across the electrode, and local spikes in current density, particularly at defects, may result in electrolyte breakdown [1-4].

Namely, as the pore walls become too thin, the charges stored on adjacent walls shield each other, reducing the overall effective electric field. Effective ion transfer at the interface electrode/electrolyte is vital for optimal charging rates [1-4]. Mesoporous structures of the electrodes improve ion accessibility and charge transport. Nanocarbons, e.g., nanotubes and graphene with the typical mesoporous structure, show moderate capacitance ranging between 20 and 60 $F \cdot g^{-1}$ [1, 11]. Additional activation or functionalisation enhances these values. Hence, activated graphene develops a surface area exceeding 2000 $m^2 \cdot g^{-1}$ and capacitance values of around 200 $F \cdot g^{-1}$ in organic mediums [1, 11]. However, the current limitations of practical applications of this material concern challenges related to the expansion of high-quality production and the synthesis of low-density graphene associated with the small inherent volumetric capacitance of the system [10].

Factors that additionally influence the selection of electrode materials for electrochemical capacitors include material chemical and thermal stability, oxidation and corrosion resistance, and stable electrode structure under different operating conditions. The requirements mentioned above make carbon-based materials and metal oxides popular electrode materials. Electrodes must possess sufficient mechanical strength and also endure physical stress [17]. Carbon materials are sometimes bound with numerous polymers, mainly poly(vinylidene difluoride) (PVDF) and poly(tetrafluoroethylene) (PTFE), to ensure sufficient electrode stability [11]. On the other hand, these polymers not only negatively affect the wettability of electrodes by electrolyte, but also due to the high fluorine content, they raise environmental concerns. Materials' environmental impact and cost are becoming increasingly significant selection factors. Sustainability is pushing researchers and manufacturers to find eco-friendly and affordable alternatives [10]. Biomass-based materials offer suitable alternatives for supercapacitors, replacing traditional options. They reduce the environmental impact and promote a circular economy [10-15,17].

Carbon-based electrode precursors, synthesis methods, and their influence on the properties of the final product are shown in Table 2.

Table 2 *Precursors, synthesis methods, and their influence on the properties of the carbon-based materials [*10-15,17*]*

Precursor type	Examples	Synthesis methods	Effect on properties	Common applications
Biomass-derived carbon	Coconut shell, wood, lignin, cellulose, corn husk, algae, sucrose	Pyrolysis, activation (KOH, $ZnCl_2$, CO_2), Hydrothermal carbonisation	- High porosity (micro-/mesoporous) - Moderate electrical conductivity - Tunable surface chemistry (oxygen/nitrogen doping)	- Supercapacitors - Li-ion and Na-ion batteries - Fuel cells - Electrochemical sensors
Polymers	Polyacrylonitrile (PAN), Polyaniline (PANI), Polypyrrole (PPy), Phenolic resins	Electrospinning + Carbonisation, chemical Activation, Templating	- High conductivity (after graphitisation) - Controllable porosity - High structural flexibility	- Flexible electronics - Supercapacitors - Batteries (anode/cathode materials)
Graphene-Based	Graphite, Graphene oxide	Chemical vapour deposition	- Ultra-high conductivity	- High-performance

	(GO), Reduced GO (rGO)	(333CVD), Chemical/ Electrochemical exfoliation, Hydrothermal reduction	- High surface area - Excellent mechanical strength	supercapacitors - Li-S and Li-ion batteries - Electrocatalysis - Wearable energy storage
Carbon nanostructures	Carbon nanotubes (CNTs), Fullerenes, Carbon nanofibres (CNFs)	CVD, Arc discharge, Electrospinning, Template-Assisted growth	- Superior conductivity - High mechanical strength - Tunable pore structure	- Conductive additives in electrodes - Supercapacitors - Batteries - Sensors
Hydrocarbons	Petroleum pitch, Coal tar, Natural gas	High-Temperature Carbonisation, graphitisation	- Highly graphitised structure - Excellent thermal and electrical conductivity - Low porosity	- High-power lithium-ion batteries - Supercapacitors - High-temperature fuel cells
Biochar and Activated carbon	Sawdust, Coconut shell, Peat, Waste biomass	Pyrolysis + Physical or chemical activation	- High surface area - Moderate conductivity - Environmentally friendly	- Low-cost supercapacitors - Water purification - Gas storage

Graphite is a source of pure carbon and, in conjunction with synthetic resins, polymers, and biomass derived from agricultural waste, wood, or other lignocellulosic materials, is the conventional precursor for carbon-based electrodes in electrochemical capacitors. The nature of the precursor used affects parameters essential for electrochemical performance, such as the surface area, conductivity, and porosity of the resultant carbon material [18].

Techniques that ensure high process and structure control and precision of fabricated carbon-based materials implement pyrolysis, chemical vapour deposition, and electrospinning [11]. Pyrolisis is performed in an inert atmosphere, where thermally decomposes (carbonised) biomass or organic precursors [11]. Chemical vapour deposition is a technique used to synthesise graphene and CNTs [12]. Nanostructured carbon fibre electrodes are obtained through electrospinning applied on the polymer solution to form fibres and their carbonisation to nanoscale dimensions. These synthesis methods control graphitisation level, doping capabilities, and microstructure, impacting charge storage and cycling stability [12].

The following text focuses on the characteristics of activated carbon derived from bio-based precursors.

ACTIVATED CARBONS FROM BIO-BASED PRECURSORS

Because of their distinctive structure and features and their environmentally safe, renewable and abundant sources, activated carbons with a biomass origin have lately gained great attention. These materials demonstrate elements of pseudocapacitance effects, enhanced electron density, and the capacity for simultaneous activation. Generally, when subjected to high temperatures in an inert atmosphere, any biomass material, such as almond shell, cane bagasse, coffee husks, walnut shell, soya coconut shell, peanut shell, palm kernel shell, etc., produces char. Additional activation processes include chemical methods using acids (HCl, H_2SO_4, H_3PO_4, etc.), alkalis (KOH, NaOH, etc.), and salts ($FeCl_3$, $ZnCl_2$, K_2CO_3, etc.), physical methods applying CO_2 and steam, biological means, and hydrothermal carbonisation, where char is transformed into activated carbon [11].

Using steam and continuous application of high temperatures during the entire process causes technical problems and difficulties in the physical activation. During the treatments, hydrothermal carbonisation doesn't use chemicals, which makes it recognized as a green process. Also, it is the most energy-efficient process compared to the other methods, but the large water consumption and the lack of waste management increase the cost of this treatment. The advantage of chemical activation is the application of smaller temperatures and shorter processing times. The environmentally safe properties of phosphoric acid increased its popularity in the activation processes of carbon precursors [11].

The constituents of lignocellulosic-based biomass are mainly cellulose, hemicellulose, and lignin and low molecular weight organic compounds (lipids, waxes, oils, etc.) and minerals in small percentages. Different chemical compositions characterise biomass of various origins. Usually, 30% to 50% of the dry lignocellulosic biomass belongs to cellulose, lignin participates with 15% - 30%, while hemicellulose typically represents 20% to 35% [11].

Implementing additional chemical treatment using the impregnation process improves the surface area and adsorption volume of activated carbon. The bigger the impregnation ratio, representing the ratio of the mass of the chemical used and the mass of the biomass due to the carbonisation and removal of volatile organic substances, the better the specific surface area of activated carbon. Thus, the impregnation ratio four was implemented on the rice husks at 500 °C for one hour, yielding around 1800 $m^2 \cdot g^{-1}$ of specific surface area [13].

Activated carbon from lignocellulosic precursors typically has a pore size between 20 and 190 μm. Longer activation time results in smaller yields of activated carbon, and because of the decreased carbon content, instead of micropores, the final product develops mesopores or even macropores [11,19].

The electrochemical performance of activated carbon electrodes in Table 3 indicates values of the specific capacity, power and energy density, and rate capability for different carbon sources, including corn stalk, rice husks, wood sawdust, wheat straw and sugarcane bagasse. Specific capacity varies between 255 and 300 $F \cdot g^{-1}$, power density from 10 500 to 12 300 $W \cdot kg^{-1}$, and energy density 34-39 $Wh \cdot kg^{-1}$, while rate capability ranges between 85% after 7 000 cycles and 93% after 9 000 cycles [11,19-21].

Table 3 *Electrochemical characteristics of biomass-based activated carbon electrodes for supercapacitors [11,19-21]*

Biomass source	Specific capacity ($F \cdot g^{-1}$)	Power density ($W \cdot kg^{-1}$)	Energy density ($Wh \cdot kg^{-1}$)	Rate capability (%)	Conditions of activation
Corn stalk	280	11 500	38	92% after 8 000 cycles	Pyrolysis, $ZnCl_2$ activation
Rice husk	270	11 000	37	88% after 6 000 cycles	Physical activation, steam
Wood sawdust	260	10 500	36	85% after 7 000 cycles	Chemical activation, H_3PO_4
Wheat straw	255	10 200	34	87% after 5 000 cycles	Hydrothermal method, KOH activation
Sugarcane bagasse	290	12 300	39	93% after 9 000 cycles	Chemical activation, KOH

Similarly, microporous material obtained by coffee ground carbonisation and activated by $ZnCl_2$ reached more than 350 $F \cdot g^{-1}$. Carbon from glucosamine precursors, activated with KOH, showed capacitance values of 250 $F \cdot g^{-1}$, while activated carbon from tobacco stems obtained by carbonisation indicated similar capacitance values of 240 $F \cdot g^{-1}$ in the aqueous solution [1].

CONCLUSIONS

Tunable properties, such as substantial energy and power density, long cycle life, and the possibility of usage in a flexible range of working temperatures, enable activated carbon to be applied in various high-power applications. Because of its high conductivity and reasonable electrochemical cycling rates, activated carbon is required for energy storage devices, e.g., supercapacitors. In the realm of

natural resource depletion, exploring powerful alternatives is a paradigm of research activities. Although biomass is widely employed in carbon generation, among various natural organic resources, only those that are reliable should be considered suitable precursors. The eco-friendly nature, cost-efficiency, and easy accessibility of biomass-based materials support continued research in this field for designing advanced energy storage systems.

REFERENCES

1. K. Fic, A. Platek, J. Piwek, E. Frackowiak, Sustainable materials for electrochemical capacitors, *Materials Today* **21** (2018) 437-454. https://doi.org/10.1016/j.mattod.2018.03.005
2. Y. Wang, Y. Xia, Recent Progress in Supercapacitors: From Materials Design to System Construction, *Advanced Materials* **25** (2013) 5336-5342 https://doi.org/10.1002/adma.201301932
3. P. Simon, Y. Gogotsi, Materials for electrochemical capacitors, *Nature Materials* **7** (2008) 845-854. https://doi.org/10.1038/nmat2297
4. B.E. Conway, *Electrochemical Supercapacitors: Scientific Fundamentals and Technological Applications*, Springer, Springer, Berlin, 1999. https://doi.org/10.1007/978-1-4757-3058-6
5. Zhu, S. Murali, M.D. Stoller, K.J. Ganesh, W. Cai, P.J. Ferreira, R.S. Ruoff, Carbon-Based Supercapacitors Produced by Activation of Graphene, *Science* **332** (2011) 1537-1541. https://doi.org/10.1126/science.1200770
6. F. Béguin, V. Presser, A. Balducci, E. Frackowiak, Carbons and electrolytes for advanced supercapacitors, *Advanced Materials* **26** (2014) 2219-2251. https://doi.org/10.1002/adma.201304137
7. E. Taer, F. Febriyanti, A. Apriwandi, R. Taslim, A. Agustino, W. Sinta Mustika, Investigation of H_2SO_4 and KOH aqueous electrolytes on the electrochemical performance of activated carbon derived from are cacatechu husk, *Journal of Physics: Conference Series* **1940** (2021) 012033. https://doi.org/10.1088/1742-6596/1940/1/012033
8. Y. Wang, K. Xue, C. Yan, Y. Li, X. Zhang, K. Su, P. Ma, S. Wan, J. Lang, Tuning of Ionic Liquid–Solvent Electrolytes for High-Voltage Electrochemical Double Layer Capacitors: A Review, *Batteries* **10** (2024) 54. https://doi.org/10.3390/batteries10020054
9. K. Yu, H. Zhu, H. Qi, C. Liang, High surface area carbon materials derived from corn stalk core as electrode for supercapacitor, *Diamond and Related Materials* **88** (2018) 18-22. https://doi.org/10.1016/j.diamond.2018.06.018
10. Q. Navid, M. Taali, M. Khosravy, M.S.S. Danish, Recent advances in bio-based electrode materials in supercapacitor applications: Energy storage materials and technologies, *Journal of Sustainable Energy Revolution* **3** (2022) 1-13. https://doi.org/10.37357/1068/jser/3.1.01
11. I. Neme, G. Gonfa, C. Masi, Activated carbon from biomass precursors using phosphoric acid: A review, *Heliyon* **8** (2022) e11940. https://doi.org/10.1016/j.heliyon.2022.e11940

12. A. Al Rai, M. Yanilmaz, High-performance nanostructured bio-based carbon electrodes for energy storage applications, *Cellulose* **28** (2021) 5169-5218. https://doi.org/10.1007/s10570-021-03881-z
13. S.E. Kayode, F.J. González, Treatment of Biowaste for Electrodes in Energy Storage Applications: A Brief Review, *Journal of Composites Science* **7** (2023) 127. https://doi.org/10.3390/jcs7030127
14. S.D. Reis, S. Petnikota, C.M. Subramaniyam, H.P. de Oliveira, S. Larsson, M. Thyrel, U. Lassi, F. García Alvarado, Sustainable Biomass-Derived Carbon Electrodes or Potassium and Aluminum Batteries: Conceptualizing the Key Parameters for Improved Performance, *Nanomaterials* **13** (2023) 765. https://doi.org/10.3390/nano13040765
15. N.M. Keppetipola, C.Olivier, T.Toupance, L.Cojocaru, Biomass-derived carbon electrodes for super capacitors and hybrid solar cells: towards sustainable photosupercapacitors, *Sustainable Energy & Fuels* **5** (2021) 4784-4806. https://doi.org/10.1039/D1SE00954K
16. D.Tian, C.Wang, X.Lu, (2021). Metal–Organic Frameworks and Their Derived Functional Materials for Supercapacitor Electrode, *Application, Advanced Energy and Sustainability Research* **2** (2021) 2100024. https://doi.org/10.1002/aesr.202100024
17. S. Ghosh, S.R. Polaki, A. Macrelli, C.S. Casari, S. Barg, S.M. Jeong, K. Ostrikov, Nanoparticle-enhanced multifunctional nanocarbons—recent advances on electrochemical energy storage applications, *Journal of Physics D Applied Physics* **55** (2022) 413001. https://doi.org/10.1088/1361-6463/ac7bb5
18. Y.W. Yap, N. Mahmed, M.N. Norizan, S.Z. Abd Rahim, M.N. Ahmad Salimi, K. Abdul Razak, I.S. Mohamad, M.M.A.-B. Abdullah, M.Y. Mohamad Yunus, Recent Advances in Synthesis of Graphite from Agricultural Bio-Waste Material: A Review, *Materials* **16** (2023) 3601. https://doi.org/10.3390/ma16093601
19. W. Hu, R. Xiang, J. Lin, Y. Cheng, C. Lu, Lignocellulosic Biomass-Derived Carbon Electrodes for Flexible Supercapacitors: An Overview, *Materials* **14** (2021) 4571. https://doi.org/10.3390/ma14164571
20. E.S. Esakkimuthu, V. Ponnuchamy, T. Yumak, D. De Vallance, *Lignin-Derived Carbonaceous Materials for Supercapacitor Applications*, in Handbook of Porous Carbon Materials, A.N. Grace, P. Sonar, P. Bhardwaj, A. Chakravorty, Eds., Springer, Singapore, 2023, p. 65. https://doi.org/10.1007/978-981-19-7188-4_4
21. P-H.Li, Y-M.Wei, C-W.Wu, Ch.Yang, B. Jiang, W-J. Wu, Lignin-based composites for high-performance supercapacitor electrode materials, *RSC Advances* **12** (2022) 19485-19494. https://doi.org/10.1039/D2RA02200A

APPLICATION OF SOLAR ENERGY IN HOME TEXTILE PRODUCTION

Zorica Cvetkovska, Elena Tomovska

Faculty of Technology and Metallurgy, University „Ss. Cyril and Methodius" Skopje, North Macedonia

zorica@tmf.ukim.edu.mk

Abstract: *The home textile industry is characterized by energy intensive manufacturing processes, contributing notably to greenhouse gas emissions. As this sector faces growing pressure to reduce its environmental footprint and transition away from fossil fuels, the adoption of renewable energy-particularly solar power has emerged as a viable solution. This study investigates the implementation of solar energy in a home textile manufacturing facility in North Macedonia. Through a case study methodology, the research highlights both the benefits and challenges associated with solar energy use. Findings show that while solar energy reduces operational costs and supports sustainability certifications, there are gaps in energy monitoring and seasonality issues that must be addressed. Enhanced energy data tracking and expanded government incentives for solar technologies are recommended to optimize energy use and support long-term sustainability in home textile production.*

Keywords (up to 5 words): sustainability in textiles industry, solar energy, home textiles

INTRODUCTION

The home textile industry, which is a vital segment of the global textile sector, is characterized by energy-intensive manufacturing processes that contribute significantly to environmental degradation [1]. Ranked among the most polluting industries globally, the textile sector as a whole is projected to account for up to 26% of the world's carbon footprint by 2050. This is largely due to its reliance on non-renewable energy sources, which are expected to result in the emission of hundreds of millions of tons of carbon dioxide, along with substantial microplastic pollution entering marine ecosystems [2]. Specifically, home textile production, which includes items such as quilts, pillows and mattress protectors, involves machinery with high energy demands. The sustainability of this sector hinges on a shift toward renewable energy sources.

Environmental pressures arise across the entire home textile supply chain, from the sourcing of raw materials to the dyeing and finishing stages. These processes require vast amounts of land, water and fossil fuel-based energy, contributing to pollution of air, water and soil. Moreover, most home textiles are not designed for recyclability and a significant portion ends up in landfills after use [3]. Despite

emerging ideas, such as extending product life cycles through multifunctional design, the industry continues to face major sustainability challenges.

The home textile sector is also one of the largest industrial consumers of energy, with a heavy dependence on coal and natural gas to power machinery and maintain optimal indoor conditions such as lighting, temperature and humidity in labour-intensive production environments. For countries like China, India, and Indonesia, where the energy mix is still largely coal-based, the environmental burden from textile manufacturing is especially severe [4]. Notably, China the world's largest producer of textiles, has estimated the environmental cost of textile production to be no less than nine trillion euros [5].

According to Sing S. & Ru J. promoting access to clean, affordable energy is crucial [6]. Solar energy stands out as a practical and accessible option for home textile SMEs, especially when supported by government incentives. In North Macedonia, although solar panel installations in small enterprises are relatively new, the interest is growing due to rising energy prices and environmental pressures. This study focuses on a medium-sized home textile production company that adopted solar energy and maintained detailed energy consumption records, allowing for a comprehensive evaluation of the benefits and limitations of this approach.

EXPERIMENTAL

A case study approach was used to analyze the energy transition of a factory specializing in home textile products located in Prilep, North Macedonia. The company operates two automated quilt production lines and one pillow production automate. Nominal energy consumption for quilting machines is 60 kWh each, while the pillow automate consumes 25 kWh.

Data were collected from April 2024 onward and include:

- Document analysis: Reviewing monthly energy consumption and solar production data per production line.
- Interview: Conducted with management and energy personnel to assess experiences with solar energy integration.
- Field observations: On-site visits enabled direct observation of solar panel usage and operational practices.

The factory was selected for its detailed tracking of energy usage and its recent implementation of photovoltaic systems. The quantitative data included energy produced and consumed monthly, while the qualitative analysis focused on stakeholder perceptions and operational adjustments linked to solar energy use.

RESULTS AND DISCUSSIONS

The production facility includes two quilt manufacturing lines equipped with automatic lockstitch multi-needle quilting machines, each with a nominal energy consumption of 60 kWh, along with an automated pillow production system consuming 25 kWh. Unlike apparel manufacturing, home textile production requires substantial energy and maintains a consistent monthly demand, as illustrated in Table 1. Although monthly productivity fluctuates based on order sizes, the average production capacity is 58,648 pieces per month. Energy consumption varies according to the number of units produced. The factory monitors the energy usage of each machine individually, which is determined by the total monthly operating hours of each machine. The total energy needs are 704 MWh per year.

Table 1 *Total productivity and energy consumption, 2024*

Month	Production (pcs)	Energy consumption (kWh)
January	50233	262599
February	56184	381252
March	61078	457930
April	38885	242625
May	60274	524086
June	62695	375433
July	55970	365341
August	51496	348164
September	62838	357422
October	68553	443030
November	73145	567171
December	62424	378907
Total	703775	4703960
Average	58648	391997

A comparison of produced and consumed solar energy of home textiles manufacturers is given on the graph of figure 1. The company introduced solar panels in two stages, part of the capacity was installed in August, 2023, and the system was upgraded in January 2024. The implementation of solar energy in textile factories is significantly influenced by the local continental climate. According to the national Hydrometerological Service in 2023 the average

summer temperatures were reaching 34° C and winter temperatures dropping to around 7° C. This temperature variation affects solar energy production, as the highest energy output occurs during the sunniest summer months, while winter months see a marked decrease in production. Therefore, energy production reaches its peak in July and August, as can be seen on Figure 1.The company is considering expanding its photovoltaic capacity to become fully energy self-sufficient year-round, even if this leads to summer overproduction.

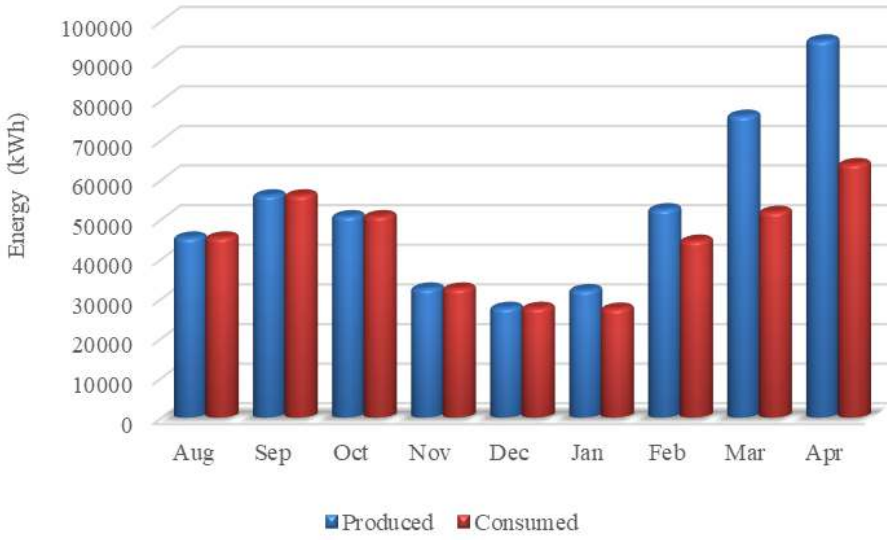

Figure 1 *Comparison of produced and consumed solar energy of home textiles manufacturer*

The qualitative data obtained from interviews with key stakeholders in the home textile factory revealed a number of benefits arising from the application of sollar energy. First of all, government incentives were pivotal in facilitating the installation of solar panels.The factory benefited from a 15% subsidy on solar equipment and gained additional revenue by selling surplus energy to the national grid.

Significant cost reduction was identifed as a key factor, as electricity expenses were reduced by up to 70%, especially in summer months when solar energy production peaks. The economic benefit from instalation of photovoltaic cells gave an impetus to increase the installed capacity and strive towards energy independence. In addition to financial advantages, factories recognized the acquisition of sustainability certificates as a significant advantage of implementing solar energy. Solar energy use contributed to obtaining eco-

labels, increasingly demanded by international buyers. These certificates, which are becoming more sought after by buyers, are shaped by regulations like the EU's Renewable Energy Directive (2009/28/EC), aimed at encouraging renewable energy use and helping companies showcase their dedication to sustainability.

However, challenges were also identified, namely seasonal variations in production, energy monitoring gaps and storage limitations. Regarding seasonal variations in energy production solar output was highest in July and August, but dropped significantly in winter. Despite the installation of solar panels in August, energy needs were not fully met during colder months. Although production line energy consumption was carefully measured, energy monitoring gaps occuras ancillary energy use (lighting, climate control) was not tracked, limiting optimization opportunities. Finally, the company lacked battery storage due to cost and space constraints, making it reliant on grid power during low-sunlight periods.

CONCLUSIONS

This case study affirms that solar energy is a cost-effective and sustainable solution for production facilities in the home textile industry. Financial savings, environmental compliance and access to premium markets through certification are key drivers of adoption. Nonetheless, challenges remain-particularly in energy storage and comprehensive energy monitoring. Policy support is essential, particularly in facilitating access to storage technology and incentivizing full-spectrum energy tracking. By addressing these gaps, home textile factories can achieve long-term sustainability and energy independence through solar power implementation.

REFERENCES

[1] N. Pensupa, S.Y Leu, Y. Hu, C. Du, H. Liu, H. Jing, H. Wang, C. S. K. Lin, Recent Trends in Sustainable Textile Waste Recycling Methods: Current Situation and Future Prospects, *Topics in Current Chemistry* **375** (2017) 189-228. https://doi.org/10.1007/s41061-017-0165-0.

[2] B. Ütebay, P. Çelik, A. Çay, *Waste in Textile and Leather Sectors*, Textile Wastes: Status and Perspectives, IntechOpen [E-book], Rijeka, Croatia, 2020. https://doi.org/10.5772/intechopen.90014

[3] M. Avadanei, S. Olaru, I. Ionescu, A. Florea, A. Curteza, E. Loghin, I. Dulgheriu, C. D. Radu, Clothing development process towards a circular model, *Industria Textila* **72** (2021) 89-96. https://doi.10.35530/IT.072.01.1563B

[4] B. Huang, J. Zhao, Y. Geng, Y. Tian, P. Jiang, Energy-related GHG emissions of the textile industry in China, *Resource, Conservation and Recycling* **119** (2017) 69-77.

https://doi.org/10.1016/j.resconrec.2016.06.013
[5] J. Chu, L. Sun, F. Chen, X. Ji, Z. Tian, L. Wang, Assessing the environmental profit and loss of the textile industry: A case study in China, *Industria Textila* **72** (2021) 55-61. https://10.35530/IT.072.01.1787
[6] S. Sanjeet, J. Ru, Accessibility, affordability and efficiency of clean energy: a review and research agenda, *Environmental Science and Pollution Research* **29** (2022), 18333-18347. https://doi.org/10.1007/s11356-022-18565-9

PHOTOCATALYTIC ILLITE CLAY/TiO_2 COMPOSITE POWDER SYNTHESIZED BY MECHANICAL ACTIVATION

Vojo Jovanov[1], Snežana Vučetić [2], Biljana Angjusheva[1], Jonjaua Ranogajec[2], Emilija Fidanchevski[1]

[1] - *Faculty of Technology and Metallurgy, Ss. Cyril and Methodius University in Skopje, North Macedonia*

[2]- *University of Novi Sad, Faculty of Technology, bul. Cara Lazara 1, 21000 Novi Sad, Serbia*

vojo@tmf.ukim.edu.mk

Abstract: *Recent advancements in photocatalytic technologies, driven by environmental concerns related to industrialization, highlight the potential of combining illite clay and TiO2, which can lead to improved photocatalytic activity and operational efficiency, filling existing gaps in the sustainable use of titanium-based photocatalysts. The present study investigates illite clay/TiO_2 composites synthesized via mechanical activation using an attritor mill. Two TiO_2 contents were examined - 3 wt.% and 10 wt.% - introduced into the illite clay matrix. A commercial TiO_2 suspension, comprising 80 wt.% anatase and 20 wt.% rutile was used for impregnation. The composite containing 10 wt.% TiO_2 demonstrated favorable properties in terms of grain size, morphology, and photocatalytic performance. Photocatalytic activity was evaluated by monitoring the degradation efficiency of Rhodamine B under UV/VIS irradiation. The results reveal a significant influence of both the impregnation parameters and TiO_2 content on the photocatalytic behavior of the illite clay/TiO_2 composites.*

Keywords: nano-TiO_2, illite clay, composites, mechanical activation, photocatalysis

INTRODUCTION

Consequently, natural and synthetic clay minerals possess unique physicochemical properties, such as large surface area, high adsorption capacity, swelling, and ion exchange, which make them suitable matrices for TiO_2 nanosized particle fixing [i,ii]. In particular, clay minerals are non-corrosive, low-cost, and can be separated easily in the reaction system for reuse. In recent years, clay minerals have been widely used as photocatalyst supports, and their special layer structures, large specific surface area, and high adsorption capacity are promising for the enrichment of organic pollutants and the load of TiO_2 [iii,iv].

The impregnation of TiO_2, by mechanical activation, into the interlayer of the clay is one of the most promising methods for synthesizing TiO_2 pillared clay composites with enhanced photocatalytic activity. Mechanical activation changes the overall reactivity of the composites, their chemical nature, and structure as

well as catalytically active sites. During mechanical activation, the composite catalyst accumulates excess potential energy, elastic and plastic deformations as well as a great variety of defects, which usually leads to an increase in its reactivity and formation of catalytic systems [v].

This study aimed to fabricate and characterize an illite clay/TiO_2 photocatalytically active composite with pottencial to be used for environmental protection of building materials. For that purpose, TiO_2 in contents of 3 and 10 wt.%, respectively, was impregnated into the structure of illite clay by mechanical activation in an attritor mill. The obtained composites were characterized in terms of physical, mineralogical, and morphological aspects. The decomposition of Rhodamine B was chosen as the test reaction for the investigation of photocatalytic activity.

EXPERIMENTAL

Materials

The natural illite clay from the eastern part of the Republic of Macedonia was used in this study. The Illite clay was characterized in terms of chemical and mineralogical composition, as well as particle size distribution.

The chemical composition determined by X-ray fluorescence spectroscopy (S8 TIGER WDXRF spectrometer, Brucer, Germany), presented in Table 1, shows the typical oxides: SiO_2, Al_2O_3 and Fe_2O_3 are the most represented in the clay, while CaO, MgO, Na_2O and K_2O are present in minor content.

Table 1 *Chemical composition of illite clay*

Oxides	SiO_2	Al_2O_3	Fe_2O_3	CaO	MgO	Na_2O	K_2O	LOI	Total
Content, wt.%	58.79	13.6	9.28	3.59	1.72	3.83	2.51	5.79	99.11

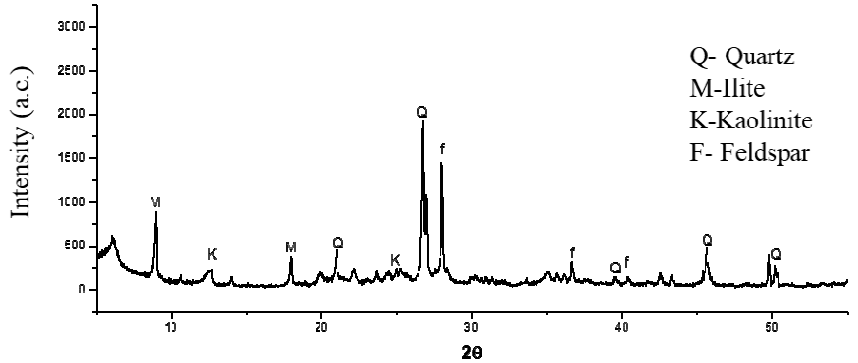

Figure 1 XRD data of the clay

The mineralogical composition of the clay (Figure 1) confirmed the illite type of clay, containing also quartz, feldspar, and kaolinite, as well.

The particle size distribution of the pre-treated illite clay was measured using a Malvern Mastersizer 2000. As shown in Figure 2, the clay exhibits a monomodal particle size distribution ranging from 1.8 to 20 µm, with the highest particle abundance observed at approximately 2 µm.

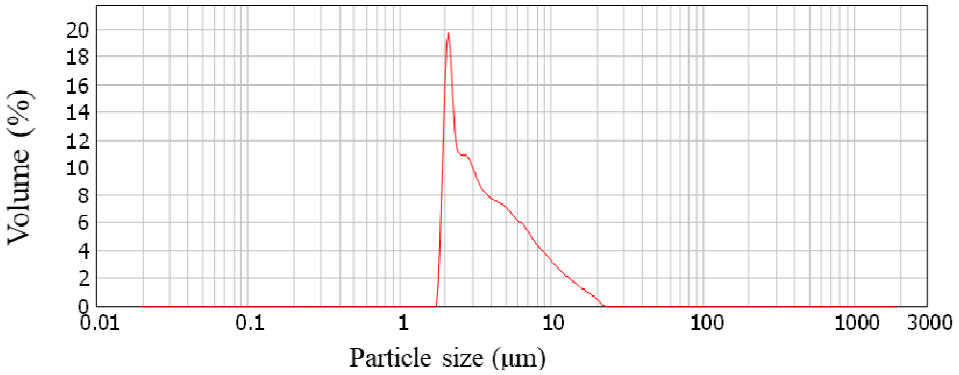

Figure 2 *Particle size distribution of the clay*

A commercial TiO_2 suspension from Degussa (Germany) was used as the photocatalytic precursor. The suspension consisted of 80 wt.% anatase and 20 wt.% rutile, with a grain size less than 100 nm. The dry matter content was 30.0 ± 1.0 wt.%, and the pH was 7.

Illite clay/TiO_2 composite preparation

Illite clay/TiO_2 composites were prepared using an attritor mill under the following conditions: 90 minutes of milling at a speed of 1500 rpm, with a material-to-ball ratio of 1:5, and at a pH of 9–9.5. After impregnation by milling, the powders were dried at 105 °C for 24 h. The composite powders containing 3 wt.% and 10 wt.% TiO_2 were assigned as H1 and H2, respectively, while the reference sample consisting solely of mechanically activated illite clay was labeled as H0.

Characterization methods

The particle size distribution of the reference H0 and illite clay/TiO_2 composite powders was determined by Malvern Instruments zeta-nanoseries, NanoZS. X-ray diffraction (XRD) patterns of the samples were recorded under CuKα irradiation (λ=1.5418Å) using Phillips PW 1710 diffractometer. Photocatalitic activity of powders after milling in attritor mill was determined in line to the procedure described by Jovanov et al. [4] and the values were measured using

UV/VIS spectroscopy (EVOLUTION 600 spectrophotometer). The morphology of the composite particles was observed by Scanning Electron Microscopy on SEM JOEL JSM-6460LV. Elemental composition of the samples was determined using Energy Dispersive Spectroscopy analysis (EDS).

RESULTS AND DISCUSSIONS

It is well known that the photo-induced capacity of a photo-catalyst can be strongly influenced by its physicochemical properties, which include particle size distribution, phase compositions and morphology. Therefore, in this section, primary emphasis was given to these physicochemical characteristics of the prepared samples.

The particle size distribution of the illite clay (H0) and the composite powders, H1 and H2, is presented in Figure 4.

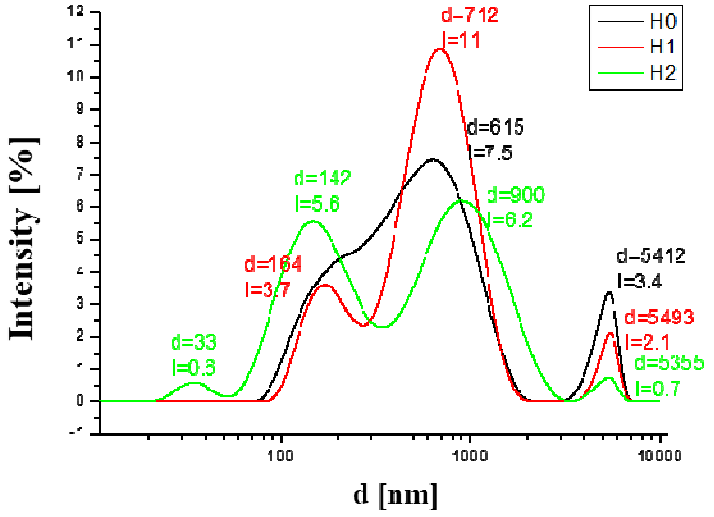

Figure 3 *The particle size distribution of the illite clay (H0) and the composite powders, H1 and H2*

The data obtained from Figure 3 suggests that there is a relationship between the TiO_2 content in the illite clay/TiO_2 composite and the changes in the particle size distribution of the composite. Namely, the increasing amount of impregnated TiO_2 reduces the presence of large microparticles and increases the amount of finer nanoparticles. This phenomenon of an increased distribution of fine nanoparticles has a positive effect on the stability, photocatalytic activity, and other characteristics of this composite powder.

The phase composition of the illite clay, H0, as well as the composite powders, H1 and H2, is illustrated in Figure 4. Mainly the dominant mineral phases are quartz, feldspar, illite, kaolinite and Na_2CO_3, which is added during impregnation with mechanical activation in order to maintain the required pH value.

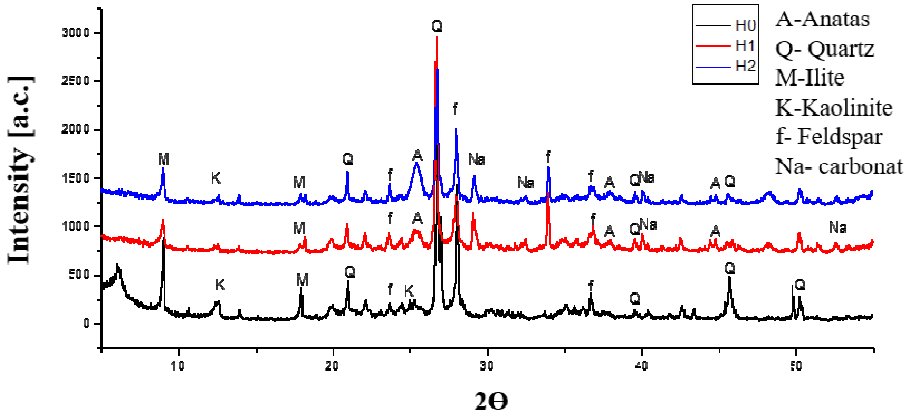

Figure 4 *XRD patterns of the illite clay, H0, and the composite powders, H1 and H2*

The XRD spectra in Figure 4 also indicate there is a progressive decrease in intensity in Ilite and kaolinite specific reflections after TiO_2 impregnation at both varied concentrations. The TiO_2 consists of anatase structure alone in both composite samples, H1 and H2, identified by 25.3° (2Θ) for anatase (101), while no significant appearance of 27.5° (2Θ) for rutile (101) phase is evident. Nishimoto et al. [vi] reported that the anatase TiO_2 performed a more prominent photocatalytic activity than rutile TiO_2. Regarding the change in the amount of impregnated TiO_2, it can be observed that the increase in the amount contributes to a change in the (101) anatase diffraction peak, which signals an increase in crystal size.

The photocatalytic activity of the reference illite clay and illite clay/TiO_2 composite powders (H0, H1, and H2), evaluated by monitoring the photocatalytic degradation of RhB under 210 minutes of UV/VIS irradiation, is presented in Figure 5. The results show that H2 composite powder has the highest photocatalytic activity value (42%), and the photocatalytic activity of pure clay used as a carrier of TiO_2 is negligible. Obviously, the higher photodegradation activity achieved with the H2 composite than with the H1 composite can be ascribed to the higher amount of TO_2 in the nanosized anatase form, as well as to the general finer particle distribution in that composite, which also means a larger specific surface area for RhB absorption.

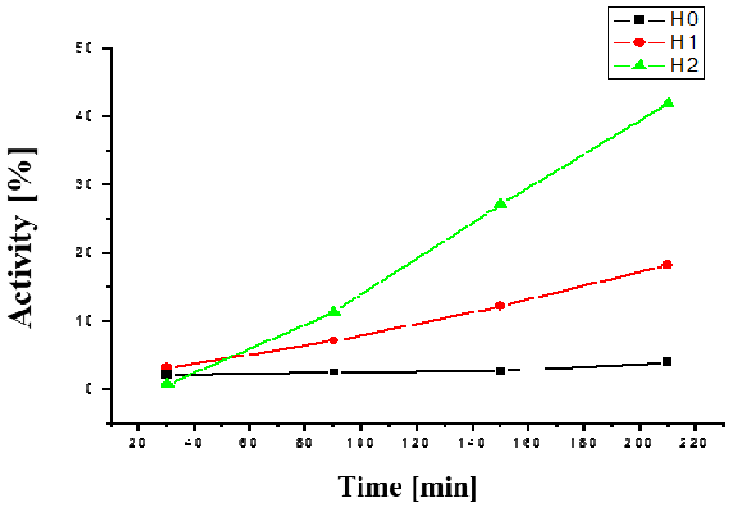

Figure 5 *The photocatalytic activity of the reference illite clay and illite clay/TiO_2 composite powders (H0, H1, and H2)*

Changes in the surface morphology of the H2 composite (illite clay impregnated with 10 wt.% TiO_2) were compared with the reference sample, i.e., mechanically activated illite clay (H0), using SEM imaging, as shown in Figure 6.

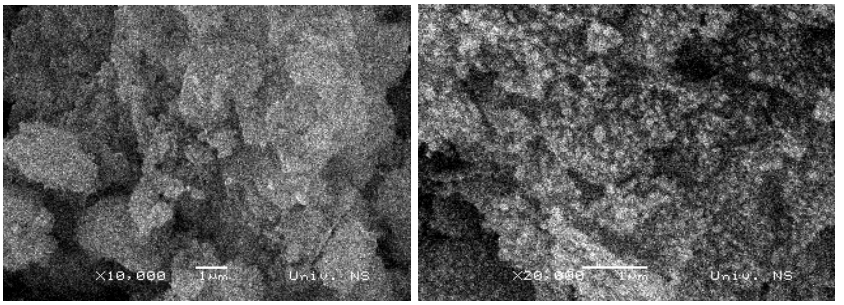

a. b.

Figure 6 *SEM microphotographs of the morphology of the activated illite clay (a- x 10 000, bar 1μm) and H2 composite (b- x 10 000, bar 1μm)*

Figures 6a show the typical morphology of the structure of illite clay material, where the presence of agglomerates with dimensions from 0.5 to 3 μm is evident. While the SEM images presented in Figures 6b show the presence of white TiO_2 nanoparticles (below 0.2μm) homogeneously distributed on the surface of the clay substrate.

The performed EDS analysis of H2 composite (Figure 7), Spectrum 1, Table 2,

confirmed by the presence of expected elements such as aluminum-Al, silicon-Si, sodium-Na, potassium-K, magnesium-Mg, oxygen-O, and iron-Fe. Also, the EDS results confirm the presence of Ti on the composite surface, resulting from mechanical impregnation of TiO_2.

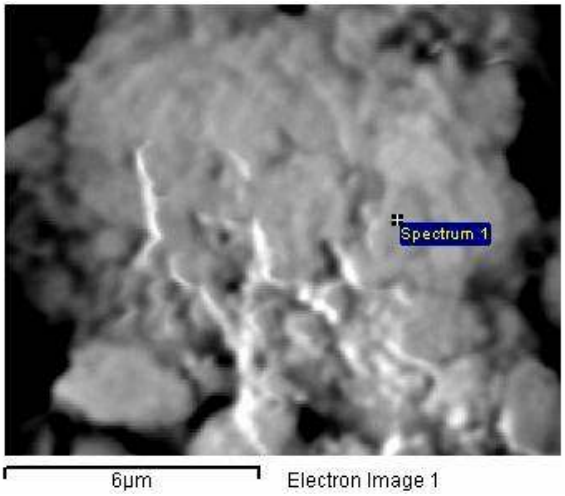

Figure 7 SEM micrograph of the EDS spectra in the sample H2

Table 2 Results of the EDS analysis in Spectrum 1 of the sample H2

O	Na	Mg	Al	Si	K	Ti	Mn	Fe	Total
49.64	6.39	1.98	6.35	16.33	0.98	13.90	0.34	4.09	100

CONCLUSIONS

This study demonstrates the successful impregnation of nano TiO_2 onto illite clay via mechanical activation using an attritor mill. The resulting illite clay/TiO_2 composites exhibited notable characteristics in terms of particle size distribution, surface morphology, and photocatalytic efficiency. The enhanced photocatalytic activity observed in the composite containing 10 wt.% nano TiO_2 is attributed to the homogeneous distribution of TiO_2 nanocrystals on the illite clay surface, finer particle size distribution, and improved crystallinity, achieved through mechanical activation during impregnation.

Overall, the results indicate that natural illite clay is a promising support material for nano TiO_2-based photocatalysts. Its layered structure, large specific surface

area, and high adsorption capacity make it well-suited for the effective loading of photocatalytically active TiO_2

REFERENCES

1. M. Ozawa, H. Matui, Y. Setsuhara, Microstructure and surface/interface characterization of TiO2-pillared mica for photocatalytic acetaldehyde degradation, *Hybrid Advances*, **10** (2025)100435.
https://doi.org/10.1016/j.hybadv.2025.100435

2. V. Jovanov, O. Rudic, J. Ranogajec, E. Fidanchevska, Synthesis of nanocompositecoating based on TiO2/ ZnAl layer double hydroxides, *Materiales de Construcción* **67** (2017) 112–120. https://doi.org/10.3989/mc.2017.07215

1. Y. Cardona, S.A. Korili, A. Gil, Use of clays and pillared clays in the catalytic photodegradation of organic compounds in aqueous solutions. *Catalysis Reviews* **66**(5), (2023) 2063–2110. https://doi.org/10.1080/01614940.2023.2178736

B. Szczepanik, Photocatalytic degradation of organic contaminants over clay-TiO2 nanocomposites: A review. *Applied Clay Science* **141** (2017) 227-239.
https://doi.org/10.1016/j.clay.2017.02.029

1. V. Jovanova, V. Zečević, T. Vulić, J. Ranogajec, E. Fidanchevska, Preparation and characterization of protective self-cleaning TiO2/kaolin composite coating, *Materiales de Construcción* **68** (2018)163. https://doi.org/10.3989/mc.2018.08517

1. Y. Qi, S. Zhao, Y. Shen, X. Jiang, H. Lv, C. Han, W. Liu, Q. Zhao, A Critical Review of Clay Mineral-Based Photocatalysts for Wastewater Treatment. *Catalysts* **14**(9), (2024), 575. https://doi.org/10.3390/catal14090575

1. S.-I. Nishimoto, B. Ohtani, H. Kajiwara, T. Kagiya, Correlation of the crystal structure of titanium dioxide prepared from titanium tetra-2-propoxide with the photocatalytic activity for redox reactions in aqueous propan-2-ol and silver salt solutions, *J. Chem. Soc. Faraday Trans. I* **81** (1985) 61-68. https://doi.org/10.1039/f19858100061

INVESTIGATION OF THE THERMAL BEHAVIOR OF COAL FLY ASH BY HOT STAGE MICROSCOPY

Biljana Angjusheva[1,*], Vojo Jovanov[1]

Faculty of Technology and Metallurgy, Ss. Cyril and Methodius University in Skopje, North Macedonia

biljana@tmf.ukim.edu.mk

Abstract: *Coal fly ash, a byproduct of coal combustion in thermal power plants, offers valuable opportunities for reuse in construction and material engineering. This study explores the thermal behavior of fly ash samples collected from different sections of the REK Bitola Power Plant. Thermal characteristics of the fly ashes obtained from hot stage microscopy revealed distinct transformation stages, including sintering, softening, and melting intervals. XRF analysis was employed for determination of the chemical composition, while sieve analysis was used for investigation of granulometry of the materials. The physical and chemical characteristics of the ashes particularly their grain size and content of silica, alumina, calcium oxide, and iron oxide play a crucial role in determining their response to heat. These findings help guide more effective use of fly ash in environmentally friendly applications, supporting waste reduction and promoting sustainable practices.*

Keywords: coal fly ash, heating microscopy, thermal properties, circular economy

INTRODUCTION

Coal fly ash, a fine particulate residue generated during coal combustion in thermal power plants, has emerged as a valuable secondary resource due to its pozzolanic activity and potential for environmental sustainability. Its incorporation into construction materials [1-3], ceramics [4-6], and thermal insulation systems [7-9] support the dual goals of industrial waste reduction and material performance enhancement. Among these applications, the use of fly ash in ceramic production is particularly promising, as its mineralogical and chemical characteristics can be leveraged to influence sintering behavior, microstructure development, and final product properties [10].

Hot-stage microscopy, a technique developed in the 1950s by Welch, enables direct visual observation of the morphological changes a material undergoes during heating [11]. Through digital or photographic recording, this method allows for the determination of characteristic temperatures associated with sintering, softening, melting, and flow—phenomena fundamental to ceramic processing. In ceramic and glass ceramics manufacturing, hot-stage microscopy

is also used to define sintering curves and to assess material viscosity and surface tension under high temperatures. Modern systems provide automated data acquisition and image analysis, offering high accuracy and reproducibility.

By applying image-based analysis of sample shape changes, the study further explores sintering kinetics and correlations between chemical composition and granulometric properties, which are critical for optimizing formulations, particularly for products like ceramics and glass-ceramics.

A comprehensive understanding of these thermal behaviors is essential for optimizing the use of coal fly ash from REK Bitola Power Plant in ceramic applications, thereby advancing sustainable manufacturing practices and contributing to the circular economy.

EXPERIMENTAL

Fly ash originating from lignite combustion at the REK Bitola thermal power plant (Republic of North Macedonia) was used as the raw material to identify the thermal behaviour of the material. Five samples were analyzed: four obtained from different zones of the electrostatic precipitator, coded FA1, FA2, FA3, and FA4, and one composite sample from the collection zone, coded CZ.

The chemical composition of the samples was determined using X-ray fluorescence (XRF) spectroscopy (ARL 990XP). Loss on ignition (LOI) was quantified by heating the samples at 900 °C for 2 hours. Particle size distribution was determined by dry sieve analysis (Retsch AS200)

Thermal properties of the fly ash samples (3x3 mm, prepared pressureless) were examined with a hot-stage microscope (Leitz Wetzlar) under air atmosphere. The measurements were carried out from room temperature up to 1400 °C, at a constant heating rate of 10 °C/min, to identify key thermal transformation points such as sintering, softening, and melting behavior.

RESULTS AND DISCUSSIONS

The data for particle size analysis presented in Figure 1 indicate that the fineness of the fly ash increases from CZ to FA4. This is reflected in both the increased proportion of fine particles and the reduced proportion of coarse and medium fractions. The fine particle size of FA4 may enhance its reactivity and sintering behavior, making it particularly suitable for applications in ceramics or pozzolanic materials where high surface area and homogeneity are advantageous.

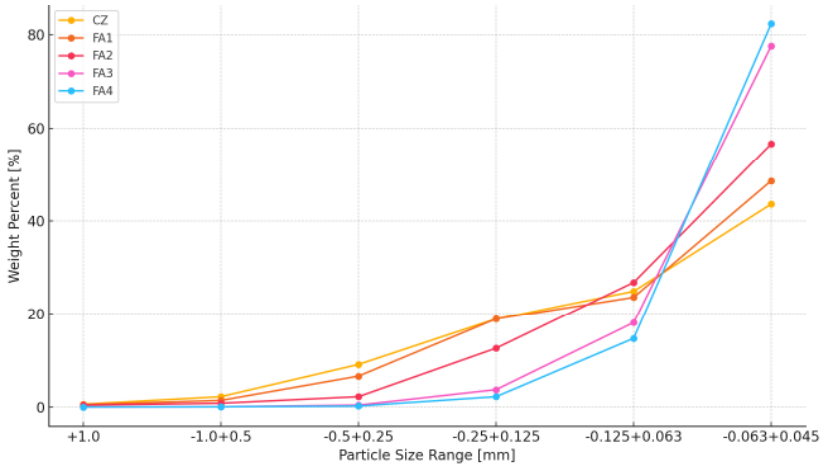

Figure 1 *Particle size distribution of fly ash samples*

Results from the investigation of the chemical composition of the fly ashes, presented in Table 2, reveal that the major chemical components in all fly ash samples are SiO_2, and Al_2O_3. These oxides are crucial for the formation of phases, which contribute to mechanical strength, thermal stability, and chemical durability in sintered ceramics. Notably, the CaO content exceeds 10% in all samples, indicating that these materials can be classified as Class C fly ashes [12]. In sintering CaO acts as a fluxing agent, lowering the sintering temperature and promoting liquid phase formation. Additionally, free CaO was not detected in the analyzed samples. As stated by Kiattikomol et al. [13], pozzolanic activity is primarily influenced by calcium present in the glass phase, rather than by free or crystalline calcium oxide. Present consistently around 7.68–7.91 wt.%, Fe_2O_3 can serve as both a flux and a colorant in fired products. Also, iron oxides can contribute to thermal conductivity and magnetic properties, which may be advantageous or disadvantageous depending on the ceramic application. SO_3 content increases from CZ (1.44 wt.%) to FA4 (3.52 wt.%), possibly indicating the presence of calcium sulphates, which may lead to gas evolution during sintering.

Table 1 *Chemical Composition of the investigated fly ash samples*

Oxide	CZ [wt.%]	FA1 [wt.%]	FA2 [wt.%]	FA3 [wt.%]	FA4 [wt.%]
SiO_2	50.33	53.31	49.20	48.81	49.51
Al_2O_3	18.59	19.92	18.78	17.81	17.62
Fe_2O_3	7.71	7.68	7.72	7.80	7.91
CaO	13.76	10.74	13.23	14.31	13.77

MgO	3.05	2.70	3.04	3.39	3.36
Na_2O	1.07	0.84	0.78	0.70	0.69
K_2O	1.41	1.51	1.45	1.38	1.46
SO_3	1.44	1.03	1.78	2.76	3.52
LOI	2.60	2.20	2.03	1.78	1.57
Σ	**99.96**	**99.93**	**98.01**	**98.74**	**99.41**

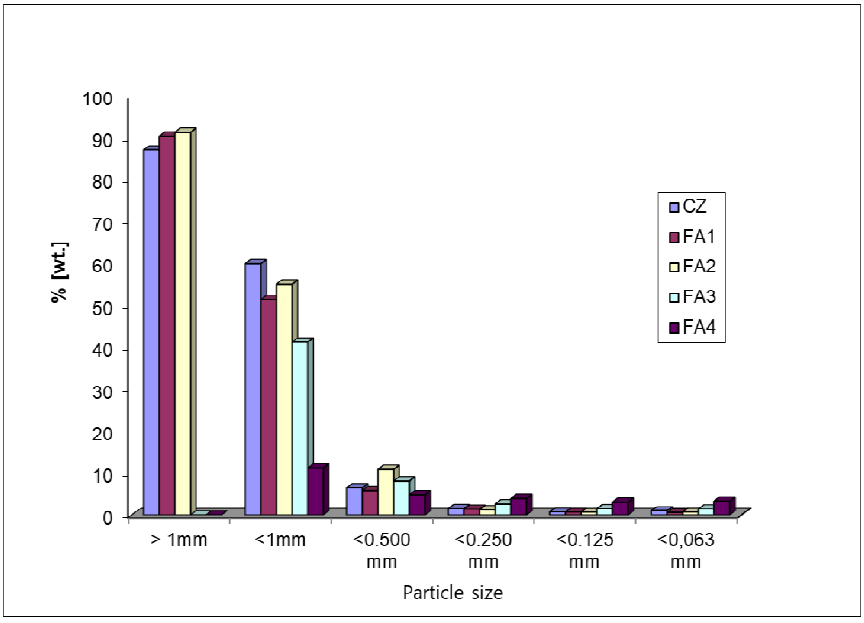

Figure 2 *LOI of different particle size distribution*

The Loss on Ignition (LOI) values show a slight decreasing trend from CZ (2.60 wt.%) to FA4 (1.57 wt.%). LOI values are indicative of unburnt coal particles, which are more present in the coarser fraction of the samples, Figure 2. Also, as described in literature [14], LOI can result from the thermal decomposition of some ash components.

The photographs of the hot-stage microscopy of the five investigated fly ash samples are presented in Figures 3-7, while characteristic thermal transformation stages are presented at Table 2.

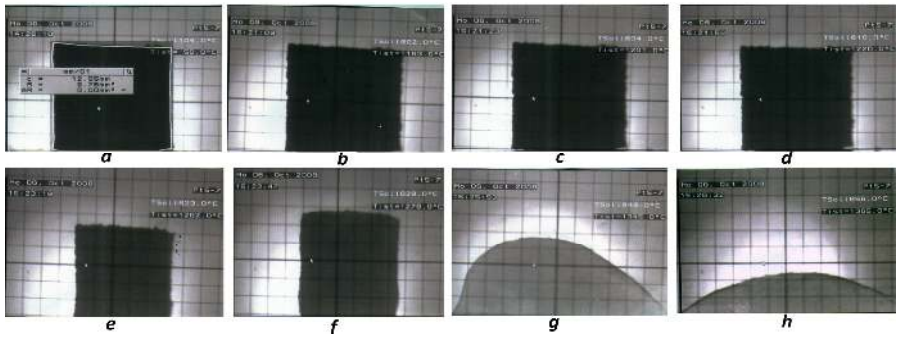

Figure 3 *Photographs from the hot-stage microscope of fly ash CZ,* *a-50°C, b-1190 °C, c-1200 °C, d-1220 °C, e-1260 °C, f-1280 °C, g-1345 °C, h-1365 °C*

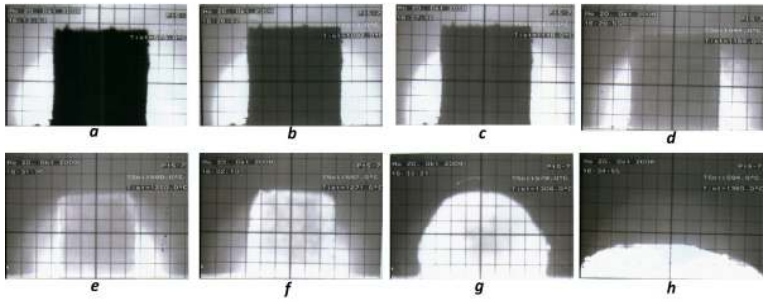

Figure 4 *Photographs from the heating microscope of fly ash FA1, a-60°C, b-1090 °C, c-1100 °C, d-1190 °C, e-1250 °C, f-1270 °C, g-1300 °C, h-1360 °C*

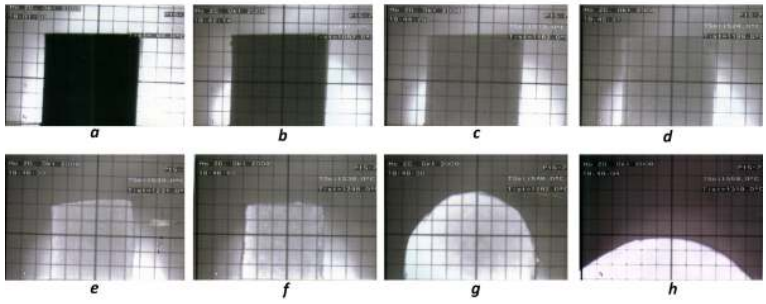

Figure 5 *Photographs from the heating microscope of fly ash FA2, a-90°C, b-1080 °C, c-1160 °C, d-1200 °C, e-1230 °C, f-1250 °C, g-1280 °C, h-1300 °C.*

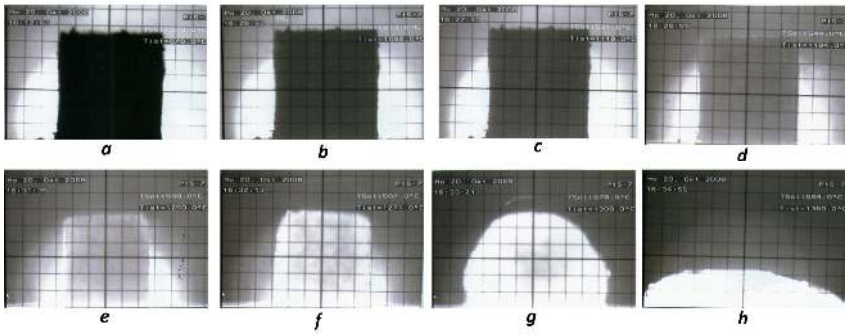

Figure 6 *Photographs from the heating microscope of fly ash FA3, a-60°C, b-1010 °C, c-1140 °C, d-1180 °C, e-1210 °C, f-1220 °C, g-1270 °C, h-1280 °C.*

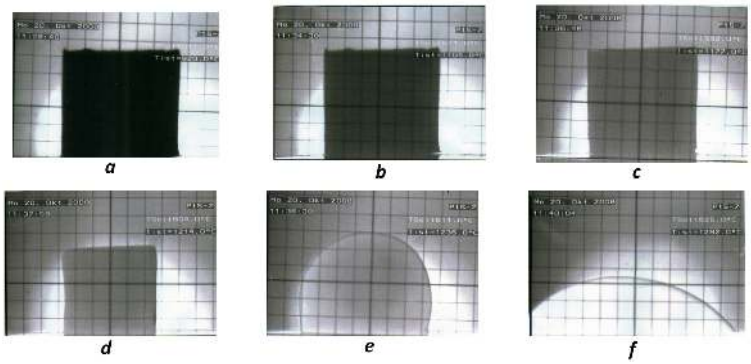

Figure 7 *Photographs from the heating microscope of fly ash FA4, a-900°C, b-1100 °C, c-1170 °C, d-1210 °C, e-1230 °C, f-1280 °C*

Table 2 *Characteristic temperatures of thermal transformation of fly ash samples*

Fly ash	Shrinkage temperature °C	Softening temperature °C	Melting temperature °C	Sintering interval °C
CZ	1200±10	1260±10	1310±10	1200-1260±10
FA1	1194±10	1250±10	1320±10	1194-1250±10
FA2	1200±10	1246±10	1310±10	1200-1246±10
FA3	1180±10	1220±10	1270±10	1180-1220±10
FA4	1110±10	1200±10	1240±10	1110-1200±10

According to the data presented in Table 2, it is evident that all types of fly ashes have a narrow region of sintering (1190-1250±10 °C), except for FA4 (1110-1220±10 °C). The melting temperature for CZ, FA1 and FA2 is 1310±10 °C, while for the FA3 and FA4 is 1270 °C, and 1240±10 °C, respectively. Higher melting temperatures of CZ, FA1, and FA2 are related to the slightly higher content of SiO_2 and Al_2O_3 compared to the samples FA3 and FA4, as well as the proportion of coarse, medium and fine fractions present in the investigated fly ashes.

CONCLUSIONS

The investigation of the thermal behavior of coal fly ash from the REK Bitola Power Plant has provided valuable insights into its potential applications in sustainable construction and ceramics. Heating microscopy analysis revealed distinct thermal transformation stages, including the sintering region (1110 - 1200°C), the softening region (1200 - 1260°C), and the melting temperature range (1240 - 1320°C). The chemical composition of the fly ash, particularly the presence of SiO_2 (48.81 - 50.33 wt.%) and Al_2O_3 (17.62 - 18.59 wt.%), significantly influences its thermal properties, including fusion temperature and sintering characteristics, while CaO (10.74 - 13.76 wt.%) lowering the melting point. By understanding the thermal properties and behavior of coal fly ash, this research contributes to the advancement of sustainable manufacturing practices and supports the circular economy.

REFERENCES

1. S. Kramar, L. Žibret, E. Fidanchevska , V. Jovanov , B. Angjusheva , V. Ducman, Use of fly ash and phosphogypsum for the synthesis of belite-sulfoaluminate clinker, *Materiales de Construcción* **69** (333) (2019), e176. https://doi.org/10.3989/mc.2019.11617
2. D. Kumar Nayak, P.P. Abhilash, R. Singh, R. Kumar, V. Kumar, Fly ash for sustainable construction: A review of fly ash concrete and its beneficial use case studies, *Cleaner Materials*, **6** (2022), 100143. https://doi.org/10.1016/j.clema.2022.100143
3. K. Akmalaiuly, N. Berdikul, I. Pundienė, J. Pranckevičienė, The Effect of Mechanical Activation of Fly Ash on Cement-Based Materials Hydration and Hardened State Properties, *Materials* **16** (8) (2023) 2959; https://doi.org/10.3390/ma16082959
4. V. Jovanov, S. Vučetić, S. Markov, B. Angjusheva, E. Fidancevska, J. Ranogajec, Resistance to frost action and microbiological corrosion of novel ceramics composites, *Chemical Industry & Chemical Engineering Quaterly* **29** (2) (2023) 99-109. https://doi.org/10.2298/CICEQ210904016J
5. B. Angjusheva, E. Fidancevski, V. Jovanov, Conversion of coal fly ash into glass-ceramics by controlled thermal treatment, *Macedonian Journal of Chemistry and Chemical Engineering* **40** (2) (2021) 307-319. https://doi.org/10.20450/mjcce.2021.2429
6. B. Angjusheva, E.Fidanchevska, V.Jovanov, Production ans characterization of porous ceramics from coal fly ash and clay, *Quality of life* **7**(3-4) (2016) 59-65.

https://doi.org/10.7251/QOL1603053A
7. A. Saygılı, G. Baykal, A new method for improving the thermal insulation properties of fly ash, *Energy and Buildings* **43** (11) (2011) 3236-3242. https://doi.org/10.1016/j.enbuild.2011.08.024
8. Y. Ji, Q. Ren, X. Li, P.Zhao, V. Vandeginste, On Thermal Insulation Properties of Various Foaming Materials Modified Fly Ash Based Geopolymers, *Polymers* **15**(15) (2023) 3254. https://doi.org/10.3390/polym15153254
9. X.D. Zhang, Y. Han, Thermal Insulation Properties of Fly Ash and Waste Polystyrene Mixed Block Building Materials, *Chemical Engineering Transactions* **55** (2016) 253-258. https://doi.org/10.3303/CET1655043
10. B. Angjusheva, E. Fidancevska, V. Jovanov, Production of Ceramics from Fly Ash, *Chemical Industry & Chemical Engineering Quarterly* **18** (2) (2012) 245-254. https://doi.org/10.2298/CICEQ110607001A
11. W. Panna, P. Wyszomirski, P. Kohut, Application of hot-stage microscopy to evaluating sample morphology changes on heating, *Journal of Thermal Analysis and Calorimetry* **125** (2016) 1053–1059. https://doi.org/10.1007/s10973-016-5323-z
12. Annual Book of ASTM Standards, B618-03, pp.459-467
13. K. Kiattikomol, C. Jataurpitakkul, S. Songpiriyakij, S. Chutubtim, A study of ground coarse fly ashes with different finenesses from various sources as pozzolanic material, *Cement and Concrete Research* **23** (2001) 335-343, https://doi.org/10.1016/S0958-9465(01)00016-6
14. G. Itskos, S. Itskos, N. Koukouzas, Size fraction characterization of highly-calcareous fly ash, *Fuel Processing Technology*, **91** (2010) 1558-1563. https://doi.org/10.1016/j.fuproc.2010.06.002

STUDY OF POLLUTANT EMISSIONS FROM AN ELECTRIC ARC FURNACE IN STEEL PRODUCTION FROM SCRAP

Aleksandar T. Dimitrov, Sara Petrova, Kiril Stoimcev, Beti Andonović

Faculty of Technology and Metallurgy, University SS Cyril and Methodius, Skopje, North Maceonia

aco@tmf.ukim.edu.mk

Abstract: *The International Energy Agency (IEA) has found that energy consumption in most industrial processes is 50% higher than the theoretical minimum, though significant improvements are still possible. High-energy industrial facilities contribute to one-third of global greenhouse gas emissions, with 70% coming from fossil fuels. Despite reductions in CO_2 emissions in developed countries, overall emissions continue to rise due to increased production, particularly in the steel, cement, chemical, petrochemical, and non-ferrous metal industries.*

Efforts are underway to harmonize clean production standards globally (PASS 55) to minimize waste and improve efficiency. However, implementing Best Available Techniques (BAT) faces barriers such as poor management, lack of monitoring, financial constraints, and inadequate planning—known as the "energy efficiency gap." A key factor in BAT adoption is the transfer of expertise between EU and non-EU countries to align industries with harmonized standards.

The EU enforces strict environmental regulations under the Integrated Pollution Prevention and Control Directive, requiring industries to reduce emissions and protect air, water, and soil. Integrated pollution prevention focuses on optimizing resource use, minimizing environmental impact, and designing eco-friendly equipment while promoting circular technologies.

North Macedonia's steel company, Makstil, applied for BAT compliance and received conditional approval. This research examines BAT techniques for steel production using electric arc furnaces, analysing gas emissions and their impact while comparing environmental performance before and after implementing BAT standards.

Keywords: Steel industry, EAF, gas emissions, environmental protection, BAT.

INTRODUCTION

The International Energy Agency (IEA) has conducted comprehensive research on the implementation of Best Available Techniques (BAT) and technologies across various industrial sectors, highlighting that energy consumption in most industrial processes is typically 50% higher than the theoretical minimum. While it may not be feasible to achieve this minimum, there is significant potential for energy savings through improved practices. Furthermore, data from high-energy

industrial facilities reveal that they account for one-third of global greenhouse gas emissions, with 70% of these emissions attributed to the burning of fossil fuels. Although CO2 emissions have decreased in highly developed countries, global emissions continue to rise due to increased production in developing economies. Industries that contribute most to CO2 emissions—such as steel, cement, chemical, petrochemical, and non-ferrous metals—collectively account for approximately 70% of global industrial emissions.

In response to these challenges, international efforts are being made to standardize clean production practices, enabling data comparison across different countries (PASS 55). These measures emphasize integrated resource management to reduce waste and extend product durability. However, the adoption of BAT faces significant obstacles, often referred to as the "energy efficiency gap." This gap arises due to factors such as inadequate management, insufficient monitoring, lack of financial resources, and poor strategic planning.

A key component of promoting global BAT adoption is the transfer of expertise between the European Union (EU) and non-EU countries, helping align industrial capabilities with the latest harmonized standards. Adhering to EU environmental regulations has become a crucial factor for industrial development, with strict laws under the EU's Integrated Pollution Prevention and Control Directive. These regulations require businesses to take action to reduce emissions and protect air, water, and soil quality [1-6].

Integrated pollution prevention is a vital part of cleaner production and sustainable development. It focuses on improving production processes through better use of raw materials and energy, minimizing waste, and reducing harmful emissions. It also emphasizes product design, aiming to reduce negative environmental and health impacts throughout the product's life cycle—from production to disposal. Additionally, it encourages the use of cyclical technologies that allow raw materials to be reused in production, mimicking nature's circular processes.

In line with this, the European Commission, through its Integrated Pollution Prevention and Control Bureau in Seville, Spain, has defined BAT standards for various industrial sectors.

This research specifically focuses on studying BAT reference techniques for steel production using electric arc furnaces (EAF), a major industry in North Macedonia with significant environmental impact. The study aims to assess gas emissions, their health and environmental consequences, and identify the best techniques for mitigating them. The objective is to compare the environmental performance of the industry before and after implementing the operational plan

and obtaining the Integrated Environmental Permit (IEP) from the Ministry of Environment and Public Health to ensure alignment with BAT standards.

RESULTS AND DISCUSSIONS

Emission status before obtaining IEP

The main sources of dust originate from scrap iron, lime, dolomite, coke, desulfurization additives and ferroalloys. During the charging and desulfurization process, dust is emitted, which is solid technogenic waste and leads to pollution of the environment and the immediate human environment. The presence of CO2, N2, as well as dust containing heavy non-ferrous metals such as Zn, Pb and others undoubtedly pose a threat to human health and the environment.

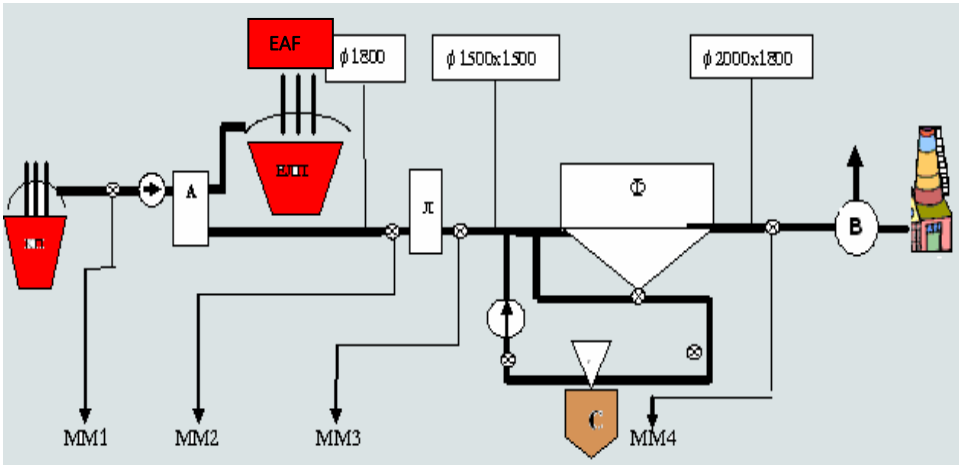

Figure 1 *Scheme of the EAF and Pot dedusting system - measuring points for monitoring filter efficiency [8]*

The dust removal system of the ELP and CP is shown in Figure 1. The efficiency of the filter plant is monitored through the four measurement points shown by measuring: temperature; gas velocity; gas flow; static and dynamic pressure. The obtained parameters are presented in Table. 1.

As a result of the metallurgical processes for obtaining and processing steel, industrial waste is also generated, which if it contains substances with properties hazardous to the environment and human health (toxicity, carcinogenic properties, flammability or reactivity) is classified as hazardous waste and it is necessary to provide adequate space for its disposal, proper handling and transport, processing and disposal. Table no. 15 shows the amount of waste

generated before the introduction of the operational plan for obtaining IED.

Table 1 *List of emission sources and emissions into the atmosphere - Previous situation*

Electric Arc Furnace and Pot Description of Emission Control Procedure		
Parameter	**Unit**	**Average annual**
Diameter	m	2.30
Temperature	°C	85.20
Flow	Nm^3/h	148627.00
CO_2	%	1.20
CO	mg/Nm^3	93.50
NO_x	mg/Nm^3	78.80
SO_2	mg/Nm^3	20.21
SO_3	mg/Nm^3	-
Dust	mg/Nm^3	9.52
H_2O	g/Nm^3	(no data)

Primary emission from the EAF

The electric arc furnace used for steel production in Makstil-Skopje operates with a system of three carbon electrodes. The furnace has a built-in fourth opening for extraction of primary gases. The removal of fugitive gases was not resolved before the operational plan, i.e. there was no system for their capture. Therefore, the secondary gases that were created during charging, pouring the metal and the gases that came out of the furnace during melting could not be captured.

From the analysis of the comparative data shown in Table 2 it can be concluded that except for the NOX values, all others are within the limits permitted by the BAT requirements. The NOX value exceeds the maximum permitted value by about 120 g/t.

In similar EAF steel production plants in the EU, namely Germany and Austria, using a combination of gas flow recirculation and low-NOX burners, a reduction of NOX emissions by 38% was achieved, which is more effective than using only one of the mentioned techniques [12 – 13].

Table 2*. BAT-recommended values for primary emissions from ELP and Pot*

Emission	**Unit**	**BAT recommended values**
Dust	mg/Nm^3	< 20
SO_2	g/t	20-100

NO_x	g/t	120-240
CO	g/t	740-2000
Solid waste		
ELP slag	kg/t	100-150
Boiler slag	kg/t	10-30
Dust*	kg/t	10-20
Refractory material	kg/t	

Table 3 *Effectiveness of primary measures in reducing NOX emissions* *******

Primary measures	**Efficiency in reducing NOX emissions (%)**
Low-NOX burners	28
Gas flow recirculation	13
Air injection from above for combustion of residues via substoichiometric burners	23
Reduction fuel injection	13
Low-NOX burners and gas flow recirculation	38

* Reference steelmaking plants: *Voestalpine Stahl GmbH, Linz*, Австрија и *TKS, Huckingen-Duisburg*, Germany

The dust present in the gases is 10-30 kg/t of liquid carbon steel and 10-18 kg/t of liquid high alloy steel before the use of techniques to reduce its concentration. In the production of stainless steel in ELP, the maximum value for dust emission is about 30 kg/t. The composition of the dust can be seen from the analysis of the dust retained in the bag filters of the electrostatic precipitator.

Table 4 *Chemical composition of ELP dust from carbon/low alloy steel and high alloy/stainless steel production in the EU*

Component	**Dust from carbon/low alloy steel production (wt %)**	**Dust from alloy steel production (wt %)**	**Stainless steel production dust (wt %)**
Fe - tot	10 – 45	17 – 37	20 – 65
SiO2	0.6 – 5.1	1.7 - 5	3 – 9
CaO	3- 17	2 – 16	8 – 20
Al_2O_3	0.3 – 3 1тот	1 – 4	0.4 – 2
MgO	0.5 – 6	1.2 - 3	1 – 5
P_2O_5	0.1 – 0.37	0.01 – 0.1	0.03 – 0.1
MnO	1.1 - 6	1.5 – 6.9	2.2 -6.3

Cr_2O_3	0.13 – 2	0.12 – 6	9 – 20
Na_2O	0.3 - 3	-	0.6 - 2
K_2O	0.5 - 2.3	-	0.7 – 3
Zn	21 - 43	2 – 15	2 - 25
Pb	0.4 - 10	0.05 -3.6	0.2 4.5
Cd	0.02 – 0.18	0.01 – 0.04	0.01 – 0.08
Cu	0.08 - 0.5	0.01 – 0.8	0.015 -0.5
Ni	0.01 - 0.8	0.01 – 0.5	1 - 8
V	0.01 -0.09	0.01 – 0.2	0.05 0.12
W	-	0.5 – 1.5	-
Co	0.001 -0.01	0.01 – 0.2	0.02 – 0.04
As	0.001 -0.02	0.01	0.01
Hg	0.0001 -0.005	0.05 – 0.7	0.0002 -0.015
Cl	0.8 – 5	0.7 – 1.7	0.8 - 1
F	0.02 – 0.9	0.01 -0.65	0.3 - 2.4
S	0.1 – 3	0.25 – 1.42	0.2 - 0.5
C	0.4 -3.3	0.5 – 3.1	0.05 – 1.3
Alkalinity	2.0 – 6.5	-	-
Moisture	6 -16	-	-

Optimal approach to BAT-Primary measures

To approach or achieve the measures recommended by BAT, the following recommended BAT procedures or combinations thereof should be applied in the production of steel in electric arc furnaces. The choice of technique (procedure) or combination of techniques depends on local possibilities.

Any other technique or combination of techniques that can give the same or better results than the recommended ones should also be considered. Recommended measures to approach or achieve the BAT norms in electric arc furnace operations are:

Extraction of dust from the electric arc furnace

By a combination of direct extraction with a fourth opening and a hood system (Diagram) or Dog-house and hood system or Complete evacuation of the plant. By applying one of these techniques or their combination, the degree of dust and gas capture is expected to be greater than 98%.

From the attached results and tables it can be seen that the production of steel in Makstil is carried out in an electric arc furnace with three electrodes, the characteristic of which is the extraction or collection of dust and gases with the

so-called fourth opening. The furnace, before the operational plan, was not equipped with a system for the extraction of fugitive gases and dust that are created during charging, melting and pouring of the metal. The finishing of the steel is carried out by the so-called out-of-furnace procedure in a boiler equipped for that purpose. The fugitive gases generated during this process were also not extracted, i.e. there was no system for their capture.

According to the operational plan, a combination of a fourth vent and complete evacuation of the plant with the installation of a roof hood with a filter was applied, the introduction of which required additional financial resources.

Waste gas dedusting

A well-designed bag filter can provide less than 5 mg/Nm3 for new plants and less than 15 mg dust/Nm3 when installed in existing plants. The values are average daily concentrations.

The reduction in dust is positively correlated with the reduction in heavy metal emissions, with the exception of heavy metals present in the gas phase such as mercury. At international level, special attention is paid to the prevention of mercury emissions by avoiding, as far as possible, raw materials and other materials containing mercury. The parameters for Hg content according to BAT ≤ 0.05 mg/Nm3 determined for an average experimental period at certain measuring points of at least 4 hours.

Dust emissions according to BAT ≤ 5 mg/Nm3 determined as a daily average value.

PCDD/F and PCB abatement by post-combustion and rapid cooling in combination with filters

PCDD/F and PCB abatement is carried out by means of an appropriate post-combustion system equipped with a gas collection system or in a separate post-combustion system with subsequent rapid cooling to avoid re-synthesis and/or

Injection of lignite dust before the gas inlet to the bag filter in combination with the filters. and PCB emissions through post-combustion and rapid cooling of gases.

The afterburning in the combustion chamber primarily aims to ensure complete combustion of CO and H2 in the emissions to avoid uncontrolled reactions in the exhaust gas cleaning equipment.

However, a well-optimized afterburning process, i.e. with appropriate temperature and gas retention time, ensures an effective reduction of the emission of organic and organochlorine compounds, such as RAN, PCB or

PCDD/F. The basic factors that should be observed during afterburning in orde to minimize organic micropollutants are the so-called three T-Timing (retention time), turbulence and temperature.

To prevent the resynthesis of PCDD/F, it is essential to bring the gases after afterburning as soon as possible, by rapid cooling to a temperature lower than 250 °C, thereby excluding the possibility of resynthesis.

By applying one of the proposed techniques, PCDD/F emissions are expected to be reduced to 0.1 - 0.5 ng I- TEQ/Nm^3.

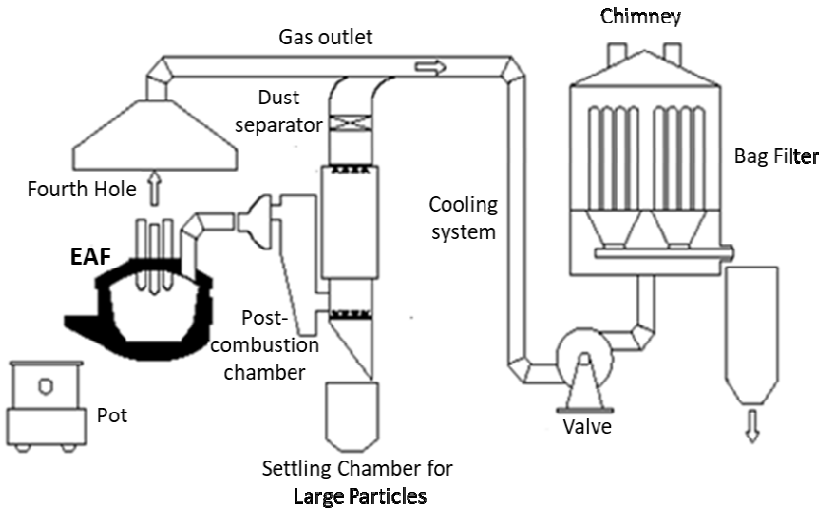

Figure 2 Schematic representation of equipment for reducing PCDD/F and PCB emissions through post-combustion and rapid cooling of gases

Additional tests indicate that as long as the temperature of the cleaned gases is below 75 °C, PCDD/F emissions will remain lower than 1 ng I- TEQ/Nm3, which is explained by the fact that the volatility of PCDD/F decreases with decreasing temperature and their adsorption to dust in the filters increases. [8]

COMPARATIVE RESULTS

State before obtaining with state after obtaining A – IEP and values recommended by BAT

The FTP (Fume Treatment design) design by Danieli Environment for the installation of the Dog house was optimized according to the conditions set by the Integrated Environmental Permit as well as the ELP capacity, the charging method and the ambient conditions of the plant

The dimensioning of the dedusting system did not only depend on the size of the ELP and the arrangement in the plant, but also on the specifications of the charging material, the positioning of the KP, the volume and temperature of the gas emissions, as well as the charging method.

For example, in Makstil, the fact that recycled scrap iron and steel are contaminated with oil, paints and plastics had to be taken into account. Appropriate solutions had to be provided for covering the secondary emission. [9]

The above-mentioned technical improvements were essential for the continuation of Makstil's operation according to the new environmental standards. Table 26 shows the comparative results of the primary emission and air emissions from the ELP and CP of the state before obtaining, the state after obtaining the A-IED and the values recommended by BAT.

The values of the measured parameters shown in table no. 26 refer to the maximum volume of emissions /hour of 165000 m3, while the average value of the emission /day is about 3 700 000 m3 [10] [11].

Table 5 *Comparative results of primary emissions and emissions to air from EAF and Pot: the situation before obtaining with the situation after obtaining A – IED and the values recommended by BAT*

Emission Parameters	**Maximum values recommended by BAT (mg/Nm^3)**	**Previous state (mg/ Nm^3)**	**Maximum allowed limits according to IED (mg/ Nm^3)**
Dust	<20	9.52 – 20	20
SO_2	20-100	500	300
NO_x	120-240	79 - 400	400
CO	740-2000	200	200

From the above table it is evident that the SO2 emissions in the previous state exceeded the limit allowed by the IED. Further activities and recommendations given by BAT should aim to reduce the SO2 emission to the minimum recommended limit by the ND.

CONCLUSION

The primary gases from the ELP and KP are accepted by the filter plant consisting of a cooler, a bag filter (Pulse Jet) and a dust silo. The secondary emissions to the air resulting from the charging of scrap iron into the ELP and

the pouring of steel were covered in the activities of the Operational Plan, i.e. by installing a new filter plant to accept the primary and secondary emissions from the EAF, Pot and the system for accessories with a hood - Dog house for dedusting the plant (Traditional Fume Treatment Plant). This operation, worth around 12 - 15 million euros, enables the capture of secondary emissions and satisfies the condition that their emission does not exceed the level of 20mg/m3.

BAT for primary and secondary dedusting in order to prevent and reduce the emission of polychlorinated dibenzodioxins / furans and polychlorinated biphenyls include avoiding, as much as possible, raw materials containing PCDD / F and PHB or their precursors and using a combination of the following techniques together with an appropriate dust removal system: appropriate post-combustion and rapid cooling, as well as injection of appropriate adsorption agents into the gas outlets before dedusting. The emission level of (PCDD / F) according to BAT is <0.1 ng I-TEQ / Nm3, per sample monitored for 6-8 hours during stable operating conditions of the plants.

According to BAT, in order to prevent mercury emissions, monitoring and checking of raw materials is recommended in order to avoid, as much as possible, raw materials and additives containing mercury. The level of dust emissions according to BAT is <5 mg / Nm3, as a daily average value, and the level of mercury emissions according to BAT should be <0.05 mg / Nm3, as a daily average value per sample taken with recommended discontinuous measurement of at least four hours, during stable operation of the plants.

As for CO_2 emissions, the implementation of activities in the Steelworks production plant includes not only the modifications of the electric arc furnace, but also the effects achieved from the installation of the boiler furnace. The reduction of CO2 emissions is significant.

It is recommended to introduce strict and frequent monitoring of emission points, install measuring instruments for continuous monitoring of dust from emission point A1 (Electric arc furnace stack) to determine the concentration of Dioxins and Furans emissions. Assuming that Dioxins and Furans are above 1ng I-TEQ/Nm3, it is recommended to install a post combustion chamber.

REFERENCES

1. Brown T., Gambhir A., Florin N.and.Fennell P, International Energy Agency, Reducing CO_2 emissions from heavy industry: a review of technologies and considerations for policy makers, Grantham Institute for Climate Change Briefing paper No 7 February 2012, Imperial College London, UK

2. European Commission – Strategic energy technologies information system –SETIS- Energy Efficiency and CO_2 emission reductions in the Iron and Steel Industry- Providing information for decision making. Iron and Steel Brief 2011
and costs, No. 80/December 2013, Centre for European Policy Studies ▪ Place du Congrès 1 ▪ B-1000 Brussels
https://www.ceps.eu/system/files/Steel%20Report.pdf
3. European Commission, Integrated Pollution Prevention and Control (IPPC), 2001 Reference Document on Best Available Techniques in the Ferrous Metals Processing Industry
4. *BREF*, 2007, Contribution from Germany to the revision of the I&S BREF Sander. K, Jepsen.D., Schilling S. Tebert C., Ipsen A.,Neutralisation of waste specific environmental risks- Final Report March 2004, Waste recovery and disposal operations, OKOPOL gmbH Institute for Environmental Startegies ,Hamburg , Germany
http://ec.europa.eu/environment/waste/studies/pdf/r_d_part_b.pdf
5. EPA, 2008. Framework for Application of the Toxicity Equivalence Methodology for Polychlorinated Dioxins, Furans, and Biphenyls in Ecological Risk Assessment. Risk Assessment Forum, U.S. Environmental Protection Agency, Washington, DC.
6. R. Remus, M. A. Aguado Monsonet,, S. Roudier, L.Delgado Sancho. Best Available Techniques (BAT) Reference Document for Iron and Steel Production, Industrial Emissions Directive 2010/75/EU, (IPPC)
http://eippcb.jrc.ec.europa.eu/reference/BREF/IS_Adopted_03_2012.pdf
7. J.-P. Birat, A. Arion, M. Faral, F. Baronnet, P.-M. Marquaire, P. Rambaud, Abatement of organic emissions in EAF exhaust flue gas, *Revue de Métallurgie* **98** (2001) 839-854. doi:10.1051/metal:2001132.
8. *Makstil AD-Skopje* , Прилог VIII.2.1.
http://www.moepp.gov.mk/wpcontent/uploads/2014/10/Makstil%20PRILOG%20VIII.2.1.pdf
9. Traditional Fume Treatment Plant
http://www.danielienvironment.net/Traditional-FT
10. Hoffmann, M. 1997, Die Rueckgewinnung von Zink und Blei aus Staeuben der Elektrostahlerzeugung, Dusiburg
11. Strohmeier, G. Bonestell, J. E. 1996, Steelworks Residues and the Waelz Kiln Treatment of Electric Arc Furnace Dust Iron and Steel Engineer
12. Plickert, 2007. Performance values of iron and steel plants in Germany, UBA.
https://www.umweltbundesamt.de/sites/default/files/medien/367/dokumente/bvt-merkblatt_eisen-_und_stahlerzeugung_endfassung.pdf
13. Wiesenberger, Review of the BREF Iron and Steel Production - Austrian Comments, BAT Guide for electric arc furnace iron & steel installations Project TR-2008-IB-EN-03 Mission no: 2.1.4.c.3, UBA, 2007, p. 35.

2nd Conference for Green Engineering, Sustainable Materials and Technologies for Circular Economy, GREEN CIRC 2025
PROCEEDINGS

MODELING AND PREDICTION OF AIR POLLUTION USING LASSO REGRESSION

Mare Srbinovska[1], Sijche Pechkova[2], Aleksandar Pechkov[3], Maja Celeska Krstevska[1], Aleksandra Krkoleva Mateska[1], Vesna Andova[1], Pavel Dimovski[2]

[1] - *Faculty of Electrical Engineering and Information Technologies, Ss. Cyril and Methodius University in Skopje, North Macedonia*

[2] - *Faculty of Technology and Metallurgy, Ss. Cyril and Methodius University in Skopje, North Macedonia*

[3] *Industrialmathinstitute.com Perth, 12 Coci Road*

dimovski@tmf.ukim.edu.mk

Abstract: *This study applies LASSO regression to forecast PM2.5 concentrations in Skopje using data from 2018 to 2022, including meteorological variables and pollution measurements from three sensor nodes. Models were trained on pre-COVID-19 data and then tested on post-COVID-19 observations to assess the pandemic's impact on air quality. Results show that models consistently overpredicted pollution levels during the pandemic, suggesting a positive effect of COVID-19 restrictions on air quality.*

Key words: air pollution, particular matter, lasso regression, prediction.

INTRODUCTION

Air pollution represents a critical and escalating environmental threat with profound consequences for public health, ecosystems, and cultural heritage. According to the World Health Organization [1], air pollution is responsible for approximately 7 million premature deaths globally each year, accounting for over one in every ten recorded deaths. Numerous studies [13,14] have linked elevated concentrations of airborne pollutants such as ozone (O_3), particulate matter (PM), and sulfur dioxide (SO_2) with increased mortality rates and a range of respiratory and cardiovascular diseases.

The European Environment Agency reports that in Europe air pollution contributes to over 400,000 premature deaths annually [1], underscoring the gravity of its impact across the continent. Beyond human health, air pollutants significantly affect physical structures and cultural assets; for instance, urban pollutants such as PM, SO_2, CO, O_3, nitrogen oxides (NO_x), and volatile organic compounds (VOCs) have been shown to accelerate the deterioration of monuments and artworks [9,10].

Fossil fuel combustion remains the predominant source of air pollutants, particularly in rural regions where traditional household heating and cooking practices prevail. Household air pollution (HAP), stemming from the inefficient burning of biomass fuels, poses acute health risks, especially for women and children. Evidence from Chakraborty [5] and Graydon [6] demonstrates that interventions such as improved cook stoves and cleaner fuel alternatives can substantially lower PM2.5 exposure levels and enhance respiratory health. Furthermore, Bond et al. [4] highlight the broader atmospheric implications of residential fuel combustion, noting that its contribution to pollution varies regionally based on factors such as transportation and open burning practices.

Meteorological conditions also play a significant role in modulating air quality. Wind speed, precipitation, and temperature influence the dispersion and concentration of pollutants; for example, higher wind velocities are generally associated with reductions in particulate levels [7]. Moreover, the presence of urban green spaces has been shown to mitigate PM2.5 and PM10 levels [11], pointing to the co-benefits of green infrastructure in pollution control.

Efforts to mitigate air pollution span both local and global initiatives. Locally, strategies include expanding green infrastructure, transitioning to low-emission transportation, and promoting clean energy solutions. Globally, comprehensive decarbonization efforts across the energy, transport, and industrial sectors are imperative. As noted by Alberto, Ramos, and Almeida [2], green buildings and vegetated surfaces also offer additional benefits such as improved thermal insulation, reduced noise pollution, and lower energy demands.

The COVID-19 pandemic has unintentionally provided a natural experiment in pollution mitigation. Numerous studies have reported significant reductions in pollutant concentrations during lockdown periods [12, 13, 14]. The findings of these studies indicate that the social distancing led to marked declines in PM2.5, NO_2, and CO (c.f. [15 ,16]). Results in [3] illustrate the measurable environmental benefits of reduced anthropogenic activity.

In the context of North Macedonia, a country in the Western Balkans, air pollution remains a persistent concern driven by industrial activity, transportation, energy production, and biomass burning. The resulting health and ecological challenges necessitate targeted, evidence-based interventions.

Through a rigorous analysis of historical air quality data, meteorological parameters, and other relevant environmental variables, this study aims to uncover the underlying dynamics of air pollution in North Macedonia.

To achieve this, we have developed a hybrid predictive framework, integrating LASSO linear regression with decision tree-based modeling. Decision trees are particularly effective in contexts where data can be segmented according to input attributes approach well-suited to air pollution, which often exhibits distinct patterns depending on temporal or contextual factors, such as increased pollutant levels during weekdays compared to weekends. LASSO regression, known for its ability to manage multicollinearity and perform variable selection, assigns weights to coefficients with the objective of shrinking them toward zero, thereby enhancing model interpretability. In the proposed hybrid model, each node of the decision tree is replaced with a LASSO regression sub-model. Predictions are generated by traversing from the root to the leaf, with final outputs computed through weighted aggregation of model estimates along the path.

SYSTEM DESCRIPTION

Node (sensor) configuration

To evaluate the effects of green spaces, vehicular traffic, and human activity on air quality, sensor nodes were strategically deployed across various locations. In 2018, the sensors were installed near the Faculty of Electrical Engineering and Information Technologies. Specifically, sensor node n3′ was positioned adjacent to a secluded green area, node n2′ was located near a vertical green wall structure, and node 1′ was placed alongside a high-traffic roadway. Detailed findings on the air quality improvements associated with the green wall installation are presented in [11]. In 2019, the sensor layout was modified: node n1 was relocated to a pedestrian pavement area, while node n2 was positioned near a small green space within the building's internal courtyard.

LASSO Regression Framework

LASSO (Least Absolute Shrinkage and Selection Operator) regression is a linear modeling technique particularly effective in high-dimensional datasets, where the number of predictors is large. It performs both variable selection and regularization to enhance model interpretability and predictive accuracy. In the context of this study, LASSO is used to model the relationship between meteorological and environmental variables (predictors) and air pollution levels-specifically the concentrations of PM2.5 (target variable).

The LASSO algorithm minimizes the residual sum of squares subject to the constraint that the sum of the absolute values of the coefficients is less than a fixed value (often denoted by λ). One of the key features of LASSO is that variable selection is performed by shrinking the coefficients of irrelevant predictors to exactly zero. This means that the most important predictors are

automatically selected while the less important ones are disregarded. The amount of regularization applied is controlled by the tuning parameter λ. A larger λ results in more coefficients being pushed to zero, leading to a simpler model with fewer predictors.

Prediction Model: Hybrid Tree–LASSO Approach

The prediction model combines decision tree structures with LASSO regression. The tree is constructed using the CART algorithm [18] as implemented in the *scikit-learn* library [17]. Unlike traditional trees that assign constants at leaf nodes, this hybrid model embeds LASSO linear regressions at every node.

Tree construction:

- Let T be a tree with a root node (vertex) $t_{0,0}$ and n levels.
- The nodes in level i are defined as follows: $t_{i,j}$ is j^{th} node from left to right.
- Each node contains data that we split into 2 subsets. For the divided data, one observe "left child" (one subset of the data) and "right child" (the second subset of the data). For each subset of the data, one considers linear regression and calculates the mean squared error. From all possible splits of the data set, we are interested in the split that minimize the mean squared error. Hence, one obtains two nodes in the next level, "left child" and "right child". The tree is built until the stopping criteria are satisfied: the tree reaches depth n, or the minimum number of leaves is reached.

Let t_{n,j_n} be a leaf node (there is no node in level j_{n+1} connected to the node t_{n,j_n}). Choose a path from the root node tot_{n,j_n}, $(t_{0,0}, t_{1,j_1}, \dots t_{n,j_n})$.

- Linear regression model $f_{i,j}$ is fitted to every node $t_{i,j}$ from the tree. For a given λ, the prediction function p is defined as

$$p_{n,j_n} = \frac{f_{0,0} + \lambda f_{1,j_1} + \lambda^2 f_{2,j_2} + \cdots + \lambda^n f_{n,j_n}}{1 + \lambda + \lambda^2 + \cdots + \lambda^n}$$

for the data at the leaf node t_{n,j_n}.

Next, we discuss the role of parameterλ. One can consider two cases: case I for small values of λ, the models of the tree which occur higher in the tree are most important or the models are more global, and case II for bigger λ the models closer to the leafs become more important, making the model mode localized.

Decision tree models typically treat observations as independent and do not inherently consider the temporal continuity present in time series data. To address

this, the predictions can be smoothed using standard window-based techniques, such as a Hanning window, with adjustable window sizes to better reflect temporal continuity.

Additionally, the model can be configured to use either the full set of input features or a selected subset. If historical values of the target variable (e.g., past pollution levels) are excluded, the model becomes more suitable for predicting future pollution based solely on external factors, such as weather or traffic. While including historical pollution values can improve short-term prediction accuracy, it also introduces challenges, especially during unexpected events like COVID-19, because such models may accumulate error over time and become unstable when facing sudden shifts or shocks.

Data Preparation

In this study, the LASSO regression model is applied to predict the concentrations of PM2.5 which serve as the target (dependent) variable. Historical averages of these pollutant, specifically 12, 24, 36, 48, 72, 168, 336, and 672 hours prior, are incorporated as predictive features. The model is constructed using 20 independent variables, including meteorological factors (temperature, pressure, humidity, wind speed, and wind direction) and environmental indicators (such as workday/weekend and heating/non-heating season). These variables are extracted over various timeframes (1, 24, 48, 72, 168, 336, and 672 hours) and are collectively referred to as "tree attributes."

To analyze the potential influence of the COVID-19 pandemic, the dataset is split into two subsets: Set N: Data collected before March 11, 2020 (pre-COVID, or "normal conditions") and Set C: Data from March 12, 2020, to March 1, 2022 (during COVID-19 restrictions).

Set N is further divided into training set T, which is used for model fitting, and validation set V, which is the last 45 days of Set N and is reserved for tuning and model selection.

RESULTS AND DISCUSSIONS

In this study (for technical details see [8]), a vast variety of models were developed to predict PM2.5 concentrations. Models were built under different configurations based on the choice of input attributes and forecasting time intervals. Two attribute sets were considered: a reduced set, which excluded historical values of the target variable, and a full set, which included lagged target values.

The models targeted different time intervals, specifically: 1 hour (1h), 1 day (1d), 2 days (2d), 3 days (3d), 1 week (1w), and 2 weeks (2w). For each configuration, models were trained on a designated training set T, and a comprehensive grid search was performed over several parameters. The best-performing model, based on validation performance, is selected for final evaluation on the test set C.

The parameters included:

- Parameter λ varied in the range [0.2, 3.0], controlling the influence of local vs. global linear models;
- Smoothing window size, varied from 1 to 168 (hours), corresponding to smoothing periods ranging from 1 hour to 3 weeks;
- Two smoothing techniques were evaluated: uniform (ones) and Hanning window [16];
- Maximum tree depth, varied from 0 to 8, controlling tree complexity;
- Minimum number of samples per leaf, set between 80 and 150, to ensure model stability and prevent overfitting.

Each node in the decision tree included a linear regression model, and no restriction was placed on the sign of the coefficients allowing both positive and negative influences of predictors. As a result, for each combination of time interval and attribute set, a single best performing model was selected for evaluation on the final test set C.

The primary objective of this study is to determine the most effective predictive model for PM2.5 pollution levels in the city of Skopje, and subsequently to evaluate whether the COVID-19 pandemic had a measurable impact on air quality. To investigate the second objective, the best performing validated models, identified through training on dataset T, were applied to the post-pandemic period data contained in dataset C.

To assess deviations, the difference between the predicted values $\hat{y}$ and the actual recorded pollution values y in C was calculated. This discrepancy is denoted as PmR (Pollution Model Residual). A positive PmR suggests that the recorded pollution levels were lower than expected, indicating a positive impact of the COVID-19 pandemic on air quality. Conversely, a negative PmR suggests a worsening of air quality relative to predictions, while a PmR value close to zero implies no substantial deviation.

To benchmark model performance, the Relative Error (RE) metric is used. RE is computed as the ratio of the sum of squared residuals of the model to the sum of squared residuals from a trivial model that predicts the mean of the target variable.

This metric provides a normalized view of performance relative to a baseline. Lower RE values indicate stronger predictive performance, with RE = 0 representing a perfect model and RE = 1 meaning the model performs no better than the mean predictor.

In this work, we focus on a clearer visualization of the obtained results by presenting comparative charts of the recorded versus predicted values using the optimal models, specifically for data collected (PM2.5) from sensor node n1. For the technical methodology underlying this study, we refer the reader to a recent publication by the same authors [8]. Additionally, we note that every other pollutant can be treated in the same way; every sensor node from configuration as shown in [8].

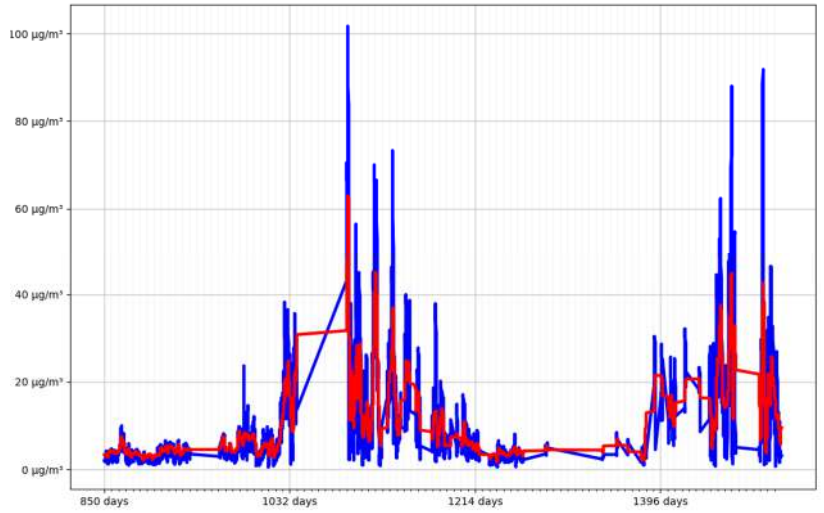

Figure 1 *Predicted values (red) and recorded values (blue) of* ***PM2.5*** *for the data set C for sensor node n1, where the target interval is 1h. The model is using historical values. The best model in this case is using λ = 0.2, the maximum depth of the tree is 0, i.e., a linear model. The coefficients can be positive and negative. The predictions are then smoothed with a window length of 36 using the ones method - just a standard mean.*

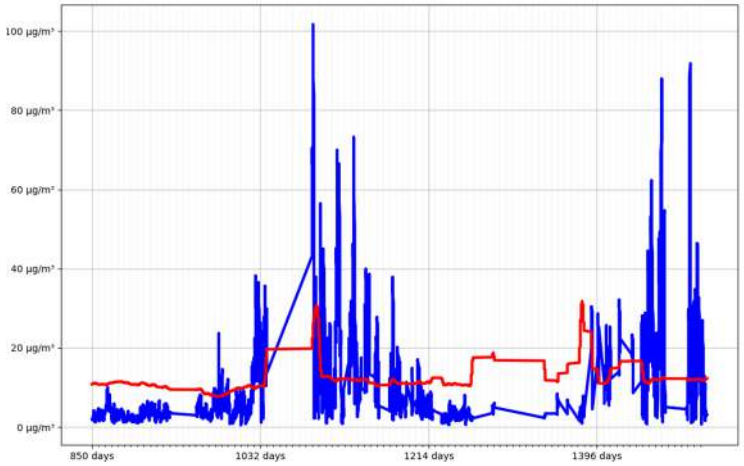

Figure 2 *predicted values (red) and recorded values (blue) of PM2.5 for the data set C for sensor node n1, where the target interval is 1h, and historical data are not used. The best model in this case is obtained for λ= 3, the maximum depth of the tree was 2, the minimum number of samples for leafs was set to 80. The linear models were set to be only positive. In the end the predicted values were smoothed with a hanning window of length 168.*

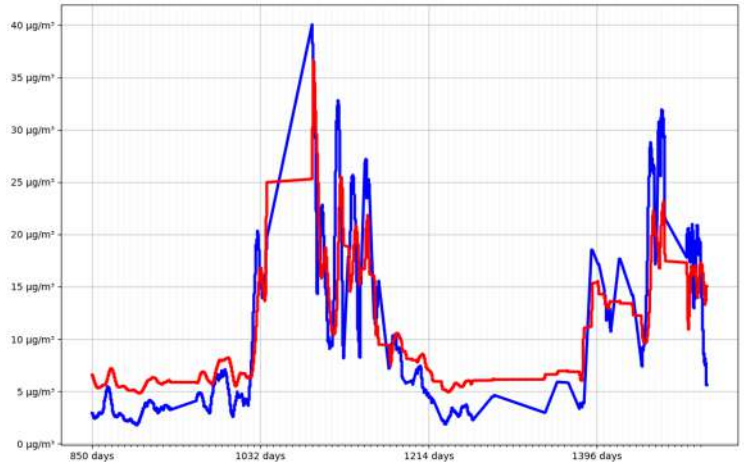

Figure 3 *Predicted values (red) and recorded values (blue) of PM2.5 where the target interval is 1week. The model is using historical values. The best model had parameters λ = 3, the maximum depth of the tree was set to 1. The predictions were smoothed with a window of size 72.*

CONCLUSIONS

In this study, a hybrid predictive modeling approach combining decision trees and LASSO-regularized linear regression was applied to air pollution forecasting. The use of LASSO (Least Absolute Shrinkage and Selection Operator) allowed for automatic feature selection by penalizing large coefficients, effectively reducing model complexity and mitigating overfitting capabilities not offered by standard linear regression. This approach is particularly advantageous in high dimensional settings where many features may be irrelevant or redundant.

The dataset used in the analysis comprises air quality measurements collected from three sensor nodes located on the technical campus of Ss. Cyril and Methodius University in Skopje, covering the period from 2018 to 2022. The onset of the COVID-19 pandemic in March 2020 introduced substantial changes in human activity, including reduced traffic and the closure of schools, universities, industrial facilities, and public spaces. To assess the impact of these changes on air quality, a wide range of predictive models were trained and validated using only pre-pandemic data, i.e., data collected before the enforcement of COVID-19-related restrictions in the Republic of Macedonia.

The modeling framework explored various parameters, including multiple values of the regularization parameter λ, different decision tree depths, two smoothing techniques (uniform and Hanning windows), and multiple prediction time frames. In total, 2,520 distinct models were generated and evaluated for each target variable.

Using the best performing models, the concentrations of PM2.5 were predicted based on meteorological and environmental attributes, both with and without incorporating historical pollutant concentration values. The predicted values were then compared to actual recorded measurements during the post-COVID period. Results showed that models using the full feature set, including historical concentration data, achieved higher predictive accuracy. However, in both modeling scenarios, the predicted pollution levels were consistently higher than the observed values during the pandemic period. This systematic overestimation suggests a positive impact of the COVID-19 pandemic on air quality in Skopje, likely attributable to the reduced anthropogenic activity.

Furthermore, the developed models demonstrate the capability to predict pollution levels in the post COVID period and can be readily extended to other pollutants (e.g., PM10, CO, NO_2, O_3) and additional geographic locations, making them versatile tools for environmental monitoring and public policy evaluation.

REFERENCES

1. Y. Yorozu, M. Hirano, K. Oka, and Y. Tagawa, Electron spectroscopy studies on magneto-optical media and plastic substrate interface, *Institute of Electrical and Electronics Engineers Transl. J. Magn. Japan* **2** (1987) 740–741.
2. A. Alberto, N. Ramos, R. Almeida, Parametric study of double-skin facades performance in mild climate countries. *Journal of Building Engineering* **12** (2017) 87-98. https://doi.org/10.1016/j.jobe.2017.05.013
3. V. Andova, V. Andonovic, M. Celeska Krstevska, V. Dimcev, A. Krkoleva Mateska, M. Srbinovska, Estimation of the Effect of COVID-19 Lockdown Impact Measures on Particulate Matter (PM) Concentrations in North Macedonia, *Atmosphere* 14(2) (2023) 192. https://doi.org/10.3390/atmos14020192
4. T. V. Bond, Global atmospheric impacts of residential fuels, *Energy for Sustainable Development* **8**(3) (2004) 20-32 https://doi.org/10.1016/S0973-0826(08)60464-0.
5. D. M. Chakraborty, Reduction in household air pollution and associated health risk: a pilot study with an improved cookstove in rural households, *Clean Technologies and Environmental Policy* **23** (2021) 1993–2009. https://doi.org/10.1007/s10098-021-02098-9
6. G. Snider, E. Carter, S. Clark, J. Tseng, X. Yang, M. Ezzati, J. J. Schauer, C. Wiedinmyer, J. Baumgartne, Impacts of stove use patterns and outdoor air quality on household air pollution and cardiovascular mortality in southwestern China, *Environment International* **117** (2018) 116-124. https://doi.org/10.1016/j.envint.2018.04.048
7. R. J. Hosker, Review: atmospheric deposition and plant assimilation of gases and particles, *Atmospheric Environment* **16**(5) (1982) 889-910. https://doi.org/10.1016/0004-6981(82)90175-5
8. M. Srbinovska, S. Pechkova, A. Pechkov, M. Celeska Krstevska, A. Krkoleva Mateska, P. Dimovski, V. Andova, A Comprehensive Study on Air Pollution Prediction in North Macedonia: Insights from LASSO Modeling, *11th International Conference on Electrical, Electronic and Computing Engineering (IcETRAN)*, 2024, pp. 1-8.
9. H. Mayer, Air pollution in cities, *Atmospheric Environment* **33** (1999) 4029-4037. https://doi.org/10.1016/S1352-2310(99)00144-2
10. J. Samet, S. Zeger, F. Dominici, F. Curriero, I. Coursac, D. Dockery, A. Zanobetti, The national morbidity, mortality, and air pollution study. Part II: Morbidity and mortality from air pollutionin the United States, *Res. Rep. Health Eff. Inst.* **94** (2000) 5-79.
11. M. Srbinovska, V. Andova, A. Krkoleva Mateska, M. Celeska Krstevska, The effect of small green walls on reduction of particulate matter concentration in open areas, *Journal of Cleaner Production* **279** (2021) 123306. https://doi.org/10.1016/j.jclepro.2020.123306
12. C.-L. Wu, H.-W. Wang, W.-J. Cai, H.-D. He, A. N. Ni, Z. R. Peng, Impact of the COVID-19 lockdown on roadside traffic-related air pollution in Shanghai, China., *Building and Environment* **194** (2021) 107718. https://doi.org/10.1016/j.buildenv.2021.107718
13. M. J. Ju, J. Oh, Y. H. Choi, Changes in Air Pollution Levels After COVID-19 Outbreak in Korea, *Science of The Total Environment* 750 (2021) 141521. https://doi.org/10.1016/j.scitotenv.2020.141521
14. Y. H. Kang, S. You, M. Bae, E. Kim, K. Son, C. Bae, Y. Kim, B. -U. Kim, H. C. Kim, S. Kim, The impacts of COVID-19, meteorology, and emission control policies on PM2.5 drops in

Northeast Asia, *Scientific Reports* 10 (2020) 22112. https://doi.org/10.1038/s41598-020-79088-2
15. B. S. Han, K. Park, K. H. Kwak, , S. B. Park, H. G. Jin, S. Moon, J. W. Kim, J. J. Baik, Air Quality Change in Seoul, South Korea Under COVID-19 Social Distancing: Focusing on PM2.5, *International Journal of Environmental Research and Public Health* **17** (2020) 6208. https://doi.org/10.3390/ijerph17176208
16. J. H. Seo, H. W. Jeon, U. J. Sung, J. R. Sohn, Impact of the COVID-19 Outbreak on Air Quality in Korea, *Atmosphere* **11** (2020) 1137. https://doi.org/10.3390/atmos11101137
17. F. Pedregosa, G. Varoquaux, A. Gramfort et al., Scikit-learn: Machine Learning in Python, *Journal of Machine Learning Research* **12** (2011) 2825-2830.
18. R. A. Berk, *Classification and Regression Trees (CART). In: Statistical Learning from a Regression Perspective*, Springer Texts in Statistics. Springer, 2016, p. 129-186. https://doi.org/10.1007/978-3-319-44048-4_10.

CORRELATION OF MECHANICAL PROPERTIES WITH CHEMICAL COMPOSITIONS AND DEFORMATION PARAMETERS OF HOT ROLLED STEEL PLATES THROUGH MATHEMATICAL MODELLING

Ruzica Manojlović[1], Andrej Cheshnovar[2], Katerina Atanasova Zdravevska[1], Sara Petrova[3]

[1] - *Faculty of Technology and Metallurgy, Ss. Cyril and Methodius University in Skopje, North Macedonia*

[2] - *OKTA AD, 1 Str. 25 Miladinovci, Ilinden, 1000 Skopje, North Macedonia*

[3] - *Pakomak DOO, Blvd. Partizanski Odredi, Porta Vlae, 4, 1000, Skopje, North Macedonia*

ruzica@tmf.ukim.edu.mk

Abstract: *This paper examines the impact of chemical composition and hot rolling process parameters on the strength characteristics of low-carbon manganese steel plates with final thicknesses of 60 and 50 mm. A review of existing mathematical models was conducted to establish the influence of these factors. The model by J. Noppon and S. Chandra-Ambhorn was selected due to the similarity of variables and was partially adapted to our conditions. The application of this model indicates that the chemical elements C, Mn, and Si have the most significant impact on the strength characteristics of the plates. Among the geometric parameters, the final thickness of the plate is crucial. Although the influence of the final rolling temperature is well-documented, its impact is less pronounced in this case, likely due to the narrow range of variation in this variable. The model allows for the straightforward prediction of the strength characteristics of steel plates based on known chemical composition and hot rolling process parameters. The predicted tensile characteristics differ from actual values by a maximum of 1.22% and 1.55% for plates with final thicknesses of 60 and 50 mm, respectively. This minimal discrepancy indicates a well-established mathematical model.*

Keywords: Hot rolling, Steel plates, Chemical composition, Rolling parameters, Strength characteristics

INTRODUCTION

Automated control of the hot rolling process for steel plates involves predefined values of process parameters that primarily depend on the degree of slab thickness reduction and the chemical composition of the steel [1-5]. Depending on the type of steel, the basic parameters of the hot rolling process are defined: slab temperature, rolling force and speed, as well as the number of passes [5-10]. The number of passes is most often determined by the degree of slab thickness reduction. Certainly, the greater the degree of thickness reduction, i.e., the

greater the initial slab thickness and the smaller the final steel plate thickness, the greater the number of passes.

Rolling process parameters, such as slab temperature in the final stages of the process, rolling force, and speed, are mainly defined by the type of steel slabs, specifically their chemical composition and, again, the degree of slab thickness deformation [9-11]. In this study, the hot rolling processes of low-carbon manganese steel plates were monitored, with the aim of establishing a connection between the chemical composition of the steel and the most relevant parameters of the hot rolling process with the strength characteristics of the steel plates.

EXPERIMENTAL

The hot rolling processes of low-carbon manganese steel plates with final thicknesses of 60 and 50 mm were monitored. Their chemical composition is provided in Table 1.

Table 1 *Chemical composition of low-carbon manganese steel*

Content of elements, %									
C	Mn	Si	S	P	Al	Ni	V	Nb	Cu
0.08-0.1	1.2-1.35	0.2-0.3	0.004-0.005	0.014-0.015	0.02-0.035	0.25-0.35	0.045-0.06	0.035-0.045	0.23-0.3

A total of 38 processes were analysed, of which 18 had a final thickness of 60 mm and 20 had a final thickness of 50 mm.

For all hot rolling processes, all relevant process parameters were monitored, from rolling force, speed, and temperature to the number of passes. The mechanical characteristics of all steel plates were determined: yield strength (*Reh*), ultimate tensile strength (Rm), toughness (*ak*), and percentage of elongation (*A*). The results are presented in Table 2.

Table 2 *Mechanical properties of low-carbon manganese steel plates*

Final thickness, mm	Mechanical properties			
	Reh, MPa	*Rm*, MPa	*ak*, J	*A*, %
60	400-431	514-531	128-193	25.9-28
50	398-432	529-567	149-241	26.3-28.4

According to the requirements of standards EN10025 and EN10029, the minimum value for Reh is 355 MPa, while the values for Rm range from 470 to 630 MPa [12]. Comparing the obtained mechanical properties of the monitored steel plates with the standard requirements, it was determined that they meet the conditions of the S355J2+N grade [13]. This indicates that the material is

low-carbon manganese steel, with exceptionally good strength characteristics, excellent cold forming properties, as well as high weldability. All these favorable properties make S355J2+N hot rolled steel plates widely applicable in the industry [14].

RESULTS AND DISCUSSIONS

The aim of this paper is to establish the relationship between the chemical composition of the steel and the most important parameters of the hot rolling process with the strength characteristics of the steel plates [15-18]. Within regular hot rolling processes, based on both previous theoretical knowledge and long-term practical experience, all relevant rolling process parameters vary within very narrow intervals. This, along with the application of passive experiments, complicates the process of establishing a relationship between the chemical composition and the parameters of the hot rolling process with the strength characteristics of steel plates, which is the subject of this study.

To establish the relationship between the chemical composition of steel and process parameters, a large number of existing mathematical models were reviewed [19-24]. One of them, by authors N. Jiratthanakul and S. Chandra-Ambhorn, attracted our attention due to the similarity of variables in the model, primarily because of the similar chemical composition of the steel [24].

Their mathematical model was applied here, partially adapted to our conditions. It is a regression equation that includes the values of the chemical composition of the steel, the geometric parameters of the steel plates (thickness and width), and the final rolling temperature [24]:

$$\begin{aligned} Reh = {} & 461 + 418 \cdot C + 61.6 \cdot Mn + 796 \cdot P - 303 \cdot S + 159 \cdot Si + 146 \cdot Cu + 204 \cdot Ni + \\ & + 49.7 \cdot Cr + 1127 \cdot V + 1072 \cdot Ti + 3674 \cdot Nb - 266 \cdot Mo - 6299 \cdot B - 76.3 \cdot Al - \\ & - 557 \cdot Sn - 3.54 \cdot THK - 0.00758 \cdot WID - 0.114 \cdot FT - 0.223 \cdot CT, \end{aligned} \quad (1)$$

where C, Mn, P, Si, Cu, Ni, Cr, V, Ti, Nb, Mo, B, Al, and Sn are the contents of the given elements in the steel in percentages, THK – final thickness of the plates, WID – width of the plates, FT – final rolling temperature, and CT – cooling temperature.

Our adapted model has the following form:

$$\begin{aligned} Reh = {} & 461 + 418 \cdot C + 61.6 \cdot Mn + 796 \cdot P - 303 \cdot S + 159 \cdot Si + 146 \cdot Cu + 204 \cdot Ni + \\ & + 49.7 \cdot Cr + 1127 \cdot V + 1072 \cdot Ti + 3674 \cdot Nb - 266 \cdot Mo - 76.3 \cdot Al - \\ & - 3.54 \cdot THK - 0.00758 \cdot WID - 0.114 \cdot FT, \end{aligned} \quad (2)$$

where C, Mn, P, Si, Cu, Ni, Cr, V, Ti, Nb, Mo, Al, THK, WID, and FT have the same meanings as in equation (1).

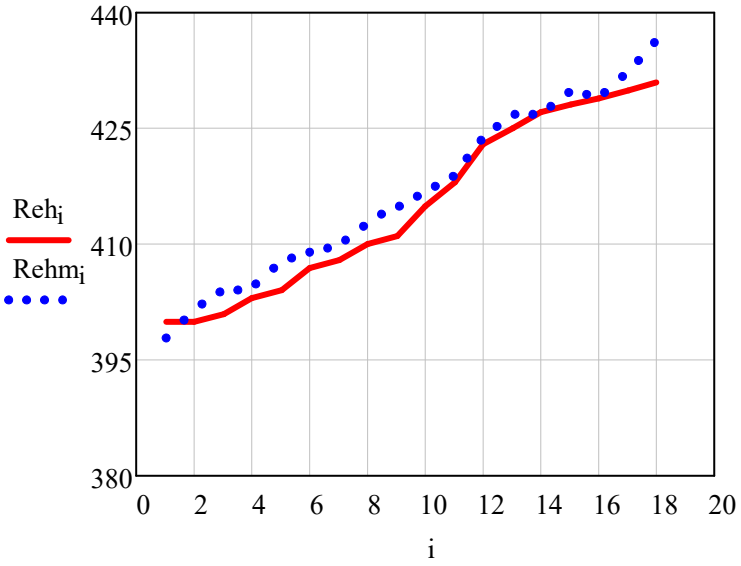

Figure 1 *Actual values (Reh_i) and values obtained through mathematical modeling ($Rehm_i$) for steel plates with a final thickness of 60 mm*

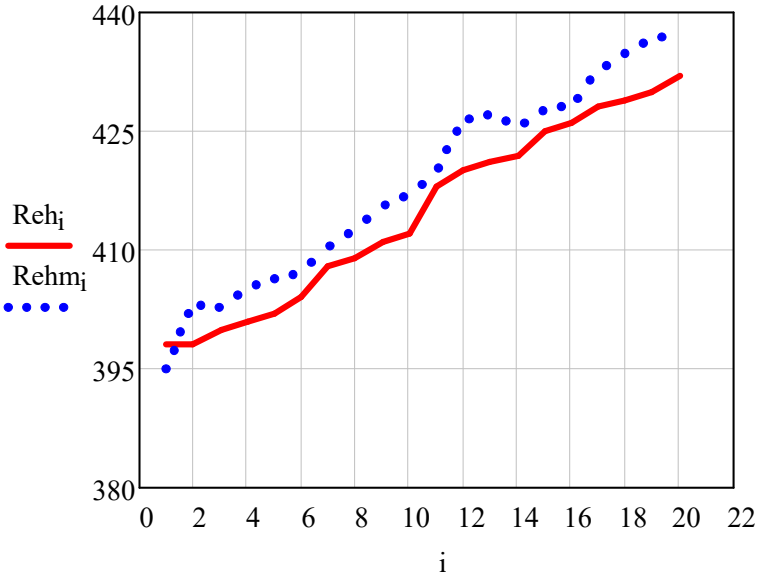

Figure 2 *Actual values (Reh_i) and values obtained through mathematical modeling ($Rehm_i$) for steel plates with a final thickness of 50 mm*

The actual, measured values of *Reh* and the values obtained through mathematical modeling for steel plates with final thicknesses of 60 and 50 mm are shown in Fig. 1 and Fig. 2, respectively.

Table 3 presents the minimum and maximum deviations of the modeled values for *Reh* for both final thicknesses of the plates.

Table 3 *Difference between modeled and measured values of Reh*

Final thickness, mm	Discrepancies between the modeled and measured *Reh* values			
	Δ*Reh*, MPa		δ*Reh*, %	
	min.	max.	min.	max.
60	0.31	5.26	0.07	1.219
50	1.70	6.67	0.43	1.552

For steel plates with a final thickness of 60 mm, the actual *Reh* values range from 400 to 431 MPa, whereas the values obtained through mathematical modeling range from 397.97 to 436.256 MPa. The difference between the actual and mathematically modeled values ranges from 0.31 to 5.26 MPa, or from 0.07 to 1.22%. For steel plates with a final thickness of 50 mm, the actual *Reh* values range from 398 to 432 MPa, while the values obtained through mathematical modeling range from 394.983 to 437.132 MPa. Compared to steel plates with a final thickness of 60 mm, the difference between the actual and mathematically modeled *Reh* values is slightly higher, ranging from 1.7 to 6.67 MPa, or from 0.43 to 1.55%.

In summary, the mathematical model, specifically regression equation (2), effectively describes the actual yield stress (*Reh*) values, with a maximum deviation of up to 1.22% for plates with a thickness of 60 mm and up to 1.55% for plates with a thickness of 50 mm. The model indicates that the strength characteristics are predominantly influenced by the concentrations of C, Mn, and alloying elements V, Ti, and Nb, as well as the final thickness of the plates.

Although the final rolling temperature is known to significantly impact the mechanical properties of the plates, its effect is not as pronounced in this study. This is likely because the mathematical modeling was based on a limited number of passive experiments and the narrow range of this variable: the final rolling temperature varied within a narrow interval of only 10°C, from 800 to 810°C, in all examined cases.

CONCLUSIONS

The impact of chemical composition and hot rolling process parameters on the strength characteristics of low-carbon manganese steel plates with final

thicknesses of 50 and 60 mm was investigated. This impact was then mathematically modeled using a simple regression equation (2). Analysis of the obtained results led to the following insights:

The strength characteristics of the examined steel plates meet the requirements of the S355J2+N grade. The *Reh* values range from 400 to 431 MPa, while the minimum value according to standard requirements is 355 MPa.

The mathematical modeling, which defines the influence of the chemical composition of the steel and the significant parameters of the hot rolling process on the strength characteristics of the plates, was successfully performed using the adapted regression equation (2).

The maximum deviations of the mathematically obtained *Reh* values from the actual are 1.22% for plates with a final thickness of 60 mm and 1.55% for plates with a final thickness of 50 mm.

The mathematical model indicates that, within these intervals of change under the conditions of the passive experiment, the values of C, Mn, and alloying elements V, Ti, and Nb, as well as the final thickness of the plates, have the most significant influence on the obtained strength characteristics.

REFERENCES

1. V.B. Ginzburg, *High-quality Steel Rolling: Theory and Practice*, Ed. Marcel Dekker Inc., New York, 1993 https://doi.org/10.1201/9781466564640
2. W. Tafel, *The Theory and Practice of Rolling Steel*, Penton Publishing Company, University of Wisconsin, Madison, 2007.
3. B.L. Juneja, *Fundamental of Metal Forming Process*, New Delhi, New Age International Publishers, 2007.
4. S. Ray, *Principles and Applications of Metal Rolling*, Pub. Cambridge University Press, 2016 https://doi.org/10.1017/CBO9781139879293
5. O. Ikumapayi, E. Akinlabi, P. Onu, O. Abolusoro, Rolling operation in metal forming: Process and principles — A brief study, *Materials Today: Proceedings 26* (2020) 1644-1649. https://doi.org/10.1016/j.matpr.2020.02.34
6. P.U. Nwachukwu, O.O. Oluwole, Effects of rolling process parameters on the mechanical properties of hot-rolled St60Mn steel, *Case Studies in Construction Materials* **6** (2017) 134-146. https://doi.org/10.1016/j.cscm.2017.01.006
7. M. Jahazi, B. Egbali, The influence of hot rolling parameters on the microstucture and mechanical properties of an ultra-high strength steel, *Journal of Material Processing Technology* **103** (2000) 276-279. https://doi.org/10.1016/S0924-0136(00)00474-X
8. Y.W. Kim, J.H. Kim, S.G. Hong, C.S. Lee, Effects of rolling temperature on the microstructure and mechanical properties of Ti–Mo microalloyed hot-rolled high strength steel, *Materials Science and Engineering*, *A* **605** (2014) 244-252.

https://doi.org/10.3390/met6120323
9. H. Tamehiro, N. Yamada N, H. Matsuda, Effect of the thermo-mechanical control process on the properties of high-strength low alloy steel, *Transactions of the Iron and Steel Institute of Japan* **25** (1985) 54-62. https://doi.org/10.2355/isijinternational1966.25.54
10. S.A. Balogun, Influence of finishing temperature on the mechanical properties of conventional hot rolled steel bar, *Journal of Engineering and Technology Research* **3**(11) (2011) 307-313. https://doi.org/10.5897/JETR.9000044
11. Y.W. Kim, J.H. Kim, S.G. Hong, C.S. Lee, Effects of rolling temperature on the microstructure and mechanical properties of Ti–Mo microalloyed hot-rolled high strength steel, *Materials Science and Engineering*, *A* **605** (2014) 244-252. http://dx.doi.org/10.1016/j.msea.2014.03.054
12. EN 10025-2, *Hot rolled products of structural steels - Part 2: Technical delivery conditions for non-alloy structural steels* (2019).
13. https://specialsteels.co.za/wp-content/uploads/PLT-S355J2N.pdf
14. https://soluckysteel.com/what-is-s355j2cn-steel-materials/
15. R.A. Evdokimov, E.V. Derbisher, V.E. Derbisher, I.V. Germashev, Correlation analysis of the dependence of the properties of steel on its composition based on the processing of reference information, *Journal of Physics*: *Conference Series* **1353** (2019) 012064. https://doi:10.1088/1742-6596/1353/1/012064
16. R. Esterl, M. Sonnleitner, B. Gschöpf, R. Schnitzer, Influence of V and Nb micro-alloying on direct quenched and tempered ultra-high strength steels, *Steel Research International* **90**(6) (2019) 800640. http://dx.doi.org/10.1002/srin.201800640
17. H. Pouraliakbar, G. Khalaj, M.R. Jandaghi, M.J. Khalaj, Study of the correlation of toughness with chemical composition and tensile test results in microalloyed API pipeline steels, *Journal of Mining and Metallurgy, Section B: Metallurgy* **51**(2) (2015) 173-178. https://doi.org/10.2298/JMMB140525025P
18. R. Manojlovic, J. Magdeski, B. Rizov, Mechanical and structural characteristic of hot rolled micro-alloyed with vanadium steel sheets, 41th International October Conference on Mining and Metallurgy,Proceedings, Kladovo, Serbia, 2009, 637-642.
19. F. Siciliano, Mathematical Modelling of Hot Rolling: A Practical Tool to Improve Rolling Schedules and Steel Properties, *Materials Science Forum* **762** (2013) 210-217. http://dx.doi.org/10.4028/www.scientific.net/MSF.762.210
20. Ch. Cang, *Correlation between the Microstructure of Dual Phase Steel and Industrial Tube Bending Performance*, Degree of Master, Windsor, Ontario, Canada, 2010.
21. D.K. Matlock, G. Krauss, L.F. Ramos, G.S. Huppi, Correlation of Processing Variables with Deformation Behavior of Dual-Phase Steels, *Structure and Properties of Dual-Phase Steels*, (1979), 62-90.
22. P.D. Hodgson, R.K. Gibbs, A Mathematical Model to Predict the Mechanical Properties of Hot Rolled C-Mn and Microalloyed Steel, *The Iron and Steel Institute of Japan* **32**(12) (1992) 1329-1338. https://doi.org/10.2355/isijinternational.32.1329
23. I. Juutilainen, J. Röning, L. Myllykoski, Modelling the strength of steel plates using regression analysis and neural networks, Proceedings of *International Conference on Computational Intelligence for Modelling, Control and Automation* (2003), 681-691.

24. N. Jiratthanakul, S. Chandra-Ambhorn, Prediction of the Mechanical Properties of Hot-Rolled Low Carbon Steel Strips in Correlation to Chemical Compositions and Rolling Conditions, *Key Engineering Materials* **462-463** (2011) 401-406. http://dx.doi.org/10.4028/www.scientific.net/KEM.462-463.401

2nd Conference for Green Engineering, Sustainable Materials and Technologies for Circular Economy, GREEN CIRC 2025
PROCEEDINGS

RANDOM FOREST FOR DETECTING THORACIC PATHOLOGIES IN CHEST RADIOGRAPHS

Sijche Pechkova[1], Mile Jovanov[2]

[1]- *Ss. Cyril and Methodius University, Skopje, Faculty of Technology and Metallurgy*

[2] - *Ss. Cyril and Methodius University, Skopje, Faculty of Computer Science and Engineering*

sijche@tmf.ukim.edu.mk; mile.jovanov@finki.ukim.mk

Abstract: Thoracic diseases like pneumonia, enlarged heart (cardiomegaly), collapsed lung (pneumothorax), and lung scarring (fibrosis) are among the leading causes of illness around the world. Chest X-rays (CXRs) are the most common tool used to detect these conditions, but reading and interpreting them accurately can be very difficult. Many signs are subtle and often missed, and even experienced radiologists may disagree on the diagnosis.

To help address these challenges, we propose using a Random Forest classifier—a machine learning model known for its accuracy, speed, and ability to handle complex data. Random Forests work by combining the results of many decision trees, making them more stable and less prone to overfitting. They also handle noisy or imbalanced datasets well, which is important in medical imaging where some diseases are much rarer than others.

In our approach, we first identify key regions in the chest X-ray—such as the lungs and heart—and extract important features from those areas. These features include patterns, textures, and shapes that are often linked to specific diseases. We then use the Random Forest model to learn from these features and classify whether a patient might have a particular thoracic condition.

Compared to deep learning models, our method is much lighter, easier to interpret, and requires fewer computational resources. Despite this, it still delivers strong performance in detecting various thoracic pathologies. This makes it especially suitable for use in hospitals or clinics with limited access to high-end computing power.

Keywords Thoracic pathology, Random Forest, Decision Trees, CXR analysis.

INTRODUCTION

Thoracic diseases like atelectasis, cardiomegaly, pneumonia, and pneumothorax are serious health issues that account for over 15% of hospital admissions related to respiratory problems worldwide [7]. Chest X-rays (CXRs) are the most commonly used imaging tool for diagnosing these conditions, thanks to their low cost and fast results. However, interpreting CXRs accurately is not easy—it requires experienced radiologists and is often affected by human error. Many chest pathologies appear with subtle signs or are hidden by overlapping structures in the image, which makes diagnosis difficult [5, 9].

Chest imaging reveals various conditions with distinct appearances: atelectasis (lung collapse) demonstrates volume loss, while cardiomegaly (enlarged heart) is identified by an

increased cardiothoracic ratio. Pleural effusion presents with blunted costophrenic angles, and lung infiltration appears as diffuse haziness. Suspicious masses (>3 cm) may indicate malignancy, whereas smaller nodules require monitoring. Pneumonia typically shows lobar opacities, and pneumothorax is marked by absent lung markings. Consolidation appears as homogeneous opacities, pulmonary edema as bilateral haziness, and emphysema causes hyperinflated lungs. Fibrosis displays reticular patterns, pleural thickening suggests chronic inflammation, and thoracic hernias are identified by air-fluid levels. Each finding aids in accurate diagnosis and treatment planning.

Random Forests are a popular and powerful machine learning method used for classification and regression tasks. They are based on the idea of combining multiple decision trees to improve overall performance and reduce the risk of overfitting [2].

A single decision tree learns patterns in data by making a series of simple "yes" or "no" decisions, but it can often be too sensitive to small changes in the data. Random Forests solve this problem by creating an ensemble of decision trees, each trained on a random subset of the data and features. The final prediction is made by combining the outputs of all trees, usually through majority voting for classification tasks.

In medical imaging tasks such as chest X-ray classification, Random Forests are particularly attractive because they are easy to use, require fewer computational resources than deep learning models, and are often more interpretable to clinicians [1,4]. They are well-suited to datasets where labeled examples may be limited and where transparency in decision-making is important.

We are developing a simple and efficient framework for analyzing chest X-rays (CXRs), and tested it using the widely used NIH ChestX-ray dataset [8]. Our goal is to compare the performance of Random Forest (RF) classifiers with traditional Support Vector Machines (SVMs). We are going to evaluate all models using common performance metrics: accuracy, sensitivity, specificity, and AUC.

Random Forests offer several advantages for medical image analysis, especially in clinical settings where resources or data may be limited. Their key strengths include:

- **Easy to Interpret:** Random Forests can show which features are most important for making decisions. This helps clinicians understand why the model gave a certain result.
- **Handles Noisy** Data Well: Because they combine many decision trees, Random Forests are less affected by noisy, missing, or low-quality data—common issues in real medical images.
- **Avoids Overfitting:** Unlike SVMs with complex kernels or large deep learning models, Random Forests are less likely to overfit, especially when working with small or unbalanced datasets.
- **Fast and Resource-Efficient:** Training and running Random Forests is quick and does not require expensive hardware. This makes them usefull in hospitals or clinics with limited computing power.

- **Simple to Set Up:** Random Forests need only a few settings to work well, such as the number of trees or how deep the trees go. This makes them easier to use compared to more complex models.
- **Works Well with Preprocessed Features:** They are effective when using features from traditional image processing methods (like wavelets or texture patterns), which is helpful when deep learning cannot be applied.

METHODOLOGY

We will use the ChestX-ray dataset , which contains over 112,000 chest X-rays (CXRs) labeled for 14 diseases using natural language processing (NLP) on radiology reports. This dataset, provided by the National Institutes of Health (NIH), is one of the most widely used public resources for detecting and classifying thoracic pathologies. It includes a large collection of de-identified X-rays collected from routine clinical care.

For the feature extraction part of our machine learning pipeline, we will use the method from CheXmask: A Large-Scale Dataset of Anatomical Segmentation Masks for Multi-Center Chest X-Ray Images . This method generates anatomical segmentation masks that help identify key structures, such as the lungs and heart, in a CXR. Instead of using the whole image, which may include unnecessary background, we focus on specific areas like the lung tissue, heart outline, and costophrenic angles to extract more useful and interpretable features.

To ensure good quality feature extraction, we apply a preprocessing pipeline to the CXRs. This includes image enhancement and noise reduction techniques to make the important structures and patterns more visible, while minimizing irrelevant noise or artifacts. We use different filters in the spatial and frequency domains to enhance edges, smooth the image, and refine frequency details.

Once the images are preprocessed, we extract a variety of radiomic and texture features from the segmented anatomical regions. We do this separately for the left and right lung fields, as asymmetries can indicate conditions like fluid in one lung, pneumothorax, or localized lung consolidation.

By combining these different features, our system builds a comprehensive set of information that includes intensity statistics, spatial textures, frequency characteristics, and fractal features. This multi-dimensional approach helps the model better distinguish between normal and abnormal lung patterns, improving its accuracy and robustness for pathology detection.

To evaluate accuracy, we'll use -fold cross-validation, training the model on folds and testing on the remaining fold, repeating this process times. Cross-validation gives a more reliable estimate of model accuracy by testing on multiple data splits rather than just one train-test split. This prevents overfitting and better reflects real-world performance.

RESULTS

As previously outlined, our analysis employs a Random Forest ensemble composed of multiple classification trees. Below, we present the performance metrics for individual base classifiers (decision trees) evaluated separately for each target variable, using different depths of the trees:

Error rates for Atelectasis, Cardiomegaly, Consolidation, Edema, Effusion, Emphysema, Fibrosis, and Hernia

Depth	Atelectasis	Cardiomegaly	Consolidation	Edema	Effusion	Emphysema	Fibrosis	Hernia
1	0.111	0.111	0.111	0.111	0.111	0.111	0.111	0.111
2	0.111	0.111	0.111	0.111	0.111	0.111	0.111	0.111
3	0.111	0.111	0.111	0.111	0.111	0.111	0.111	0.111
4	0.111	0.111	0.111	0.111	0.114	0.111	0.111	0.111
5	0.111	0.111	0.111	0.111	0.117	0.111	0.111	0.111
6	0.121	0.111	0.112	0.112	0.12	0.112	0.111	0.111
8	0.123	0.111	0.113	0.113	0.124	0.111	0.111	0.111
10	0.132	0.112	0.113	0.114	0.124	0.111	0.111	0.111

Error rates for Infiltration, Mass, Nodule, Pleural Thickening, Pneumonia, and Pneumothorax

Depth	Infiltration	Mass	Nodule	Pleural Thickening	Pneumonia	Pneumothorax
1	0.111	0.111	0.111	0.111	0.111	0.111
2	0.111	0.111	0.111	0.111	0.111	0.111
3	0.112	0.111	0.111	0.111	0.111	0.112
4	0.113	0.111	0.111	0.111	0.111	0.112
5	0.115	0.112	0.111	0.111	0.111	0.113
6	0.12	0.113	0.111	0.111	0.111	0.114
8	0.124	0.114	0.112	0.111	0.111	0.116
10	0.129	0.112	0.112	0.111	0.111	0.113

CONCLUSION

We started by identifying the challenges in detecting lung diseases from chest X-ray (CXR) images and created a plan to address them. First, we selected a large, publicly available dataset with labeled examples of different lung conditions. To focus on the most important areas, we used segmentation techniques to separate the lungs and heart from the rest of

the image.

After identifying these key areas, we extracted useful features such as shape, texture, and intensity patterns that help distinguish between healthy and diseased tissue. These features were then used in our classification system.

We presented the results of Classification with Random Forests of Decision Trees. We intend to make results with different algorithms including support vector machines and neural networks. These will help us find the most effective approach for this kind of medical image analysis.

Our goal is to show that Random Forests can match the accuracy of methods like SVM and Deep Learning, while being more robust. We want to prove that Random Forests, with their ability to handle noisy data and need for fewer resources, can provide consistent and reliable results in detecting thoracic diseases from chest X-ray images. This would make Random Forests a practical choice for clinical settings where robustness and interpretability are important.

Acknowledgments This paper has been supported by the Science and Research Fund of Ss. Cyril and Methodius University in Skopje.

REFERENCES

1. R.S. Akinbo, O. A Daramola. *Ensemble machine learning algorithms for prediction and classification of medical images*, in *Algorithms, Models and Applications*, J. Sen Ed, IntechOpen, 2021, p. 59. https://doi.org/10.5772/intechopen.100602
2. L. Breiman, Random forests, *Machine learning* 45 (2001) 5-32. https://doi.org/10.1023/A:1010933404324
3. N. Gaggion, C. Mosquera, L. Mansilla, J. Mariel Saidman, M. Aineseder, D.H. Milone, E. Ferrante, Chexmask: a large-scale dataset of anatomical segmentation masks for multicenter chest x-ray images, *Scientific Data* **11**(1) (2024) 511. https://doi.org/10.1038/s41597-024-03358-1
4. M.L. Gige, Machine learning in medical imaging, Journal of the American College of Radiology **15**(3) (2018) 512-520.
5. J. Irvin, P. Rajpurkar, M. Ko, Y. Yu, S. Ciurea Ilcus, C. Chute, H. Marklund, B. Haghgoo, R. Ball, K. Shpanskaya, et al. Chexpert: A large chest radiograph dataset with uncertainty labels and expert comparison. In Proceedings of the AAAI conference on artificial intelligence, **33** (2019) p. 590–597.
6. G. Litjens, T. Kooi, B. E. Bejnordi, A.A.A. Setio, F. Ciompi, M. Ghafoorian, J.A.W. van der Laak, B. van Ginneken, C.I. Sánchez, A survey on deep learning in medical image analysis, *Medical Image Aanalysis* **42** (2017) 60–88. https://doi.org/10.1016/j.media.2017.07.005
7. G. Viegi, S. Maio, S. Fasola, S. Baldacci, Global burden of chronic respiratory diseases, *Journal of Aerosol Medicine and Pulmonary Drug Delivery* **33**(4) (2020) 171-177. https://doi.org/10.1089/jamp.2019.1576
8. X. Wang, Y. Peng, L. Lu, Z. Lu, M. Bagheri, R.M Summers, Chestx-ray8: Hospital-scale chest x-ray database and benchmarks on weakly-supervised classification and localization of

common thorax diseases, Proceedings of the IEEE Conference on Computer Vision and Pattern Recognition (CVPR) (2017) pp. 2097–2106.
9. H.M. Yang, T. Duan, D. Ding, A. Bagul, C. Langlotz, K. Shpanskaya, et al., Chexnet: radiologist-level pneumonia detection on chest x-rays with deep learning. arXiv preprint arXiv:1711.05225, 2017.

2nd Conference for Green Engineering, Sustainable Materials and Technologies for Circular Economy, GREEN CIRC 2025
PROCEEDINGS

EFFECT OF TOMATO POMACE ADDITION IN CRACKERS ON BOLUS FORMATION AND SALIVATION

Andrijana Kiroska [1], Mishela Temkov [1,*], Gjore Nakov [2], Elena Velickova Nikova[1]

[1] - *Faculty of Technology and Metallurgy, Ss. Cyril and Methodius University in Skopje, North Macedonia*

[2] - *Technical University of Sofia - College of Sliven, Burgasko Shose Blvd 59A, 8800 Mladost, Sliven, Bulgaria*

mishela@tmf.ukim.edu.mk

Abstract: *Tomatoes are among the most widely produced fruits globally, with an estimated annual production of approximately 190 million metric tons. While they are commonly consumed fresh, the majority are processed into products such as tomato juice, ketchup, purée, and sauce. These processing methods generate significant amounts of by-products, the most notable being tomato pomace. Tomato pomace is often regarded as industrial waste, posing a challenge for the food industry. However, due to its high nutritional value—particularly its rich content of dietary fiber, lycopene, and minerals—tomato pomace has potential as a functional food ingredient. Especially, dietary fiber constitutes up to 50% of its dry weight, making it a promising candidate for partial wheat flour replacement in various food applications.*

This study investigates the effect of incorporating tomato pomace as a wheat flour substitute in functional crackers, specifically examining its impact on mastication, bolus formation, and salivation. Seven trained evaluators participated in sensory tests conducted in the food laboratory at the Faculty of Technology and Metallurgy in Skopje. Each evaluator assessed a control cracker made with wheat flour and a test sample in which 5% of the wheat flour was replaced with tomato pomace (granulation: 0.5 mm). The findings provide correlation between bolus formation, bolus texture, mastication and saliva absorption in crackers containing tomato pomace.

Keywords: tomato pomace, functional crackers, food waste, textural characteristics, bolus formation.

INTRODUCTION

Modern consumers increasingly seek food products with added health benefits, encouraging the food industry to develop functional alternatives to conventional snacks. Among these, salty crackers—typically formulated from wheat flour, water, salt, sugar, leavening agents, and fat—present an opportunity for nutritional enhancement through ingredient innovation.

One effective approach to improving the nutritional profile of food products is the incorporation of dietary fiber, especially from plant-based sources, cereal by-

products, or food industry waste streams rich in bioactive compounds. Tomato pomace, a by-product of industrial tomato processing composed of tomato peels, seeds, and residual pulp, represents a promising ingredient in this context. Although commonly classified as industrial waste, tomato pomace poses both challenges and opportunities. If not appropriately managed, its high moisture and nutrient content can lead to spoilage and environmental concerns. Conversely, when valorized effectively, tomato pomace can serve as a valuable source of nutritional and functional compounds [1–3].

Tomato pomace is particularly rich in dietary fiber, proteins, carotenoids (such as lycopene), phenolic compounds, and minerals [4,5]. It also contains notable amounts of essential amino acids—especially lysine—as well as bioactive compounds including rutin, naringenin, and chlorogenic acid [5]. Due to its high dietary fiber content, tomato pomace has potential use as a partial flour substitute, reducing the caloric value of food products while offering health-promoting benefits. Dietary fiber intake is associated with a reduced risk of chronic disease development, further supporting the incorporation of such ingredients in daily diets [4].

The objective of this study was to develop functional salty crackers by partially substituting wheat flour with tomato pomace and to evaluate the impact of this substitution on texture-related properties, particularly during the processes of mastication, bolus formation, and salivation.

Two formulations of crackers were prepared: a control sample containing only wheat flour, and an experimental sample in which 5% of the wheat flour was replaced with tomato pomace (granulated to 0.5 mm). The crackers were evaluated using instrumental texture analysis, complemented by a sensory evaluation involving 7-trained panelists. Sensory tests were conducted in the food laboratory at the Faculty of Technology and Metallurgy in Skopje. The panelists assessed both cracker types in terms of ease of mastication, bolus formation, and salivation characteristics.

EXPERIMENTAL

Production of crackers

The experimental procedures were carried out in the food laboratory of the Faculty of Technology and Metallurgy, Ss. Cyril and Methodius University in Skopje. Two distinct formulations of salty crackers were prepared following a modified version of the method described by Nakov and Ivanova [7]. The control formulation consisted entirely of wheat flour, while the experimental formulation included a 5% substitution of wheat flour with tomato pomace, granulated to a particle size

of 0.5 mm.

Tomato pomace, composed of peels, seeds, and stems, was obtained as a by-product of industrial tomato processing. The pomace was dried in a hot air oven at 50 °C for 24 hours, then ground to a fine powder. The resulting material was sieved to obtain four distinct particle size fractions: >1 mm, 1 mm, 0.5 mm, and 0.25 mm. For this study, the 0.5 mm fraction was selected for incorporation into the cracker formulation.

Crackers were prepared using a two-phase dough system comprising a main dough and an oily dough. The main dough was prepared by mixing wheat flour, salt, and sugar. In the experimental formulation, 5% of the wheat flour was replaced with tomato pomace. The dry ingredients were combined with activated yeast dissolved in water, and homogenized using a hand mixer. Margarine and the remaining water were then added. The resulting dough was covered with plastic wrap and subjected to fermentation for 16 hours at 27 °C. The oily dough was prepared by mixing wheat flour, salt, sugar, baking powder, and margarine. For the experimental sample, 5% of the flour was substituted with tomato pomace. This dough was also covered with plastic wrap and fermented under refrigeration for 16 hours.

Following fermentation, the main dough was rolled out, and the oily dough was layered on top. The composite dough underwent a lamination process, involving multiple foldings and rollings to achieve uniform thickness.

The laminated dough was cut into circular shapes and baked in a preheated oven at 240 °C for 10 minutes, or until the crackers developed a golden-yellow color. The final products were allowed to cool to room temperature before subsequent texture and sensory analysis.

Table 1 *Recipes for control sample and sample with fraction 0.5 mm*

	Control sample		Sample with fraction 0.5 mm	
Ingredients (g)	Main dough	Oily dough	Main dough	Oily dough
Wheat flour T500	250	52.5	237.5	49.875
Tomato pomace	/	/	12.5	2.625
Yeast	6.25	/	6.25	/
Salt	3.75	0.94	3.75	0.94
Sugar	3.125	/	3.125	/
Margarine	37.5	40	37.5	40
Baking powder	/	1	/	1
Water	100	/	100	/

The recipes used are shown in table 1.

Bolus formation and salivation

Bolus formation and salivation characteristics of the cracker samples were evaluated using a TA.XT texture analyzer (Stable Micro Systems, UK). Prior to analysis, the instrument was calibrated using a 1000 g standard weight placed at a designated position.

Texture Profile Analysis (TPA) was performed using the instrument's standard software. The following input parameters were configured prior to each measurement: sample weight (24 g), sample height (20 mm), diameter (46 mm), and probe contact surface area (314.16 mm^2). A cylindrical P/20 probe (20 mm diameter) was employed for all analyses. The probe penetrated the sample at a constant speed of 5 mm/s, retracted at the same speed, and after a 5-second pause, performed a second identical compression cycle.

Samples were prepared by instructing each evaluator to chew a portion of crackers until a swallowable bolus consistency was achieved. The resulting bolus was expectorated into a plastic measuring cup and leveled to ensure a uniform height of 20 mm. The cup was then placed under the probe on the analyzer platform.

Bolus hardness was recorded as the peak force during the first compression. Stickiness was determined from the negative peak force upon the probe's first retraction. Cohesiveness was assessed by comparing the area under the force-time curve for the first and second compressions.

Samples were prepared by instructing each evaluator to chew a portion of crackers until a swallowable bolus consistency was achieved. The resulting bolus was expectorated into a plastic measuring cup and leveled to ensure a uniform height of 20 mm. The cup was then placed under the probe on the analyzer platform.

Bolus hardness was recorded as the peak force during the first compression. Stickiness was determined from the negative peak force upon the probe's first retraction. Cohesiveness was assessed by comparing the area under the force-time curve for the first and second compressions. The percentage of absorbed saliva in the bolus is calculated in the following way:

$$\text{Saliva } (\%) = \left[\left(\frac{W_1}{D_1}\right) * D_2\right] - W_2$$

where:
W_1 – content of moisture in bolus (%)
D_1 – dry matter of bolus (%)
D_2 – dry matter of sample (%)
W_2 – content of moisture in sample (%).
The method for bolus formation and salivation was performed with 7 examiners,

testing the control sample and the recipe with 5% tomato pomace fraction 0.5 mm.

RESULTS AND DISCUSSIONS

Food texture plays a critical role in the mastication process, directly influencing parameters such as chewing effort, salivation, and the subsequent release of flavor compounds, odors, and volatile aromas within the oral cavity. During mastication, food is mechanically broken down and simultaneously hydrated by saliva, increasing the surface area of the food matrix that interacts with the enzymatic and biochemical components of saliva, including salts, proteins, and enzymes. This interaction results in structural and compositional modifications that facilitate bolus formation and swallowing.

In the case of crackers, the presence of a fine porous structure enhances these interactions. The small, interconnected pores promote capillary action, facilitating rapid hydration. As the cracker matrix absorbs saliva, cohesion is established between water molecules within the food structure and the components of saliva, resulting in greater moisture retention and integration within the bolus.

The results of the TPA measurements (for hardness, cohesiveness, stickiness, chewiness, elasticity and gumminess) are presented in histograms (Figures 1–8), providing a comparative overview of the control and tomato pomace-substituted samples.

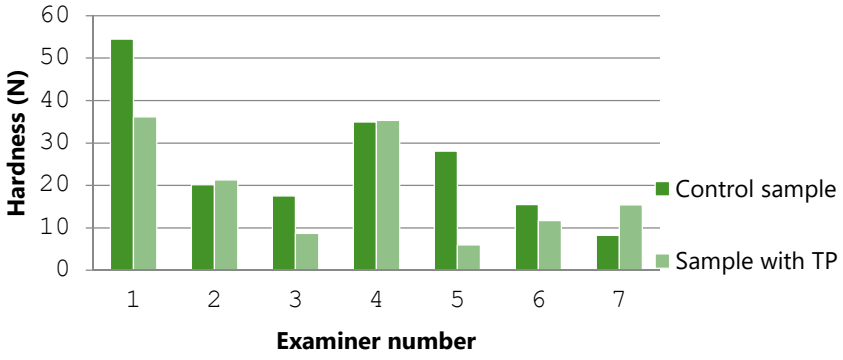

Figure 1 *Bolus hardness*

The results indicate that the control sample produced a significantly harder bolus compared to the sample containing a 5% substitution of wheat flour with tomato pomace. The incorporation of tomato pomace contributed to a softer bolus texture, suggesting a modification of the internal structure of the cracker matrix during mastication. Notably, for the first evaluator, both samples exhibited

relatively high bolus hardness, which may be attributed to a lower proportion of saliva absorption. Increased salivary absorption is generally associated with reduced bolus hardness, as the structural integrity of the food matrix is progressively weakened. This is likely due to the enzymatic activity of salivary amylase, which hydrolyzes starch during mastication, thereby facilitating the softening of the bolus. The presence of dietary fiber in tomato pomace may further promote water retention and interaction with saliva, enhancing the formation of a cohesive and less rigid bolus.

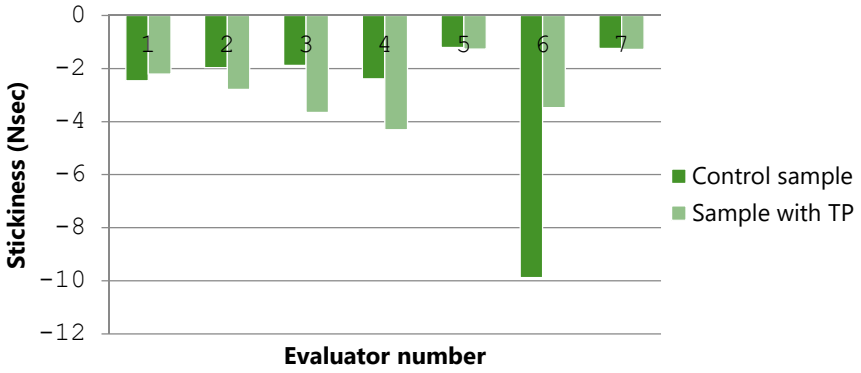

Figure 2 *Bolus stickiness*

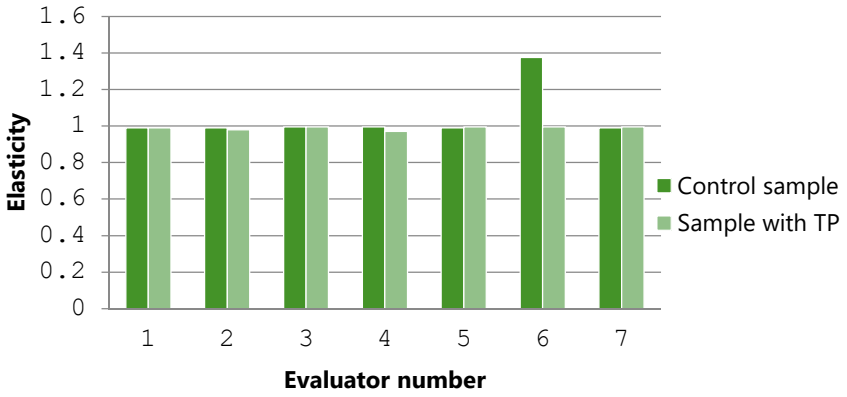

Figure 3 *Bolus elasticity*

Stickiness was most prominently observed in the results of Examiner 6, particularly for the control sample. However, a general trend across all evaluators indicates that the samples containing tomato pomace exhibited higher stickiness values compared to the control samples. This increase in stickiness may be attributed to the presence of dietary fiber and other hydrophilic components in the tomato

pomace, which enhance water-binding capacity and interaction with saliva, thereby increasing the adhesive properties of the bolus.

Elasticity reflects the ability of a deformed material to recover its original shape following the removal of an applied force. Among the elasticity measurements, only one sample deviated notably from the general trend—specifically, the control sample evaluated by Examiner 6, which exhibited a significantly higher elasticity value compared to all other samples. This suggests potential individual variation in mastication dynamics or bolus formation that may influence the mechanical response of the sample.

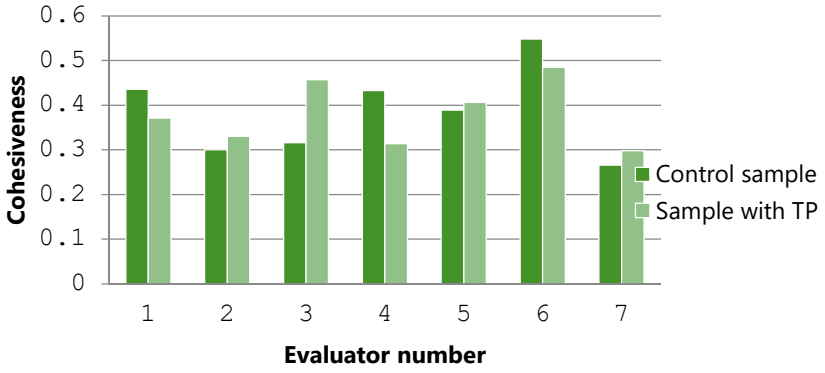

Figure 4 *Bolus cohesiveness*

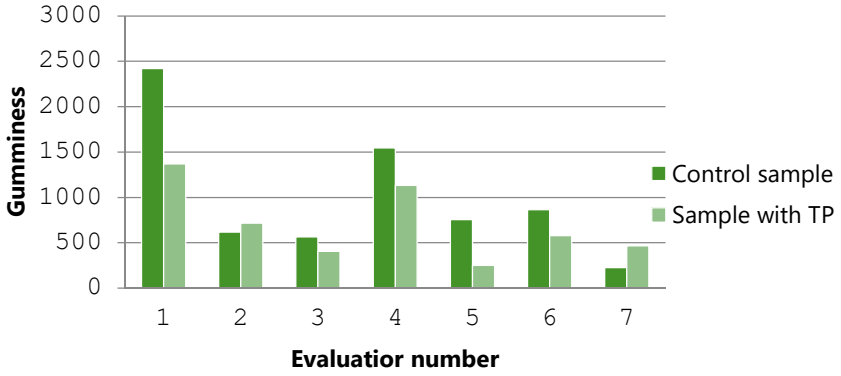

Figure 5 *Bolus gumminess*

Cohesiveness represents the degree to which particles within the food matrix tend to bind together during mastication, particularly through interactions with saliva during lubrication and agglomeration. The variation in cohesiveness values appears to be more strongly influenced by the individual mastication behavior of

the evaluators rather than the formulation of the sample itself. Notably, the results for Examiner 6 indicated the highest level of cohesiveness, suggesting enhanced interaction and binding between the sample particles and salivary components during bolus formation.

With respect to gumminess, the highest values were recorded for the bolus formed from the control samples. Gumminess represents the amount of energy required to disintegrate a semi-solid food to a state suitable for swallowing. The elevated gumminess values observed in the control group indicate that greater masticatory effort is necessary to achieve a swallowable consistency, in comparison to the samples containing tomato pomace.

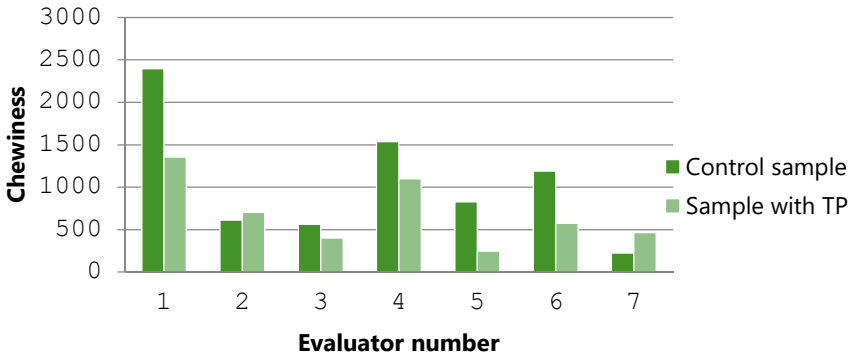

Figure 6 *Bolus chewiness*

Chewiness quantifies the amount of energy required to masticate a solid food until it reaches a swallowable state. The results indicate that the control samples exhibited higher chewiness values compared to those containing tomato pomace, suggesting that greater masticatory effort is required to process the control samples. The incorporation of tomato pomace appears to reduce the structural resistance of the crackers, thereby facilitating easier breakdown during chewing. The results for absorbed saliva content, number of bites and chewing time are presented in figures 7 and 8.

As shown in Figure 7, the control samples exhibited higher values for absorbed saliva compared to the samples containing tomato pomace, indicating greater salivary uptake. This suggests that the control crackers were comparatively drier, requiring more moisture for adequate bolus formation. When correlating the absorbed saliva percentage with the number of masticatory cycles, a trend emerges whereby increased salivary absorption is associated with a reduced number of bites and shorter chewing time. The number of bites may serve as an

indirect indicator of sample hardness, with harder samples necessitating more chewing effort. These findings suggest that control samples were harder than those with tomato pomace. The data show longer chewing duration for control samples, confirming that more bites lead to longer mastication.

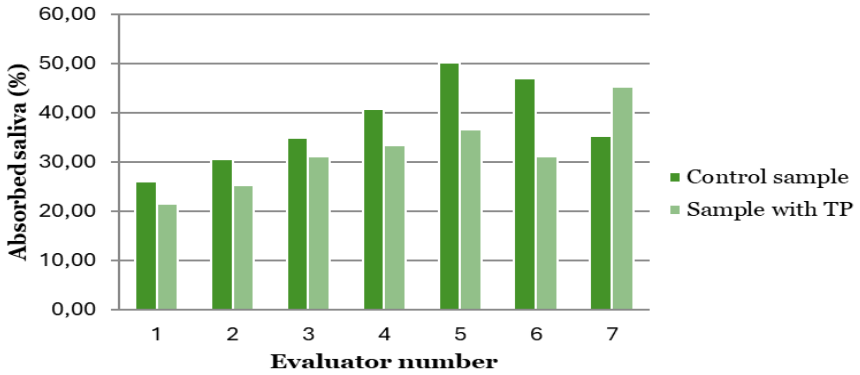

Figure 7 *Absorbed saliva in bolus*

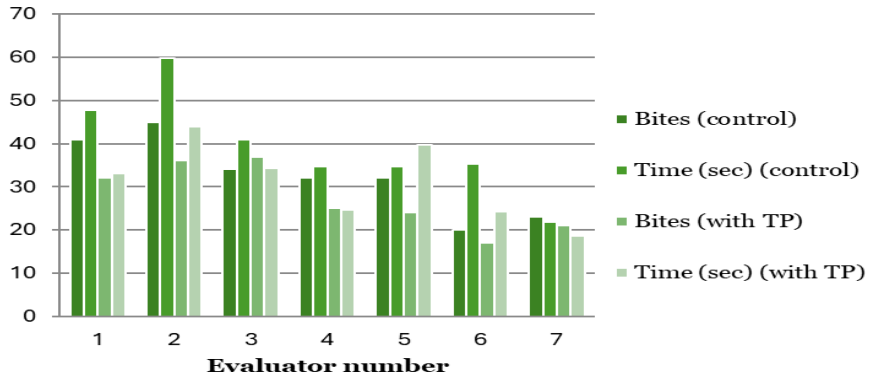

Figure 8 *Number of bites and chewing time*

CONCLUSIONS

The results show that tomato pomace samples had lower bolus parameter values, fewer bites, and shorter chewing time, indicating softer texture and improved oral comfort compared to the control.

REFERENCES

1. M. Del Valle, M. Cámara, M.E. Torija. Chemical characterization of tomato pomace., *Journal of the Science of Food and Agriculture* **86** (2006) 1232-1236. https://doi.org/10.1002/jsfa.2474
2. Z. Lu, J. Wang, R. Gao, F. Ye, G. Zhao. Sustainable valorization of tomato pomace: A comprehensive review. *Trends in Food Science & Technology* **86** (2019) 172-187. https://doi.org/10.1016/j.tifs.2019.02.020
3. V. Nour, M.E. Ionica, I. Trandafir. Bread enriched in lycopene and other bioactive compounds by addition of dry tomato waste. *Journal of Food Science Technology* **52** (2015) 8260-8267. https://doi.org/10.1007/s13197-015-1934-9
4. F. Isik, C. Topkaya. Effects of tomato pomace supplementation on chemical and nutritional properties of crackers. *Italian Journal of Food Science* **28** (2016) 525-535. https://doi.org/10.14674/1120-1770/ijfs.v510
5. Z. Özbek Aksoylu, K. Çelik, P. G. Ergönül, A. Z. Hepiçimen. A promising food waste for food fortification: Characterization of dried tomato pomace and its cold pressed oil. *Journal of Food Chemistry & Nanotechnology* **6** (2020) 9-17. https://doi.org/10.17756/jfcn.2020-078
6. G. Nakov, N. Ivanova. The effect of different methods for production of crackers on their physical and sensory characteristics. *Technologica Acta* **13** (2020) 41-45. https://hrcak.srce.hr/ojs/index.php/technologicaacta/article/view/17494/9368

APPLICATION OF EDIBLE COATINGS ON FRESH-CUT CELERY

Irina Mladenoska*, Maja Kochoska

Faculty of Technology and Metallurgy, Ss. Cyril and Methodius University in Skopje, North Macedonia

irina@tmf.ukim.edu.mk

Abstract: *In this project we investigated the effect of edible coatings used to extend the shelf life of the celery. The research was conducted through 10-day and 18-day monitoring period. The celery pieces were stored both in the refrigerator and at a room temperature. The idea for this topic stems from the common issues faced by consumers regarding the freshness, color, texture, and shelf life of vegetables and fruits.*

For this experiment we used pieces of celery and edible coatings made from gelatin, sodium alginate, starch. Spices were applied according to their flavor and functional properties. Additionally, as an extra trial, the coated celery were packed in low-density polyethylene (LDPE) packaging in the presence of nitrogen and air. Those samples were also stored at a room temperature and in the refrigerator. Changes in color, texture, mass, smell and taste were monitored.

The purpose of this research was to compare the characteristics of edible coatings and assess their ability to extend the shelf life of the celery. The edible coatings were evaluated based on factors such as coating thickness, mass loss of the product, color change, optical properties, and textural characteristics.

Keywords: gelatin, starch, Na-alginate, nitrogen, spices, celery

INTRODUCTION

Nowadays consumers are looking for products that are safe for consumption with certain sensory properties and biological value. With the increase of population the need for food increases and with it the need for a more complete utilization of raw materials. Vegetables are one of the most sought-after food products and have an important place in the human diet. Although some vegetables are available seasonally, they are demanded throughout the whole year due to their high nutritional value. When fresh they are sensitive to external influences and prone to rapid decomposition and therefore it is necessary to apply various techniques to preserve their freshness, appearance, texture, aroma and color. Recently, new ways of packaging and storing vegetables and fruits have been investigated in order to extend their shelf life and to be able to be used for a longer period of time, even during periods of the year when they are not produced. One way to achieve this is by applying edible coatings and films. This technique of minimal processing is involving thin layers of biopolymers that

are used for coating, packaging, wrapping food, i.e. a thin layer of material applied to fresh or processed food that the consumer can consume together with the food. The main function of edible films and coatings is to minimize the interaction of products with the external environment. This refers to the absorption or release of moisture, transport of gases, migration of oils, loss of aromatic components and contamination with microorganisms. Edible coatings or films that are also used as carriers of additives, aromas, enzymes, antioxidants, antibacterial substances and more, can be based on carbohydrates, proteins, lipids and composites.

The aim of this work is to investigate how edible coatings affect the shelf life of celery. The best solution, which meets the above criteria, is the use of biosynthetic coatings such as alginate, chitosan, gelatin, starch, pectin and many others.

The procedure for preserving the celery with an edible coating was performed with using the following materials: Na-alginate, gelatin and corn starch. In order to improve and extend the shelf life of the celery, the samples of this product were also packed in an anaerobic atmosphere of nitrogen as a gas, as well as in air atmosphere. During the experiment changes in color, mass of celery, texture and taste were monitored. The research in this work focuses on studying the influence of edible coatings of corn starch, sodium alginate and gelatin on the qualitative parameters of celery samples. Additionally, as an innovative approach, some of the samples were packaged in low-density polyethylene (LDPE) packaging in an atmosphere of nitrogen and air in order to investigate their impact on celery degradation.

EXPERIMENTAL

For the purpose of this experiment seven formulations of edible coatings with varying concentrations were applied, based on corn starch, sodium alginate, and gelatin. Spices compatible with the characteristics of the celery were added to enhance the organoleptic properties, while simultaneously contributing to the antimicrobial effects of the coating. It is expected that the edible coatings will reduce the degree of mass and moisture loss, while also preventing changes in visual characteristics, color, and texture. The celery, which has been washed and cut into appropriate size, is ready for the application of the coating. The brushing method was used as the most suitable technique for coating, except for the formulation number six, where application method is dipping and cross-linking.

Table 1 *Edible Coating Formulations for Celery Slices*

	Base Composition	Additives	Preparation	Application
F1	- 60 ml distilled water - **7,2%** w/v beef gelatin - 30 ml olive oil	- 2.1% garlic powder - 2.3% salt	Gelatin dissolved, cooled, olive oil added, spices were added and mixed.	Brushing
F2	- 60 ml distilled water - **0,7%** w/v beef gelatin - 30 ml olive oil	- 1% garlic - 1,2% salt	Same as F1	Brushing
F3	- 60 ml distilled water - **3,6%** w/v beef gelatin - 20 ml olive oil	- 1,3% garlic - 1,3% salt	Same as F1	Brushing
F4	- 30 ml distilled water - **3,2%** w/v beef gelatin - 30 ml distilled water - **2,5%** w/v beef gelatin - 4 ml olive oil	- 1,5% garlic - 1,5% salt	Gelatin dissolved, cooled, olive oil added, spices were added and mixed.	Brushing
F5	- 300 ml distilled water - **2%** sodium alginate - 1% v/v glycerol - 1% calcium chloride (separate bath)	4 samples with individual spices: 0,5% each of garlic, pepper, thyme, salt.	Alginate dissolved in water, glycerol added, mix split and spiced. Celery dipped, then cross-linked in $CaCl_2$.	Dipping + Cross-linking

F6	- 200 ml distilled water - **5%** w/v corn starch - 0.5% citric acid	4 samples with individual spices: - 0,5% each of garlic, black pepper, thyme, salt.	Base mixture divided into 4 parts, each mixed with one spice	Brushing
F7	- 120 ml distilled water - **4,2%** beef gelatin - 20 ml olive oil	4 samples with individual spices: 0,1% each of garlic, pepper, thyme, salt.	Gelatin dissolved, cooled, then olive oil added. Mixture split, spices added.	Brushing

For the third formulation the coating was prepared and applied accordingly. The coated slices were then dried at room temperature and packaged in low-density polyethylene (LDPE) bags, sealed on the filling side. Packaging was performed in an atmosphere with nitrogen with three celery slices per bag. The packages were stored at both room temperature and under refrigeration. Throughout the storage period, changes in packaging and celery quality were monitored. Additionally, a sensory evaluation was carried out on celery slices coated with formulations and stored in the refrigerator under open-air conditions.

RESULTS AND DISCUSSIONS

The mass of the control samples and samples with applied edible coating, stored at room temperature and in a refrigerator, was measured over a period of 10 and 18 days. The weight loss rates of all samples were calculated in order to compare the rate of deterioration between coated and uncoated samples, as well as to identify the edible coating formulation that yields the best results. We used the following formula:

Mass Loss (%) = [(Initial Mass – Final Mass) / Initial Mass] × 100

Storage at low temperature, in a refrigerator, significantly reduced the rate of weight loss compared to storage at room temperature, highlighting the importance of controlled conditions in preserving minimally processed celery. Packaging in a nitrogen atmosphere at room temperature and in a refrigerator did not yield positive results, as it led to softening, undesirable odors, and the appearance of mold and bacteria, likely due to anaerobic degradation processes (Fig.1 and Fig. 2).

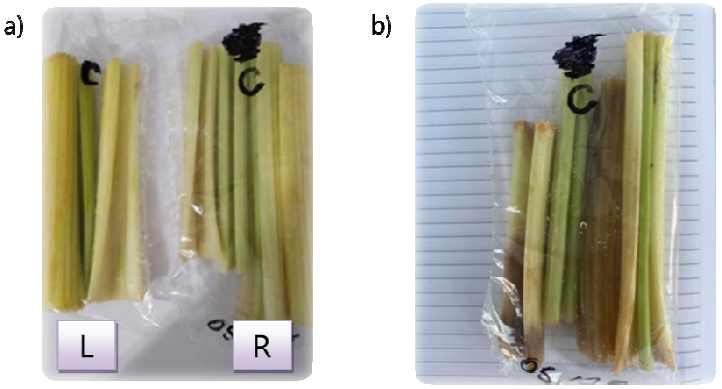

Figure 1 *Nitrogen-packaged samples stored at room temperature: a) 2nd day, control sample (left) and edible coating (right); b) 7th day edible coating.*

Water droplets on the inner side of the bag in the nitrogen packaging are most likely a result of condensation. The cause of water droplet formation in the bag is the temperature difference. The plastic bag, hermetically sealed, prevents moisture from escaping, creating a microclimate with high relative humidity over time.

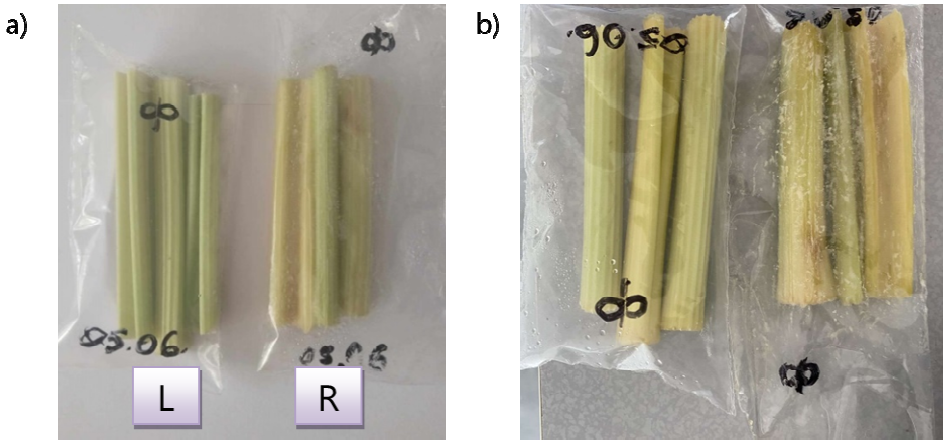

Figure 2 *Nitrogen-packaged samples stored in the refrigerator: a) 2nd day, control sample (left) and edible coating (right); b) 7th day, control sample (left) and edible coating (right).*

Texture deterioration (softening) is likely due to the increased metabolic activity and the transformation of starch and other polysaccharides into sugar, along with water evaporation, which reduces cell turgor. Anaerobic catabolism is the

main factor contributing to the development of undesirable flavors and aromas, softening, and the formation of a slimy, moist surface. In this case, putrefactive bacteria occur. High humidity can be a significant factor contributing to the development of putrefactive bacteria. The change in color from green to brown is a signal of a the process of decomposition. These changes are associated with the activity of bacteria, fungi and enzymes that affect the plants and can cause significant changes in food quality.

We can conclude that the edible coating with sodium alginate does not provide sufficient protection (Fig.3). It can be assumed that it is due to the hydrocolloid quality of this coating that it cannot provide very good protection against the drying and the weight loss of the moisture.

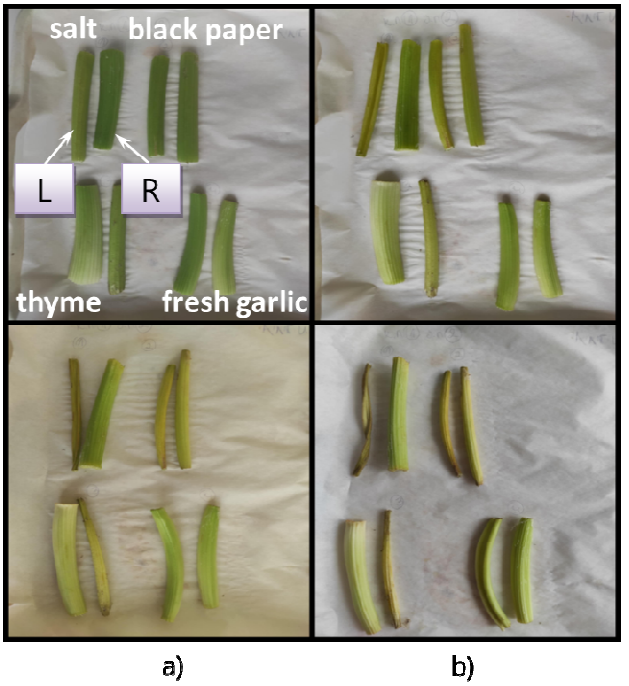

Figure 3 *Celery slices coated with sodium alginate-based edible coating with 4 spices: 1. Salt; 2. Black pepper; 3. Thyme; 4. Fresh garlic; Left: control samples, right: edible coatings. a) day 1; b) day 18 of monitoring.*

The lowest degree of mass loss was observed in celery pieces with a starch coating with black pepper (Fig. 4).

Black pepper proved to be a good antimicrobial agent.

The high degree of shedding was observed in samples with a starch coating with added salt.

The mass recorded a constant decrease over time. However, the obtained values for the degree of mass loss are close to those of the control samples.

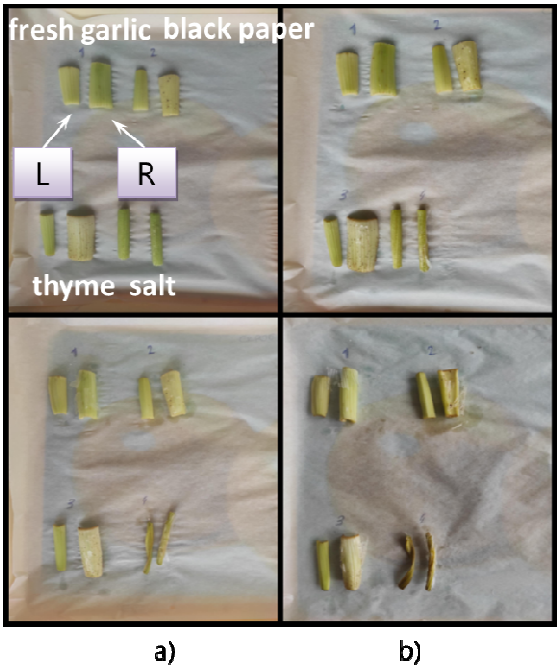

Figure 4 *Celery slices coated with starch edible coating with 4 spices: 1. Fresh garlic; 2. Black pepper; 3. Thyme; 4. Salt. Left: control sample; right: edible coatings: a) day 1; b) day 18 of monitoring.*

The starch coating without added plasticizer is not a good barrier to water. The edible coating served as a barrier against visible microbiological spoilage and contributed to color retention.

Visually the celery slice with the edible coating containing salt appeared the best, followed by the ones with fresh garlic and black pepper. The slices were rough, with an uneven, rough surface. The mass showed a constant decrease over time. The obtained values for the degree of mass loss are close to those of the control samples.

The most effective coating among all those tested was the gelatin and olive oil formulation (Fig. 5).

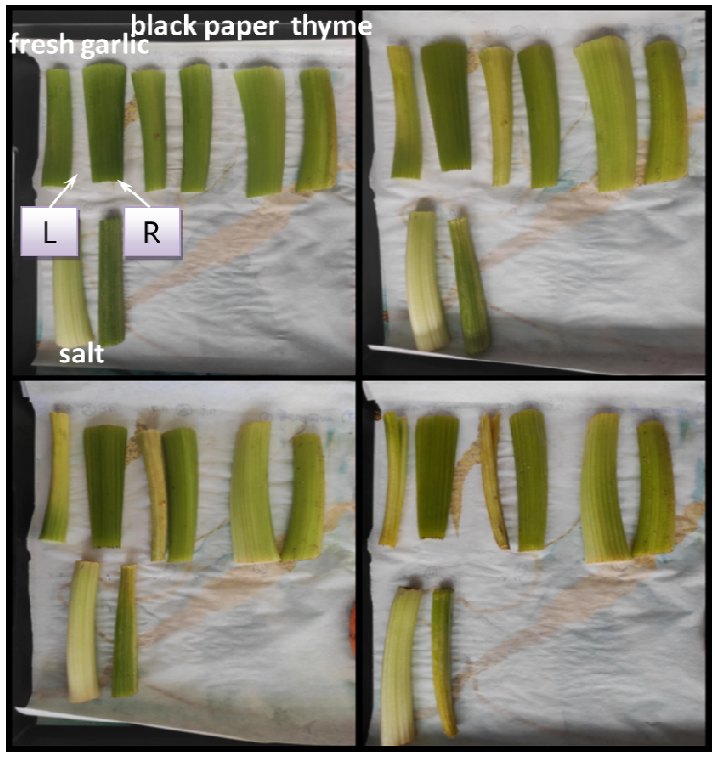

Figure 5 *Celery pieces coated with an edible gelatin and olive oil coating with 4 spices: 1. Fresh garlic; 2. Black pepper; 3. Thyme; 4. Salt. Left: control samples; right: edible coatings. a) day 1; b) day 18 of monitoring.* The best results from the gelatin coatings were achieved with formulation number 2 with 0,7% beef gelatin, 30 ml olive oil, 1% garlic and 1,2% salt (w/v).

On the first day, celery pieces treated with this coating displayed a fresh appearance, an intense green color, and a smooth, glossy surface, attributed to the presence of olive oil. By the eighteenth day, this coating demonstrated the least moisture loss. Although the texture became slightly elastic, the surface remained hydrated, unlike in other treatments where drying was evident. The color not only remained stable, but appeared even more vibrant. The green color was well preserved, with no visible signs of discoloration or spoilage. However, changes in texture were noticeable by day 8, indicating that the coating maintains optimal quality for up to 8 days under refrigerated storage.

Regarding weight loss, the gelatin and olive oil coating infused with black pepper and thyme yielded the best results. The results of the mass loss of some formulations are presented in the Table 2.

Table 2 *Mass loss of the samples coated with edible coatings prepared with different formulations and compared to the control sample*

Edible coating formulation	Mass loss rate with edible coating %	Mass loss rate of control sample %
Edible coating with gelatin (second formulation)	24,59%	46,32%
Edible coating with gelatin (third formulation)	49,68%	72,73%
Edible coating with gelatin (fifth formulation)	47,98%	62,48%
Sodium alginate-based edible coating (sixth formulation)	50,98%	66,18%
Starch edible coating (seventh formulation)	63,99%	61,86%
Edible coating with gelatin (eight formulation)	28,23%	44,60%

It is obvious that the result of 24.59% of the mass loss (formulation 2), compared to the control one with 46.32% of the control one, was the best result obtained.

It can be assumed that this is the result of the addition of the oil to the gelation biopolymer, and thus the coating could better prevent drying of the product and its mass loss.

CONCLUSIONS

Edible coatings and films are one of the modern techniques of minimal food processing and are used to extend the shelf life of the products. They have been used especially in recent years, because they have many advantages as retaining the food properties and biodegradability in nature. This contributes to reducing environmental pollution. The aim of this work was to prove whether and how edible coatings will affect the appearance, aroma, taste, texture of celery slices. The research was carried out using chopped celery slices and edible coatings.

From the results obtained it can be concluded that edible coatings have a positive effect on celery. They retain moisture in the celery, act as a barrier to certain gases, maintain the freshness of the fruit, and improve the texture of the product. The edible gelatin coating shows very good results compared to other coatings, with a 30-50% lower degree of spoilage. Its utilization resulted in mass loss prevention. The formulation 2 of the edible coating, the one that consisted of gelation and olive oil, showed best results with only 24. 59% of mass loss. From the given pictures we can see that celery pieces that are not coated with an edible coating quickly darken and dry out, and these are the consequences of enzymatic oxidation of phenolic compounds. For the reaction to occur, it is necessary to establish contact between phenolic compounds that are predominantly located in the vacuoles and oxidative enzymes that are located in the cytoplasm, in the presence of oxygen. This darkening can be prevented in several ways, including minimal processing with an edible coating.

REFERENCES

1. M.A. Rojas-Grau., R. Soliva-Fortuny, O. Martin-Belloso, Edible coatings to incorporate active ingredients to fresh-cut fruits: a review, *Trends in Food Science & Technology* **20** (2009) 438-447. https://doi.org/10.1016/j.tifs.2009.05.002
2. F.M. Pelissari, D.C. Ferreira, L. Batista Louzada, F. dos Santos, A.C. Correa, F.K. Vieira Moreira, L.H. Mattoso, *Starch-Based Edible Films and Coatings: An Eco-friendly Alternative for Food Packaging*, in *Chemical, Technological and Health Properties*, M.T.P.S. Clerici, M. Schmiele Eds., 2025 Elsevier B.V., 2019, pp. 359-420. https://doi.org/10.1016/B978-0-12-809440-2.00010-1
3. E.M. Zactiti, T.G. Kieckbusch, Release of potassium sorbate from active films of sodium alginate crosslinked with calcium chloride, *Packaging Technology and Science* **22** (2009) 349-358. https://doi.org/10.1002/pts.860
4. D. Lin, Y. Zhao, Innovations in the development and application of edible coatings for fresh and minimally processed fruits and vegetables, *Comprehensive Reviews in Food Science and Food Safety* **6** (2007) 60-75. https://doi.org/10.1111/j.1541-4337.2007.00018.x

APPLICATION OF EDIBLE COATINGS ON FRESH-CUT CARROTS

Irina Mladenoska*, Elena Tancheva

Faculty of Technology and Metallurgy, Ss. Cyril and Methodius University in Skopje, North Macedonia

irina@tmf.ukim.edu.mk

Abstract: *This work investigates and examines the impact of edible coatings used to extend the shelf life of carrots. The research was conducted through 10-day and 18-day monitoring of chopped carrot pieces coated with edible coatings, stored in a refrigerator and at room temperature.*

Carrot is a root vegetable that is widely available in our region, inexpensive, and rich in nutrients. Therefore, carrots were chosen for the experiment and were preserved with edible coatings made from gelatin, sodium alginate, starch, and spices that enhance flavor and are suitable according to their function. The formulations were adjusted to achieve the best results. For two of the edible coatings, starch and gelatin, a sensory analysis was conducted over a period of 10 and 18 days. Additionally, as an extra trial, the coated carrots were packed in low-density polyethylene (LDPE) packaging in the presence of nitrogen and air and stored at room temperature and in the refrigerator. At precisely determined storage intervals, changes in color, texture and optical properties were monitored.

The aim of this research is to compare the characteristics of the applied edible coatings and to extend the shelf life of ready-to-use carrot pieces. The applied edible coatings on carrots, in various concentrations, were characterized in terms of determining the degree of mass loss of the coated products, color and texture changes, as well as optical properties. As part of this study, the benefits of edible coatings are also discussed.

Keywords: Chopped carrot pieces, Edible coatings, Nitrogen atmosphere, Polyethylene bags, Spices

INTRODUCTION

In a world where healthy eating and convenience are increasingly important to the modern consumer, and the fast-paced lifestyle highlights the need to reduce meal preparation time, carrot slices with edible coatings represent an innovative solution for a functional and on-the-go healthy snack that offers both natural freshness and prolonged shelf life. This approach maintains the concept of a minimally processed, natural, and environmentally sustainable product.

Carrots, as one of the most widely consumed vegetables with high nutritional value, are used in various culinary applications—both fresh and cooked. However, their freshness rapidly declines after cutting. Fresh-cut produce undergoes tissue damage, which leads to cellular disruption, biochemical

degradation, physiological changes, loss of texture and nutritional value, increased microbial growth, reduced shelf life and an overall decline in quality. The need to extend shelf life and preserve the original characteristics of fresh vegetables without synthetic additives opens the door to the application of edible coatings—thin layers of natural ingredients that form a protective barrier around minimally processed carrot slices, preserving their freshness and quality.

This research work focuses on studying the effects of edible coatings made from corn starch, sodium alginate, and gelatin on the quality parameters of carrot slices. Additionally, as an innovative approach, some samples were packaged in low-density polyethylene (LDPE) under nitrogen and air atmospheres to investigate their impact on carrot degradation. The mass of control samples was measured alongside each trial to compare coated carrot slices with uncoated ones.

The results obtained by monitoring changes in visual characteristics, texture, color, aroma, taste, and mass of the carrots will provide valuable insights into their application in the food industry, with the potential for developing new, practical, and healthy products for the market.

EXPERIMENTAL

For the purpose of this experiment, six formulations of edible coatings with varying concentrations of basic components were applied, based on corn starch, sodium alginate and gelatin. Spices compatible with the characteristics of carrots were added to enhance their organoleptic properties while simultaneously contributing to the antimicrobial effects of the coating. It is expected that the edible coatings will reduce the degree of mass and moisture loss, while also preventing changes in visual characteristics, color, and texture. The carrot, which has been washed, peeled, and cut into thin strips, is ready for the application of the coating. The brushing method was used as the most suitable technique for coating, except for the formulation number 5, where application method is dipping and cross-linking.

Table 1 *Edible Coating Formulations for Carrot Slices*

Formulation	Base Composition	Additives	Preparation	Application
F1	- 200 ml distilled water - **10%** w/v corn starch	- 2.5% ginger - 2.5% turmeric - 2.5% citric acid - 1% salt	Starch heated with water to form gel; while warm, spices and acid added and mixed	Brushing

F2	- 200 ml distilled water - **5%** w/v corn starch	- 2.5% ginger - 2.5% turmeric - 1% citric acid - 1% salt	Same as F1	Brushing
F3	- 200 ml distilled water - **5%** w/v corn starch	- 1% ginger - 1% turmeric - 1% citric acid - 1% salt	Same as F1	Brushing
F4	- 200 ml distilled water - **5%** w/v corn starch - 0.5% citric acid	6 samples with individual spices: - 1% each of garlic, black pepper, thyme, salt, ginger, turmeric	Base mixture divided into 6 parts, each mixed with one spice	Brushing
F5	- 400 ml distilled water - **2%** sodium alginate - 1% v/v glycerol - 1% calcium chloride (separate bath)	6 samples with individual spices: - **1%** each of turmeric, ginger, salt, pepper, garlic, thyme	Alginate dissolved in water, glycerol added, mix split and spiced. Carrots dipped, then cross-linked in $CaCl_2$	Dipping + Cross-linking
F6	- 120 ml distilled water - **0.5%** beef gelatin - 20 ml olive oil	6 samples with individual spices: **1%** each of garlic, pepper, thyme, salt, ginger, turmeric	Gelatin dissolved, cooled, then olive oil added. Mixture split, spices added.	Brushing

For the third formulation, the coating was prepared and applied accordingly. The coated slices were then dried at room temperature and packaged in low-density

polyethylene (LDPE) bags, sealed on the filling side. Packaging was performed in two different atmospheric conditions: nitrogen and ambient air, with three carrot slices per bag. The packages were stored at both room temperature and under refrigeration. Throughout the storage period, changes in packaging and carrot quality were monitored. Additionally, a sensory evaluation was carried out on carrot slices coated with formulation 3 and stored in the refrigerator under open-air conditions.

The mass of the control samples and samples with applied edible coating, stored at room temperature and in a refrigerator, was measured over a period of 10 and 18 days. Based on the collected mass data, the weight loss rates of all samples were calculated in order to compare the rate of deterioration between coated and uncoated samples, as well as to identify the edible coating formulation that yields the best results. We used the following formula:

Mass Loss (%) = [(Initial Mass – Final Mass) / Initial Mass] × 100

RESULTS AND DISCUSSIONS

We expected the applied coatings to prevent dehydration, color changes, delay texture degradation, and inhibit the development of microbiological processes. Additionally, a sensory analysis was conducted on the starch- and gelatin-based formulations. It is assumed that the added spices will enhance and intensify the aroma and flavor of the carrots. Furthermore, the active compounds present in the spices may possess antioxidant properties and act as antimicrobial agents within the coating. The visual appearance was evaluated in terms of color and shape, surface characteristics, and texture.

Figure 1 *Nitrogen-packaged samples stored at room temperature: a) 5th day, control sample (left) and edible coating (right); b) 10th day, control sample (left) and edible coating (right)*

Storage at low temperature, in a refrigerator, significantly reduced the rate of weight loss compared to storage at room temperature, highlighting the importance of controlled conditions in preserving minimally processed carrots (Figure 1 and Figure 2). Packaging in a nitrogen atmosphere at room temperature did not yield positive results, as it led to softening, undesirable odors, and the appearance of slimy surfaces, likely due to anaerobic catabolism.

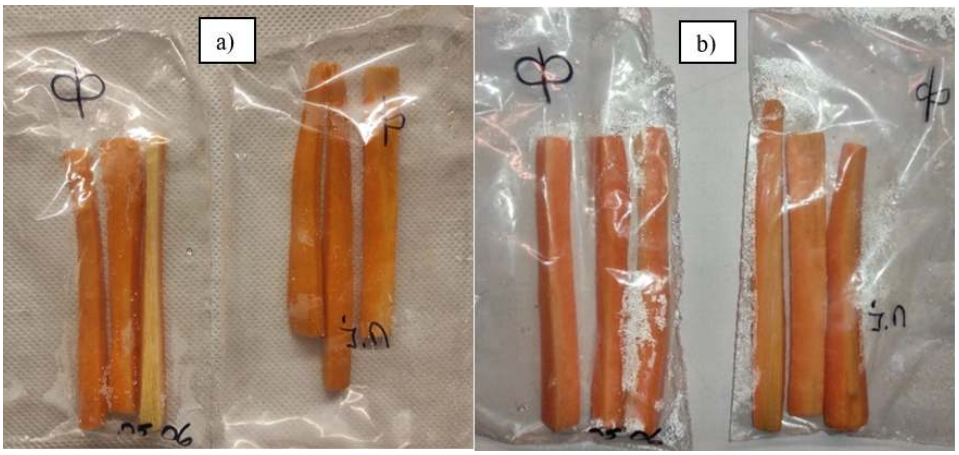

Figure 2 *Nitrogen-packaged samples stored in the refrigerator: a) 1st day, control sample (left) and edible coating (right); b) 10th day, control sample (left) and edible coating (right).*

Water droplets on the inner side of the bag in the nitrogen packaging are most likely a result of condensation. The cause of water droplet formation in the bag is the temperature drop. The plastic bag, hermetically sealed, prevents moisture from escaping, creating a microclimate with high relative humidity over time. Texture deterioration – softening is likely due to increased metabolic activity and the transformation of starches and polysaccharides into sugars, along with water evaporation, which reduces cell turgor. Anaerobic catabolism is the main factor contributing to the development of undesirable flavors and aromas, softening, and the formation of a slimy, moist surface. Therefore, we concluded that packaging with a high nitrogen content is not the most suitable for carrot slices unless accompanied by proper storage conditions. Due to the anaerobic atmosphere and the high respiration rate, undesirable quality changes occur rapidly.

On the other hand, air-packaged samples (around 21% oxygen and 78% nitrogen) stored at refrigerator temperature maintained their quality and extended shelf life. Studies conducted on minimally processed carrots indicate that due to the high initial oxygen concentration in the packaging, oxygen is not fully consumed, even though the carbon dioxide percentage increases during

storage. At refrigerator temperature, the quality of carrots with edible coating did not decrease; the coating created a barrier that reduced moisture loss, while the control samples experienced color fading and surface drying due to dehydration.

The best results from the starch coatings were achieved with formulation number 4 with 5% corn starch and 0.5% citric acid and 1% spices (w/v). The appearance of those samples are presented at the Figure 3.

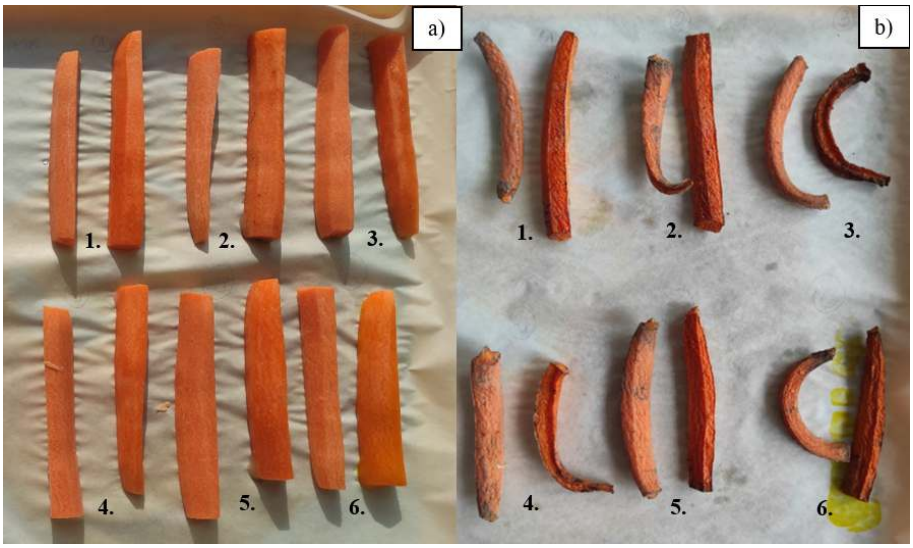

Figure 3 *Carrot slices coated with starch edible coating with 6 spices: 1. Fresh garlic; 2. Black pepper; 3. Thyme; 4. Salt; 5. Ground ginger; 6. Ground turmeric. Left: control sample; right: edible coating labeled with corresponding numbers: a) Day 1; b) Day 18 of monitoring.*

Visually, the carrot slice with the edible coating containing fresh garlic appeared the best, followed by the ones with black pepper and ground ginger. The slices were soft and easily bendable, with an uneven, rough surface. However, an intense orange color was retained even after the 18th day, without visible signs of darkening, indicating good protection against oxidation compared to the control samples, which showed whitening and mold development. The edible coating served as a barrier against visible microbiological spoilage and contributed to color retention.

At the Figure 4 the appearance of the carrot slices coated with sodium alginate is presented.

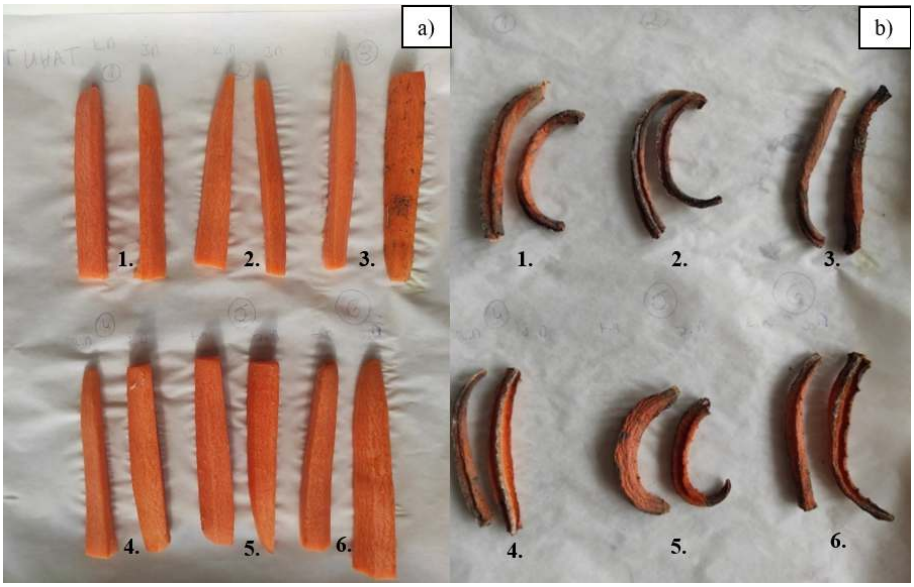

Figure 4 *Carrot slices coated with sodium alginate-based edible coating with 6 spices: 1. Turmeric powder; 2. Ginger powder; 3. Salt; 4. Black pepper; 5. Fresh garlic; 6. Thyme. Left: control samples; right: edible coatings labeled with corresponding numbers. a) Day 1; b) Day 18 of monitoring.*

The poorest results were obtained with formulation number 5, containing sodium alginate. On the eighteenth day, dark discoloration and visible mold growth were observed on the carrot pieces. This coating did not provide adequate microbiological protection. Furthermore, it appears that the sodium alginate did not form a homogeneous, elastic coating, leading to micro-cracks and increased exposure to oxygen. Since the dipping method was used for the application of the edible coating, uneven coating thickness may have occurred, causing the development of oxidation zones and uneven color changes. As a result, some parts of the carrot darkened more quickly. The samples were dry, with darkened and shriveled edges, and the surface was rough and coarse. The appearance of the coated samples was nearly identical to that of the control samples.

The appearance of the slices covered with the gelatin/olive oil coatings is presented at the Figure 5.

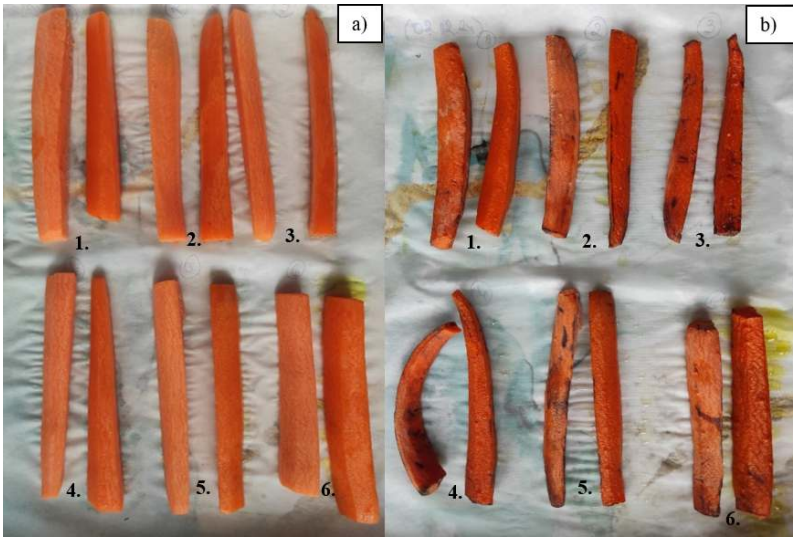

Figure 5 *Carrot pieces coated with an edible gelatin and olive oil coating with 6 spices: 1. Fresh garlic; 2. Black pepper; 3. Thyme; 4. Salt; 5. Ground ginger; 6. Ground turmeric. Left: control samples; right: edible coatings labeled with corresponding numbers. a) Day 1; b) Day 18 of monitoring.*

The best results among all coatings were obtained with the gelatin and olive oil coating. On the first day, the carrot pieces had a fresh appearance, an intense orange color, and a smooth, glossy surface due to the added olive oil. On the eighteenth day, it was evident that this type of coating resulted in the lowest moisture loss. Although the texture was slightly altered—the pieces became soft and elastic—the surface did not become completely dry as in other experiments. The color was retained and even intensified. The best sensory characteristics were observed in the carrot pieces coated with the gelatin and olive oil edible coating containing fresh garlic and ground ginger. The orange color was preserved, and there were no signs of discoloration or spoilage. Changes in texture were observed as early as day 5, suggesting that the shelf life for optimal quality retention is limited to 5 days when stored at refrigerated temperature.

In terms of weight loss, the best results were achieved with the gelatin and olive oil coating with fresh garlic and ground ginger. The results are presented in Figure 6.

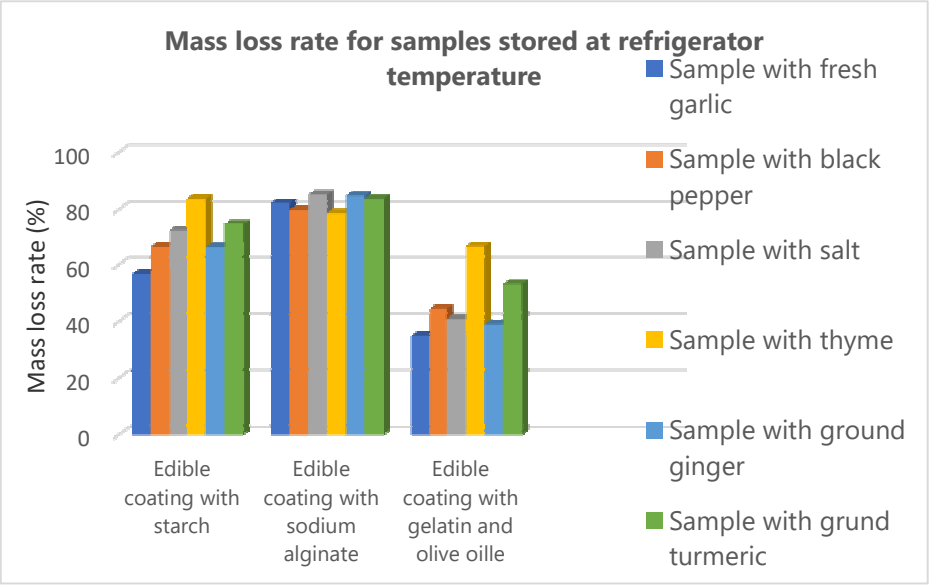

Figure 6 *Mass loss rate for samples stored at refrigerator temperature*

CONCLUSIONS

In this study, the effect of edible coatings on sliced carrot pieces was examined in terms of mass loss and sensory characteristics.

The first four experiments showed that the starch-based edible coating successfully prevented microbiological spoilage and preserved the color of the carrots, but did not provide an adequate barrier against moisture loss. The carrot pieces coated with this formulation became dry, with curled edges and a rough texture. The mass loss rate was high for all samples, both at room temperature and in the refrigerator.

Storage at low temperature, in a refrigerator, significantly reduced the mass loss rate compared to storage at room temperature, highlighting the importance of controlled conditions when storing minimally processed carrots before considering the packaging atmosphere. Packaging in a nitrogen atmosphere at room temperature did not yield positive results, as it led to softening, undesirable odors, and slimy surfaces as a result of anaerobic catabolism.

The best results were obtained with the gelatin-based edible coating with olive oil, especially in combination with fresh garlic, which proved to be a strong antimicrobial agent. This coating resulted in the lowest mass loss values and the best sensory characteristics. Additionally, ginger powder also contributed to the preservation of good sensory properties. The lipid component helped retain moisture, and the carrots maintained a fresh appearance and intense orange color even on the eighteenth day.

The results indicate that long-term preservation of the quality of minimally processed carrots requires an appropriate combination of edible coating, proper packaging, and optimal storage conditions, with temperature playing a key role in preventing spoilage and preserving sensory properties.

The innovation in edible coatings for fresh, ready-to-use vegetables represents a significant step toward sustainable packaging and quality preservation of products. These coatings are based on natural materials that create a protective layer, extending shelf life and maintaining the fresh appearance of vegetables. Modern consumers seek products that are eco-friendly, safe, and free of artificial additives, making edible coatings an ideal solution. Additionally, they allow for the preservation of texture and aroma in fresh vegetables, which is crucial to meeting consumer expectations. Such innovations align with the trend of a healthy lifestyle and responsible consumption.

REFERENCES

1. F. Villafañe, Edible coatings for carrots, *Food Reviews International* **33**(1) (2017) 84-103. https://doi.org/10.1080/87559129.2016.1150291
2. G.I Olivas, G.V. Barbosa-Cánovas, Edible coatings for fresh-cut fruits, *Critical Reviews in Food Science and Nutrition* **45**(7-8) (2005) 657-70. https://doi.org/10.1080/10408690490911837
3. A. Valdés, A.C. Mellinas, M. Ramos, N. Burgos, A. Jiméneza, M. C. Garrigós Use of herbs, spices and their bioactive compounds in active food packaging, RSC Advances **5** (2015) 40324-40335. https://doi.org/10.1039/C4RA17286H
4. Z. Ayhan, O. Esturk, E. Tas, Effect of modified atmosphere packaging on the quality and shelf life of minimally processed carrots, Turkish Journal of Agriculture and Forestry **32**(1) (2008) 57-64.

AN INVESTIGATION OF WATER QUALITY IN THE LARGEST LAKE OF THE MARMARA REGION

Cem Tokatlı

Trakya University, Evrenos Gazi Campus, Department of Laboratory Technology, İpsala, Edirne, Türkiye

tokatlicem@gmail.com

Abstract: *İznik Lake, located in the Marmara Region of Türkiye, holds significant ecological, historical, and socio-economic importance. Therefore, preservation of İznik Lake is vital for maintaining ecological balance, cultural heritage, and economic stability in the region. Despite the mentioned importances, İznik Lake is subject to significant pollution from surrounding anthropogenic activities. This study undertook a comparative hydrochemical assessment of the water quality in the west (WC-İL) and east (EC-İL) coasts of İznik Lake. During the winter season of 2025, water samples were collected and analyzed for 11 limnological parameters: Electrical Conductivity (EC), Total Dissolved Solids (TDS), salinity, Dissolved Oxygen (DO), O2 saturation, pH, turbidity, Suspended Solids (SS), nitrite nitrogen (NO_2-N), orthophosphate phosphorus (PO_4-P), and Chemical Oxygen Demand (COD). The findings indicated that the water of WC-İL exhibited a more alkaline character than EC-İL. Although the salinity parameter data of coasts were quite close to each other, the organic pollution parameter data were much higher in EC-İL than in WC-İL. Also, NO_2-N and PO_4-P values in water of EC-İL were 1.5 – 2 times higher than in water of WC-İL, respectively.*

Keywords: İznik Lake, Water quality, Risk assessment.

INTRODUCTION

Over the past century, industrial activities, agricultural practices, and the overexploitation of natural resources have substantially contributed to environmental degradation, exerting adverse effects on all components of the biosphere. Freshwater contamination poses a critical threat to aquatic ecosystems, disrupting their natural balance and leading to severe ecological and public health concerns, including biodiversity loss [1 – 5]. The excessive influx of contaminants, particularly nutrient-rich agricultural runoff and wastewater discharge, promotes algal blooms, particularly in lentic ecosystems [6 – 10]. These pollutants accumulate in aquatic organisms, facilitating the bioaccumulation and biomagnification of toxins through trophic levels, ultimately posing risks to higher predators and human health [11 – 15]. Key physicochemical parameters, including oxygenation, turbidity, salinity, and nitrogen-phosphorus concentrations, are essential for the stability of aquatic

ecosystems; however, their imbalance can lead to profound ecological disturbances [16 – 20].

İznik Lake is a large freshwater lake located in northwestern Türkiye. With a surface area of approximately 298 km² and an average depth of 10 meters, it is the country's fifth-largest natural lake. The lake is primarily fed by small streams and groundwater, while its outflow occurs through the Karsak Stream, which connects it to the Marmara Sea. İznik Lake serves as a critical habitat for various fish species, including endemic and economically significant ones, and supports a diverse range of aquatic birds. However, the lake faces increasing environmental pressures due to agricultural runoff, domestic wastewater, and industrial discharges. Excessive nutrient input, particularly nitrogenous and phosphorous compounds, has led to eutrophication, while declining dissolved oxygen levels and rising salinity pose significant threats to aquatic biodiversity. Given its ecological and economic importance, urgent conservation measures are necessary to mitigate pollution and ensure the long-term sustainability of İznik Lake [21]. This study undertook a comparative hydrochemical assessment of the water quality in the west (WC-İL) and east (EC-İL) coasts of İznik Lake.

EXPERIMENTAL

Selected Locations and Water Collection

Figure 1 provides a detailed map of the lake under investigation, highlighting the specific sampling locations that were strategically selected for the study. The water sampling was conducted with great precision during the winter season of 2025 to ensure the collection of relevant data during this specific time frame. In order to accurately represent the subsurface water quality, water samples were gathered using a telescopic water sampler, designed to collect samples at a distance of approximately 2.5 to 3 meters from the shoreline. This distance was chosen to reflect the typical subsurface conditions in the region of study. Following the collection process, the samples were carefully transferred into 500 mL polyethylene bottles, which were sealed and stored under controlled conditions at a constant temperature of 4°C to minimize any potential alterations in their composition, in accordance with the guidelines established by APHA [22]. Once the sampling process was completed, all samples were securely transported to Trakya University, where they were subjected to further, detailed chemical analyses.

Chemical Analysis

On-site measurements of several water quality parameters were conducted in the field to assess the aquatic conditions. These parameters included Electrical

Conductivity (EC), Total Dissolved Solids (TDS), salinity, Dissolved Oxygen (DO), oxygen saturation, pH, and turbidity. Measurements were performed using a multiparameter device (Hach Lange – HQ40D) and a turbidimeter (Hach Lange – 2100Q), as outlined by APHA [22, 23].

For laboratory analysis, Suspended Solids (SS), nitrite nitrogen (NO_2-N), phosphate phosphorus (PO_4-P), and Chemical Oxygen Demand (COD) levels were determined in filtered water samples. The filtration was carried out using a 0.45 µm cellulose nitrate filter, in accordance with APHA [22]. These filtered samples were then analyzed using a colorimeter (Hach Lange – DR890) and a spectrophotometer (Hach Lange – DR3900) to accurately quantify the chemical parameters.

Figure 1 *Study area and selected stations*

RESULTS AND DISCUSSIONS

The measured water quality parameters of WC-İL and EC-İL are presented in Figure 2. The results indicate that the water of WC-İL (pH: 8.31) exhibited a more pronounced alkaline character compared to EC-İL (pH: 7.44). Despite this variation, both stations met the criteria for first-class water quality in terms of pH, which falls within the acceptable range of 6–9 (TSWQR, 2021). Similarly, the dissolved oxygen (DO) concentrations in WC-İL (8.33 mg/L; O_2 saturation: 93.8%) and EC-İL (8.82 mg/L; O_2 saturation: 99.6%) were relatively comparable, with both stations classified as first-class in terms of DO levels (>8 mg/L) [24].

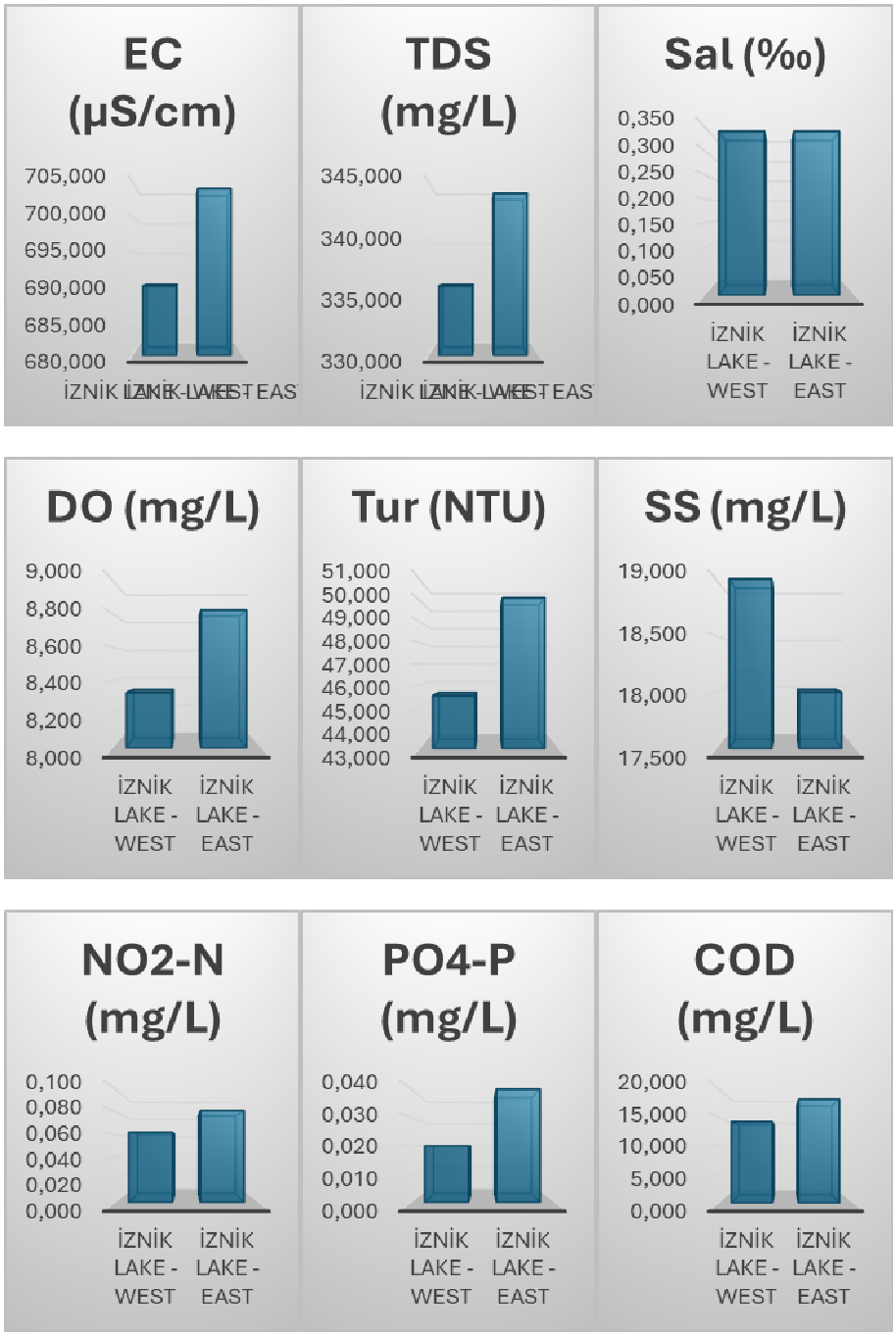

Figure 2 *Limnologic variables detected in water of WC-İL and EC-İL*

The turbidity and suspended solids (SS) levels in both stations also showed minor differences, with WC-İL exhibiting a turbidity of 45.5 NTU and SS concentration of 19 mg/L, while EC-İL recorded slightly higher values of 50.1 NTU and 18 mg/L, respectively. Despite these slight variations, the overall similarity in these parameters suggests relatively stable hydrodynamic and sedimentary conditions across the two coastal regions of İznik Lake.

In terms of salinity-related parameters, both WC-İL (EC: 690 µS/cm; TDS: 336 mg/L; salinity: 0.34‰) and EC-İL (EC: 704 µS/cm; TDS: 344 mg/L; salinity: 0.34‰) exhibited comparable values. However, based on electrical conductivity (EC) levels, both stations were classified as second-class water quality, as their EC values ranged between 400 and 1000 µS/cm [24]. This classification indicates a moderate level of dissolved ions in the water, which may be influenced by geological formations, anthropogenic activities, or seasonal variations in hydrological inputs.

Furthermore, while the chemical oxygen demand (COD) values were slightly elevated in EC-İL (14.2 mg/L) compared to WC-İL (18.1 mg/L), both stations remained within the first-class water quality limit for COD (<25 mg/L) [24]. However, a more significant disparity was observed in terms of organic pollution indicators, particularly nitrite-nitrogen (NO_2-N) and phosphate-phosphorus (PO_4-P). EC-İL exhibited markedly higher concentrations of NO_2-N (0.062 mg/L) and PO_4-P (0.081 mg/L) compared to WC-İL (NO_2-N: 0.020 mg/L; PO_4-P: 0.040 mg/L). As a result, the water of WC-İL was classified as second-class for NO_2-N (0.01–0.06 mg/L) and first-class for PO_4-P (<0.05 mg/L), whereas EC-İL was classified as third-class for NO_2-N (>0.06 mg/L) but retained first-class status for PO_4-P (<0.05 mg/L) [24].

CONCLUSIONS

In this research, water qualities of west (WC) and east (EC) coasts of İznik Lake (İL) were investigated. The findings indicate that the water quality of both the west (WC-İL) and east (EC-İL) coasts of İznik Lake generally falls within acceptable limits, with minor variations between the two stations.

The water of WC-İL exhibited a more alkaline character than EC-İL, but both stations met the first-class water quality standards for pH and dissolved oxygen (DO). Similarly, turbidity and suspended solids (SS) levels were comparable at both locations. While the salinity parameters were nearly identical, both stations were classified as second-class in terms of electrical conductivity (EC). Notably, the chemical oxygen demand (COD) values remained within first-class water quality limits at both stations. However, organic pollution indicators, specifically

nitrite-nitrogen (NO_2-N) and phosphate-phosphorus (PO_4-P), revealed significant differences between the stations. The EC-İL site exhibited considerably higher NO_2-N and PO_4-P levels than WC-İL, leading to a third-class classification for NO_2-N. Overall, while both stations maintain good water quality, localized variations highlight the influence of different environmental or anthropogenic factors affecting the east and west coasts of İznik Lake.

These findings underscore the necessity for continuous monitoring and targeted management strategies to mitigate localized pollution and preserve the lake's ecological balance. Also, the current results suggest that while the overall water quality of both coastal areas remains within acceptable limits for most parameters, the elevated levels of certain pollutants, particularly in EC-İL, may indicate localized sources of organic contamination. Such discrepancies highlight the need for ongoing water quality monitoring and potential mitigation measures to address site-specific pollution dynamics in İznik Lake.

Acknowledgements: This research was funded by Trakya University (Project Number: 2024/231).

REFERENCES

1. Y. Mia, A. R. T. İslam, J. N. Jannat, M. M. F. Jion, A. Sarker, C. Tokatlı, A. B. Siddique, S. M. İbrahim, V. Senapathi, Identifying factors affecting irrigation metrics in the Haor Basin using integrated Shannon's entropy, fuzzy logic and automatic linear model, *Environmental Research* **226** (2023), 115688.
2. C. Tokatlı, A. Uğurluoğlu, S. Muhammad, Ecotoxicological evaluation of organic contamination in the world's two significant gateways to the Black Sea using GIS techniques: Turkish Straits, *Marine Pollution Bulletin* **194** (2023), 115405.
3. B. Yüksel, F. Ustaoglu, H. Topaldemir, M. M. Yazman, C. Tokatlı, Unveiling the nutritional value and potentially toxic elements in fish species From Miliç Wetland, Türkiye: a probabilistic human health risk assessment using Monte Carlo simulation, *Marine Pollution Bulletin* **211** (2025), 117417.
4. S. Muhammad, A. Zeb, R. Ullah, S. Amin, A. Ahmad, C. Tokatli, Spatial distribution of drinking, irrigation water quality, and health risk indices of high-altitude lakes, *Physics and Chemistry of the Earth* Parts A/B/C **134** (2024), 103597.
5. S. Muhammad, T. Ahmed, S. Amin, C. Tokatlı, F. Ustaoğlu, Spatial distribution of hazard index via heavy metals consumption in water from the Himalayan lacustrine ecosystems, *Physics and Chemistry of the Earth* **138** (2025), 103858.
6. T. Atıcı, C. Tokatlı, A. Çiçek, Diatoms of Seydisuyu Stream Basin (Turkey) and assessment of water quality by statistical and biological approaches, *Sigma Journal of Engineering and Natural Sciences* **36** (2018), 271-288.

7. J. N. Jannat, M. S. I. Khan, H. M. T. Islam, M. S. Islam, R. Khan, M. A. B. Siddique, M. Varol, C. Tokatli, S. C. Pal, A. Islam, A. M. Idris, G. Malafaia, A. R. M. T. Islam, Hydro-chemical assessment of fluoride and nitrate in groundwater from east and west coasts of Bangladesh and India, *Journal of Cleaner Production* **372** (2022), 133675.
8. E. Mutlu, C. Tokatlı, A. R. M. T. Islam, M. S. Islam, S. Muhammad, Water quality assessment of Şehriban Stream (Kastamonu, Türkiye) from a multi-statistical perspective, *International Journal of Environmental Analytical Chemistry* **104** (19) (2024), 8229–8245.
9. C. Tokatlı, E. Mutlu, F. Ustaoğlu, A. R. T. Islam, S. Muhammad, Spatiotemporal variations, health risk assessment, and source changes of potentially toxic elements in potamic water of the Anday Stream Basin (Türkiye), Black Sea Region, *Environmental Monitoring and Assessment* **196** (2024), 420.
10. I. U. Din, W. Ali, S. Muhammad, M. R. Shaik, B. Shaik, I. Rehman, C. Tokatli, Spatial distribution and potential health risk assessment for fluoride and nitrate via water consumption in Pakistan, *Journal of Geochemical Exploration* **259** (2024), 107413.
11. R. Howarth, F. Chan, D. J. Conley, J. Garnier, S. C. Doney, R. Marino, G. Billen, Coupled biogeochemical cycles: eutrophication and hypoxia in temperate estuaries and coastal marine ecosystems, *Frontiers in Ecology and the Environment* **9** (2011), 18-26.
12. A. Borrell, V. Tornero, D. Bhattacharjee, A. Aguilar, Organochlorine concentrations in aquatic organisms from different trophic levels of the Sundarbans mangrove ecosystem and their implications for human consumption, *Environmental Pollution* **251** (2019), 681-688.
13. C. Tokatlı, M. Varol, Variations, health risks, pollution status and possible sources of dissolved toxic metal(loid)s in stagnant water bodies located in an intensive agricultural region of Turkey, *Environmental Research* **201** (2021), 111571.
14. F. Ustaoğlu, S. İslam, C. Tokatlı, Ecological and probabilistic human health hazard assessment of heavy metal in Sera Lake Nature Park sediments (Trabzon, Turkey), *Arabian Journal of Geosciences* **15** (2022), 597.
15. M. M. Yazman, B. Yüksel, F. Ustaoğlu, N. Şen, Y. Tepe, C. Tokatlı, Investigation of groundwater quality in the southern coast of the Black Sea: application of computational health risk assessment in Giresun, Türkiye, *Environmental Science and Pollution Research* **31** (2024), 52306–52325.
16. B. O. Isiuku, C. E. Enyoh, Pollution and health risks assessment of nitrate and phosphate concentrations in water bodies in South Eastern, Nigeria, *Environmental Advances* **2** (2020), 100018.
17. M. Varol, F. Ustaoğlu, C. Tokatlı, Ecological risks and controlling factors of trace elements in sediments of dam lakes in the Black Sea Region (Turkey), *Environmental Research* **205** (2022), 112478.
18. M. Varol, C. Tokatlı, Evaluation of the water quality of a highly polluted stream with water quality indices and health risk assessment methods, *Chemosphere* **311** (2023), 137096.
19. M. Varol, C. Tokatlı, Metals and phosphorus in the sediments of streams emptying into the Çanakkale strait (Dardanelles): spatial distribution, pollution status, risk assessment and source identification, *Environmental Research* **252** (2024), 118795.

20. C. Tokatlı, A. Uğurluoğlu, S. Muhammad, Spatiotemporal variations of organic contaminants and their ecotoxicological risk in the Uluabat Lake Basin, Türkiye: a Ramsar living wetland, *Physics and Chemistry of the Earth* **138** (2025), 103851.
21. https://www.marmara.gov.tr/ (access date: 03.03.2025)
22. APHA (American Public Health Association) *Standard methods for the examination of water and wastewater,* American Water Works Association, Washington, DC, 2017.
23. APHA (American Public Health Association) S*tandard methods for the examination of water and wastewater*, American Water Works Association, Washington, DC, 1998.
24. TSWQR (Turkish Surface Water Quality Regulation) *Turkish Surface Water Quality Regulation*, Ankara, Türkiye, 2021.

ASSESSING EUTROPHICATION RISKS IN İZNIK LAKE (TÜRKIYE) USING MODIFIED BIODEGRADABLE POLLUTION INDICES

Cem Tokatlı

Trakya University, Evrenos Gazi Campus, Department of Laboratory Technology, İpsala, Edirne, Türkiye

e-mail: tokatlicem@gmail.com

Abstract: *Due to their lentic and enclosed nature, lakes are more susceptible to organic pollution and eutrophication. İznik Lake, which is an ideal place for various recreational activities such as fishing, swimming and water sports, is the largest natural stagnant water ecosystem in the Marmara Region and has a rich biodiversity. Despite its natural beauty and importances, İznik Lake is exposed to organic pollution from surrounding agricultural activities, industrial discharges, domestic wastewater, and agricultural chemicals. This study evaluated and compared the eutrophication threat for the west (WC) and east (EC) coasts of the İznik Lake by means of some modified biodegradable contamination indices (MBCI) using Turkish Standards. For this purpose, nutrient pollution index (NPI), organic pollution index (OPI) and eutrophication index (EI) were selected as the organic pollution risk assessment indicators. Water samples were collected in the winter season of 2025 and measured for 4 limnological parameters (DO, COD, NO_2-N and PO_4-P) that are used to calculate the MBCIs. The results revealed that although the WC exhibits a lower potential eutrophication risk compared to EC, the water of both WC and EC were highly polluted and had an eutrophic character.*

Keywords: İznik Lake, Water quality, Risk assessment.

INTRODUCTION

Organic contaminants, particularly nutrients originating from agricultural runoff and wastewater, play a significant role in triggering algal blooms in lacustrine ecosystems [1 – 5]. These blooms, characterized by excessive algal proliferation, disrupt aquatic ecosystems by depleting dissolved oxygen, obstructing light penetration, and altering trophic interactions. Moreover, organic contamination contributes to the formation of hypoxic zones, where oxygen levels become critically low. Such hypertrophic and hypoxic conditions pose severe challenges to aquatic organisms, often resulting in mass mortality events among fish and invertebrates [6 – 8]. Assessing organic contaminants is essential for understanding their cumulative impacts on aquatic biodiversity, water quality, and overall ecosystem integrity [9 – 13]. A holistic approach is necessary to comprehensively evaluate aquatic ecosystem health and to develop effective

management strategies. Key indicators used for assessing eutrophication risks and the synergistic effects of organic contamination include the Nutrient Pollution Index (NPI), the Organic Pollution Index (OPI), and the Eutrophication Index (EI) [14 – 17].

İznik Lake, located in Bursa Province of Türkiye, is a deep freshwater lake with a surface area of approximately 298 km² and a maximum depth of 80 meters. It is primarily fed by small streams and groundwater, while its outflow occurs through the Karsak Stream, which connects it to the Marmara Sea. The lake supports diverse aquatic vegetation and provides habitat for various fish species, including economically important ones. Additionally, it serves as a crucial stopover site for migratory birds. Despite its ecological and economic significance, İznik Lake faces increasing environmental threats, particularly from agricultural runoff, domestic wastewater, and industrial discharges. Excessive nutrient input, especially nitrogenous and phosphorous compounds, has accelerated eutrophication, leading to deteriorating water quality and habitat degradation. Therefore, comprehensive conservation measures are urgently needed to mitigate pollution and safeguard the ecological integrity of İznik Lake [18]. This study evaluated and compared the eutrophication threat for the west (WC) and east (EC) coasts of the İznik Lake (İL) by means of some modified biodegradable contamination indices (MBCI) using Turkish Standards.

EXPERIMENTAL

Selected Locations and Water Collection

Figure 1 presents the map of the lake under investigation, highlighting the specific sampling locations that were carefully selected based on their relevance to the study. The water sampling process was conducted meticulously during the winter of 2025, ensuring the collection of accurate and representative data for this period. To capture subsurface water quality, samples were gathered using a telescopic water sampler, which allowed for the collection of water from approximately 2.5 to 3 meters from the shoreline. Once the samples were collected, they were immediately transferred into 500 mL polyethylene bottles, which were then sealed and stored at a constant temperature of 4°C, in accordance with the guidelines outlined by APHA [19]. This storage method was carefully chosen to minimize any changes in the water's chemical composition and to maintain the integrity of the samples for future analysis. After proper storage, the samples were securely transported to Trakya University, where they underwent a series of detailed chemical analyses to assess a variety of water quality parameters, providing a comprehensive understanding of the lake's environmental status.

Chemical Analysis

Dissolved Oxygen (DO) levels were measured on-site in the field, following the procedures outlined by APHA [19, 20], using a multiparameter device (Hach Lange – HQ40D). This allowed for real-time monitoring of oxygen concentrations in the water, providing essential data on the lake's aerobic conditions.

For more detailed chemical analysis, laboratory tests were performed on filtered water samples to determine the concentrations of nitrite nitrogen (NO_2-N), phosphate phosphorus (PO_4-P), and Chemical Oxygen Demand (COD). The filtration process was carried out using a 0.45 µm cellulose nitrate filter to ensure the removal of particulate matter, in accordance with APHA [20] guidelines. These filtered samples were then analyzed using a spectrophotometer (Hach Lange – DR3900), which provided precise measurements of the target chemical parameters, allowing for an in-depth assessment of the water quality.

Figure 1 *Study area and selected stations*

Ecological Indices

The details of the formulas and computation techniques for the modified biodegradable contamination indices (MBCI) applied in this study, based on the Turkish Standards [21], are provided in Table 1 [17]. These indices were carefully selected to assess the level of contamination and biodegradability in the water samples, ensuring an accurate representation of the environmental conditions.

Table 1 *Methods of applied modified organic pollution risk assessment indices*

Index	Calculation	Formula Explanations	Rating of Water Quality
NPI	$NPI = (C_N/MAC_N) + (C_P/MAC_P)$	C_N: The levels of NO_2-N in water sample C_P: The levels of PO_4-P in water sample MAC_N: The maximum limit of NO_2-N MAC_P: The maximum limit of PO_4-P	<1: No polluted 1-3: Moderate polluted 3-6: Considerable polluted >6: Very high polluted
OPI	$OPI = (COD/COD_S) + (NO_2\text{-}N/NO_2\text{-}N_S) + (PO_4\text{-}P/PO_4\text{-}P_S) - (DO/DO_S)$	COD: The chemical oxygen demand DO: Dissolved oxygen ...$_S$: Standard levels of variables	<0: Excellent water quality 0-1: Good water quality 1-2: Beginning to be polluted 2-3: Lightly polluted 3-4: Moderately polluted >4: Heavily polluted
EI	$EI = \frac{COD \times NO2-N \times PO4-P}{CODs \times NO2-Ns \times PO4-Ps}$	COD: The chemical oxygen demand ...$_S$: Standard levels of variables	EI > 1: Water quality is regarded as eutrophic

RESULTS AND DISCUSSIONS

The data for the calculated modified biodegradable contamination indices (MBCI) for the water of the west and east coasts of İznik Lake are presented in Figure 2. The results indicate that among the examined coastal areas of this important natural stagnant water body, EC-İL demonstrates a slightly higher potential eutrophication risk compared to WC-İL. According to the applied Modified Biodegradable Pollution Index (MBPI), it was determined that the water quality of both coasts of İznik Lake is considerably degraded, exhibiting high levels of pollution. Specifically, the Nutrient Pollution Index (NPI) was recorded as 6.60 for WC-İL and 8.90 for EC-İL, both falling into the "very high pollution" category. Similarly, the Organic Pollution Index (OPI) values were recorded as 6.13 for WC-İL and 8.52 for EC-İL, classifying both stations as "heavily polluted." These results further indicate that the lake exhibits an eutrophic nature, with an Eutrophication Index (EI) of 1.41 for WC-İL and a significantly higher EI of 4.69 for EC-İL, suggesting a more severe eutrophic state in the eastern region.

The widespread use of chemical fertilizers, which contain substantial amounts of nitrogenous and phosphorous compounds, is a common practice in agricultural lands surrounding the lake. These fertilizers, along with organic pollutants from agricultural runoff, can be transported into nearby water bodies through various pathways, including irrigation, precipitation, and soil erosion [22 – 23]. The accumulation of these pollutants in the lake contributes to excessive nutrient enrichment, further intensifying the risk of eutrophication. Additionally, domestic wastewater discharges from nearby settlements are believed to be a significant factor contributing to the high ecological risk index values and eutrophication indicators observed in the study.

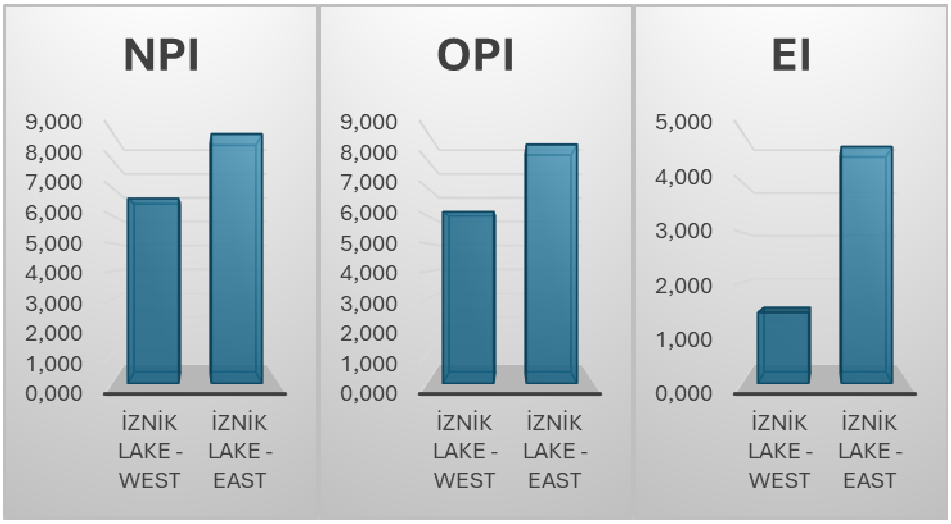

Figure 1 *Results of applied MBCI in water of WC-İL and EC-İL*

CONCLUSIONS

In this research, eutrophication threat for the west (WC) and east (EC) coasts of İznik Lake (İL) were compared and evaluated by means of some modified biodegradable contamination indices (MBCI) using Turkish Standards. The results indicate that both the west (WC) and east (EC) coasts of İznik Lake (İL) exhibit significant levels of biodegradable contamination, with EC-İL showing a slightly higher potential for eutrophication compared to WC-İL. The Modified Biodegradable Pollution Index (MBPI) analysis confirms that both coastal regions of the lake are highly polluted. Specifically, the Nutrient Pollution Index (NPI) values classify both stations as very highly polluted, while the Organic Pollution Index (OPI) results indicate heavy pollution. Furthermore, the Eutrophication Index (EI) confirms that both stations exhibit eutrophic characteristics, with EC-İL experiencing a more severe eutrophic state than WC-İL. These findings suggest that anthropogenic influences, particularly agricultural activities and domestic wastewater discharge, are the primary contributors to the observed high pollution levels and eutrophication risk. The extensive use of chemical fertilizers rich in nitrogen and phosphorus in surrounding agricultural areas likely contributes to nutrient runoff into the lake through irrigation, precipitation, and soil erosion. Given the severe ecological risks associated with these factors, implementing effective watershed management strategies, improving wastewater treatment infrastructure, and promoting sustainable agricultural practices are essential for mitigating pollution and preserving the ecological health of İznik Lake.

Acknowledgements: This research was funded by Trakya University (Project Number: 2024/231).

REFERENCES

1. T. Atıcı, C. Tokatlı, A. Çiçek, Diatoms of Seydisuyu Stream Basin (Turkey) and assessment of water quality by statistical and biological approaches, *Sigma Journal of Engineering and Natural Sciences* **36** (2018), 271-288.
2. F. Ustaoğlu, S. İslam, C. Tokatlı, Ecological and probabilistic human health hazard assessment of heavy metal in Sera Lake Nature Park sediments (Trabzon, Turkey), *Arabian Journal of Geosciences* **15** (2022), 597.
3. C. Tokatlı, A. Uğurluoğlu, S. Muhammad, Ecotoxicological evaluation of organic contamination in the world's two significant gateways to the Black Sea using GIS techniques: Turkish Straits, *Marine Pollution Bulletin* **194** (2023), 115405.
4. C. Tokatlı, E. Mutlu, F. Ustaoğlu, A. R. T. Islam, S. Muhammad, Spatiotemporal variations, health risk assessment, and source changes of potentially toxic elements in potamic water of the Anday Stream Basin (Türkiye), Black Sea Region, *Environmental Monitoring and Assessment* **196** (2024), 420.
5. S. Muhammad, T. Ahmed, S. Amin, C. Tokatlı, F. Ustaoğlu, Spatial distribution of hazard index via heavy metals consumption in water from the Himalayan lacustrine ecosystems, *Physics and Chemistry of the Earth* **138** (2025), 103858.
6. R. Howarth, F. Chan, D. J. Conley, J. Garnier, S. C. Doney, R. Marino, G. Billen, Coupled biogeochemical cycles: eutrophication and hypoxia in temperate estuaries and coastal marine ecosystems, *Frontiers in Ecology and the Environment* **9** (2011), 18-26.
7. A. Borrell, V. Tornero, D. Bhattacharjee, A. Aguilar, Organochlorine concentrations in aquatic organisms from different trophic levels of the Sundarbans mangrove ecosystem and their implications for human consumption, *Environmental Pollution* **251** (2019), 681-688.
8. Y. Mia, A. R. T. İslam, J. N. Jannat, M. M. F. Jion, A. Sarker, C. Tokatlı, A. B. Siddique, S. M. İbrahim, V. Senapathi, Identifying factors affecting irrigation metrics in the Haor Basin using integrated Shannon's entropy, fuzzy logic and automatic linear model, *Environmental Research* **226** (2023), 115688.
9. B. O. Isiuku, C. E. Enyoh, Pollution and health risks assessment of nitrate and phosphate concentrations in water bodies in South Eastern, Nigeria, *Environmental Advances* **2** (2020), 100018.
10. M. Varol, C. Tokatlı, Evaluation of the water quality of a highly polluted stream with water quality indices and health risk assessment methods, *Chemosphere* **311** (2023), 137096.
11. M. Varol, C. Tokatlı, Metals and phosphorus in the sediments of streams emptying into the Çanakkale strait (Dardanelles): spatial distribution, pollution status, risk assessment and source identification, *Environmental Research* **252** (2024), 118795.
12. M. M. Yazman, B. Yüksel, F. Ustaoğlu, N. Şen, Y. Tepe, C. Tokatlı, Investigation of groundwater quality in the southern coast of the Black Sea: application of computational

health risk assessment in Giresun, Türkiye, *Environmental Science and Pollution Research* **31** (2024), 52306–52325.
13. B. Yüksel, F. Ustaoglu, H. Topaldemir, M. M. Yazman, C. Tokatlı, Unveiling the nutritional value and potentially toxic elements in fish species From Miliç Wetland, Türkiye: a probabilistic human health risk assessment using Monte Carlo simulation, *Marine Pollution Bulletin* **211** (2025), 117417.
14. C. Tokatlı, M. Varol, Variations, health risks, pollution status and possible sources of dissolved toxic metal(loid)s in stagnant water bodies located in an intensive agricultural region of Turkey, *Environmental Research* **201** (2021), 111571.
15. M. Varol, F. Ustaoğlu, C. Tokatlı, Ecological risks and controlling factors of trace elements in sediments of dam lakes in the Black Sea Region (Turkey), *Environmental Research* **205** (2022), 112478.
16. S. Muhammad, A. Zeb, R. Ullah, S. Amin, A. Ahmad, C. Tokatli, Spatial distribution of drinking, irrigation water quality, and health risk indices of high-altitude lakes, *Physics and Chemistry of the Earth* Parts A/B/C **134** (2024), 103597.
17. C. Tokatlı, A. Uğurluoğlu, S. Muhammad, Spatiotemporal variations of organic contaminants and their ecotoxicological risk in the Uluabat Lake Basin, Türkiye: a Ramsar living wetland, *Physics and Chemistry of the Earth* **138** (2025), 103851.
18. https://www.marmara.gov.tr/ (access date: 03.03.2025)
19. APHA (American Public Health Association) *Standard methods for the examination of water and wastewater,* American Water Works Association, Washington, DC, 2017.
20. APHA (American Public Health Association) S*tandard methods for the examination of water and wastewater*, American Water Works Association, Washington, DC, 1998.
21. TSWQR (Turkish Surface Water Quality Regulation) *Turkish Surface Water Quality Regulation*, Ankara, Türkiye, 2021.
22. J. N. Jannat, M. S. I. Khan, H. M. T. Islam, M. S. Islam, R. Khan, M. A. B. Siddique, M. Varol, C. Tokatli, S. C. Pal, A. Islam, A. M. Idris, G. Malafaia, A. R. M. T. Islam, Hydro-chemical assessment of fluoride and nitrate in groundwater from east and west coasts of Bangladesh and India, *Journal of Cleaner Production* **372** (2022), 133675.
23. E. Mutlu, C. Tokatlı, A. R. M. T. Islam, M. S. Islam, S. Muhammad, Water quality assessment of Şehriban Stream (Kastamonu, Türkiye) from a multi-statistical perspective, *International Journal of Environmental Analytical Chemistry* **104** (19) (2024), 8229–8245.
24. I. U. Din, W. Ali, S. Muhammad, M. R. Shaik, B. Shaik, I. Rehman, C. Tokatli, Spatial distribution and potential health risk assessment for fluoride and nitrate via water consumption in Pakistan, *Journal of Geochemical Exploration* **259** (2024), 107413.

ECONOMIC INCENTIVES AND PUBLIC AWARENESS: DUAL ENGINES FOR DRIVING CARBON MITIGATION

Besa Shahini

University of Tirana, Faculty of Economy, Albania

besashahini@feut.edu.al

Abstract: *This presentation addresses the combined strength of economic incentives and public education in obtaining sustainable carbon emission reductions. The research examines the effect of financial development, industrial performance, and trade on CO2 emissions for EU and non-EU nations using strong empirical evidence analysis and theoretical models. The necessity to have well-thought out economic policies that are informed by economic realities and social justice is stressed in order to ensure maximum utilization of carbon decrease efforts. In Albania, 305 individuals were surveyed to estimate public awareness and opinion on CO2 emissions, climate change, and Carbon Capture and Storage (CCS). Although more aware of CO2 emissions and climate change, CCS awareness is low with the majority of the respondents not knowing this crucial mitigation technology. The research demonstrates the influence of media on public perception, observing that information is largely obtained from print, electronic, and social media, and hence can cause mass misconceptions. Methodologically, two dynamic panel regression models were employed to examine the data of 2000 to 2023. These models established that finance development is good for carbon emission in developing economies, something which is not aligned with developed economies. This is due to the fact that developing countries lack as strict environmental protection regulations and as intense industrialized economies as the former. Developed nations have their resources more focused on green finance as well as innovative ideas for the future in order to maintain ecosystems. The results highlight the importance of country-specific environmental policies that consider the individual economic and social context of each nation, and indicate that economic incentives and increased public awareness are key to successful carbon reduction.*

Keywords : Carbon mitigation, Public Awareness, Financial development, Policy

INTRODUCTION

This presentation explores the combined effectiveness of coupling economic mechanisms with targeted public education to foster a more robust and sustainable reduction in carbon emissions. This study explores the multifaceted role of economic tools—including financial development, Industrial index, and trade over $C0_2$ emission in EU and non-EU countries. The analysis draws on empirical evidence and theoretical frameworks to assess the effectiveness of economic factors in reducing emissions, highlighting the importance of carefully designed policies that account for economic realities and social equity concerns. Public awareness [1] and understanding of climate change are crucial for the

success of mitigation efforts. This study refers to the measurement of public awareness in Albania about CO2 emissions and carbon capture and storage, which are linked to climate change and renovated energy.

EXPERIMENTAL

I surveyed individuals from across Albania using a self-administered five-part questionnaire. The questionnaire consisted of 5 sections and examined their awareness and knowledge of CO2 emissions, climate change, and CCS. It also asked for their agreement or disagreement with implementing CCS in the future. 305 participants took part in the survey. According to empirical research, financial development [2] affects carbon emissions differently in various countries and regions. Considering the above limitations, I collected a comprehensive list of countries based on panel data from the EU (developed) and non-EU countries (developing) that fall on the European continent. Two dynamic panel regressions, (1) and (2), were conducted to examine the effects of financial development on carbon emissions from 2000 to 2022.

Developing: $CE_{it} = 0.85*CE_{it-1} + 0.02FD_{it} - 0.004Trade_{it} + 0.024INDUSTRIAL_{it} + \varepsilon_{it}$

(1)

Developing: $CE_{it} = 0.67*CE_{it-1} + 1.23*FD_{it} + 0.112*Trade_{it} + 0.98*INDUSTRIAL_{it} + \varepsilon_{i}$ *(2)*

CEit represents carbon emissions, while FDit signifies financial development. (financial institutions and markets) [3]; Trade refers to (Exp +Imp)/GDP; INDUSTRIAL refers to Industrial added value/GDP. The term "ε" represents the residual value, "i" refers to the country, while "t" means the time. The above model is estimated using the two-step estimation of the generalized method of moments [4] in EViews. Afterward, a test of serial correlation is conducted, which verifies the reliability and consistency of the estimators based on reference statistics.

RESULTS AND DISCUSSIONS

Utilizing dynamic panel regression models, the findings detailed the varying influences of financial development on carbon emissions across these groups over the years 2000-2023.

Developed Countries:

- *Model Findings:* The regression for developed countries indicated a coefficient of FD at 0.02, with a negative coefficient for trade (-0.004), and positive interaction of industrial activity (0.024) on carbon emissions.

- *Interpretation:* In those lands, the positive FD coefficient, though small, was statistically not significant. This means that during financial development, its direct effect on carbon emissions remains negligible. This could result from entrenched industrial systems, advanced technologies, and rigorous regulations that tend to favor sustainability without the need for any appreciable increments in financial development.

Developing Countries:

- *Model Findings*: The regression for developing countries had a very high FD coefficient of 1.23, with trade positively affecting carbon emissions by 0.112 and industrial activity having a considerable positive effect of 0.98.
- *Interpretation:* The FD coefficient is substantially positive in developing countries, indicating a far-reaching association of financial development with carbon emissions increase. This further shows that it's imperative to green the financial frameworks in this part of the world, where such growth baskets mainly capital-intensive projects and industrial pursuits, ignoring environmental considerations and hence reaping high carbon outputs.

The survey feedback presented in this session revealed an abysmal gap in public awareness, especially regarding CCS technologies. Whereas general knowledge about climate change and CO2 emissions was perceived to be much higher, actual understanding of CCS was characterized by misconceptions, as well as ignorance. The sources of knowledge for most of the participants were the different media, implying that media greatly influence public perception as well as understanding of environmental issues.

Implications for Policy and Education: The gaps in understanding among the surveyed will call for specific educational campaigns and focused communication strategies to enhance public awareness and support for CCS technologies. Media outreach and educational programs need to be enhanced to fill this gap in awareness and generate an informed public that works towards the acceptance and promotion of sustainable practice and technologies. The survey feedback and empirical analysis undertaken in this session raise the concern of what is perhaps a complex interplay between financial development, industrial activity, and public awareness in crystalizing carbon emission outcomes. For developed countries, finding a balance between financial development and environmental sustainability seems to work, though it does matter far less. However, in lesser-developed parts of the globe, financial development is greatly aggravating carbon emissions, therefore needing urgent mainstreaming of environmental consideration into the economic planning and development agendas. Furthermore, the gaps manifested in public awareness and education regarding

CCSs and other sustainable technologies warrant amplification of the efforts towards educational interventions that do not just provide information but actively engage the public to motivate proactive participation in carbon mitigation endeavors. These approaches are critical in realizing long-term sustainability objectives and must be contextualized to address the varied needs of the different regional constructions.

CONCLUSIONS

The study shows public awareness of CO2 emissions and climate change is higher than CCS's. This is due to some respondents needing to be made aware of CCS. The study also found that individuals surveyed had a range of misunderstandings relating to CO2 emissions, climate change, and CCS. Most of them had gained knowledge about these topics through various media channels, including print, electronic, and social media. These findings have significant implications for environmental policies towards C02 emissions in Albania. The study's empirical results showed that the FD coefficient is positive for developed countries but not statistically or economically significant. However, the coefficient of FD is positive and significant at the 5% level for emerging markets and developing countries. This indicates that financial development positively affects carbon emissions in emerging markets and developing countries, but there is no significant impact in developed countries. This result can be explained by the fact that developed countries generally have well-developed industries, systems, and strict environmental regulations. Enterprises typically prioritize investing in technology and innovation rather than expanding their scale. Meanwhile, the government tends to focus on promoting the growth of green finance, which results in increased funding for projects related to environmental protection.

Acknowledgements: This article/publication is based upon work (ITC Conference Grant) from TrANsMIT COST Action CA21127 "Techno-Economic Analysis of Carbon Mitigation Technologies" supported by COST (European Cooperation in Science and Technology). COST (European Cooperation in Science and Technology) is a funding agency for research and innovation networks. Our Actions help connect research initiatives across Europe and enable scientists to grow their ideas by sharing them with their peers. This boosts their research, career and innovation. Web: www.cost.eu

REFERENCES

1. Z. Ghazali, M. Zahid, T. Kee, M. Ibrahim**,** A step towards sustainable society : the awareness of carbon dioxide emissions, climate change and carbon capture in Malaysia, *International Journal of Economics and Financial Issues* **6** (2016) 179-187.
2. C. Jiang, X. Ma, The Impact of Financial Development on Carbon Emissions: A Global Perspective, *MDPI Sustainability* **11** (2019) 5241. https://doi.org/10.3390/su11195241
3. K Svirydzenka, Introducing a New Broad-Based Index of Financial Development, *IMF Working papers* **5** (2016), 1–42.
4. R. Blundell and S. Bond, Initial conditions and moment restrictions in dynamic panel data models, *J. Econom.* **87** (1998), pp. 115–143. https://doi.org/10.1016/S0304-4076(98)00009-8

The 2ndt Conference for Green Engineering, Sustainable Materials and Technologies for Circular Economy CIRC 2025 was supported by:


EVN
macedonia


БУЧИМ


VATROSTALNA
LLC SKOPJE


ПИВАРА СКОПЈЕ
Најдобрите од Македонија
19
24


M6
EDUCATIONAL
CENTRE SKOPJE
We see further ahead


МАКПРОГРЕС


TITAN
USJE


MAKSTIL


Vardar
Dolomit


АЛКАЛОИД
СКОПЈЕ


Alma M


varus
partnership through science